



HAL
open science

An automated approach to derive and optimise reduced chemical mechanisms for turbulent combustion

Nicolas Jaouen

► **To cite this version:**

Nicolas Jaouen. An automated approach to derive and optimise reduced chemical mechanisms for turbulent combustion. Fluid Dynamics [physics.flu-dyn]. Normandie Université, 2017. English. NNT : 2017NORMIR03 . tel-01522644

HAL Id: tel-01522644

<https://theses.hal.science/tel-01522644>

Submitted on 15 May 2017

HAL is a multi-disciplinary open access archive for the deposit and dissemination of scientific research documents, whether they are published or not. The documents may come from teaching and research institutions in France or abroad, or from public or private research centers.

L'archive ouverte pluridisciplinaire **HAL**, est destinée au dépôt et à la diffusion de documents scientifiques de niveau recherche, publiés ou non, émanant des établissements d'enseignement et de recherche français ou étrangers, des laboratoires publics ou privés.



Normandie Université

THÈSE

Pour obtenir le diplôme de doctorat

Spécialité Energétique

Préparée à l'INSA de Rouen Normandie

AN AUTOMATED APPROACH TO DERIVE AND OPTIMISE REDUCED CHEMICAL MECHANISMS FOR TURBULENT COMBUSTION

présentée et soutenue par

NICOLAS JAOUEN

**Thèse soutenue publiquement le 21 Mars 2017
devant le jury composé de**

C. ANGELBERGER	Expert combustion, IFP Énergies Nouvelles	Rapporteur
O. GICQUEL	Professeur à l'école Centrale Paris, EM2C - CNRS	Rapporteur
G. DAYMA	Professeur à l'université d'Orléans, ICARE - CNRS	Examineur
A. CAYRE	Expert combustion, Safran Aircraft Engines	Examineur
G. LODIER	Ingénieur de recherche, Air Liquide	Examineur
P. DOMINGO	Directrice de recherche CNRS, CORIA - CNRS	Directrice de thèse
L. VERVISCH	Professeur à l'INSA de Rouen, CORIA - CNRS	Co-directeur de thèse

■ **Thèse dirigée par Pascale DOMINGO et Luc VERVISCH, laboratoire CORIA (UMR 6614 CNRS)**

INSA | INSTITUT NATIONAL
DES SCIENCES
APPLIQUÉES
ROUEN NORMANDIE



UMR 6614
coRia
COMPLEXE DE RECHERCHE
INTERPROFESSIONNEL EN AÉROTHERMOCHIMIE

Abstract

Complex chemistry is an essential ingredient in advanced numerical simulation of combustion systems. However, introducing detailed chemistry in Computational Fluid Dynamics (CFD) softwares is a non trivial task since the time and space resolutions necessary to capture and solve for a flame are very often smaller than the turbulent characteristic scales by several orders of magnitude. A solution based on the reduction of chemical mechanisms is proposed to tackle this issue. An automated reduction and optimisation strategy is suggested relying on the construction of reference trajectories computed with the evolution of stochastic particles that face mixing, evaporation and chemical reactions. The methodology, which offers strong reduction in CPU cost, is applied to the derivation of several mechanisms for canonical and industrial applications, for simple fuel such as methane up to more complex hydrocarbon fuels, as kerosene, including an optimised lumping procedure for isomers.

Résumé

La complexité de la chimie joue un rôle majeur dans la simulation numérique de la plupart des écoulements réactifs industriels. L'utilisation de schémas cinétiques chimiques détaillés avec les outils de simulation actuels reste toutefois trop coûteuse du fait des faibles pas de temps et d'espaces associés à la résolution d'une flamme, bien souvent inférieurs de plusieurs ordres de grandeur à ceux nécessaires pour capturer les effets de la turbulence. Une solution est proposée pour s'affranchir de cette limite. Un outil automatisé de réduction de schémas cinétiques est développé sur la base d'un ensemble de trajectoires de références construites dans l'espace des compositions pour être représentatives du système à simuler. Ces trajectoires sont calculées à partir de l'évolution de particules stochastiques soumises à différentes conditions de mélange, de réaction et d'évaporation dans le cas de combustible liquide. L'ensemble est couplé à un algorithme génétique pour l'optimisation des taux de réaction du schéma réduit, permettant ainsi une forte réduction du coût calcul. L'approche a été validée et utilisée pour la réduction de divers mécanismes réactionnels sur des applications académiques et industrielles, pour des hydrocarbures simples comme le méthane jusqu'à des hydrocarbures plus complexes, comme le kérosène en incluant une étape optimisée de regroupement des isomères.

Acknowledgments (remerciements)

En premier lieu j'adresse de sincères remerciements à Mr Christian Angelberger, Mr Olivier Gicquel et Mr Guillaume Dayma pour avoir accepté de faire partie des membres de mon jury et pour les commentaires avisés qu'ils m'ont apportés.

Je tiens également à remercier mes encadrants de thèse, Pascale Domingo et Luc Vervisch. La relation de confiance que nous avons rapidement mise en place m'a permis de faire librement évoluer mes travaux de recherche constamment alimentés par leurs conseils inspirés. Pour rester côté CORIA, je souhaite vivement remercier Ghislain Lartigue et Vincent Moureau. Le duo qui m'a initié dès 2012, aux joies de la simulation numérique. C'est sans aucun doute à leur contact que m'est venu la motivation pour poursuivre sur cette folle aventure qu'est la thèse. De même, merci à Guillaume Ribert pour ses nombreux conseils.

J'ai réalisé ce doctorat dans le cadre d'un contrat CIFRE co-financé par Snecma (nouvellement Safran Aircraft Engines) et Air Liquide. Les nombreuses interactions que j'ai eu avec les ingénieurs des deux entités ont toujours été cordiales et enrichissantes. Je tiens tout particulièrement à adresser mes remerciements à Alain Cayre, Juan-Carlos Larroya ainsi qu'à Guillaume Lodier et Bernard Labegorre. J'ai beaucoup appris à leurs cotés...

Par peur d'omettre quelques noms (j'ai rencontré beaucoup trop de personnes exceptionnelles au cours de ces trois années), je vais simplement remercier ici tous mes collègues et amis. J'ai notamment une pensée particulière pour les quelques-uns qui m'auront supporté de près (parfois même de très près) du début à la fin de cette thèse et avec qui j'ai partagé du rire (lol, mdr, xptdr, doublechapeauchinois), un appartement, du sport, de la musique, des soirées (déguisées ou non), des voyages... Votre présence aura clairement marqué ma vie et j'espère avoir de nombreuses occasions de vous revoir. Pour finir, j'adresse mes plus chaleureux remerciements à la petite famille Jaouen. Sans votre soutien, cette thèse n'aurait très certainement pas abouti.

à ma colombienne ...

Contents

1	Introduction	21
1.1	Industrial context	21
1.1.1	Energy demand growth	21
1.1.2	Consequences	22
1.2	Thesis objectives	22
1.2.1	Importance of CFD tools in the combustion industries	22
1.2.2	Chemistry reduction for reactive flow simulations	23
1.3	Manuscript content	23
1.4	Publications	25
1.4.1	Peer-reviewed international journals	25
1.4.2	International conferences	25
2	Equations and models for reacting turbulent and two-phase flows	27
2.1	Equations to solve for reactive turbulent flows	28
2.1.1	Mixture properties	28
2.1.1.1	Mixture composition	28
2.1.1.2	Thermodynamic of the mixture	28
2.1.1.3	Equation of state	29
2.1.2	Conservation equations	30
2.1.2.1	Mass conservation	30
2.1.2.2	Momentum conservation	30
2.1.2.3	Species conservation	30
2.1.2.4	Energy conservation	31
2.2	Introduction to chemical kinetics	32
2.2.1	Species source terms	32
2.2.2	Reaction rates	33
2.2.2.1	Arrhenius law	33
2.2.2.2	Reverse reaction rate constant and equilibrium	34
2.2.2.3	Gibbs free energy	34
2.2.2.4	Reactions orders	35
2.2.2.5	Third-body reactions	35
2.2.2.6	Fall-off correction	36
2.2.3	Reducing the costs for solving chemistry	37
2.2.3.1	Chemistry reduction	37
2.2.3.2	Chemistry tabulation	38

2.3	Combustion regimes	38
2.3.1	Canonical problem: The perfectly premixed flame	39
2.3.1.1	Premixed flame structure	39
2.3.1.2	Simplified equations for freely propagating 1D flames	39
2.3.1.3	Controlling variables	40
2.3.1.4	Flame speed, flame thickness	41
2.3.2	Canonical problem: The diffusion flame	41
2.3.2.1	Passive mixture fraction	41
2.3.2.2	Steady strained diffusion flame	42
2.3.3	Partially premixed combustion	43
2.3.3.1	Combustion regimes in real systems	43
2.3.3.2	Stratified combustion	44
2.4	Aerothermochemical equations in the LES formalism	44
2.4.1	Introduction to turbulence	44
2.4.2	Strategies for the simulation of turbulent flows: RANS, LES, DNS	45
2.4.3	Filtered equations for LES	47
2.4.4	Sub grid modelling for turbulence	49
2.4.5	Turbulent combustion models	50
2.4.6	The thickened flame model: TFLES	51
2.4.6.1	Overall principal	51
2.4.6.2	Conditions for the thickening \mathcal{F}	51
2.4.6.3	Interaction between the flame and the turbulence	51
2.4.6.4	Dynamic TFLES	53
2.5	Numerical description of the liquid phase	54
2.5.1	Two-phase flows modelling	54
2.5.2	Equations for the Lagrangian description	54
2.5.2.1	Kinematic of the droplets	54
2.5.2.2	Evaporation	56
2.5.3	Coupling with the gaseous phase	59
2.5.3.1	Interaction between the dispersed phase and the gas	59
2.5.3.2	Formalism in LES	59
2.6	Numerical solvers	59
2.6.1	Chemistry 1D solver: CANTERA	60
2.6.2	Large-Eddy Simulation 3D solver: YALES2	60
3	A review on chemistry reduction methodologies	61
3.1	Introduction	62
3.1.1	Reduced mechanisms types	62
3.1.2	Basic kinetic simplifications	62
3.1.2.1	Pool chemical hypothesis	63
3.1.2.2	Rate-determining step	63
3.1.2.3	Quasi-steady state approximation	63
3.1.2.4	Partial equilibrium	64
3.1.2.5	Conserved properties	65
3.1.2.6	Lumping of reactions	65

3.2	The derivation of global mechanisms	66
3.2.1	Species and reactions selection	66
3.2.2	Optimisation of the chemical rates	67
3.2.3	Corrections functions	67
3.3	Reduction to skeletal mechanisms	68
3.3.1	Jacobian-based methodologies	69
3.3.1.1	Finding redundant species	69
3.3.1.2	Finding redundant reactions	69
3.3.2	Directed relation graph	70
3.3.3	Directed relation graph-aided sensitivity analysis	71
3.3.4	Directed relation graph with error propagation	71
3.3.5	Path flux analysis	72
3.3.6	Optimisation-based reduction	73
3.3.7	Species lumping	74
3.3.7.1	An automatic linear lumping procedure for isomers	74
3.4	Reduction based on analytical expressions	75
3.4.1	Selection of QSS species	76
3.4.1.1	Comparison of creation and destruction rates	76
3.4.1.2	Time scale analysis	78
3.4.1.3	LOI - Sensitivity	79
3.4.1.4	LTC - Concentration	79
3.4.1.5	Selecting the optimum QSS set using optimisation	80
3.4.2	Implementing the QSS assumption	81
3.4.2.1	Output global reaction rates	81
3.4.2.2	Output chemical source terms	82
3.4.3	Non-linearity of the algebraic system	82
3.4.3.1	Iterative procedure to solve a non-linear set of equations	83
3.4.3.2	Truncation of the non-linear direct or reverse part of the reactions	83
3.4.3.3	Lower the number of QSS species to linearise the system	83
3.4.4	QSS matrix simplification	84
3.4.4.1	Optimisation procedure to diagonalise sparse matrices	84
3.4.4.2	Identification of inter-dependent chemical species	85
3.5	Application: Methane-air combustion modelling	86
3.5.1	The history of methane chemistry modelling for flame simulation	86
3.5.1.1	Detailed kinetics	88
3.5.1.2	Reduced kinetics	90
3.5.2	Assessment of global and analytical reduced methane-air mechanisms	94
3.6	Conclusion	99
4	A reduction and optimisation strategy applied to premixed methane-air flames	101
4.1	Introduction	101
4.2	Optimisation strategy	102
4.2.1	Single-step optimisation methodology	102
4.2.1.1	Target profiles and chemical sources	102
4.2.1.2	Fitness function definition	103

4.2.1.3	Uncorrelated reactions solving	104
4.2.2	Genetic algorithm	104
4.3	Global chemistry for methane-air flames	108
4.3.1	Optimisation of a 3-step mechanism	108
4.3.2	Optimisation of a mechanism with 11 reactions	109
4.4	Skeletal and analytical chemistry for methane-air flames	113
4.4.1	DRGEP for species removal	113
4.4.2	DRGEP for reactions removal	114
4.4.3	Quasi-steady state assumption	114
4.4.4	Application	114
4.5	Conclusion	117
5	A new canonical problem for turbulent combustion	121
5.1	Introduction	121
5.2	Formalism	122
5.2.1	Lagrangian framework	122
5.2.2	Stochastic mixing of elementary particles	122
5.2.3	Evaporation	123
5.2.4	Deterministic closure	124
5.3	Test under the conditions of a methane-air jet flame in vitiated coflow	125
5.3.1	Problem settings	125
5.3.2	Impact of mixing time and number of particles	126
5.3.3	Global mechanism tests	127
5.3.4	Automated reduction with optimisation of the chemical rates	129
5.3.4.1	Application of DRGEP and QSS	129
5.3.4.2	Optimisation of the chemical rates	133
5.3.5	Results in stochastic micro-mixing, premixed and strained diffusion flame	133
5.3.5.1	Application to the two-inlet methane/vitiated-air problem	133
5.4	Application to a four-inlet methane/vitiated-air/hydrogen-air/steam problem	140
5.5	Conclusion	141
6	Reduced kinetics for the partial oxidation part of an auto-thermal reformer	143
6.1	Introduction	143
6.1.1	Syngas production	143
6.1.2	Canonical modelling of the flow in an ATR reactor	145
6.1.3	Mechanisms reduction	145
6.2	Conditions for the study and for the reduction	145
6.2.1	Flow composition	145
6.2.2	Preliminary equilibrium study	146
6.3	Reduced mechanisms for ATR reactors	149
6.3.1	Reduction of the RAMEC	149
6.3.1.1	Reference trajectories	149
6.3.1.2	DRGEP and QSS reduction	150
6.3.2	Other reductions	152
6.4	Reduced schemes assessment using RANS simulations	158

6.5	Conclusion	159
7	Application to kerosene-air combustion: CO and NO_x levels prediction	161
7.1	Introduction	161
7.1.1	Combustor design	162
7.1.2	Pollutants emissions	162
7.1.2.1	Certifications	162
7.1.2.2	CO formation	163
7.1.2.3	Influence of the operating conditions on the CO levels	163
7.1.2.4	NO _x formation	164
7.1.2.5	Influence of the operating conditions on the NO _x production	165
7.1.2.6	Constraints	166
7.1.3	LEMCOTEC project	167
7.2	Studied configuration	167
7.2.1	Multipoint injection	168
7.2.2	Previous LES study	168
7.3	Reduced chemical schemes for kerosene combustion	169
7.3.1	Kerosene oxidation detailed mechanisms	169
7.3.2	ORCh for kerosene	169
7.3.2.1	Stochastic particles definition and deterministic trajectories construction	170
7.3.2.2	Impact of the mixing on particles trajectories	170
7.3.3	Mechanism reduction	171
7.3.3.1	DRGEP analysis	172
7.3.3.2	Isomers lumping	173
7.3.4	QSS species and optimisation	176
7.3.5	Results and comparison between a surrogate composition and n-decane	178
7.3.5.1	Deterministic trajectories	178
7.3.5.2	Premixed response	179
7.3.5.3	QSS matrix simplification	180
7.3.6	Reduction limits	180
7.4	Large-Eddy Simulation of an ultra-low NO _x combustor	183
7.4.1	Numerical settings	183
7.4.1.1	Modelling of the injection, transport and evaporation of the n-decane droplets	184
7.4.1.2	TFLES settings	186
7.4.2	Simulation	186
7.4.2.1	Characteristic time of the flow	186
7.4.2.2	Topology of the reacting two-phase flow within the mono-sector	187
7.4.2.3	Pollutants levels: comparison with experimental measurements	190
7.5	Conclusion	190
8	Conclusions and perspectives	193
8.1	Conclusions	193
8.1.1	Global chemistry assessment	193
8.1.2	Reduction strategy relying on skeletal and analytical formalisms	194

8.1.3	A new canonical problem for reduction	194
8.1.4	Applications	195
8.2	Perspectives	196
8.2.1	Stochastic modelling	196
8.2.1.1	Enhancing the mixing model	196
8.2.1.2	Analysis of the impact of evaporation, dilution and staged combustion on the chemical reduction	196
8.2.2	Reduction methodology	197
8.2.2.1	Optimisation limits for large mechanisms	197
8.2.2.2	Correction function to recover flame speed for very reduced schemes .	197
8.2.3	Flame-turbulence interaction	197
8.2.4	Other applications	197
	Bibliography	199

Nomenclature

Abbreviations

Symbol	Description
ACARE	Advisory Council for Aeronautics Research in Europe
ARC	Analytically Reduced Chemistry
ATR	Auto Thermal Reforming
CAEP	Committee on Aviation environmental Protection
CFD	Computational Fluid Dynamics
CFL	Courant Friedrichs Lewy
CPU	Central Processing Unit
DNS	Direct Numerical Simulation
DRG	Directed Relation Graph
DRGEP	DRG with Error Propagation
FPI	Flame Prolongation of ILDM
FGM	Flamelet Generated Manifold
GA	Genetic Algorithm
HC	Unburned Hydrocarbons
ICAO	International Civil Aviation Organisation
ILDM	Intrinsic Low-Dimensional Manifold
INSA	National Institute of Applied Sciences
ISAT	In Situ Adaptative Tabulation
LAQ	Local Air Quality
LEMCO TEC	Low EMISSIONS CORE-Engine TECHNOLOGIES
LES	Large-Eddy Simulation
LOI	Level Of Importance
LPP	Lean Partially Premixed
LTC	Life Time analysis and Concentration
LTO	Landing Take-Off
MPI	Message Passing Interface

NOMANI	Nitrogen Oxide emission model with one-dimensional MANIfold
ODE	Ordinary Differential Equation
OPR	Overall Pressure Ratio
ORCh	Optimised Reduced Chemistry
PDF	Probability Density Function
PCM	Presumed Conditional Moments
PLIF	Planar Laser-Induced Fluorescence
POX	Partial Oxidation
PSR	Perfectly Stirred Reactor
PVC	Precessing Vortex Core
QSS	Quasi-Steady State
RANS	Reynolds-Averaged Navier-Stokes
RMS	Root Mean Square
SMR	Steam Methane Reforming
SMD	Mean Sauter Diameter
TFLES	Thickened Flame for Large-Eddy Simulation
YALES2	LES solver developed at CORIA

Roman letters

Symbol	Description	Unit
A_j	Pre-exponential factor of reaction j	Variable
c	Normalised progress variable	–
C_k	Consumption rate of species k	$\text{kg}\cdot\text{m}^{-3}\cdot\text{s}^{-1}$
C_p	Mixture mass heat capacity at constant pressure	$\text{J}\cdot\text{kg}^{-1}\cdot\text{K}^{-1}$
$C_{p,k}$	Specific heat capacity of species k at constant pressure	$\text{J}\cdot\text{kg}^{-1}\cdot\text{K}^{-1}$
C_p^m	Mixture molar heat capacity at constant pressure	$\text{J}\cdot\text{mol}^{-1}\cdot\text{K}^{-1}$
$C_{p,k}^m$	Molar heat capacity of species k at constant pressure	$\text{J}\cdot\text{mol}^{-1}\cdot\text{K}^{-1}$
C_S	Smagorinski model constant	–
C_W	Wale model constant	–
d_j	Droplet diameter for inlet j	m
D_k^H	Hirschfelder and Curtiss diffusion coefficient of species k	$\text{m}^2\cdot\text{s}^{-1}$
D_{kj}	Binary diffusion coefficient of species j into species k	$\text{m}^2\cdot\text{s}^{-1}$
d_p	Diameter of particle p	m
D_{th}	Thermal diffusivity coefficient	$\text{m}^2\cdot\text{s}^{-1}$
E_j	Activation energy of reaction j	$\text{J}\cdot\text{mol}^{-1}$

\mathcal{E}	Efficiency factor	–
\mathcal{F}	Thickening factor	–
F	Troe or Lindemann fall-off correction term	–
F_i	Component i of the force applied onto the Lagrangian particle	–
f	Fitness function for genetic algorithm	–
f_1	Fitness function for gradient-based optimisation	–
\mathcal{G}	Convolution kernel of the filter	–
H	Mixture mass enthalpy	J.kg ⁻¹
H_k	Mass enthalpy of species k	J.kg ⁻¹
H^m	Mixture molar enthalpy	J.mol ⁻¹
H_k^m	Molar enthalpy of species k	J.mol ⁻¹
h_s	Mass sensible enthalpy	J.kg ⁻¹
$h_{s,k}$	Mass sensible enthalpy of species k	J.kg ⁻¹
\mathcal{I}_k	Error assuming k in QSS	–
K_j	Arrhenius term of reaction j	Variable
K_0	Low pressure limit Arrhenius term of reaction j	Variable
K_∞	High pressure limit Arrhenius term of reaction j	Variable
$K_{\text{eq},j}$	Equilibrium constant of reaction j	–
K_{fj}	Forward Arrhenius term of reaction j	Variable
K_{rj}	Reverse Arrhenius term of reaction j	Variable
k_t	Turbulent kinetic energy	m ² .s ⁻²
L_e	Energetic length	m
L_v	Latent heat of evaporation	J.kg ⁻¹
l_k	Kolmogorov length	m
l_t	Integral length	m
L	Characteristic size of the flow	m
\mathcal{M}_k	Molecular formula of species k	–
m_p	Mass of particle p	kg
n	Normal to the flame front	–
N_{bits}	Number of chromosome binary digits	–
N_p	Number of stochastic particles	–
N_r	Number of reactions	–
N_{sp}	Number of species	–
P°	Reference pressure	Pa
P	Pressure	Pa
P_k	Production rate of species k	kg.m ⁻³ .s ⁻¹

P_r	Fall-off pressure correction term	mol.m^{-3}
\dot{Q}	External heat sources	W.m^{-3}
\dot{Q}_m	Total mass flow rate	kg.s^{-1}
\dot{q}_m	Elementary mass flow rate	kg.s^{-1}
\dot{q}_{mG}	Gaseous elementary mass flow rate	kg.s^{-1}
\dot{q}_{mL}	Liquid elementary mass flow rate	kg.s^{-1}
\dot{Q}_{fj}	Forward rate of reaction j	$\text{mol.m}^{-3}.\text{s}^{-1}$
\dot{Q}_i	Heat flux	W.m^{-2}
\dot{Q}_j	Rate of reaction j	$\text{mol.m}^{-3}.\text{s}^{-1}$
\dot{Q}_{rj}	Reverse rate of reaction j	$\text{mol.m}^{-3}.\text{s}^{-1}$
\mathcal{R}	Ideal gas constant	$\text{J.mol}^{-1}.\text{K}^{-1}$
r_{A-B}	DRG interaction of species 'B' to produce/consume species 'A'	–
r_{A-B}^*	DRGEP interaction of species 'B' to produce/consume 'A'	–
s	Stoichiometric ratio	–
S	Mixture mass entropy	$\text{J.kg}^{-1}.\text{K}^{-1}$
\mathbf{S}	Strain tensor	s^{-1}
\mathcal{S}	Flame sensor	–
S_{ij}	Strain tensor component	s^{-1}
S_k	Mass entropy of species k	$\text{J.kg}^{-1}.\text{K}^{-1}$
S^m	Mixture molar entropy	$\text{J.mol}^{-1}.\text{K}^{-1}$
S_k^m	Molar entropy of species k	$\text{J.mol}^{-1}.\text{K}^{-1}$
S_L^0	Laminar flame speed	m.s^{-1}
T	Temperature	K
T_{eq}	Equilibrium temperature	K
T_0	Fresh gases temperature	K
T°	Reference temperature	K
T^∞	Temperature in the ambient atmosphere surrounding a particle	K
\mathcal{T}_i	Threshold for lumping	–
\mathcal{T}_{QSS}	Threshold for the QSS analysis	–
\mathcal{T}_r	Threshold for the DRGEP reaction analysis	–
\mathcal{T}_s	Threshold for the DRGEP species analysis	–
t	Time	s
\mathbf{u}	Velocity vector	m.s^{-1}
u_i	Component i of the velocity vector	m.s^{-1}
$V_{c,i}$	Correction velocity of species k in direction i	m.s^{-1}
$V_{k,i}$	Diffusion velocity of species k in direction i	m.s^{-1}

W	Mean molecular weight	kg.mol^{-1}
W_k	Species k molecular weight	kg.mol^{-1}
\mathbf{x}	Vector of position	m
x_i	Component i of the position vector	m
X_k	Species k mole fraction	—
$[X_k]$	Species k concentration	mol.m^{-3}
Y_k	Mass fraction of species k	—
$Y_{k,\infty}$	Mass fraction of species k in the ambient atmosphere of a particle	—
$Y_{F,0}$	Fuel mass fraction in fresh gases	—
$Y_{O,0}$	Oxidiser mass fraction in fresh gases	—
$Y_{F,eq}$	Fuel mass fraction at equilibrium	—
Z	Mixture fraction	—

Greek letters

Symbol	Description	Unit
β_j	Temperature exponent for reaction j	—
β_k	Third body coefficient of species k	—
δ_{ij}	Kronecker symbol	—
δ_L	Laminar flame thickness	m
δ_L^{th}	Thermal thickness	m
Δ	Mesh size	m
$\Delta h_{f,k}^{\circ,m}$	Molar standard enthalpy of species k at reference conditions	J.mol^{-1}
ΔG_j°	Gibbs free energy change per mole of reaction j	J.mol^{-1}
ϵ	Viscous dissipation of the turbulent kinetic energy	$\text{m}^2.\text{s}^{-3}$
θ_k	Thermal diffusion coefficient of species k	$\text{m}^2.\text{s}^{-1}.\text{K}^{-1}$
θ	Source term for the Lagrangian phase	Variable
λ_{th}	Mixture thermal conductivity	$\text{W.m}^{-1}.\text{K}^{-1}$
μ	Dynamic viscosity coefficient	$\text{kg.m}^{-1}.\text{s}^{-1}$
ν	Kinematic viscosity coefficient	$\text{m}^2.\text{s}^{-1}$
ν_{kj}	$\nu_{kj}'' - \nu_{kj}'$	—
ν_{kj}'	Species k stoichiometric coefficient in the reactants of reaction j	—
ν_{kj}''	Species k stoichiometric coefficient in the products of reaction j	—
ρ	Density	kg.m^{-3}
ρ_0	Fresh gases density	kg.m^{-3}
ρ_k	Partial density of species k	kg.m^{-3}

ρ_p	Density of particle p	kg.m^{-3}
τ	Characteristic time	s
τ_{ij}	Viscous tensor	$\text{kg.m}^{-1}.\text{s}^{-2}$
χ_j	Thermal diffusion ratio of species j	K^{-1}
χ_q	Quenching dissipation rate	s^{-1}
$\dot{\omega}_k$	Mass reaction rate of species k	$\text{kg.m}^{-3}.\text{s}^{-1}$
$\dot{\omega}_T$	Combustion heat release	$\text{J.m}^{-3}.\text{s}^{-1}$

Mathematical operators

Symbol	Description
$\langle \phi \rangle$	Statistical averaging
$\bar{\phi}$	Spatial filtering
$\hat{\phi}$	Fourier transform
$\tilde{\phi}$	Favre averaging
ϕ'	Deviation from the mean: $\phi' = \phi - \langle \phi \rangle$
ϕ''	Fluctuations: $\phi'' = \phi - \bar{\phi}$

Non dimensional numbers

Symbol	Description
B_M	Mass Spalding number
B_T	Thermal Spalding number
Da	Damköhler number
Ka	Karlovitz number
Le_k	Lewis number associated to species k
Nu	Nusselt number
Pr	Prandtl number
Re	Reynolds number
Sc	Schmidt number
Sh	Sherwood number

Principal chemical species

Symbol	Description
CH	Methylidyne

CH ₂	Methylene
CH ₃	Methyl radical
CH ₄	Methane
CH ₂ O	Formaldehyde
CH ₃ O	Methoxy radical
C ₂ H ₂	Acetylene
C ₂ H ₃	Vinyl radical
C ₂ H ₄	Ethylene
C ₂ H ₅	Ethyl radical
C ₂ H ₆	Ethane
CO	Carbon monoxide
CO ₂	Carbon dioxide
H	Hydrogen atom
H ₂	Dihydrogen
H ₂ O	Water
HCO	Formyl radical
HO ₂	Hydroperoxyl radical
H ₂ O ₂	Hydrogen peroxide
O	Oxygen atom
OH	Hydroxyl radical
N ₂	Nitrogen
NO	Nitric oxide
N ₂ O	Nitrous oxide
NO ₂	Nitrogen dioxide

Chapter 1

Introduction

Contents

1.1 Industrial context	21
1.1.1 Energy demand growth	21
1.1.2 Consequences	22
1.2 Thesis objectives	22
1.2.1 Importance of CFD tools in the combustion industries	22
1.2.2 Chemistry reduction for reactive flow simulations	23
1.3 Manuscript content	23
1.4 Publications	25
1.4.1 Peer-reviewed international journals	25
1.4.2 International conferences	25

1.1 Industrial context

1.1.1 Energy demand growth

The world energy demand has more than doubled since the seventies and it is expected to grow a further 48% between 2012 and 2040 [1]. This increasing trend is attributed to two major reasons: (1) the growth of the earth's population and (2) the economic development of the emerging countries. The pie charts of Figure 1.1 show that despite the expansion of renewable energy, the major power sources largely come from the combustion of fossil fuels (oil, coal and natural gas) and biofuels. Cumulated they form a total contribution of 78.6% of the world energy consumption [2] in 2014. This reliance on fossil fuels may be curtailed in a few sectors including agriculture, commercial, public services and residential. Nevertheless there are industries for which this dependence is hardly replaceable. Transportation is the primary sector that is concerned and specifically air transportation. Indeed, although the traditional automobile will be largely replaced by electric cars in the next decades, creating electric planes is a more complicated challenge. The main reason for this, is that the energetic density of batteries is not going to reach anytime soon, the energetic density of fossil fuels. This dependence also applies to the process industries that often rely on the use of combustion to generate large amount of chemical compounds to be employed by other sectors including medical, chemical and electronic manufacturers.

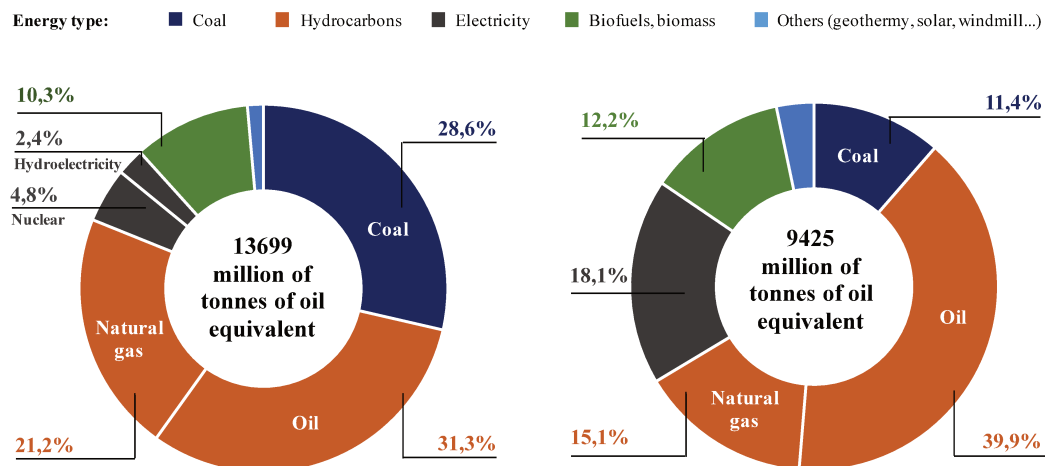


Figure 1.1: Fuel shares of world production (left pie chart) and of total final consumption (right pie chart) in the year 2014 [2].

1.1.2 Consequences

Consuming energy from these carbon rich combustibles comes at the expense of releasing tonnes of CO_2 into the atmosphere along with other toxic pollutants such as carbon monoxide, oxides of nitrogen and sulphur. These emissions have multiple impacts on human health and are responsible for a variety of environmental issues. First of all, the observed rise of the green-house gases such as CO_2 and H_2O results in an increase of the trapped thermal energy of the sun, leading to a global augmentation of the earth temperature. This phenomena is popularly known as global-warming. Secondly, oxides of nitrogen (NO and N_2O) cause ozone depletion resulting in the entry of the carcinogenic solar ultra violet rays. Finally, the partial oxides are known to cause acid rains and several other health problems.

In this respect, the optimisation of the burning systems that are used in process industries and in transportation is of primary importance. The objectives are toward the reduction of the pollutants emissions, and to ensure maximum benefit from the fuel that is consumed. To achieve this, the chemical transformation must be performed in optimal conditions so that the composition of the gases exiting the reactor or combustion chamber is understood and controlled.

1.2 Thesis objectives

1.2.1 Importance of CFD tools in the combustion industries

Computational Fluid Dynamics (CFD) is routinely used in a large variety of disciplines including ground, air and naval transportation, energy generation, chemical processing, medical and biological research, meteorology and astrophysics. CFD tools in the manufacture industries have shortened the time necessary for the process development, reduced the design costs by lowering the need for physical experiments and improved yield and product reliability. As a result, substantial economical benefits are achieved thanks to the use of CFD.

This particularly applies to the study and the design of combustion systems, for which experiments are difficult and expensive to install/operate essentially because of the temperature and pressure levels

achieved. Moreover, the operation of a burner is piloted by a complex multi-physic that couple fluid mechanics to chemistry under a variety of different time-scales. Depending on the application, the problem may be complicated by introducing liquid atomisation, evaporation, radiation effects, heat transfer through the combustor walls... The majority of these phenomena are already difficult to measure when seen separately. Capturing a detailed interaction of these physical effects within a real geometry is a true challenge than can be solved only with simulation. In that context, most of the combustion industries share the interest of being able to perform reactive flow simulations at reasonable costs.

1.2.2 Chemistry reduction for reactive flow simulations

The inclusion of complex chemistry plays a dominant role for the numerical simulation of most of the turbulent combustion applications found in industry. Indeed, predicting the CO, NO_x or soot emissions of a lean premixed gas turbine can only be achieved accounting for a finite-rate chemistry. The same applies to the chemical process industries. For instance, the estimation of the level of hydrogen leaving a Partial Oxidation (POX) system necessitates the use of a chemical solver. Introducing complex chemistry in CFD softwares is a non trivial task since the time and space resolutions necessary to capture and solve for a flame are very often smaller than the turbulent characteristic scales by several orders of magnitude. Moreover the number of scalars to be transported dramatically increases with the introduction of complex chemistry. As a consequence, the cost associated to reactive flow simulations becomes prohibitive.

Several solutions have been proposed to overcome this limitation. One typical approach consists of storing in a look-up table the chemical trajectories computed *a priori* from a reference canonical problem and for conditions which are limited to the study. A second well employed methodology relies on a simplified description of the chemical system through the introduction of a limited number of reactions. The present thesis is focused on the creation of an automated tool to derive such reduced combustion schemes.

1.3 Manuscript content

During this thesis, several reduced combustion mechanisms are constructed, gradually increasing the complexity of the employed reduction method and the complexity of the configuration to which the mechanisms apply. The methodology followed to end up with an automated reduction/optimisation tool (named ORCh) and for its use to create the reduced mechanisms is depicted within this manuscript along 8 chapters. An indicative content of the thesis is as follows:

Chapter 1: Context of the thesis

This chapter introduces the specific industrial context into which the study is set along with the importance of chemistry reduction. A description of the thesis objectives is then provided.

Chapter 2: Aerothermochemical equations

The manuscript first introduces the equations used to model reactive turbulent flows. The methods employed today for the calculation of the species thermodynamic, of the associated chemical equilibrium and of the source terms are highlighted. The combustion regimes are then presented with their specific characteristics. The chapter ends with a presentation of the interaction between turbulence, combustion and evaporating liquid droplets. The concepts for the modelling of the coupled effects are given.

Chapter 3: Literature review on chemistry reduction

Chapter three starts with a description of the concept behind chemistry reduction. The most significant reduction methodologies from the literature are then presented to end up with either global, skeletal or analytical mechanisms. The chapter ends with a short review of the existing relevant reduced combustion schemes for methane-air flames.

Chapter 4: Strategy for chemistry reduction

This chapter presents a reduction/optimisation approach relying on several existing methodologies. The optimisation procedure is first applied to global chemistry reduction. Then a methodology is depicted for the derivation of skeletal/analytical combustion mechanisms and for their optimisation. Both approaches are illustrated in the context of methane-air combustion for lean/stoichiometric mixtures and at atmospheric conditions.

Chapter 5: New canonical problem for chemistry reduction

A new reference problem is introduced in this chapter. This canonical approach is proposed to account for multiple inlet problems, for evaporation, for flames submitted to high levels of dilution and for heat losses conditions. The approach relies on the evolution (in terms of mixing, evaporation and reaction) of stochastic particles initiated to the specific conditions of the studied problem. A two-inlet and single phase methane flame developing in vitiated air is tested to validate the approach for chemistry reduction.

Chapter 6: An application for the Auto-Thermal Reforming (ATR) of methane

The proposed reduction/optimisation methodology constructed along the stochastic/deterministic trajectories is employed to derive reduced mechanisms for an ATR process operated by Air Liquide. First, a brief review of the methods used for the production of syngas are presented. Then several mechanisms are derived for the conditions of a chamber operating at very high pressure and in which fuel, oxidiser and steam are injected over three separated inlets. The reduced mechanisms are finally compared to the detailed ones over RANS simulations performed by Air Liquide.

Chapter 7: An application to kerosene combustion in aeronautical chambers

The applicability of the developed reduction and optimisation methodology is further demonstrated for pollutants prediction. It is applied to the conditions of an aero combustion chamber for the estimation of CO and NO_x levels. Several mechanisms are derived for several levels of accuracy in the reproduction of temperature, species mass fractions for diffusion and premixed flames and the estimation of the correct laminar freely propagating flame speed for a large range of equivalence ratios. The results of a 3D two-phase flow Large-Eddy Simulation (LES) are then presented based on a mechanism composed of 26 transported species and 338 chemical reactions for CO and NO_x prediction.

Chapter 8: Conclusion and perspectives

This last chapter provides general conclusions for the study of chemistry reduction and suggests perspectives in regards to the improvement of the developed reduction/optimisation approach and to its extension to other related reactive problems.

1.4 Publications

1.4.1 Peer-reviewed international journals

- N. Jaouen, L. Vervisch, P. Domingo, G. Ribert, *Automatic reduction and optimisation of chemistry for turbulent combustion modelling: Impact of the canonical problem*, *Combustion and Flame* 175, pp.69-79 (2017).
- N. Jaouen, L. Vervisch, P. Domingo, *Auto-thermal reforming (ATR) of natural gas: An automated derivation of optimised reduced chemical schemes*, *Proceedings of the Combustion Institute* 36(3), pp.3321-3330 (2017).

1.4.2 International conferences

- N. Jaouen, L. Vervisch and P. Domingo, *Auto-thermal reforming (ATR) of natural gas: An automated derivation of optimised reduced chemical schemes*, in 36th International Symposium on Combustion, Seoul, Korea (2016).
- N. Jaouen, L. Vervisch and P. Domingo, *An automated approach to derive and optimise reduced chemical schemes for oxy-fuel combustion*, in 1st International Workshop on Oxy-Fuel Combustion, Montabaur, Germany (2016).
- N. Jaouen, P. Domingo, L. Vervisch, *Using genetic algorithm for optimising reduced chemical-schemes for turbulent flames simulation*, in 15th International Conference on Numerical Combustion, Avignon, France (2015).
- N. Jaouen, P. Domingo, L. Vervisch, *Using genetic algorithm for automated optimisation of reduced chemical schemes*, in 7th European Combustion Meeting, Budapest, Hungary (2015).

Chapter 2

Equations and models for reacting turbulent and two-phase flows

Contents

2.1	Equations to solve for reactive turbulent flows	28
2.1.1	Mixture properties	28
2.1.2	Conservation equations	30
2.2	Introduction to chemical kinetics	32
2.2.1	Species source terms	32
2.2.2	Reaction rates	33
2.2.3	Reducing the costs for solving chemistry	37
2.3	Combustion regimes	38
2.3.1	Canonical problem: The perfectly premixed flame	39
2.3.2	Canonical problem: The diffusion flame	41
2.3.3	Partially premixed combustion	43
2.4	Aerothermochemical equations in the LES formalism	44
2.4.1	Introduction to turbulence	44
2.4.2	Strategies for the simulation of turbulent flows: RANS, LES, DNS	45
2.4.3	Filtered equations for LES	47
2.4.4	Sub grid modelling for turbulence	49
2.4.5	Turbulent combustion models	50
2.4.6	The thickened flame model: TFLES	51
2.5	Numerical description of the liquid phase	54
2.5.1	Two-phase flows modelling	54
2.5.2	Equations for the Lagrangian description	54
2.5.3	Coupling with the gaseous phase	59
2.6	Numerical solvers	59
2.6.1	Chemistry 1D solver: CANTERA	60
2.6.2	Large-Eddy Simulation 3D solver: YALES2	60

2.1 Equations to solve for reactive turbulent flows

2.1.1 Mixture properties

The subsequent composition and thermodynamic properties will be used to describe the mixture. They will serve for the definition of the aerothermochemical conservation equations.

2.1.1.1 Mixture composition

The mixture composition that is considered is assumed to rely on N_{sp} chemical species referenced by letter k . The mixture density is estimated from the sum of the partial density ρ_k of each chemical species,

$$\rho = \sum_{k=1}^{N_{\text{sp}}} \rho_k . \quad (2.1)$$

The species k mass fraction Y_k is defined by the species individual density to the mixture density ratio,

$$Y_k = \frac{\rho_k}{\rho} . \quad (2.2)$$

The definitions of equations 2.1 and 2.2 ensure that species mass fractions are bounded between zero and unity and that the sum of the N_{sp} mass fractions equals unity:

$$\sum_{k=1}^{N_{\text{sp}}} Y_k = 1 . \quad (2.3)$$

W is defined as the mean molecular weight of the mixture that is considered. It is computed from each species molecular weight W_k and from their mass fractions through the relation:

$$\frac{1}{W} = \sum_{k=1}^{N_{\text{sp}}} \frac{Y_k}{W_k} . \quad (2.4)$$

The molar fraction X_k of species k is then deduced from relation 2.5:

$$X_k = \frac{W}{W_k} Y_k , \quad (2.5)$$

and its concentration (number of moles per unit volume), from relation 2.6:

$$[X_k] = \frac{\rho_k}{W_k} . \quad (2.6)$$

2.1.1.2 Thermodynamic of the mixture

The molar heat capacity at constant pressure $C_{p,k}^m(T, P^\circ)$ of the species k is computed at standard pressure $P^\circ = 1$ atm according to the temperature T using the so-called NASA polynomials (relation 2.7) which have been designed in the early seventies to fit with experimental measurements:

$$\frac{C_{p,k}^m(T, P^\circ)}{\mathcal{R}} = a_{1,k} + a_{2,k}T + a_{3,k}T^2 + a_{4,k}T^3 + a_{5,k}T^4 , \quad (2.7)$$

where $\mathcal{R} = 8.314 \text{ J.mol}^{-1}.\text{K}^{-1}$ is the ideal gas constant.

Enthalpy and entropy variations are expressed as a function of the heat capacity at constant pressure through the relations:

$$H_k^m(T, P^\circ) = \int_{\theta=T^\circ}^T C_p^m(\theta, P^\circ) d\theta + \Delta h_{f,k}^{\circ,m}, \quad (2.8)$$

$$S_k^m(T, P^\circ) = \int_{\theta=T^\circ}^T \frac{C_p^m(\theta, P^\circ)}{\theta} d\theta, \quad (2.9)$$

in which $\Delta h_{f,k}^{\circ,m}$ refers to the molar standard enthalpy of formation of species k at reference pressure P° and reference temperature T° . The standard temperature is commonly set to the atmospheric conditions ($T^\circ = 298.15$ K) at which experiments are easier to perform. The NASA polynomials approximation is extended to the enthalpy and entropy properties through the relations,

$$\frac{H_k^m(T, P^\circ)}{\mathcal{R}T} = a_{1,k} + a_{2,k}T + a_{3,k}T^2 + a_{4,k}T^3 + a_{5,k}T^4 + \frac{a_{6,k}}{T}, \quad (2.10)$$

$$\frac{S_k^m(T, P^\circ)}{\mathcal{R}} = a_{1,k} \ln(T) + a_{2,k}T + a_{3,k}T^2 + a_{4,k}T^3 + a_{5,k}T^4 + \frac{a_{6,k}}{T} + a_{7,k}. \quad (2.11)$$

Note that the coefficient $a_{6,k} = \Delta h_{f,k}^{\circ,m} / \mathcal{R}$, which gives the relation $H_k^m(T^\circ, P^\circ) = \Delta h_{f,k}^{\circ,m}$ when species k is at standard pressure and temperature. For each chemical species, there is two sets of polynomials corresponding to low temperatures commonly ranging from 300 K to 1000 K and high temperatures which corresponds to variations between 1000 K and 5000 K.

The following mixture laws are used to find the molar thermodynamic properties of the mixture from species individual properties.

$$C_p^m(T, P, X) = \sum_{k=1}^{N_{sp}} X_k C_{p,k}^m(T, P^\circ), \quad (2.12)$$

$$H^m(T, P, X) = \sum_{k=1}^{N_{sp}} X_k H_k^m(T, P^\circ), \quad (2.13)$$

$$S^m(T, P, X) = \sum_{k=1}^{N_{sp}} X_k \left(S_k^m(T, P^\circ) - \mathcal{R} \ln \left(\frac{P}{P^\circ} \right) - \mathcal{R} \ln (X_k) \right). \quad (2.14)$$

Finally the mixture heat capacity at constant pressure expressed per unity of mass C_p , the mixture mass specific enthalpy H and mass specific entropy S are given by:

$$C_p = \frac{C_p^m}{W}, \quad (2.15)$$

$$H = \frac{H^m}{W}, \quad (2.16)$$

$$S = \frac{S^m}{W}. \quad (2.17)$$

2.1.1.3 Equation of state

The ideal gas law is an hypothesis that is frequently used in combustion and that relies on the assumptions that the molecules (1) behave as rigid spheres that are (2) homogeneously distributed on the macroscopic scale, that are (3) sufficiently separated from each other leading to negligible intermolecular forces and

that these molecules are submitted to (4) perfectly elastic collisions. Following this hypothesis, the following equation of state will be used all along this thesis:

$$P = \rho \frac{\mathcal{R}}{W} T = \rho \left(\sum_{k=1}^{N_{\text{sp}}} \frac{Y_k}{W_k} \right) \mathcal{R} T, \quad (2.18)$$

where ρ stands for the mixture density, W is the mixture mean molecular weight and $\mathcal{R} = 8.314 \text{ J}\cdot\text{mol}^{-1}\cdot\text{K}^{-1}$ is the ideal gas constant.

2.1.2 Conservation equations

Combustion takes place under the coupling of transport by velocity and diffusion, chemical kinetic and thermodynamic. First, the equations describing aerothermochemistry are given along with the associated thermodynamic and equilibrium principles. The derivation of the conservation equations is a non-trivial task which is reported in several publications including [3, 4]. The balanced equations express mass, momentum and energy conservations.

2.1.2.1 Mass conservation

The continuity equation that describes mass conservation reads:

$$\frac{\partial \rho}{\partial t} + \frac{\partial \rho u_i}{\partial x_i} = 0. \quad (2.19)$$

with u_i , the velocity projected on the i^{th} axis.

2.1.2.2 Momentum conservation

The equation of momentum expressed neglecting the volume force that acts on the fluid reads:

$$\frac{\partial \rho u_j}{\partial t} + \frac{\partial \rho u_i u_j}{\partial x_i} = -\frac{\partial P}{\partial x_j} + \frac{\partial \tau_{ij}}{\partial x_i}, \quad (2.20)$$

where τ_{ij} refers to the viscous tensor and is defined for Newtonian fluids by:

$$\tau_{ij} = -\frac{2}{3}\mu \frac{\partial u_k}{\partial x_k} \delta_{ij} + \mu \left(\frac{\partial u_i}{\partial x_j} + \frac{\partial u_j}{\partial x_i} \right), \quad (2.21)$$

in which μ describes the mixture dynamic viscosity and δ_{ij} is the Kronecker symbol.

2.1.2.3 Species conservation

Mass conservation applied to the conservation of the N_{sp} chemical species is written:

$$\frac{\partial \rho Y_k}{\partial t} + \frac{\partial}{\partial x_i} (\rho (u_i + V_{k,i}) Y_k) = \dot{\omega}_k, \quad (2.22)$$

where $\dot{\omega}_k$ is the species k chemical source term which must verify the relation:

$$\sum_{k=1}^{N_{\text{sp}}} \dot{\omega}_k = 0. \quad (2.23)$$

$V_{k,i}$ represents the diffusion velocity of species k in the direction i . It is written as a function of D_{kj} , a matrix constructed with the binary diffusion coefficients of species j into species k .

$$V_{k,i} = - \sum_{j=1}^{N_{sp}} D_{kj} d_{j,i} - \theta_k \frac{\partial \ln T}{\partial x_i} = - \sum_{j=1}^{N_{sp}} D_{kj} \left(d_{j,i} + \chi_j \frac{\partial \ln T}{\partial x_i} \right), \quad (2.24)$$

where θ_k is species k thermal diffusion coefficient, χ_j is the thermal diffusion ratio of species j which must satisfy $\sum_{j=1}^{N_{sp}} \chi_j = 0$ and with,

$$d_{k,i} = \frac{\partial X_k}{\partial x_i} + (X_k - Y_k) \frac{\partial \ln P}{\partial x_i}. \quad (2.25)$$

The evaluation of the diffusion velocities for the N_{sp} chemical species requires the inversion of a $N_{sp} \times N_{sp}$ matrix. The high cost associated to the resolution of this system often leads to the use of a ‘‘mixture averaged’’ simplified estimation proposed by Hirschfelder and Curtiss [5]:

$$D_k^H = \frac{1 - Y_k}{\sum_{j \neq k} X_j / D_{kj}} \quad (2.26)$$

The term $\chi_j \frac{\partial \ln T}{\partial x_i}$ in 2.24 is neglected since Soret and Dufour effects are not accounted for. Using this approximation with the Hirschfelder and Curtiss formulation, the diffusion velocity $V_{k,i}$ reads:

$$V_{k,i} = - \frac{D_k^H}{X_k} \frac{\partial X_k}{\partial x_i} + V_{c,i}. \quad (2.27)$$

$V_{c,i}$ is a correction velocity introduced to ensure mass conservation.

$$V_{c,i} = \sum_{k=1}^{N_{sp}} D_k^H \frac{W_k}{W} \frac{\partial X_k}{\partial x_i}. \quad (2.28)$$

Note that the term $\frac{\partial \ln P}{\partial x_i}$ in equation 2.25 is removed for this thesis because the thermodynamic pressure is spatially constant when using a low Mach number formalism.

2.1.2.4 Energy conservation

The conservation equation for the energy is written in terms of sensible enthalpy. The sensible enthalpy is expressed through the relation:

$$h_s(T) = \int_{\theta=T^0}^T C_p(\theta) d\theta, \quad (2.29)$$

and the corresponding conservation equation reads:

$$\frac{\partial \rho h_s}{\partial t} + \frac{\partial}{\partial x_i} (\rho u_i h_s) = \frac{DP}{Dt} + \frac{\partial Q_i}{\partial x_i} + \tau_{ij} \frac{\partial u_i}{\partial x_j} + \dot{Q} + \dot{\omega}_T. \quad (2.30)$$

The term Q_i represents the heat flux:

$$Q_i = \lambda_{th} \frac{\partial T}{\partial x_i} - \sum_{k=1}^{N_{sp}} (\rho h_{s,k} Y_k + P \chi_k) V_{k,i}, \quad (2.31)$$

where χ_k is the thermal diffusion ratio of species k and λ_{th} refers to the thermal conductivity of the mixture. The term \dot{Q} represents the external heat sources (for instance, coming from a spark or from radiative fluxes) and $\dot{\omega}_T$ is the chemical heat source term written:

$$\dot{\omega}_T = - \sum_{k=1}^{N_{sp}} \Delta h_{f,k}^0 \dot{\omega}_k \quad (2.32)$$

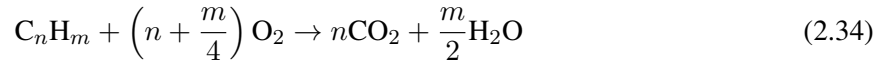
where $\Delta h_{f,k}^0$ is the formation enthalpy of species k . The operator $D \cdot / Dt$ is called the material derivative which corresponds to $D \cdot / Dt = \partial \cdot / \partial t + u_i \partial \cdot / \partial x_i$

Several approximations are set. The studied cases do not account for external heat sources, hence the source term \dot{Q} is neglected. The viscous forces term $\tau_{ij} \frac{\partial u_i}{\partial x_j}$ is not taken into account since it evolves like the square of the Mach number. Finally, without accounting for the Soret and Dufour effects, the initial formulation of the energy equation is simplified to:

$$\frac{\partial \rho h_s}{\partial t} + \frac{\partial}{\partial x_i} (\rho u_i h_s) = \frac{DP}{Dt} + \frac{\partial}{\partial x_i} \left(\lambda_{th} \frac{\partial T}{\partial x_i} \right) - \frac{\partial}{\partial x_i} \left(\rho \sum_{k=1}^{N_{sp}} h_{s,k} Y_k V_{k,i} \right) + \dot{\omega}_T. \quad (2.33)$$

2.2 Introduction to chemical kinetics

In reactive flows, the species source terms $\dot{\omega}_k$ that appear in equation 2.22 and the sensible enthalpy source term $\dot{\omega}_T$ of equation 2.32 are modelled from chemistry. Although in a global manner, the combustion of any hydrocarbon may be cast in the form of equation 2.34, in reality hundreds of species are involved interacting together over thousands of different reactions.



Some of these chemical reactions occur in both direct and reverse directions. From a macroscopic point of view, a system appears to be at equilibrium when the concentrations of the species are stable. However, on a microscopic level, both forward and backward reactions occur but at equal rates. The balance between the direct and reverse rates is described using an equilibrium constant computed from thermodynamic considerations.

Detailed mechanisms describing these chemical paths are found in the literature and are reliable today for the simulation of a large range of operating conditions (pressure, temperature, equivalence ratio). Unfortunately, these mechanisms cannot be directly used to compute for 3D turbulent combustion essentially because of the amount of chemical species i.e. the amount of transport equations involved and because of the tiny time and space resolutions necessary to capture the intermediate species that are present within these mechanisms. Several alternatives to lower the costs associated to the computation of such chemical schemes are found in the literature including the chemistry reduction and tabulation methodologies. The two approaches are briefly introduced below. The reduction approach will be discussed in detail over the following chapters since it is the primary subject addressed within this manuscript. First, the overall equations that govern chemical kinetics are given.

2.2.1 Species source terms

A chemical mechanism is made up of N_{sp} chemical species combined over N_r reversible reactions. The j^{th} reaction is associated to ν'_{kj} and ν''_{kj} which are respectively the reactants and products stoichiometric

coefficients associated to the chemical species k with molecular formula \mathcal{M}_k .

$$\sum_{k=1}^{N_{\text{sp}}} \nu'_{kj} \mathcal{M}_k \rightleftharpoons \sum_{k=1}^{N_{\text{sp}}} \nu''_{kj} \mathcal{M}_k, \text{ with } j = 1, N_r. \quad (2.35)$$

The rate associated to a given reaction j quantifies the mass variation of the chemical species involved within this reaction per unit of time:

$$\dot{Q}_j = \frac{\dot{\omega}_{kj}}{W_k \nu_{kj}}, \quad (2.36)$$

where $\nu_{kj} = \nu''_{kj} - \nu'_{kj}$. Species variation rates over every j^{th} reaction are deduced from relation 2.36, and the total reaction rate of species k corresponds to the sum of the $\dot{\omega}_{kj}$ over the N_r reactions of the mechanism:

$$\dot{\omega}_k = \sum_{j=1}^{N_r} \dot{\omega}_{kj} = W_k \sum_{j=1}^{N_r} \nu_{kj} \dot{Q}_j. \quad (2.37)$$

Summing the $\dot{\omega}_k$ source terms over the N_{sp} chemical species of the mechanism returns a null value, thus ensuring mass conservation.

2.2.2 Reaction rates

The reaction rate \dot{Q}_j of every reaction is computed from both direct and reverse rates.

$$\dot{Q}_j = \dot{Q}_{fj} - \dot{Q}_{rj} \quad (2.38)$$

The forward rate of the j^{th} reaction is modeled through the use of a relation that correlates the concentration of the reactants to a chemical constant K_{fj} . Same applies to the backward rate using this time, the products concentrations and K_{rj} , the reverse chemical constant of reaction j :

$$\dot{Q}_{fj} = K_{fj} \prod_{k=1}^{N_{\text{sp}}} [X_k]^{\nu'_{kj}}, \quad \dot{Q}_{rj} = K_{rj} \prod_{k=1}^{N_{\text{sp}}} [X_k]^{\nu''_{kj}}, \quad (2.39)$$

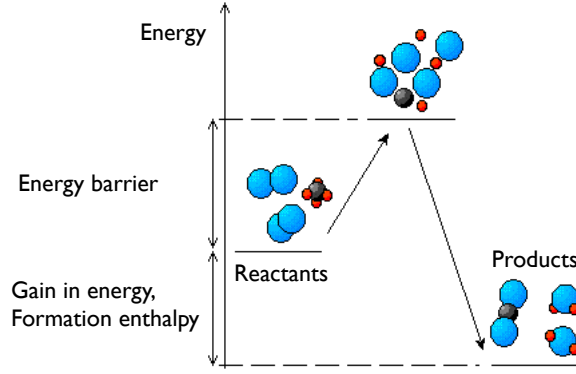
where $[X_k] = \rho Y_k / W_k$ refers to the molar concentration of species k .

2.2.2.1 Arrhenius law

The determination of the rate constant of a reaction has driven many experimental studies which have led to the description of empirical laws based on a temperature dependency. Conventionally, a modified Arrhenius form is used in combustion:

$$K_{fj} = \mathcal{A}_j T^{\beta_j} \exp\left(-\frac{E_j}{\mathcal{R}T}\right) \quad (2.40)$$

where the rate of the reaction K_{fj} is computed from the absolute temperature T of the mixture related to an activation energy E_j expressed in $\text{J}\cdot\text{mol}^{-1}$, an exponent β_j , a pre-exponential collision frequency factor \mathcal{A}_j and \mathcal{R} , the ideal gas constant. In many circumstances, the pre-exponential term is sufficient to account for the temperature dependence since binary elementary reactions behave in a classical Arrhenius way over a limited temperature range. However, to properly address the range of temperatures found in combustion, an additional dependence in temperature is introduced using the exponent β_j . The importance of the activation energy term E_j is illustrated on figure 2.1. To dissociate the initial reactants

Figure 2.1: Activation energy diagram E_j

into intermediate and radical species a sufficient amount of energy must be provided to the system. The dissociated species then recombine into more stable products while delivering energy through the form of heat. The process is called combustion, because in all cases, the volume of energy necessary to ensure the dissociation of the molecules is lower than the energy provided by the recombination step. The chemical process is exothermic.

2.2.2.2 Reverse reaction rate constant and equilibrium

The backward rate is balanced with the forward one defining an equilibrium constant. Equilibrium is achieved when the forward rate \dot{Q}_{fj} equals the backward rate \dot{Q}_{rj} , hence when:

$$K_{fj} \prod_{k=1}^{N_{sp}} [X_k]^{\nu'_{kj}} = K_{rj} \prod_{k=1}^{N_{sp}} [X_k]^{\nu''_{kj}} \quad (2.41)$$

The equilibrium constant is defined as the ratio of the reactants concentrations by the products concentrations:

$$K_{eq,j} = \prod_{k=1}^{N_{sp}} [X_k]^{\nu_{kj}} = \frac{K_{fj}}{K_{rj}} \quad (2.42)$$

The reverse reaction rate constant is deduced from $K_{rj} = K_{fj}/K_{eq,j}$ after computing for the equilibrium constant that is deduced from the thermodynamic properties of the species involved within reaction j . These thermodynamic properties are given from the computation of the Gibbs free energy.

2.2.2.3 Gibbs free energy

The estimation of the chemical equilibrium of a reaction necessitates the definition of the standard Gibbs free energy change. This reference state is used to describe the chemical potential of species and enables to quantify the difference in potential that exists between the reactants and the products of a given reaction. This is expressed, for the j^{th} reaction, through:

$$\Delta G_j^\circ = -\mathcal{R}T \ln K_{p,j}, \quad (2.43)$$

where index $^\circ$ refers to all the products and reactants in their standard state and $K_{p,j}$ is the equilibrium constant of reaction j expressed from the partial pressure of the species involved within reaction j . Note that the more negative is ΔG_j° , the larger is the equilibrium constant of reaction j and the more

spontaneous is the reaction. In addition, if the Gibbs free energy of the reactants of j is similar to the one of its products, the reaction has no tendency to proceed ($\Delta G_j^\circ = 0$). The equilibrium constant in pressure relates to the one in concentration terms $K_{eq,j}$ by:

$$K_{p,j} = K_{eq,j} \left(\frac{\mathcal{R}T}{P^\circ} \right)^{\sum_{k=1}^{N_{sp}} \nu_{kj}} \quad (2.44)$$

with P° , the reference pressure. Combining this relation with equation 2.43 allows to get an expression of the equilibrium constant in terms of concentrations $K_{eq,j}$ as a function of the standard Gibbs free energy variation across the j^{th} reaction, here expressed in terms of entropy and enthalpy change, respectively noted ΔS_j° and ΔH_j° .

$$K_{eq,j} = \exp \left(\frac{\Delta S_j^\circ}{\mathcal{R}} - \frac{\Delta H_j^\circ}{\mathcal{R}T} \right) \left(\frac{P^\circ}{\mathcal{R}T} \right)^{\sum_{k=1}^{N_{sp}} \nu_{kj}} \quad (2.45)$$

In practice, the entropy and enthalpy change necessary to calculate the equilibrium constants are computed from the NASA relations introduced in 2.10 and 2.11.

2.2.2.4 Reactions orders

The unit for the chemical rate constant and the unit for the pre-exponential factor \mathcal{A}_j varies with the order of the reaction. The \mathcal{A}_j in a reaction of 1st order is expressed in $s^{-1} \cdot K^{-\beta_j}$, of 2nd order in $m^3 \cdot mol^{-1} \cdot s^{-1} \cdot K^{-\beta_j}$ and the pre-exponential factor have the unit $m^6 \cdot mol^{-2} \cdot s^{-1} \cdot K^{-\beta_j}$ for 3rd order reactions .

2.2.2.5 Third-body reactions

Three-body reactions involve two species 'A' and 'B' as reactants and a third body 'M'. They yield as products, the species 'AB' and the unchanged catalyst species 'M' which is used to stabilise the excited product 'AB*' through the release of heat. On the contrary, in the reverse direction, heat provides the energy necessary to break the link between 'A' and 'B'. Although three-body reactions are described by only one Arrhenius equation, the chemical process undergoes the 3 steps detailed within table 2.1. The third body 'M' can be any inert molecule. The notation usually is $A + B + M \rightleftharpoons AB + M$. The

Forward direction	Backward direction
$A + B \rightarrow AB^*$	$M + \text{heat} \rightarrow M^*$
$AB^* + M \rightarrow AB + M^*$	$AB + M^* \rightarrow AB^* + M$
$M^* \rightarrow M + \text{heat}$	$AB^* \rightarrow A + B$

Table 2.1: Forward and backward decomposition of a three-body reaction.

concentration of the third body can be defined from either a single species or from a combination of species. In the first case, the notation usually takes the form $A + B + N_2 \rightleftharpoons AB + N_2$ (here with the azote species). In the second case, each of the species is seen as a more or less effective collisional partner. Third body efficiencies β_k are thus defined and the calculation of the concentration $[X_M]$ is done on the basis of equation 2.46. Species which are associated to a high efficiency are given a value above 1.0; on the contrary a value below 1.0 is defined for the species which are not effective collisional partners. A

default efficiency of 1.0 is declared for all the other species.

$$[X_M] = \sum_{k=1}^{N_{sp}} \beta_k [X_k] \quad (2.46)$$

2.2.2.6 Fall-off correction

Under specific conditions, some reaction rate expressions are dependent on pressure and temperature. This is especially true for the rate associated to unimolecular/recombination fall-off reactions which increases with pressure. As an example, let us consider the unimolecular/recombination reaction that describes the methyl recombination (table 2.2). If the chemical process takes place at either a low or high-

High pressure limit	$\text{CH}_3 + \text{CH}_3 \rightleftharpoons \text{C}_2\text{H}_6$
Low pressure limit	$\text{CH}_3 + \text{CH}_3 + \text{M} \rightleftharpoons \text{C}_2\text{H}_6 + \text{M}$

Table 2.2: Low and high-pressure reactions for methyl recombination

pressure limit, typical Arrhenius laws are applicable to the reactions described in table 2.2. However, if the pressure is in between, an accurate description of the phenomenon requires a more complicated rate expression. In such a case, the reaction is said to be in the “fall-off” region. Common practice is to write

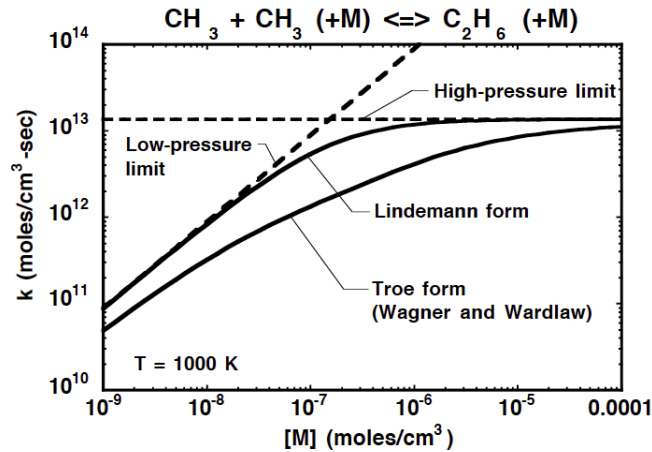


Figure 2.2: Lindemann form and Troe form applied to the methyl recombination [6]

the overall reaction as $\text{CH}_3 + \text{CH}_3 (+\text{M}) \rightleftharpoons \text{C}_2\text{H}_6 (+\text{M})$. Several formulas (derived from the Lindemann description) are available to smoothly relate the limiting low and high-pressure rate expressions. With the Lindemann approach, Arrhenius parameters need to be given for both the low pressure limit K_0 and the high pressure limit K_∞ .

$$K_0 = \mathcal{A}_0 T^{\beta_0} \exp\left(-\frac{E_0}{\mathcal{R}T}\right) \quad (2.47)$$

$$K_\infty = \mathcal{A}_\infty T^{\beta_\infty} \exp\left(-\frac{E_\infty}{\mathcal{R}T}\right) \quad (2.48)$$

The expression taken at any pressure is based on a combination of both K_0 and K_∞ (see equation 2.49). The term P_r is here equivalent to a pressure and $[M]$ represents the concentration of the mixture, possibly

estimated from third-body efficiencies.

$$K = K_{\infty} \left(\frac{P_r}{1 + P_r} \right) F \quad (2.49)$$

$$P_r = \frac{K_0[M]}{K_{\infty}} \quad (2.50)$$

The expression for the F coefficient is equal to unity with the Lindemann description. Other descriptions of F such as the Troe form have been proposed:

$$\log(F) = \left[1 + \left(\frac{\log(P_r) + c}{n - d(\log(P_r) + c)} \right)^2 \right]^{-1} \log(F_{cent}) \quad (2.51)$$

where the coefficients c , n and d are estimated through:

$$c = -0.4 - 0.67 \log(F_{cent}) \quad (2.52)$$

$$n = 0.75 - 1.27 \log(F_{cent})$$

$$d = 0.14$$

and F_{cent} through the equation 2.53 where the parameters α , T^* , T^{**} , T^{***} have to be specified as inputs (T^{**} is not always used).

$$F_{cent} = (1 - \alpha) \exp\left(\frac{-T}{T^{***}}\right) + \alpha \exp\left(\frac{-T}{T^*}\right) + \exp\left(\frac{-T^{**}}{T}\right) \quad (2.53)$$

2.2.3 Reducing the costs for solving chemistry

As introduced earlier, the detailed combustion mechanisms available in the literature require the use of tiny mesh sizes. Typically, the size of the cells found within the flame thickness, at atmospheric pressure, should be of the order of ten micrometers to properly solve for the intermediate and radical species. Moreover the time steps necessary to capture the entire chemistry of the flame are always smaller than the time steps used to solve for turbulence by several orders of magnitude. The actual computer resources are not sufficient enough to support the expensive and long simulations resulting from these tiny time and space resolutions. As a result, the use of detailed chemistry is limited to a very small number of academic studies and as of today such large mechanisms have never been employed in industry. Accordingly, most of the reactive computations are today performed from either a tabulation or from a reduction of the chemistry. The two approaches are briefly discussed here.

2.2.3.1 Chemistry reduction

The reduction of chemistry consists in lowering the complexity of the combustion mechanism by removing chemical species and reactions without significantly modifying the results for the conditions under study. A large amount of methodologies have been developed for the derivation of reduced mechanisms. A detailed review of these techniques is proposed in Chapter 3.

2.2.3.2 Chemistry tabulation

Another largely employed methodology for the reduction of the costs associated to chemistry consists in storing the chemical responses obtained from canonical 1D flame simulations into a library relying on a reduced number of parameters. The mixture composition, temperature and species source terms are thus obtained from this library also called a chemical table. The sub-space coordinates (table input parameters) are either expressed from one thermochemical variable or from the linear combination of independent variables.

Maas and Pope [7] observed that there exist a composition sub-space called manifold in which the evolution of the reactive system converges towards a group of similar trajectories. This set is called *Intrinsic Low Dimensional Manifold* (ILDM) or variety attractor. Knowing the trajectory for the attractor enables the reconstruction of the evolution of the entire system. The validity range of the attractor is directly related to the number of dimensions of the composition sub-space.

Two main models have been constructed from the ILDM methodology and from the flamelet (discussed in section 2.3.1) hypothesis namely the FPI (*Flamelet Prolongation of ILDM*) model developed by Gicquel [8] and the FGM model (*Flamelet Generated Manifold*) of Van Oijen [9]. These models rely on the assumption that there is an analogue response between the local flame front and the tabulated laminar canonical flamelet. The laminar flame responses are computed for given conditions and projected in the reduced space: tabulated as a function of a few parameters.

2.3 Combustion regimes

Two canonical combustion regimes exist. A premixed configuration is characterised by a perfect mixing of the fuel and of the oxidiser before combustion while a diffusion regime is achieved when combustion occurs at the mixing interface between the fuel injection and the oxidiser injection.

Premixed flames are interesting in the sense that they provide high burning efficiency because the mixing between the fuel and the oxidiser is done prior to the combustion. The temperature of the burnt gases is also easily monitored through the equivalence ratio of the mixture. This exhaust temperature is a key parameter for a number of industrial applications and also controls the pollutants formation. Unfortunately because of the premixing, these flames are difficult to design and finally, the reaction may accidentally be initiated as soon as the fuel encounters the oxidiser which poses real safety problems.

On the other hand, diffusion flames are much easier to design and also much safer to operate. Indeed, because no premixing is required, the flame cannot propagate in the fuel stream since the oxidiser is missing and vice versa. Notwithstanding these facts, non-premixed flames are not attractive either because the mixing by molecular diffusion is less efficient and the maximum temperature is much more difficult to control.

Most industrial applications cannot be described by these two ideal cases. Real systems lie in a regime that is in between premixed and non-premixed flames and that shares characteristics with both of them. This last regime is referred as partially-premixed combustion. The three concepts are introduced and illustrated in this section.

2.3.1 Canonical problem: The perfectly premixed flame

2.3.1.1 Premixed flame structure

The unstretched premixed flame is the most common canonical model employed to describe combustion processes at constant pressure. Premixed combustion is characterised by a fresh mixture of reactants separated from the burnt gases by a flame front that freely propagates in the direction of the fresh gases at a velocity S_L^0 , as illustrated on figure 2.3. The structure of a premixed flame is characterised by three regions:

- A **preheat zone**, where fresh reactants are heated by the thermal diffusion fluxes,
- A **reactive layer** defined by a reaction thickness in which the fuel is first decomposed in series of intermediate fuels which in turn are decomposed to form radical species as for instance H, O and OH,
- A **post-flame region** where the intermediates are combined together to form major combustion products such as CO_2 and H_2O .

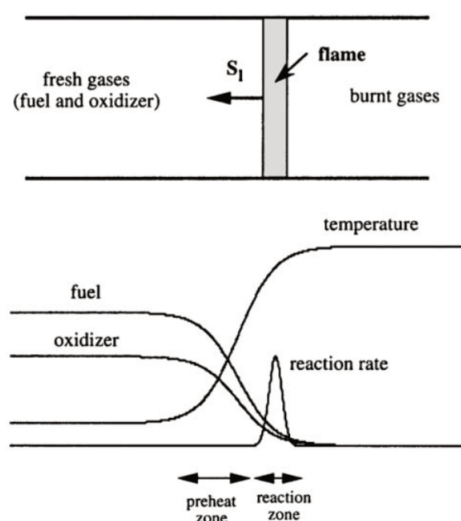


Figure 2.3: Structure of a laminar premixed flame [10].

2.3.1.2 Simplified equations for freely propagating 1D flames

The conservation equations introduced within section 2.1.2 are further simplified in the context of 1D premixed flames propagating in the x direction (at constant pressure). For a steady flame in the reference frame of the flame, mass is conserved at each point so that:

$$\frac{\partial \rho u}{\partial x} = 0 \longrightarrow \rho u = \rho_0 S_L^0, \quad (2.54)$$

where ρ_0 is the fresh gases density and S_L^0 is the laminar flame speed defined in section 2.3.1.4. Thanks to the relation 2.54, the momentum equation is no more necessary. Regarding the species conservation, the steady evolution of the chemical species along the x axe is simplified to the relation:

$$\frac{\partial}{\partial x} (\rho(u + V_k) Y_k) = \dot{\omega}_k, \quad (2.55)$$

and finally, in this context, the enthalpy conservation reads:

$$\frac{\partial}{\partial x}(\rho u h_s) = \frac{\partial}{\partial x} \left(\lambda_{th} \frac{\partial T}{\partial x} \right) - \frac{\partial}{\partial x} \left(\rho \sum_{k=1}^{N_{sp}} h_{s,k} Y_k V_k \right) + \dot{\omega}_T . \quad (2.56)$$

2.3.1.3 Controlling variables

The chemical process taking place within the reactive front of a premixed flame may be described using a progress variable c which is normalised in order to be equal to 0 in the fresh gases and 1 in the burned gases region. On the basis of the temperature variation across the flame, this progress variable reads:

$$c = \frac{T - T_0}{T_{eq} - T_0} . \quad (2.57)$$

It is also commonly expressed from Y_c which is estimated from a linear combination of the combustion products:

$$c = \frac{Y_c - Y_{c,0}}{Y_{c,eq} - Y_{c,0}} . \quad (2.58)$$

Typically $Y_c = Y_{CO} + Y_{CO_2} + Y_{H_2O}$ is defined. This definition is valid for the great majority of the premixed combustion problem, however it does not apply well for some specific cases including the capture of the NO_x levels. The progress variable c is particularly suitable for the analysis of the flame structure, to estimate the location of the reactive layer and to define the normal to the flame front through the relation:

$$n = \frac{-\nabla c}{|\nabla c|} . \quad (2.59)$$

For a premixed flame, the perfect mixing of the fuel and oxidiser is characterised by an equivalence ratio which is computed from relation:

$$\phi = s \frac{Y_{F,0}}{Y_{O,0}} , \quad (2.60)$$

where $Y_{F,0}$ and $Y_{O,0}$ respectively represent the fuel and oxidiser mass fractions in the fresh gases. The term s is the stoichiometric ratio defined by relation 2.61.

$$s = \frac{\nu_O W_O}{\nu_F W_F} , \quad (2.61)$$

where W_F and W_O are the fuel and oxidiser molecular weights. The terms ν_F and ν_O respectively stand for the fuel and oxidiser stoichiometric coefficients within the global reaction:



with F, O and P the species formula of the fuel, oxidiser and the product of the global reaction. The equivalence ratio equals unity for a stoichiometric mixture. The mixture is said to be “lean” when the fuel mass fraction in the fresh gases $Y_{F,0}$ is lower than in stoichiometric conditions *i.e.* when the equivalence ratio is lower than 1. On the other hand it is called “rich” for higher fuel mass fractions in the fresh gases *i.e.* for ϕ greater than 1.

2.3.1.4 Flame speed, flame thickness

Multiple definitions of the flame speed are commonly employed whether the combustion is analysed in an absolute reference frame (absolute speed), relatively to the local flow velocity (displacement speed) or considering the speed at which the fuel reacts (consumption speed). The so-called **laminar flame speed** is the only one studied in this thesis. It corresponds to the speed at which the fuel is consumed. It is computed from the integral of the burning rate across the flame brush:

$$S_L^0 = -\frac{1}{\rho_0(Y_{F,0} - Y_{F,\infty})} \int_{-\infty}^{+\infty} \dot{\omega}_F dx, \quad (2.63)$$

where x corresponds to the direction of the flame domain, and ρ_0 , $Y_{F,0}$ are respectively the density and the fuel mass fraction in the fresh gases and where $Y_{F,\infty}$ is the fuel mass fraction in the burned gases.

The laminar flame is also described through its thickness which varies according to the composition of the burning mixture (fuel and oxidiser type, equivalence ratio), the initial temperature and pressure. Several definitions exist including the thermal thickness δ_L^{th} , the diffusive thickness δ_L^d , the blint thickness δ_L^b and the reaction zone thickness δ_L^r . The **thermal thickness** [11] is computed from the temperature gradient:

$$\delta_L^{th} = \frac{T_{eq} - T_0}{\left| \frac{\partial T}{\partial x} \right|_{max}}, \quad (2.64)$$

where T_0 and T_{eq} are respectively the temperature in the fresh and in the burned gases. The diffusive thickness [11] provides an *a priori* estimation of the flame thickness that relies on the thermal diffusion of the fresh gases $\delta_L^d = D_{th}^0/S_L^0$. It is easy to compute although it usually underestimates the thickness value in comparison to δ_L^{th} . The blint thickness [12] is a corrected version of the diffusive thickness which relies on equilibrium thermochemistry $\delta_L^b = 2\delta_L^d(T_{eq}/T_f)^{0.7}$. It provides a much closer estimation of the thickness of the thermal layer. Finally the reaction zone thickness [13] is estimated from the region where the heat is released. It is usually one order of magnitude smaller than the thermal thickness. Along this thesis, only the thermal thickness will be employed using the relation 2.64.

2.3.2 Canonical problem: The diffusion flame

Diffusion flames are characterised by a separated injection of fuel and oxidiser. The flame develops inside of the diffusion layer and is stabilised exactly at the stoichiometric line. In opposition to the premixed flame, the diffusion one is **not associated to auto-propagative effects** and is **not characterised by any specific thickness** since it is largely piloted by the mixing of the reactants. The diffusion flame is illustrated on figure 2.6. The maximum temperature is located inside of the reaction zone and diffuses towards the fuel and the oxidiser streams. The structure inside of the diffusion flame is piloted by the external streams which influence the local stretch.

2.3.2.1 Passive mixture fraction

The mixing state is locally described using a mixture fraction Z . The use of the atomic conservation is one way to define Z as a passive scalar in a multi-species environment. Bilger [14] provides a description of the mixture fraction for hydrocarbon species of type C_mH_n :

$$Z = \frac{Z_C/(mW_C) + Z_H/(nW_H) + 2(Y_{O_2,2} - Z_O)/(\nu_O W_{O_2})}{Z_{C,0}/(mW_C) + Z_{H,0}/(nW_H) + 2Y_{O_2,2}/(\nu_O W_{O_2})}, \quad (2.65)$$

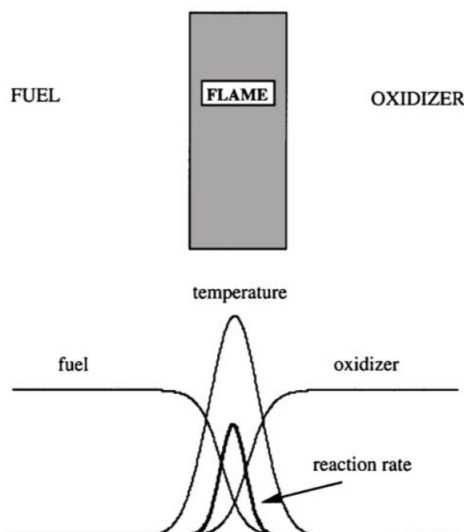


Figure 2.4: Structure of a laminar diffusion flame [10].

within which $Y_{O_2,2}$ represents the oxygen mixture fraction in the oxidiser inlet. Z_j corresponds to the mass fraction of the j^{th} atom and is computed for C, H and O atoms from relation:

$$Z_j = \sum_{k=1}^{N_{sp}} \frac{\alpha_{jk} W_j}{W_k} Y_k, \quad (2.66)$$

where α_{jk} is the number of j^{th} atom into species k , W_j is the molecular weight associated to the atom j and W_k represents the species k molecular weight.

2.3.2.2 Steady strained diffusion flame

One relevant canonical problem for the study of non-premixed combustion is the steady strained one dimensional diffusion flame. It is illustrated on figure 2.5. This approach is used frequently for the tabulated methodologies employed in non-premixed combustion.

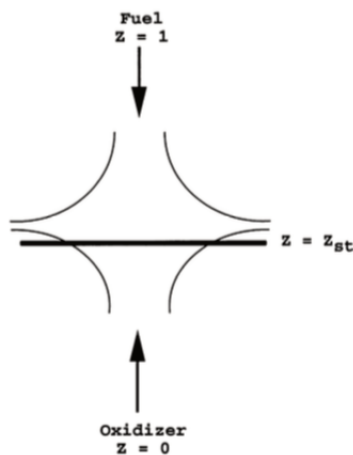
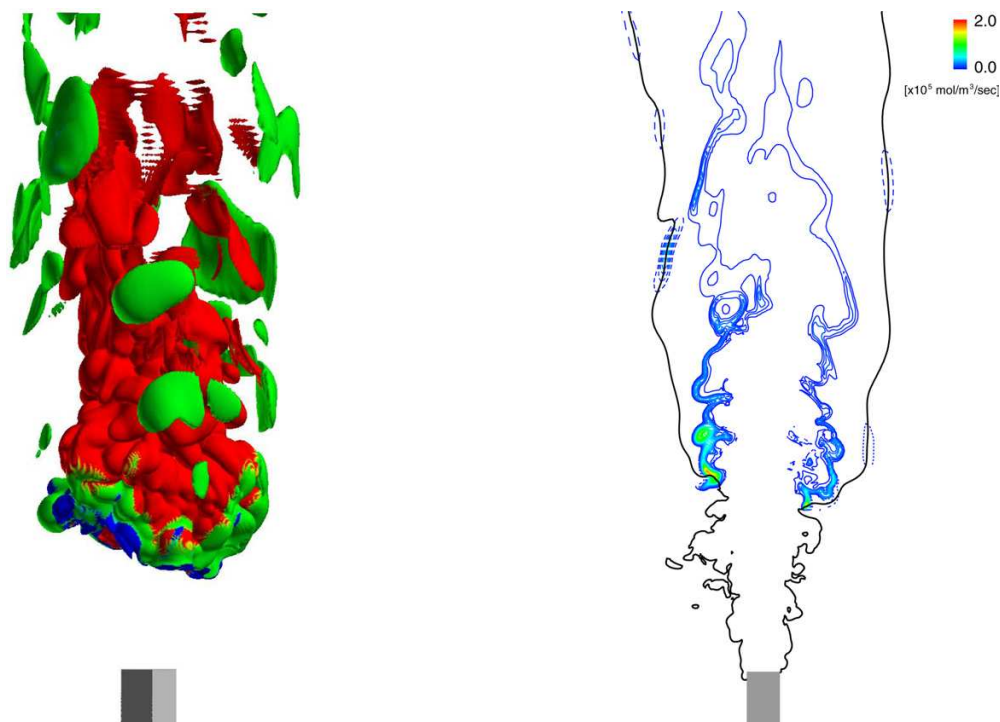


Figure 2.5: Counter-flowing diffusion flame [10]

2.3.3 Partially premixed combustion

2.3.3.1 Combustion regimes in real systems

A large part of the academic studies devoted to turbulent combustion are performed for conditions corresponding to the presented two limiting regimes. As introduced earlier this does not apply very well to real systems for which efficient, easy and safe to operate strategies are necessary. Higher performances



(a) Surface colour represents the combustion regime, red: rich premixed, blue: lean premixed and green: diffusion.

(b) Hydrogen consumption rate. Premixed rates are drawn in solid lines and diffusion ones in dashed lines. The black line shows the stoichiometric mixture fraction.

Figure 2.6: DNS of a turbulent hydrogen jet lifted flame by Mizobuchi *et al.* [15].

are reached for premixed combustion than for diffusion flames. However, to avoid any accident, the fuel and oxidiser cannot meet outside of the combustion chamber. For that reason, separated injections of the fuel and of the oxidiser are frequently retained and the actual design tendency is towards the development of technologies to enhance the mixing of the reactants before they enter the combustion zone. This may be done by increasing turbulence (introducing a swirl) or by enhancing the interaction between the fuel and the oxidiser directly through the injection system. Nevertheless, a great majority of the industrial systems operate under conditions in which the reactants are not perfectly mixed together when they start burning or in conditions where local flame extinctions favour the mixing between the fuel and the oxidiser while they react in the flame zone. Accordingly, a point situated within the reactive layer faces a combustion regime that varies from perfectly premixed combustion to non-premixed combustion. This is illustrated on figure 2.6 which gives the contours of the combustion regimes expressed here for lean and rich premixed conditions and for diffusion conditions in the case of an hydrogen/air jet lifted flame. In that case, the flame is said to operate in a partially premixed regime. This combustion mode has a drastic impact on the reaction rate. It moreover plays an important role in the stabilisation of a flame

which is the result of an intense mixing between the fuel, the oxidiser and the burned gases that leads to the creation and propagation of partially premixed flamelets. This is again illustrated by figure 2.6.

2.3.3.2 Stratified combustion

A specific application of partially premixed flames is stratified combustion. It can be seen as a propagation of a flame within several layers of premixed fuel-air mixtures at different equivalence ratios. Stratified combustion is typically found in gas turbines, and internal combustion engines as well as in the majority of the industrial furnaces. This type of combustion mode gained significance thanks to its ability to provide high efficiencies while reducing the pollutants emissions. Typically CO and NO_x levels are minimised because of overall lean conditions and thanks to the lowering of the temperature. Stratification is also frequently encountered in premixed combustion involving a dilution with cold air. The flamelet hypothesis is usually employed to model stratified combustion.

2.4 Aerothermochemical equations in the LES formalism

2.4.1 Introduction to turbulence

In the flows characterised by low velocities, the small perturbations are instantly smoothed by the molecular viscosity which tends to maintain organisation. In that case, the flow is called laminar and is characterised by regular parallel trajectories. When the velocity increases, the viscosity is not strong enough to dissipate the perturbations which are furthermore amplified by several instabilities. The flow moves towards a turbulent state characterised by a disorganised appearance which is associated to a large range of macroscopic scales. The same set of equations is used to describe both states. The transition between the laminar and the turbulent state is explained by the non-linearity of these equations. Most of the flows encountered in industrial processes, in transportation or even in nature are non stationary and turbulent.

The turbulent nature of a flow may be quantified comparing the inertial forces that tend to disrupt the flow and create new turbulent scales to the viscous forces which have the tendency to dissipate the movement and restore a laminar regime. The Reynolds number is a non-dimensional number that provides such a comparison:

$$Re = \frac{uL}{\nu} . \quad (2.67)$$

It is expressed respectively from the velocity u and characteristic size L of the flow and from ν which represents the kinematic viscosity of the fluid. Small Reynolds numbers are representative of laminar flows while large Re correspond to turbulent conditions. The Kolmogorov theory [16] introduces the concept of turbulent energy cascade towards the small scales which is one way to describe the turbulent energy spectrum. It is illustrated within figure 2.7 by expressing the turbulent kinetic energy as a function of the wave number. Three different scales are used to describe this spectrum and then to calibrate the direct and large scales simulations.

- **Macroscopic scale:** The largest scales of the turbulence are geometry dependant. These are the most energetic turbulent structures. The turbulent kinetic energy is defined from the relation:

$$k_t = \sum_{i=1}^3 \frac{1}{2} u_i'^2 . \quad (2.68)$$

Two scales may be employed to describe the macroscopic turbulent structures, namely the energetic length scale L_e and the integral length l_t . The energetic length L_e is expressed through the relation:

$$L_e = \frac{k_t^{3/2}}{\epsilon}, \quad (2.69)$$

where ϵ corresponds to the turbulent dissipation. The integral length l_t is computed by accounting for one of the three velocity component through:

$$l_t = \frac{u'^3}{\epsilon}. \quad (2.70)$$

The turbulent Reynolds number Re_t is expressed from this integral scale using:

$$Re_t = \frac{u' l_t}{\nu}. \quad (2.71)$$

In most practical applications, this ratio tends to be of the order of a thousand. Both characteristic scales may be related using the hypothesis of local isotropy for the turbulent scales hence leading to the relation 2.72 for the kinetic energy.

$$k_t = \frac{3}{2} u'^2. \quad (2.72)$$

The relation between the length scales L_e and l_t follows:

$$\frac{l_t}{L_e} = \left(\frac{2}{3}\right)^{3/2}. \quad (2.73)$$

- **Intermediate scale:** The largest eddies become unstable and break to form smaller eddies. This transfer is done following the $k_t^{-5/3}$ law. The Taylor scale λ to which this is associated is the most dissipative scale.
- **Viscous dissipation scale:** This scale refers to the the smallest structure of the flows and is limited by the molecular agitation. It is referred as the Kolmogorov scale in which length and velocity are expressed from:

$$l_K = \left(\frac{\nu}{\epsilon}\right)^{1/4} \quad \text{and} \quad u_K = (\nu\epsilon)^{1/4}. \quad (2.74)$$

ϵ refers to the dissipation rate through the form heat of the turbulent kinetic energy. A turbulent Reynolds number associated to the Kolmogorov length scale appears $Re_K = u'_K l_K / \nu \approx 1$.

2.4.2 Strategies for the simulation of turbulent flows: RANS, LES, DNS

The Computational Fluid Dynamics (CFD) aims at simulating numerically the flows by solving for the discretised conservative equations. The large variety of scales observed while numerically solving for the flows depends on the viscosity of the simulated fluid. The turbulence modelling consists in the modification of the viscosity of the studied fluid to limit the scales to the ones that can be solved on the employed mesh.

Three different approaches are used to simulate turbulent flows, namely DNS, RANS and LES.

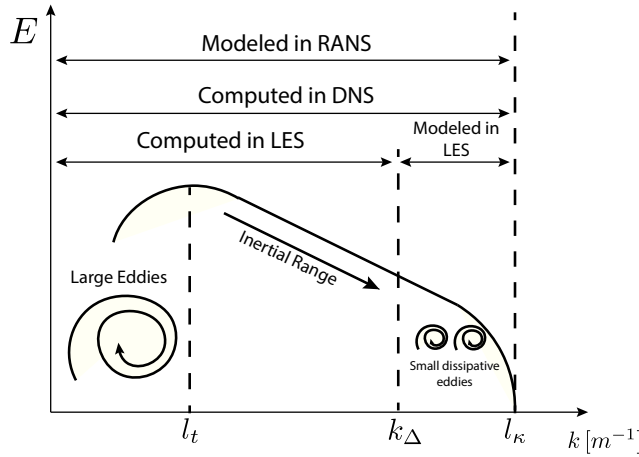


Figure 2.7: Illustration of the turbulent energetic spectrum along the energetic cascade. The solved and modelled scales are given for RANS, LES and DNS approaches. Image extracted from [17].

- The introduced set of conservative equations allows for solving directly the aerothermochemistry over all the space and time scales of the flow. This approach is called **DNS** for *Direct Numerical Simulation*. Such a method is expensive because it requires the use of a mesh capable of capturing the smallest scales of the flow through a resolution $\Delta = 2l_K$ (see [18]). This condition is expressed from the turbulent Reynolds number and the integral scale through the relation:

$$\Delta \approx \frac{l_t}{Re_t^{3/4}} \quad (2.75)$$

Because of this elevated cost, DNS is today exclusively employed for the simulation of academic configurations limited to reasonably low Reynolds number.

- To numerically solve for fluid dynamics at reasonable costs, time averaged equations have been derived. This approach is referred as **RANS** for *Reynolds Averaged Numerical Simulation*. The entire set of turbulence fluctuations are modelled and no scale from the turbulent energy spectrum is solved. Using this approach, the extracted informations concern only the mean behaviour of the flow. Since it allows for dealing with coarse meshes hence giving short runback times, the methodology has been largely studied in academia over the last decades and is still today a reference for most CFD based applications in industry.
- Finally, the **LES** for *Large-Eddy Simulation* consists in the solving of the non stationary large structures of the flow and on the modelling of the smallest scales. This approach still requires the introduction of specific models but these can be constructed from the information about the large scales of the flow which are numerically solved. The introduction of such models lies on the assumption that the cutting point between the solved and modelled informations is located within the inertial scale (as illustrated on figure 2.7). In practice, this cutting point is dependant on the used mesh. The added viscosity is of the order of the Reynolds number corresponding to the cutting length scale, hence of the order of the mesh size Δ .

2.4.3 Filtered equations for LES

The separation between the solved scales for LES and the scales that are modelled is given by a filtering operation of the equations that are solved for a DNS. For a scalar $\phi(\mathbf{x}, t)$, the filtering is performed through a spatial convolution that gives,

$$\bar{\phi}(\mathbf{x}, t) = \int_{\mathbb{R}^3} \phi(\mathbf{y}, t) \mathcal{G}_\Delta(\mathbf{y} - \mathbf{x}) d\mathbf{y}, \quad (2.76)$$

where \mathcal{G}_Δ is the filter associated to the scale Δ that provides the filtered quantity $\bar{\phi}(\mathbf{x}, t)$. The filter must be normalised so that,

$$\int_{\mathbb{R}^3} \mathcal{G}_\Delta(\mathbf{x}) d\mathbf{x} = 1, \quad (2.77)$$

and must verify the commutativity of both spatial and temporal derivation operators, so that:

$$\frac{\partial \bar{\phi}}{\partial t} = \bar{\frac{\partial \phi}{\partial t}} \quad \text{and} \quad \frac{\partial \bar{\phi}}{\partial x_i} = \bar{\frac{\partial \phi}{\partial x_i}}. \quad (2.78)$$

After the filtering separation, the ϕ variable may be seen in two parts: (1) a part $\bar{\phi}$ evolving above the scale Δ and (2) a fluctuating unresolved part ϕ' evolving at scales lower than Δ .

$$\phi(\mathbf{x}, t) = \bar{\phi}(\mathbf{x}, t) + \phi'(\mathbf{x}, t). \quad (2.79)$$

Because the density ρ of the flow varies from one point to another, the Favre filtered variable $\tilde{\phi}$ is introduced. It corresponds to a filter weighted by density.

$$\tilde{\phi} = \frac{\overline{\rho \phi}}{\bar{\rho}}. \quad (2.80)$$

The Favre convolution is applied to the system of conservative equations (2.19)-(2.20)-(2.22) and (2.30) leading to the following set of filtered relations:

- **Filtered mass conservation**

$$\frac{\partial \bar{\rho}}{\partial t} + \frac{\partial \bar{\rho} \tilde{u}_i}{\partial x_i} = 0. \quad (2.81)$$

- **Filtered momentum conservation**

$$\frac{\partial \bar{\rho} \tilde{u}_j}{\partial t} + \frac{\partial \bar{\rho} \tilde{u}_i \tilde{u}_j}{\partial x_i} = - \frac{\partial}{\partial x_i} \underbrace{[\bar{\rho}(\tilde{u}_i \tilde{u}_j - \tilde{u}_i \tilde{u}_j)]}_{(1)} - \frac{\partial \bar{P}}{\partial x_j} + \frac{\partial \bar{\tau}_{ij}}{\partial x_i}. \quad (2.82)$$

- **Filtered species conservation**

$$\frac{\partial \bar{\rho} \tilde{Y}_k}{\partial t} + \frac{\partial \bar{\rho} \tilde{u}_i \tilde{Y}_k}{\partial x_i} = - \frac{\partial}{\partial x_i} \underbrace{[\bar{\rho}(\tilde{u}_i \tilde{Y}_k - \tilde{u}_i \tilde{Y}_k)]}_{(2)} - \frac{\partial}{\partial x_i} \underbrace{(-\bar{\rho} V_{k,i} Y_k)}_{(3)} + \underbrace{\bar{\omega}_k}_{(4)}. \quad (2.83)$$

- **Filtered energy conservation**

$$\frac{\partial \bar{\rho} \tilde{h}_s}{\partial t} + \frac{\partial \bar{\rho} \tilde{u}_i \tilde{h}_s}{\partial x_i} = - \frac{\partial}{\partial x_i} \underbrace{[\bar{\rho}(\tilde{u}_i \tilde{h}_s - \tilde{u}_i \tilde{h}_s)]}_{(5)} + \frac{D\bar{P}}{Dt} + \frac{\partial}{\partial x_i} \underbrace{\left(\lambda_{th} \frac{\partial T}{\partial x_i} \right)}_{(6)} \quad (2.84)$$

$$- \frac{\partial}{\partial x_i} \underbrace{\left(\rho \sum_{k=1}^{N_{sp}} h_{s,k} Y_k V_{k,i} \right)}_{(7)} + \underbrace{\bar{\omega}_T}_{(8)}. \quad (2.85)$$

Unresolved terms (1)-(8) appear in the filtered conservative equations. Each of them is closed by introducing several models:

- **The sub grid Reynolds stress tensor (1)** $\tau'_{ij} = \bar{\rho}(\widetilde{u_i u_j} - \widetilde{u_i} \widetilde{u_j})$ requires the introduction of a turbulence model for the transport of momentum by unresolved velocity fluctuations and account for the energy transfert between resolved and unresolved structures. The Boussinesq [19] approach is employed in this thesis: turbulent fluxes are modelled using an expression similar to the laminar definition 2.21 and using a turbulent viscosity $\mu_t = \bar{\rho} \nu_t$ so that:

$$\tau'_{ij} = \mu_t \left(\frac{\partial \widetilde{u_i}}{\partial x_j} + \frac{\partial \widetilde{u_j}}{\partial x_i} \right) - \frac{2}{3} \mu_t \frac{\partial \widetilde{u_k}}{\partial x_k} \delta_{ij}, \quad (2.86)$$

Several models may be introduced from this approach. The one employed in this thesis is discussed in the next section.

- **The sub grid species (2) and enthalpy fluxes (5)** respectively written:

$$\mathcal{F}'_{k,i} = \bar{\rho}(\widetilde{u_i Y_k} - \widetilde{u_i} \widetilde{Y_k}) \quad (2.87)$$

$$\mathcal{Q}'_i = \bar{\rho}(\widetilde{u_i h_s} - \widetilde{u_i} \widetilde{h_s}) \quad (2.88)$$

are modelled using a similar approach to the one for the sub grid Reynolds stress tensor. A turbulent Prandtl number Pr_t is introduced for the enthalpy fluxes:

$$\mathcal{Q}'_i = - \frac{\mu_t}{Pr_t} \frac{\partial \widetilde{h_s}}{\partial x_i}. \quad (2.89)$$

and for the species fluxes, a turbulent Schmidt number is used Sc_t , so that:

$$\mathcal{F}'_{k,i} = - \frac{\mu_t}{Sc_t} \frac{\partial \widetilde{Y_k}}{\partial x_i}. \quad (2.90)$$

These Prandtl and Schmidt may be constant over the entire domain or may vary in space and time depending on the formulation.

- **The filtered laminar diffusive fluxes of species (3) and enthalpy (6)-(7)** may be neglected because they are low in comparison with the turbulent fluxes for large Reynolds numbers. They may also be modelled using laws based on gradients:

$$\overline{\lambda \frac{\partial T}{\partial x_i}} = \bar{\lambda} \frac{\partial \widetilde{T}}{\partial x_i}, \quad (2.91)$$

$$\overline{V_{k,i} Y_k} = - D_k \frac{W_k}{\overline{W}} \frac{\partial \widetilde{X_k}}{\partial x_i}, \quad (2.92)$$

$$\overline{\rho \sum_{k=1}^{N_{sp}} h_{s,k} Y_k V_{k,i}} = - \bar{\rho} \sum_{k=1}^{N_{sp}} D_k \frac{W_k}{\overline{W}} \frac{\partial \widetilde{X_k}}{\partial x_i} \widetilde{h_{s,k}}. \quad (2.93)$$

- **The filtered species chemical rate (4) enthalpy source term (8)** respectively $\bar{\omega}_k$ and $\bar{\omega}_T$ are critical points regarding the modelling of turbulent combustion. They will be discussed later in section 2.4.5.

2.4.4 Sub grid modelling for turbulence

Several approaches exist in the literature, however only the Boussinesq approximation is employed in this thesis. It relies on the assumption that the effect of the unresolved small structures are similar to an increase of the turbulent viscosity. The main difficulty lies in the calculation of this additional viscosity. It is at the origin of several modelling developments.

- **The Smagorinsky model** relies on an equilibrium hypothesis between production and dissipation of kinetic energy at the scale of the filter. The turbulence is therefore only considered as a dissipative phenomena.

$$\nu_t = (C_S \Delta)^2 |\tilde{\mathbf{S}}| = (C_S \Delta)^2 \sqrt{2\tilde{S}_{ij}^t \tilde{S}_{ij}^t}, \quad (2.94)$$

where C_S is the Smagorinsky constant (with a typical value $C_S = 0.17$ calculated from the Kolmogorov spectrum), Δ is the characteristic filter width and $\tilde{\mathbf{S}}$ the filtered strain tensor that is expressed:

$$\tilde{S}_{ij} = \frac{1}{2} \left(\frac{\partial \tilde{u}_i}{\partial x_j} + \frac{\partial \tilde{u}_j}{\partial x_i} \right). \quad (2.95)$$

- **The dynamic Smagorinsky model** is derived by Germano [20] and Lilly [21]. This approach relies on a dynamic and local estimation of the C_S constant. The sub grid behaviour is estimated from the resolved small structures which require the filtering written $\widehat{(\cdot)}$ of the solved velocity field at a size Δ' that is larger than the size Δ . The sub grid tensor and the sub grid tensor based on the velocity field may be expressed from the Smagorinsky model through the following formulations:

$$\tau'_{ij} = 2\bar{\rho} (C_S \Delta)^2 |\tilde{\mathbf{S}}| \tilde{S}_{ij}, \quad (2.96)$$

$$\tau''_{ij} = 2\widehat{\rho} (C_S \Delta')^2 |\widehat{\mathbf{S}}| \widehat{S}_{ij}. \quad (2.97)$$

The Germano identity is used to link both tensors through a term that depend on the solved field and which may be explicitly computed:

$$L_{ij} = \tau'_{ij} - \tau''_{ij} = \rho \left(\widehat{\tilde{u}_i \tilde{u}_j} - \tilde{u}_i \tilde{u}_j \right). \quad (2.98)$$

Combining the equations (2.96), (2.97) and (2.98) allows for computing the Smagorinsky constant from the filtered velocity field at two different scales. The dynamic Smagorinsky model applies to a large range of conditions, however it is more difficult and more expensive to use, since it requires the definition of an explicit filtering operator. This approach is the one retained for the LES simulation showed in chapter 7.

- **The WALE model** for *Wall-Adaptating Eddy-Viscosity* [22] aims at predicting the correct behaviour at walls and the transition to the turbulence. With this model the turbulent viscosity is computed from relation:

$$\nu_t = C_W^2 \Delta^2 \frac{(s_{ij}^d s_{ij}^d)^{3/2}}{(\tilde{S}_{ij} \tilde{S}_{ij})^{5/2} + (s_{ij}^d s_{ij}^d)^{5/4}}, \quad (2.99)$$

in which the C_W constant equals 0.5. The tensor s_{ij}^d reads,

$$s_{ij}^d = \frac{1}{2} \left(\tilde{h}_{ij} + \tilde{h}_{ji} \right) - \frac{1}{3} \tilde{h}_{kk} \delta_{ij} \quad \text{with} \quad \tilde{h}_{ij} = \tilde{g}_{ik} \tilde{g}_{kj} \quad \text{and} \quad \tilde{g}_{ij} = \frac{\partial \tilde{u}_i}{\partial x_j}. \quad (2.100)$$

2.4.5 Turbulent combustion models

Another major problem associated to turbulent combustion appears in the closure of the filtered source term $\overline{\omega}_k$. This term deals with the interaction between the turbulence and the combustion and is therefore a key aspect in the computation of reactive LES. A few models are briefly introduced in this section. A detailed description of the state of the art on the turbulent combustion models may be found in the work by Veynante and Vervisch [10] or Pitsch [23]. The approaches to model turbulent combustion may be organised into three groups:

- **The algebraic approach:** The reaction rate is controlled by the turbulent mixing described in terms of scalar dissipation rate [24]. The smallest structures of the dissipation rate regulate the mixing between the reactants. This approach may be employed only when the characteristic time associated to the turbulence is large compared to the time scales of the combustion *i.e.* for very large Damköhler Da numbers.
- **The statistical approach:** The filtered scalars are evaluated from an *a priori* knowledge of the unresolved structures properties obtained from a PDF (*Probability Density Function*). This function provides a statistical distribution of the sub grid scales properties. The greatest difficulty rests in the solving of this PDF. This is addressed through several methodologies:
 - **PDF transport.** The first approach proposed in the literature consists in the transport of the PDF and on its solving. A transport equation is added to the original set of conservative equations for the estimation of the filtered PDF [25]. Pope [26] proposed the use of a Monte Carlo approach to solve for the PDF: a set of stochastic lagrangian particles carries thermochemical informations into the physical space. The joint PDF is then constructed from the particles informations. Although theoretically the approach may be used with large chemistries, in practice, the number of particles necessary to maintain precision increases with the dimension of the problem making the problem unfit.
 - **Presumed PDF.** This approach allows for lowering the cost related to the joint PDF methods. This methodology relies on a reduction of the number of scalars necessary for the description of the system and by presuming the shape of the PDF. For instance, this approach is commonly linked with the FPI in tabulated chemistry for which the problem is simplified to two dimensions: the progress variable c and the mixture fraction Z .
- **The geometric approach:** The flame front is considered to be a thin moving geometric surface. Several combustion models are derived from this approach. The majority of them is intended to model perfectly premixed flames since they rely on the hypothesis that there exists a clear interface between the fresh and the burned gases. First examples are the G-Equation and Levelset [27, 28] models which are defined from a level of potential. The species properties are reconstructed depending on their distance to the potential interface. Other well employed approaches are the flame surface density concept [29] and the thickened flame model. This last model is the one employed in this thesis. A few details on its derivation are given in the next sub section.

2.4.6 The thickened flame model: TFLES

2.4.6.1 Overall principal

The size of the cells necessary to properly solve for the variations in the thin layer that forms the flame is usually small in comparison to the size of the employed mesh. The concept of flame thickening was introduced in the seventies by Butler *et al.* [30] and O'Rourke *et al.* [31] to tackle this issue. It aims at increasing the number of points within the flame so as to capture its overall structure while conserving its key properties.

Williams [32] and Kuo [33] stated that the velocity S_L^0 and the laminar flame thickness δ_L^0 can be expressed from the reaction rate $\dot{\omega}$ and from the thermal diffusion coefficient D_{th} :

$$S_L^0 \propto \sqrt{D_{th}\dot{\omega}} \quad \text{and} \quad \delta_L \propto \frac{D_{th}}{S_L^0} \propto \sqrt{\frac{D_{th}}{\dot{\omega}}}. \quad (2.101)$$

Using this analysis Colin *et al.* [34] proposed to broaden the flame by a factor \mathcal{F} from the relations,

$$D_{th}^{\mathcal{F}} = D_{th}\mathcal{F} \quad \text{and} \quad \dot{\omega}^{\mathcal{F}} = \frac{\dot{\omega}}{\mathcal{F}}, \quad (2.102)$$

hence thickening the flame while maintaining the proper laminar flame velocity since:

$$S_L^0 \propto \sqrt{D_{th}\dot{\omega}} \rightarrow S_L^{\mathcal{F}} \propto \sqrt{D_{th}\dot{\omega}}, \quad (2.103)$$

$$\delta_L^0 \propto \sqrt{\frac{D_{th}}{\dot{\omega}}} \rightarrow \delta_L^{\mathcal{F}} \propto \mathcal{F}\sqrt{\frac{D_{th}}{\dot{\omega}}}. \quad (2.104)$$

In the TFLES context, the transport of any reactive scalar ϕ is then translated to the following conservative equation,

$$\frac{\partial \bar{\rho}\tilde{\phi}}{\partial t} + \nabla \cdot \bar{\rho}\tilde{u}\tilde{\phi} = \nabla \cdot (\bar{\rho}\mathcal{F}D\nabla\tilde{\phi}) + \frac{\dot{\omega}\phi}{\mathcal{F}}. \quad (2.105)$$

2.4.6.2 Conditions for the thickening \mathcal{F}

The objective of the TFLES approach is primarily to increase the number of points for the description of the species source terms. This is dependent on the local mesh size and flame thickness. For a defined number n of points within the flame it appears that the potential

$$n = \frac{\delta_L^0}{\Delta_{DNS}} = \frac{\mathcal{F}\delta_L^0}{\Delta_{LES}}, \quad (2.106)$$

where Δ_{DNS} corresponds to the size of the mesh necessary for a DNS on which the non-thickened profiles would be properly resolved and Δ_{LES} is the size of the LES mesh on which it is desirable to use the TFLES approach. The thickening factor \mathcal{F} is then deduced:

$$\mathcal{F} = \frac{\Delta_{LES}}{\Delta_{DNS}} = \frac{n\Delta_{LES}}{\delta_L^0(\phi(x, t))}. \quad (2.107)$$

2.4.6.3 Interaction between the flame and the turbulence

Modifying the thickness of the reactive layer impacts the interaction between the turbulence and the flame. Poinso *et al.* [35] and Meneveau *et al.* [36] demonstrated that the wrinkling of the flame under the influence of an eddy decreases with the expansion of the flame thickness. The impact of the

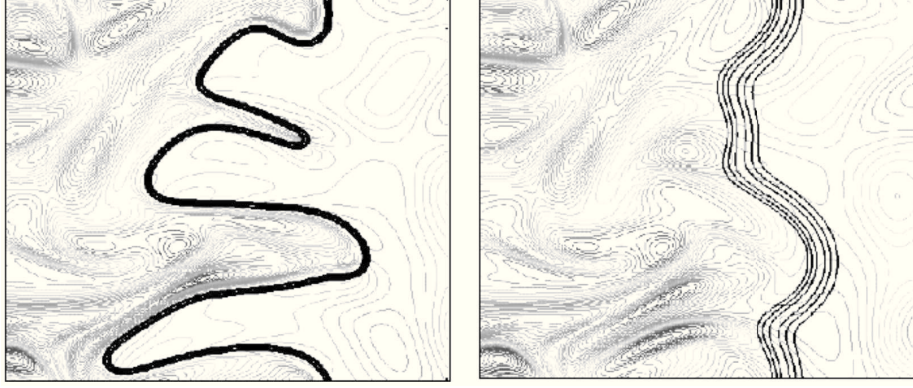


Figure 2.8: DNS of the interaction between the turbulence and the flame [11]. Left image: unthickened flame. Right image: Flame thickened by a factor $\mathcal{F} = 5$.

turbulence on the wrinkling of the flame was further studied by Angelberger *et al.* [37] and Colin *et al.* [34]. This is illustrated on figure 2.8 which compares a perfectly resolved flame structure to a thickened flame LES.

It is demonstrated that the non dimensional numbers describing the interaction between the flame and the turbulence are modified. For instance, the D amkholer number Da which gives the ratio between the integral scale (mixing) and the chemical time scale reads:

$$Da = \frac{t_t}{t_c} = \frac{l_t S_L^0}{u' \delta_L^0} \quad \text{hence leading to} \quad Da^{\mathcal{F}} = \frac{Da}{\mathcal{F}}, \quad (2.108)$$

where t_t is the turbulence characteristic time and t_c is the characteristic time associated to the chemistry. l_t is the integral scale and u' represents the sub grid fluctuations. This effect is accounted for through the introduction of an efficiency function \mathcal{E} that increases the turbulent flame speed hence compensating for the diminution of the flame surface. This function corresponds to the sub grid thickening factor defined from [34, 38]:

$$\mathcal{E} = \frac{S_t^0}{S_L^0} = \frac{A_t}{A_l} \quad (2.109)$$

where S_t^0 is the turbulent flame speed, A_t is the turbulent flame surface and A_l is the laminar flame surface. Among the efficiency functions found in the literature, Colin *et al.* [34] introduced a function based on the ratio of the wrinkling factor of the initial flame with thickness δ_L^0 by the wrinkling factor of the thickened flame characterised by $\delta_{\mathcal{F}}^0$:

$$\mathcal{E} = \frac{\Xi(\delta_L^0)}{\Xi(\delta_{\mathcal{F}}^0)} = \frac{1 + \alpha \Gamma \left(\frac{\Delta}{\delta_L^0}, \frac{u'}{S_L^0} \right) \frac{u'}{S_L^0}}{1 + \alpha \Gamma \left(\frac{\Delta}{\delta_{\mathcal{F}}^0}, \frac{u'}{S_L^0} \right) \frac{u'}{S_L^0}}, \quad (2.110)$$

where α and Γ are respectively a parameter and a function given by the model and where Δ stands for the filter size of the LES. This function may also be evaluated from a power law as introduced by Charlette [38] which writes the ratio between the surface of the resolved flame and the surface of the unresolved one from:

$$\mathcal{E} = \left(1 + \frac{\Delta}{\eta_c} \right)^{\beta}, \quad (2.111)$$

where η_c is the mean of the radius of curvature of the flame and β is a constant defined for the model. The LES results showed in the manuscript rely on the use of a corrected version of this model proposed by Wang *et al.* [39]:

$$\mathcal{E} = \left(1 + \min \left[\frac{\Delta}{\delta_L^0} - 1, \Gamma \frac{u'}{S_L^0} \right] \right)^\gamma, \quad (2.112)$$

where γ is a constant of the model. The value $\gamma = 0.5$ is used thereafter. Introducing this efficiency factor into 2.105 gives:

$$\frac{\partial \bar{\rho} \tilde{\phi}}{\partial t} + \nabla \cdot \bar{\rho} \tilde{u} \tilde{\phi} = \nabla \cdot (\bar{\rho} \mathcal{E} \mathcal{F} D \nabla \tilde{\phi}) + \frac{\mathcal{E} \dot{\omega}_\phi}{\mathcal{F}}. \quad (2.113)$$

2.4.6.4 Dynamic TFLES

Unfortunately this formulation increases the overall diffusion of the domain. In the context of a perfectly premixed flame, the model may be employed using a constant value for the thickening factor \mathcal{F} . On the contrary in the case of other combustion regimes, increasing the diffusion over all the domain provokes modifications of the mixing. L egier *et al.* [40] introduced a dynamic formulation of the TFLES approach, relying on the flame sensor \mathcal{S} : a scalar which equals 1 in the reactive zones and 0 on the remaining zones of the domain. The filtered conservative equation for the scalar ϕ is rewritten with the flame sensor to give:

$$\frac{\partial \bar{\rho} \tilde{\phi}}{\partial t} + \nabla \cdot \bar{\rho} \tilde{u} \tilde{\phi} = \nabla \cdot (\bar{\rho} \mathcal{E} \mathcal{F} J_i^{lam} + (1 - \mathcal{S}) J_i^{sgs}) + \frac{\mathcal{E} \dot{\omega}_\phi}{\mathcal{F}}. \quad (2.114)$$

where J_i^{lam} is the laminar diffusive flux and J_i^{sgs} represents the sub grid diffusive flux. The coupling between the flame sensor \mathcal{S} and both the thickening factor \mathcal{F} and efficiency function \mathcal{E} are:

$$\mathcal{F} = 1 + (\mathcal{F}_{max} - 1) \mathcal{S}, \quad (2.115)$$

$$\mathcal{E} = 1 + (\mathcal{E}_{max} - 1) \mathcal{S}. \quad (2.116)$$

where the maximum values \mathcal{F}_{max} and \mathcal{E}_{max} are respectively computed from relations 2.107 and 2.111. Several formulations have been proposed for the calculation of the flame sensor in the context of tabulated chemistry and of global chemistry (1 or 2 steps). Recently, Benard [41] proposed a methodology adapted from the one of Franzelli [42] for the implementation of a flame sensor that rely on the source terms of species CO, CO₂ and H₂O:

$$\begin{cases} \mathcal{S} = 1 & \text{if } \dot{\omega} > \dot{\omega}_S \\ \mathcal{S} = 0 & \text{if } \dot{\omega} < \dot{\omega}_S \end{cases} \quad \text{with } \dot{\omega} = \dot{\omega}_{CO_2} + \dot{\omega}_{CO} + \dot{\omega}_{H_2O}, \quad (2.117)$$

where $\dot{\omega}_S$ is a threshold value. This threshold is frequently defined from a percentage of the maximum value of $\dot{\omega}$ within the flame. As illustrated on Figure 2.9, several steps are then employed to spread the zone where the sensor \mathcal{S} equals unity over the adjacent nodes and to filter the solution; so as to finally get a smooth sensor that includes the entire flame zone. The threshold value $\dot{\omega}_S$ is often set to 10% of the maximum source term computed with a 1D premixed laminar flame in similar operating conditions. Using this procedure, note that the threshold value $\dot{\omega}_S$ must be compared with the unthickened value of the source term that is obtained from $\mathcal{F} \dot{\omega}$. Moreover, with a low Mach number formulation the time step is large in comparison to that for a compressible approach. The flame sensor may vary against time which pauses some robustness issues. To address this limitation, the flame sensor is filtered in time introducing a coefficient of relaxation α between the value \mathcal{S}^n and the value at time $n - 1$, so that:

$$\mathcal{S}^n = \alpha \mathcal{S}^n + (1 - \alpha) \mathcal{S}^{n-1}. \quad (2.118)$$

This formulation lowers the time gradients. In the present work, $\alpha = 0.7$ is used.

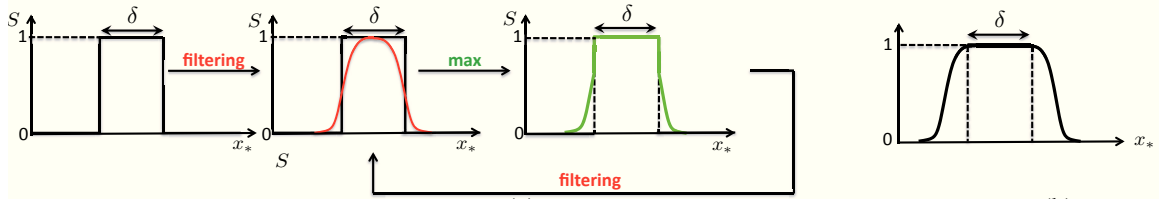


Figure 2.9: Procedure to spread the flame sensor and to filter it. Left illustrations: Initial profile and filtered profile. Right illustration: Final flame sensor. Image extracted from Benard [41].

2.5 Numerical description of the liquid phase

2.5.1 Two-phase flows modelling

A flow composed of particles rely on the presence of a carrying phase which may either be liquid or gas and on a dispersed phase composed of either liquid particles (such as kerosene droplets), solid particles (such as coal) or bubbles into a gaseous phase. The interaction of the dispersed phase with the flow highly depends on the fraction of the volume occupied by the particles in the fluid domain. In the context of this thesis, only a diluted suspension phase is considered. It requires a two-way coupling [43] which means that the influence of the moving particles on the fluid also have to be accounted for in addition to the inclusion of the impact of the fluid on the dispersed phase.

Two different descriptions are found in the literature: (1) The Euler-Euler approach consists of considering the dispersed phase as a continuous environment similar to a fluid which is given the mean properties of the droplets mist. The characteristics of the dispersed phase are thus transported on a Eulerian mesh using a set of flow equations similar to the ones employed for the carrying phase. (2) The Lagrangian approach consists of following particles individually in the flow domain. The mass transfer, momentum and energy phenomena are solved in interaction with the carrying phase. Each droplet (particle) has its own properties (temperature, velocity and diameter). Efficient interpolation methods are required with this approach since the position of the particles does not coincide with the mesh nodes. The Lagrangian description is the methodology employed for this thesis.

2.5.2 Equations for the Lagrangian description

2.5.2.1 Kinematic of the droplets

Each particle is assumed to have a spherical form, the mass m_p of a particle thus reads:

$$m_p = \rho_p \frac{\pi}{6} d_p^3, \quad (2.119)$$

where d_p refers to the diameter of the particle and ρ_p to its density. The equations for the transport of the particles are as follows:

- **The particle kinematic formalism** expresses the evolution of the position x_i^p of the particle p moving with the velocity u_i^p from relation:

$$\frac{dx_i^p}{dt} = u_i^p. \quad (2.120)$$

- **The momentum conservation** is written as a function of F_i^P which represents the projection onto the i^{th} axis of the forces acting on the particle.

$$m_p \frac{du_i^P}{dt} = F_i^P \quad \text{where} \quad F_i^P = F_{i,G}^P + F_{i,A}^P + F_{i,I}^P, \quad (2.121)$$

F_i^P is associated to three contributions: $F_{i,G}^P$ stands for the gravity and buoyancy forces, $F_{i,A}^P$ for the aerodynamical and drag forces and $F_{i,I}^P$ represents the interaction forces with the wall and the other Lagrangian particles.

- **Gravity:** The gravitational and buoyancy forces acting on the particle may be written from the relation:

$$F_{i,G}^P = (\rho_p - \rho) \frac{\pi}{6} d_p^3 g_i \quad (2.122)$$

where ρ is the density of the carrier-phase and g_i is the acceleration due to gravity. In strongly turbulent flows, the gravity force is often neglected in comparison to the aerodynamical forces. Furthermore, $\rho_p \gg \rho$ for liquid droplets into a gaseous phase, so that the buoyancy forces may be neglected.

- **Aerodynamic:** The drag force induced by the gas on the particle reads:

$$F_{i,A}^P = m_p \frac{1}{\tau_p} (u_i^P - u_i), \quad (2.123)$$

where τ_p is the time it takes to a particle to respond to the velocity fluctuations. This characteristic time is dependent on the flow regime that is defined by the particle Reynolds number Re_p expressed:

$$Re_p = \frac{d_p |u_i^P - u_i|}{\nu}, \quad (2.124)$$

τ_p is described as a function of the drag coefficient C_D from the relation,

$$\tau_p = \frac{4\rho_p d_p^2}{3C_D Re_p \rho \nu}. \quad (2.125)$$

A large variety of correlations have been proposed for the drag coefficient C_D [44]. The correlation for numbers of the particle Reynolds Re_p lower than 1 is the Stokes law.

$$C_D = \frac{24}{Re_p}. \quad (2.126)$$

For intermediate values, the correlation by Schiller and Naumann is employed [45],

$$C_D = \frac{24}{Re_p} + \frac{3.6}{Re_p^{0.313}}. \quad (2.127)$$

For values of the particle Reynolds number higher than 1000, the coefficient is considered to be constant and equal to 0.44.

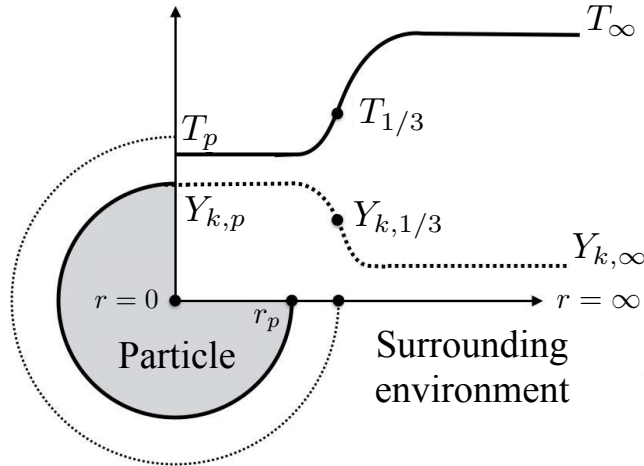


Figure 2.10: Illustration of a droplet p characterised by a temperature T_p and a composition $Y_{k,p}$ evaporating into its surrounding gaseous environment at conditions T_∞ and $Y_{k,\infty}$ [46].

2.5.2.2 Evaporation

Hypotheses of the evaporation model The temperature and the composition of the droplet are estimated from the presented conservative equations. They are highly dependent on the ambient conditions. The composition at the surface of the droplet (particle) is defined by the subscript p while the subscript notation ∞ refers to the condition of the surrounding gas. This is illustrated on figure 2.10. Several hypotheses are here formulated in the context of a single-component droplet.

1. The droplet is considered to be perfectly spherical and isolated *i.e.* its interaction with the other droplets is not accounted for.
2. The temperature of the droplet is considered uniform, its thermal conductivity being infinite.
3. The surface of the droplet is assumed to be thermodynamically in equilibrium with the environment. The Clausius-Clapeyron law is therefore employed for the estimation of the saturation vapour pressure at the surface of the droplet.
4. Except for the evaporated portion, the properties of the surrounding gas are considered constant from the surface of the droplet up to infinity.
5. The formulation proposed by Hubbard *et al.* [47] also referred as the 2/3-1/3 law is retained to consider the properties of the gas in the small layer that forms around the droplet. The composition and temperature in this small region are computed from the surface conditions and from the infinite conditions considering different ponderations. The formulation is illustrated on figure 2.10.

$$T_{1/3} = \frac{2}{3}T_p + \frac{1}{3}T_\infty, \quad (2.128)$$

$$Y_{k,1/3} = \frac{2}{3}Y_{k,p} + \frac{1}{3}Y_{k,\infty}. \quad (2.129)$$

Mass evolution of the droplet The mass evaporation rate of the droplet is computed from the integration of the conservation equations of the evaporated species from the droplet radius up to infinity. See

the work by Kuo [33] and Sirignano [48] for more details.

$$\dot{m}_p = -\pi d_p(\rho D)Sh \log(1 + B_M), \quad (2.130)$$

This formulation introduces several characteristic terms and numbers

1. The Spalding number expressed in terms of mass allows for describing the mass transfer effects as a function of the evaporated species mass fraction studied both at the droplet surface and in the surrounding gas. It is expressed from the relation:

$$B_M = \frac{Y_{k,p} - Y_{k,\infty}}{1 - Y_{k,p}} \quad (2.131)$$

The mass fraction $Y_{k,\infty}$ is expressed from an interpolation of the Eulerian mesh. The following expressions are employed for the estimation of the species mass fractions at the surface of the droplet;

$$Y_{k,p} = \frac{X_{k,p}W_k}{W_p} \quad (2.132)$$

The species molar fraction $X_{k,p}$ is computed from the Dalton's law:

$$X_{k,p} = \frac{P_{k,p}}{P}, \quad (2.133)$$

it is deduced from the Clausius-Clapeyron's law that gives the relation between the total pressure at saturation of a pure component as a function of its boiling temperature and of its latent heat of vaporisation. The estimation of the molecular weight at the surface of the droplet is deduced from the relation:

$$W_p = X_{k,p}W_k + (1 - X_{k,p})\bar{W}_{j \neq k,p}. \quad (2.134)$$

The computation of the term $\bar{W}_{j \neq k,p}$ is achieved from the relation:

$$\bar{W}_{j \neq k,p} = \bar{W}_{j \neq k,\infty} = \frac{1 - Y_{k,\infty}}{1 - Y_{k,\infty} \frac{W_\infty}{W_k}} W_\infty, \quad (2.135)$$

which states, that the molecular weight of the gaseous phase except for the evaporated species is constant from the surface of the droplet up to the infinity.

2. The Sherwood number Sh gives the ratio between the convective mass flux and the diffusive mass flux. The correlation proposed by Ranz and Marshall [49] applies in the context of a forced convection around a sphere. It reads:

$$Sh = 2 + 0.55Re_p^{1/2}Sc^{1/3} \quad (2.136)$$

3. The diffusion term (ρD) in the equation 2.130 is usually simplified to the expression:

$$\rho D = \frac{\mu^{1/3}}{Sc} \quad (2.137)$$

Temperature evolution of the droplet The temperature evolution of the droplet is computed from the integration of the energy conservative equation from the droplet surface up to infinity. Doing so, the following expression is obtained;

$$\frac{dT_p}{dt} = -\frac{1}{\tau_h} \left(T_p - \left(T_\infty - \frac{L_v B_T}{C_{p,1/3}} \right) \right), \quad (2.138)$$

where τ_h is the characteristic time associated to the heating of the spherical droplet and defined from:

$$\tau_h = \frac{\rho_p d_p^2}{6} \frac{Sc}{\mu_{1/3} Sh} \frac{C_{p,k}}{C_{p,1/3}} \frac{B_T}{\log(1 + B_M)}, \quad (2.139)$$

where $\mu_{1/3}$ and $C_{p,1/3}$ are respectively the dynamic viscosity coefficient and the specific heat capacity at constant pressure computed with the 2/3-1/3 law. An explanation on the derivation of relation 2.139 may be found in [48] or in Enjalbert's thesis [50]. The thermal Spalding number B_T is here expressed as a function of the mass Spalding number through the relation,

$$B_T = (1 + B_M)^{\frac{Sh Pr}{Nu Sc}} - 1 \quad (2.140)$$

The Nusselt number is used to describe the ratio between the convective and diffusive heat transfers. As for the Sherwood number it may be expressed from the relation by Ranz and Marshall for a spherical droplet:

$$Nu = 2 + 0.55 Re_p^{1/2} Pr^{1/3}. \quad (2.141)$$

Boiling specific condition The problem is simplified when the temperature of the carrying phase is higher than the boiling temperature T_{boil} associated to the droplet composition. In that case, the gaseous layer that forms around the droplet reaches saturation, hence $Y_{k,p}$ tends to unity and the Spalding number diverges towards infinity.

In that situation, the equation 2.138 is simplified to $dT/dt = 0$. The temperature of the droplet is assumed to be equal to T_{boil} , which gives,

$$B_T^{\text{sat}} = \frac{C_{p,\text{ref}}(T_\infty - T_{\text{boil}})}{L_v}. \quad (2.142)$$

The Spalding number at boiling conditions expressed in terms of mass is then extracted from 2.140:

$$B_M^{\text{sat}} = (1 + B_T^{\text{sat}})^{\frac{Nu Sc}{Sh Pr}}, \quad (2.143)$$

and the equation 2.130 is employed for the calculation of the mass variation of the droplet using the Spalding number at saturation B_M^{sat} .

Diameter evolution The diameter of the droplet evolves according to the formulation for the mass evolution 2.130.

$$dm_p = \left(\frac{\pi \rho_p d_p^2}{2} \right) dd_p \quad (2.144)$$

The time evolution of the particle diameter is computed from the characteristic time τ_m and the initial diameter of the particle $d_{p,0}$.

$$\frac{dd_p^2}{dt} = \frac{d_{p,0}^2}{2d_p \tau_m} \quad \text{with} \quad \tau_m = \frac{\rho d_{p,0}^2 Sc}{4Sh \mu_{1/3} \log(1 + B_M)} \quad (2.145)$$

2.5.3 Coupling with the gaseous phase

2.5.3.1 Interaction between the dispersed phase and the gas

Three source terms are introduced into 2.19, 2.20, 2.23 and 2.30 to account for the feedback information from the particle to the gaseous phase. Namely θ_M for the mass conservation, θ_D for the momentum conservation and θ_H for the enthalpy. They are computed locally where the particle is present. The expressions associated to these three terms are:

$$\theta_M(x_i, t) = \frac{1}{\Delta V} \sum_{p=1}^{N_p} -\dot{m}_p \delta(x_i - x_i^p(t)), \quad (2.146)$$

$$\theta_D(x_i, t) = \frac{1}{\Delta V} \sum_{p=1}^{N_p} -\dot{F}_p \delta(x_i - x_i^p(t)), \quad (2.147)$$

$$\theta_H(x_i, t) = \frac{1}{\Delta V} \sum_{p=1}^{N_p} \left(-\dot{m}_p C_{p,l} \frac{dT_p}{dt} + \dot{m}_p L_v \right) \delta(x_i - x_i^p(t)), \quad (2.148)$$

where δ corresponds to the Dirac distribution and ΔV to the control volume which theoretically should be of the order of the particle size. In practice the volume control is defined from the size of the cell that contains the particle.

2.5.3.2 Formalism in LES

Influence of the sub-grid fluctuations on the particles. The Lagrangian solver relies on the scalars that are solved on the Eulerian mesh. Using LES, the sub-grid scales are unresolved. Therefore, the dispersed phase only knows about the filtered information $\tilde{\phi}$. A model should be introduced [51, 52] to account for the sub-grid information and rebuild ϕ from the filtered value $\tilde{\phi}$. It is reported in the literature that the introduction of such a model is important for the drag term only when the unresolved velocity fluctuations are of the order of the particle velocity or higher to the particle velocity. For an evaporating spray this condition is encountered only at the end of the droplets life. The majority of the spray is therefore insensitive to the velocity fluctuations. Hence, in the present case the effect is neglected.

Influence of the particles on the sub-grid scale turbulence. The presence of the dispersed phase may impact the sub-grid fluctuations in two different manners: (1) the particles may dissipate the scales with the same order of magnitude [53] hence modifying the form of the energy spectrum, (2) the two-way coupling effects may be incorrectly estimated because the segregation of the particles by the sub-grid fluctuations are not accounted for. Apart from a study by Yuu *et al.* [54], most of the recent applications neglect this influence [55, 56]. The same assumption is made in the present work.

2.6 Numerical solvers

The results presented in this thesis have been derived from computations performed with two different softwares namely CANTERA and YALES2. The ORCh methodology proposed for the reduction and the optimisation of combustion mechanisms rely on the CANTERA package.

2.6.1 Chemistry 1D solver: CANTERA

CANTERA is an open source suite of object-oriented software tools employed for the computation of reacting flows involving detailed chemistry, thermodynamics and complex transport properties [57]. It is used for the computation of chemical equilibrium, and for the simulation of networks of stirred reactors. An adaptative mesh refinement algorithm is implemented in the code to optimise the mesh resolution in the regions of strong gradients. The C++ version of the code is employed in this thesis.

2.6.2 Large-Eddy Simulation 3D solver: YALES2

YALES2 is a parallel CFD code which solves the three-dimensional Navier-Stokes equations on reactive two-phase problems using DNS and LES approaches [58]. The code relies on the use of a finite volume method based on unstructured meshes composed of triangles, tetrahedrons, prisms and pyramids hence allowing for the simulation of complex geometries. YALES2 uses a low Mach number formulation which is therefore not forced to deal with the compressible tiny time scales. It relies on the *Courant Friedrichs Lewy* (CFL) criteria for the estimation of the time steps. The YALES2 solver is capable of dealing with complex chemistry [59] and with the most advanced massively parallel supercomputers [60].

Chapter 3

A review on chemistry reduction methodologies

Contents

3.1	Introduction	62
3.1.1	Reduced mechanisms types	62
3.1.2	Basic kinetic simplifications	62
3.2	The derivation of global mechanisms	66
3.2.1	Species and reactions selection	66
3.2.2	Optimisation of the chemical rates	67
3.2.3	Corrections functions	67
3.3	Reduction to skeletal mechanisms	68
3.3.1	Jacobian-based methodologies	69
3.3.2	Directed relation graph	70
3.3.3	Directed relation graph-aided sensitivity analysis	71
3.3.4	Directed relation graph with error propagation	71
3.3.5	Path flux analysis	72
3.3.6	Optimisation-based reduction	73
3.3.7	Species lumping	74
3.4	Reduction based on analytical expressions	75
3.4.1	Selection of QSS species	76
3.4.2	Implementing the QSS assumption	81
3.4.3	Non-linearity of the algebraic system	82
3.4.4	QSS matrix simplification	84
3.5	Application: Methane-air combustion modelling	86
3.5.1	The history of methane chemistry modelling for flame simulation	86
3.5.2	Assessment of global and analytical reduced methane-air mechanisms	94
3.6	Conclusion	99

3.1 Introduction

Even though detailed mechanisms are necessary to fully understand ignition, flame propagation and pollutants emission, they are still today impractical to use for many industrial applications because of their size. In fact, the combustion mechanisms developed today to describe the chemical oxidation of most hydrocarbons require the use of about fifty to several hundreds of conservative equations associated to tiny time and space scales. Over the last decades, a tremendous amount of chemistry reduction approaches have been developed in order to lower the costs arising from the use of complex mechanisms. This chapter is intended to describe the most relevant of these methodologies for the creation of reduced chemical schemes.

3.1.1 Reduced mechanisms types

The type of chemical schemes obtained from a reduction are here classified into three categories:

- **Skeletal mechanisms** are very similar to the detailed chemical schemes from which they are constructed. They do not introduce any assumptions but simply rely on the removal of the unnecessary species and reactions. For the conditions of the reduction, these schemes are usually very accurate compared to the targets defined from the reference. However, such combustion mechanisms still require the transport of a large amount of intermediate species, hence it is rarely affordable to use them for 3D simulations.
- **Analytical mechanisms** are usually derived from the introduction of quasi-steady state (QSS) and/or partial equilibrium assumptions. Both hypothesis lead to the creation of analytical expressions that relate the concentration of some intermediate species to the concentration of the major ones. The scheme may then be reduced by removing the intermediates that are computed from the analytical expressions.

The approaches employed for the derivation of either skeletal or analytical mechanisms rely on operations that are performed directly on the species and reactions of a reference detailed mechanism. A third approach consists of creating from scratch a small set of global reactions. This methodology differs from the two other approaches by the fact that the reactions of the global scheme are not selected within the reference mechanism.

- **Global mechanisms** are constructed with less than ten species and from one to four chemical reactions. They usually are *ad hoc* chemical schemes with fitted/optimised parameters. The majority of these mechanisms are developed to recover very specific properties of the flame such as the flame velocity, the equilibrium temperature and sometimes a few major species mass fractions. They are designed to match the profiles obtained with a detailed mechanism or directly the results of an experiment.

The three approaches will be discussed in more detail over the chapter. The basic concepts for the simplification of a detailed mechanism are now given to end up with a skeletal or analytical scheme.

3.1.2 Basic kinetic simplifications

This section on kinetic reduction principles is inspired from the work by Turányi and Tomlin [61].

3.1.2.1 Pool chemical hypothesis

It is frequent that the concentration of a reactant is much higher than the concentration of the other species and that the variation of this species concentration along the simulation is almost negligible. For instance, this assumption perfectly applies to nitrogen N_2 in most fuel-air flames. In that case the chemical steps in which this species is present as a reactant may be simplified to first-order reactions. As an example, let us consider the reaction $A + B \rightarrow C$. Assuming that the concentration of species 'B' remains constant, the product $K' = K[B]$ is also constant. The second order expression may then be simplified to a first-order reaction with;

$$\frac{d[C]}{dt} = K[A][B] = K'[A]. \quad (3.1)$$

3.1.2.2 Rate-determining step

Even with large combustion schemes, the production rate of a species may be dependent on the rate of a single reaction. Such a reaction is called the rate-determining step. For instance, let us consider a simple set of sequential first-order reactions.



The production rate of the final product 'E' may be estimated from the rate coefficient K_3 of the rate-limiting step multiplied by the concentration of the reactant of this chemical step, here 'C';

$$\frac{d[E]}{dt} \approx K_3[C]. \quad (3.2)$$

For large mechanisms, the rate-determining step is distinguished from the others when increasing its rate leads to a drastic increase of the production of the associated chemical products. Note that, it is usually not the reaction with the lowest rate coefficient. In general, finding rate-determining steps is done by quantifying the impact that a small change of rate coefficient has on the production rate $\dot{\omega}_k$ of a given product k (see for instance the work of Turányi [62]).

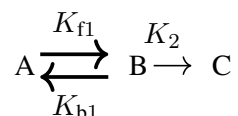
3.1.2.3 Quasi-steady state approximation

A species k is said to be in quasi-steady state (QSS) whenever the reactions by which it is produced are slower than the reacting steps by which the species is consumed i.e. whenever this species production rate P_k is low compared to its consumption rate C_k . In that case, species k is quasi-instantly consumed after it is produced thus the concentration of the species stays low and its net rate may be assumed as equal to zero ($\dot{\omega}_k = 0$):

$$\dot{\omega}_k = W_k \sum_{j=1}^{N_r} \nu_{kj} \dot{Q}_j = W_k \sum_{j=1}^{N_r} \nu_{kj} \left[K_{fj} \prod_{k=1}^{N_{sp}} [X_k]^{\nu'_{kj}} - K_{rj} \prod_{k=1}^{N_{sp}} [X_k]^{\nu''_{kj}} \right] = 0. \quad (3.3)$$

Applying the QSS assumption, one can deduce analytical equations from relation 3.3 to express the concentration of the steady state species as a function of the other (non-QSS) chemical species. The system of ODEs can then be simplified to a smaller system with fewer variables. Thus QSS principle relies on the hypothesis that the concentration of the fast intermediate species can be algebraically expressed with the concentration of a reduced set of important (major) species.

For instance, a simple case is defined from the following successive reactions where species 'B' is assumed to be a good QSS candidate.



Applying the QSS assumption, the variation of concentration [B] is assumed constant so that:

$$\frac{d[B]}{dt} = 0 \quad \text{hence} \quad [B] = \frac{K_{f1}}{K_{b1} + K_2} [A]. \quad (3.4)$$

Then using the relation 3.4, the concentration of the chemical species 'C' may be expressed directly from the concentration of species A since;

$$\frac{d[C]}{dt} = K_2[B] = \frac{K_{f1}K_2[A]}{K_{b1} + K_2} = K'[A], \quad (3.5)$$

where K' is expressed from:

$$K' = \frac{K_{f1}K_2}{K_{b1} + K_2}. \quad (3.6)$$

It is seen that from this simplification, the above set of reactions is now simplified to a single reaction,

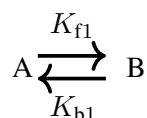


computed from an analytic rate coefficient K' . Although the species 'B' is removed from the set of transported species, its kinetic participation is accounted for thanks to the analytical term K' . Its concentration may also be estimated from the relation 3.4, although in practice it is rarely performed.

3.1.2.4 Partial equilibrium

The partial equilibrium assumption applies when chemical species that participate in fast-equilibrium reactions are then consumed by slow reactions. The chemical process hence reach a point where forward and backward rates become equal. In that case, the stoichiometry of the chemical steps and the associated equilibrium constants are used to estimate the ratios of the concentrations of the species involved. If the rates of the equilibrium reactions are much higher than the rates of the other reactions that consume the species involved within the equilibrium reactions, the concentrations of the species may be accurately estimated.

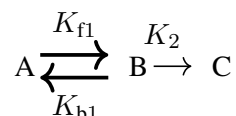
As an example, the following reaction is considered;



As introduced in Section 2.2.2.2, the equilibrium constant of the reaction is estimated from the ratio of the forward and backward rate coefficients: $K_{eq,1} = K_{f1}/K_{b1}$. If the reaction reaches equilibrium, the following relation is verified:

$$K_{f1}[A] = K_{b1}[B] \quad \text{hence} \quad [B] = \frac{K_{f1}[A]}{K_{b1}} = K_{eq,1}[A]. \quad (3.8)$$

Moving on to the relation:



where the species 'B' is consumed by a slow reaction associated to a low rate coefficient K_2 in comparison to the forward and backward rates of reaction 1. The partial equilibrium assumption still applies to reaction 1 and the relation 3.8 is therefore still valid. In that case, the relation for the production of species 'C' reads:

$$\frac{d[C]}{dt} = K_2[B] = K_2 K_{eq,1}[A]. \quad (3.9)$$

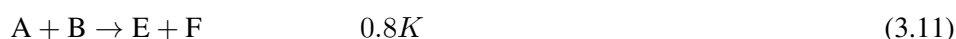
Again using this assumption, the concentration of the species 'B' is not needed anymore to solve for the system of ODEs.

3.1.2.5 Conserved properties

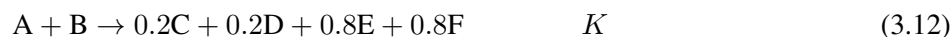
They are relations within the defined set of equations that state that some particular properties are conserved. For instance the number of moles of each element stays constant during the chemical process. Because of these conserved properties, there are some linear dependence between the rows of the stoichiometric matrix. The number of chemical species N_{sp} is usually lower than the number of reactions N_r . If there were no conserved properties, the rank of the stoichiometric matrix would be equal to N_{sp} . With N_c conserved properties, the rank of the matrix is $N = N_{sp} - N_c$. Therefore there is no need to solve for the complete system of ODEs, it can indeed be replaced by a reduced system with N variables. The other concentrations being linearly related to the ones that are solved.

3.1.2.6 Lumping of reactions

The lumping of two reactions is presented considering the following set of chemical paths;



This formulation indicates that the reaction $A + B \rightarrow$ products is a multichannel reaction that leads to the creation of combustion products $C + D$ and combustion products $E + F$. Overall the rate coefficient of the reaction is K , separated over the two chemical paths. Reaction 3.10 participates to 20% of the consumption of the reactants and reaction 3.11 to 80% of it. Such systems of reactions are commonly found in detailed combustion schemes. Following this, the system may simply be recast in the form of a single reacting step:



The principle of rate-determining step may also be employed to lump two chemical reactions. For instance, the following set of reactions is considered;



As explained earlier, reaction 3.13 is the rate-determining step, hence the rate of the lumped reaction that would be obtained while lumping these two reactions would be $\dot{Q} = K_1[A][B]$. During the reaction,

species A, B and E are consumed while species C and F are produced. Species D is produced and consumed at the same rate. To conserve the correct rate for the lumped reaction, only species A and B can be expressed in the left-hand side of the step. In that case, the following formulation may be given:



It may be surprising to find negative stoichiometric coefficients in a reaction, but there are several lumped mechanisms [63] that contain such coefficients. Interestingly not only the system of reactions is simplified to a single step but there is also the removal of the highly reactive species D. The lumping of reactions based on timescale analysis is therefore of interest for the reduction of the number of species of a combustion mechanism and for the reduction of the stiffness of the associated system of ODEs.

3.2 The derivation of global mechanisms

The use of reduced chemical schemes capable of accurately predict the main flame properties is of primary importance for a number of practical applications in the combustion domain. These include all the combustion problems for which no chemical description of the fuel oxidation has been formulated and the applications for which the use of a detailed chemistry is too costly. Various reduced chemical schemes based on a global description have been proposed in the literature and optimised to simulate particular flame features. The investigators were usually trying to reproduce the consumption speed, the temperature profile or the results of a given experiment.

3.2.1 Species and reactions selection

To understand the construction of a global scheme, one should keep in mind that the equilibrium state is exclusively piloted by the thermodynamic of the species. Reactions have no impact on this equilibrium condition but allow for describing the paths followed to reach this stable state and the speed at which it is reached.

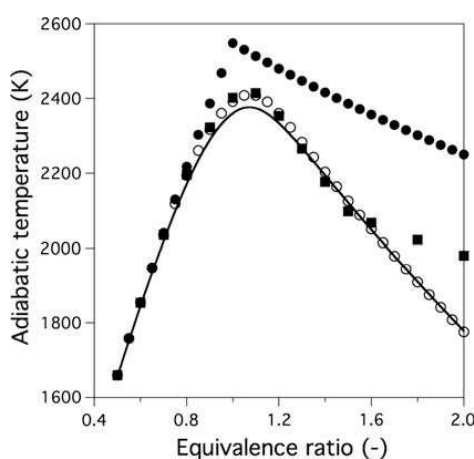


Figure 3.1: Adiabatic flame temperature as a function of the equivalence ratio in a kerosene-air mixture (Franzelli *et al.* [64]). Comparison between the Luche mechanism [65] and simplified mixtures with 5 (●), 6 (■) and 7 (○) chemical species.

As introduced earlier, global combustion mechanisms are *ad hoc* models composed of one to four chemical steps [64, 66–69]. Simple one-step models of the form of relation 2.34 have been proposed

and validated for recovering flame speed and equilibrium temperature in lean premixed conditions. To properly reproduce the behaviour of rich hydrocarbon flames, the introduction of a few more chemical species is nevertheless mandatory. This is illustrated on Figure 3.1 which gives a comparison for various simplified chemistries of the temperature equilibrium of kerosene-air mixtures expressed by considering a range of equivalence ratios from lean to rich conditions [64]. It is reported that a 5 species description (Fuel, CO₂, H₂O, N₂, O₂) is enough to account for the equilibrium behaviour of lean kerosene-air flames, however the error associated to rich conditions is large. The introduction of species CO leads to a better description of stoichiometric and moderately rich conditions. Species H₂ must be added for equivalence ratios above 1.6. Indeed, because of the lack of oxygen, an incomplete oxidation of the hydrocarbons is observed at rich conditions. CO and H₂ being the main additional products of this incomplete combustion. The same conclusion is provided in the work of Franzelli *et al.* for methane-air flames [70] and may be extended to any hydrocarbon-air flames.

3.2.2 Optimisation of the chemical rates

Once a set of chemical species and reactions has been selected, the Arrhenius constants of the reactions must be arranged to get an overall response that fits with experimental data or that matches flame trajectories computed with a more detailed mechanism. The first mechanisms proposed in the literature were manually optimised from chemical considerations.

More recently, optimisation-based approaches have been proposed to determine the chemical constants of the reduced mechanisms. The concept was introduced in 1998 by Polifke *et al.* [71] in the context of methane-air premixed combustion and considering two mechanisms: one with 2 chemical steps and the other one with 3 steps. The methodology they proposed relies on the use of a Genetic Algorithm (GA) and on a comparison with the species production rates computed with a detailed chemistry. Later, the approach was extended to much larger mechanisms by several research groups [72–76]. A similar strategy was also proposed in 2012 by Apri *et al.* [77] for biochemical kinetic systems using an optimisation procedure to fit with the original experimental data. In 2013, Gokulakrishnan *et al.* [78] employed the same approach for the combustion of several fuels relying this time on a simulated annealing algorithm. This optimisation methodology will be further discussed and analysed in the next chapter.

3.2.3 Corrections functions

Optimisation approaches are efficient ways to find the best parameters for a reduced set of reactions. However, it appears that even for optimised mechanisms, reduced low order kinetics cannot properly describe the laminar flame velocity for a large range of equivalence ratios. To overcome this limitation, a methodology relying on the adjustment of the pre-exponential factors in the Arrhenius equation of the considered global reactions has been published recently [64, 68, 79] by different teams. The idea is to introduce into some of the Arrhenius formulations a correction term that is tabulated as a function of the equivalence ratio of the mixture.

This methodology has been revised lately in the work of Cailler *et al.* [69] also introducing virtual intermediate species with optimised properties. The additional degree of freedom included thanks to these virtual species allows for recovering the proper temperature equilibrium even with a two-step chemistry.

3.3 Reduction to skeletal mechanisms

Skeletal mechanisms are constructed based on detailed ones by removing the species and reactions which participate negligibly to the chemical process. The computational costs involved for their use are still prohibitive for industrial applications, although they are significantly smaller in comparison to the ones achieved with the complex chemical schemes they have been build from. The discrepancies with the detailed chemistry are minimal in almost all combustion regimes. As a result, skeletal mechanisms often serve as reference for the creation of even more reduced mechanisms.

The species within a detailed chemical scheme may be classified into three categories (1) the *important species*, basically these include the initial reactants, the combustion products and any pollutant of interest (2) the *necessary species* which have to be present to accurately capture the concentration profiles of the important species as well as the flame temperature and other important reaction features, (3) the remaining ones also called *redundant species* [80].

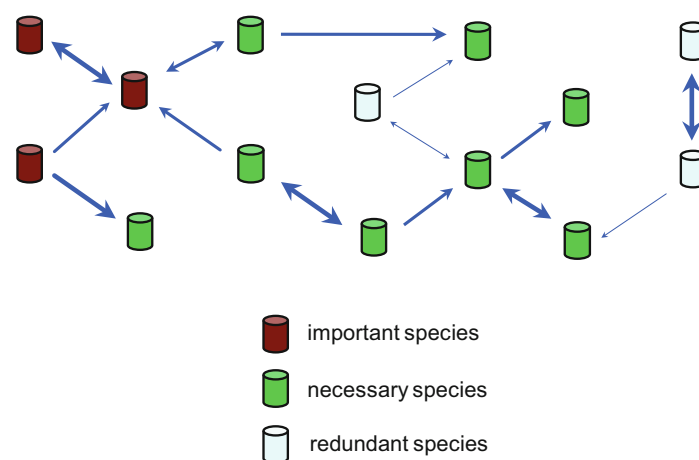


Figure 3.2: Illustration of the relationship between chemical species [61], as treated by several approaches for the estimation of unnecessary (redundant) species. The procedure is initiated from the important species. The species necessary for the reproduction of these important targets are identified. The remaining species are poorly related to the group of targets and may be removed.

Automatic identification of redundant species and reactions are used to produce skeletal mechanisms which can be seen as subsets of the original reference mechanisms. Traditional approaches focus on:

- Chemical rates and Jacobian-based inspections:** (1) The removing of the reactions slower than the rate-determining steps and of the ones producing much less heat than the main heat producing steps [81, 82]. The reduction of the number of reactions also means removing some chemical species. (2) The integration of the fluxes for each species and elements [83, 84]. Redundant species are identified as those which are poorly connected to the targets. (3) The use of the computational singular perturbation (CSP) approach to identify the modes to which important species are associated [85] and then remove the species of the other modes. (4) The study of rate sensitivities using the species connection defined by the Jacobian matrix of the differential system [80].
- Graph-based methodologies:** (1) The creation of directed relation graphs (DRG) [86] that quantify the interactions between the target species and the remaining ones. The extension of the DRG methodology to the measurements of the error introduced by each reduced scheme [87]. The in-

roduction of an error propagation along the interaction paths [88] to measure the relation between a species and the targets via the production/consumption of other species. (2) The use of the path flux analysis [89, 90].

- **Optimisation methodologies:** (1) The optimisation-based analysis of several possible reduction levels [91] and (2) of the removal of several lists of species and/or reactions [73, 74, 92]. Because the optimisation problem possesses multiple local optimums, the study is always performed using a heuristic methodology, genetic algorithms are typically employed.
- **Chemical lumping:** (1) The definition of new species whose concentrations are computed from a linear combination of the species of the starting mechanism [93]. (2) The use of timescales analysis to define lumped groups which allow for the construction of a stoichiometric matrix associated to the fast subspace of the initial matrix of the system [94]. The use of non-linear systems to find the optimal groups of species to be lumped together [95].

Among these methods, the most commonly used are now discussed. Emphasis is on the approaches relying on Directed Relation Graphs which have been largely employed in this thesis.

3.3.1 Jacobian-based methodologies

An approach relying on the analysis of the Jacobian matrix that describe the system of Ordinary Differential Equations (ODE) [80] is presented in this section for both species and reactions reduction.

3.3.1.1 Finding redundant species

Parameter B_k is defined to estimate the influence of a change in the concentration of species k on the net production rate $\dot{\omega}_n$ of the N_i important species. It is based on the investigation of the Jacobian of the kinetic system of ODEs. Within the normalised Jacobian matrix, the element $([X_k]/\dot{\omega}_n)\partial\dot{\omega}_n/\partial[X_k]$ corresponds to the percentage of variation in the production of species n due to a change of 1% in the concentration of species k . The overall sensitivity measure is based on a least squares objective function computed on the normalised Jacobian elements;

$$B_k = \sum_{n=1}^{N_i} \left(\frac{[X_k]}{\dot{\omega}_n} \frac{\partial\dot{\omega}_n}{\partial[X_k]} \right)^2. \quad (3.16)$$

The higher the value of the parameter B_k , the greater is the direct influence of the species k on the production/consumption of the important species of the system. An iterative procedure is required to capture the species that affect the important ones not through a direct coupling but by influencing other necessary species. To do so, the species found to be necessary are taken into account for the summation of each subsequent iteration, thus providing new values for the B_k parameters.

3.3.1.2 Finding redundant reactions

The participation of a given reaction to the production of important species is characterised by the parameter B_j . It measures the ratio of the global production rate of the considered species k to the production rate of species k through the reaction j (noted $\dot{\omega}_{kj}$) using a least squares objective function. This measure

provides a rank of the reactions depending on their influence on the behaviour of the system at each of the considered reaction times.

$$B_j = \sum_{k=1}^{N_{\text{sp}}} \left(\frac{\dot{\omega}_{kj}}{\dot{\omega}_k} \frac{\partial \dot{\omega}_k}{\partial \dot{\omega}_{kj}} \right)^2. \quad (3.17)$$

3.3.2 Directed relation graph

Directed relation graph approaches have first been introduced by Lu and Law [86]. Note that while various methods exist for finding species and reactions that contribute negligibly to the production rate of every species, it is not straightforward to find those who are unimportant because of the coupling with other species. A species ‘A’ may be strongly related to a species ‘B’ by being present in the same reaction or by being coupled to a species ‘C’ that also strongly influences species ‘A’. The direct influence of one species to another is quantified by r_{A-B} , here, the normalised contribution of species ‘B’ to the production/consumption of species ‘A’.

$$r_{A-B} = \frac{\sum_{j=1}^{N_r} |\nu_{Aj} \dot{Q}_j \delta_{Bj}|}{\sum_{j=1}^{N_r} |\nu_{Aj} \dot{Q}_j|}, \quad (3.18)$$

where \dot{Q}_j is the rate of reaction j and δ_{Bj} is the Kronecker symbol. It equals 1 if the j^{th} elementary reaction involves species ‘B’ and 0 otherwise. A small threshold value ϵ is defined such that if $r_{A-B} < \epsilon$, the influence of species ‘B’ on the production rate of species ‘A’ is assumed negligible. This threshold controls the level of reduction but also the capabilities of the reduced mechanism to reproduce the reference.

Figure 3.3 shows an example of a DRG description where relations between species are visible. The arrows show the species directions of influence and the width of the arrows represents the strength of the dependence. We can observe that ‘A’ is dependent on species ‘B’ whereas the opposite is not true.

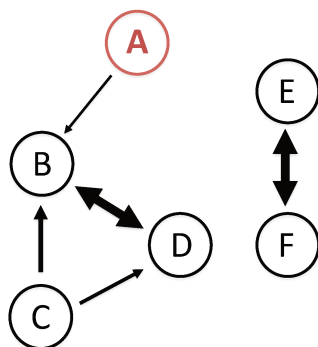


Figure 3.3: Illustration of the species inter-relations as encountered using a directed relation graph. Modified from Lu and Law [86].

It is seen that species ‘B’ and ‘D’ are strongly related, they form what is known as the dependent set $\{B, D\}$ of ‘A’. Therefore, if we assume that species ‘A’ is the target, ‘B’ and ‘D’ have to be part of the skeletal mechanism. The other species (‘C’, ‘E’ and ‘F’) can be removed from the scheme since neither ‘A’ nor the species in the dependent set of ‘A’ rely on them. Finally, note that the strongly coupled groups $\{B, D\}$ and $\{E, F\}$ should be kept or eliminated together. A starting set of species that need to be kept has to be selected. The fuel can be the only initially selected one since the oxidiser and the radicals

and products resulting from their combination will necessarily be included in the dependence. A deep first search is applied to look for the set S_A of each starting species 'A'. All the reactions which do not contain any of the species present in S_A are removed so as to build the skeletal mechanism. The obtained skeletal mechanism is bounded by the defined error scalar ϵ . To create a skeletal mechanism valid on a large range of conditions (equivalence ratio, temperature, pressure...), sub-skeletal mechanisms are constructed, adapted to given operating points. The union of these application-specific sub-mechanisms form the final skeletal chemical scheme.

3.3.3 Directed relation graph-aided sensitivity analysis

A first improvement of the DRG methodology has been proposed by Zheng *et al.* [87] in 2007 using the name of *DRG-aided sensitivity analysis*. With this methodology, the DRG estimation proposed for the group of redundant species is verified through simulations. To do so, the redundant species are first removed using a conservative threshold value. A second group of species is subsequently considered with a tighter threshold. Simulations are then performed to assess the relevance of removing these species one by one. The DRG-ASA approach is more effective than the simple DRG approach in the sense that it investigates directly the error introduced by the reduction procedure. Less species then appear to be necessary than when using the original DRG approach.

3.3.4 Directed relation graph with error propagation

The DRG approach assumes that the species are equally important and that the coupled set of species has to be entirely kept, which may not always be necessary. An improvement of this methodology has been proposed by Pepiot *et al.* [88] to address that problem. For every species 'A', a set of primary species which are directly related to 'A' is defined and the interaction coefficient r_{A-B} is estimated for each of them. Note that if a species 'B' is not in this primary set, $r_{A-B} = 0$. Let us consider a species 'C' interacting with the species A through a species 'B'. The species 'C' is important to 'A' only if it is important to 'B' and that 'B' has a significant influence on 'A'. This more sophisticated coupling is quantified through the use of a path-dependent coefficient noted $r_{A-B,i}$. For instance, on figure 3.4, if the path #1 is $A \rightarrow B \rightarrow D$, the obtained coupling coefficient is:

$$r_{A-D,1} = r_{A-B} r_{B-D} . \quad (3.19)$$

Thus, if an error on the calculation of species 'D' is made, it propagates through species 'B' and it is seen by species 'A'. The generalised interaction coefficient for species 'A' with species 'B' is noted r_{A-B}^* and it is defined to be the maximum path-dependent coefficient between 'A' and 'B'.

$$r_{A-B}^* = \max_{\text{all paths } i} \{r_{A-B,i}\} . \quad (3.20)$$

The species A depicted within the Figure 3.4 depends on the species C through the definition of the coefficient $r_{A-C}^* = \max \{r_{A-B} r_{B-C}, r_{A-C}\}$. With this new approach, the selected species are not equally important since the species that are farther from the targets are more important to the species they are related to, than to the targets themselves. Target species should thus be carefully chosen since they are the only species that will be guaranteed to be accurately reproduced.

The paths taken by conserved atoms, in relation with a given species and the overall atomic balances through the detailed schemes, are also examined with the coefficient α_{E-A} , which is computed as the number of atoms ($E \equiv C, H, O$) in 'A' times its chemical rate, normalised by the rate of 'E' atom

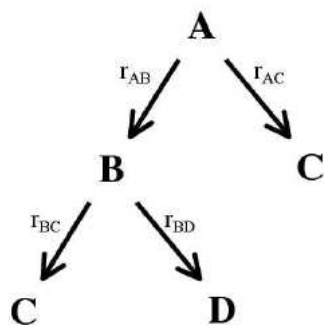


Figure 3.4: Interaction graph between four chemical species. Extracted from Pepiot and Pitsch [88].

exchanged over all forward reactions. The importance of a species ‘C’ is measured with the parameter \mathcal{T}_C , defined from the combination of the atom and species interactions. The species ‘C’ will be kept into the reduced mechanism if this combination is such that:

$$\mathcal{T}_C = \max(\alpha_{E-A} r_{A-C}^*) > \mathcal{T}_S \quad \forall 'E', \quad (3.21)$$

where \mathcal{T}_S is a threshold to be defined.

After removing the elementary reactions in which the species kept are not involved, the number of reactions may be further reduced by computing $r_{C,j}$, as the contribution of the j^{th} reaction to the net chemical rate of ‘C’ normalised by the maximum between consumption or production of ‘C’. The importance of the j^{th} reaction is measured with the parameter \mathcal{T}_j . Reaction j stays in the scheme if:

$$\mathcal{T}_j = \max(\alpha_{E-A} r_{A-C}^* r_{C,j}) > \mathcal{T}_R, \quad (3.22)$$

with \mathcal{T}_R another threshold, controlling the overall prediction capability of the reduced scheme. There is a direct link between these parameters and the number of species and reactions that will appear in the reduced scheme. Obviously, too large values of \mathcal{T}_S and \mathcal{T}_R would lead to a too drastic reduction, and the scheme would not perform well. In practice, they have to be chosen so that the precision of the reduced scheme is acceptable for the set of target chemical species defined prior to the reduction.

3.3.5 Path flux analysis

The path flux analysis is similar to the DRG methodology and was first introduced by Sun *et al.* [89] in 2010 and further studied by Gou *et al.* [90]. The production and consumption rates are seen separately. They are computed for target species A through:

$$P_A = \sum_{j=1}^{N_r} \max(\nu_{Aj} \dot{Q}_j, 0) \quad \text{and} \quad C_A = \sum_{j=1}^{N_r} \max(-\nu_{Aj} \dot{Q}_j, 0), \quad (3.23)$$

where ν_{Aj} is the stoichiometric coefficient of species ‘A’ in the j^{th} reaction similar to the one defined in Section 2.2.1 and where \dot{Q}_j is the rate of reaction j . Then the fluxes of production and consumption of the target ‘A’ via the intermediate species noted ‘B’ are computed from:

$$P_{AB} = \sum_{j=1}^{N_r} \max(\nu_{Aj} \dot{Q}_j \delta_{Bj}, 0) \quad \text{and} \quad C_{AB} = \sum_{j=1}^{N_r} \max(-\nu_{Aj} \dot{Q}_j \delta_{Bj}, 0), \quad (3.24)$$

where δ_{B_j} is the Kronecker symbol defined like for the DRG approach i.e. it equals 1 if species 'B' is involved in reaction j otherwise it equals 0. The ratio of the fluxes of target species 'A' via the interaction with other species 'B' reported to the fluxes of production/consumption of species 'A' is then computed as:

$$r_{AB}^P = \frac{P_{AB}}{\max(P_A, C_A)} \quad \text{and} \quad r_{AB}^C = \frac{C_{AB}}{\max(P_A, C_A)}. \quad (3.25)$$

The reduction is initiated with the target species and identifies whether or not the species 'B' should be retained by measuring the species flux of 'A' via the production or consumption of species 'B'. It is defined from $\max(r_{AB}^P, r_{AB}^C) > \epsilon$ where ϵ is a threshold value. The process is iterated in order to follow the path flux of every selected species. The species present along the tested paths are tagged as necessary and the process is repeated until no more necessary species are found.

3.3.6 Optimisation-based reduction

Genetic algorithm-based methodologies have recently been proposed for the derivation of skeletal mechanisms. The potential solutions are commonly defined from binary vectors of 0s and 1s. In the context of mechanisms reduction, a 0 represents a species (or a reaction) that is removed while a 1 refers to a species (or a reaction) that is kept within the reduced mechanism. For instance, the procedure to reduce a 12 species mechanism in order to get a 6 species scheme may be initiated with the following population composed of four individuals:

Individual 1: 110101001001

Individual 2: 110010110010

Individual 3: 111001010001

Individual 4: 110001110100 .

In the example, the first and second species are forced to 1 hence being always present in the reduced schemes that are evaluated. Each step of the optimisation process starts with the calculation of the error associated to the individuals. A mechanism is first constructed from the list of 1s of a chromosome, and trajectories representative of the evolution of the chemical system are computed with the obtained scheme in order to compare with the reference data. The analysis is repeated for each individual. Then, the best chromosomes are selected to perform crossover and mutation operations, hence providing a new list of individuals (a new generation). A child is constructed by selecting two parents and by keeping the species (or reactions) which are common to both parents. New 1s are also randomly added from unused positions in the chromosome to maintain diversity. The procedure is repeated for several generations up to convergence of the population of solutions.

The earlier work of Edwards *et al.* [91] relied on a reduction performed to find the minimum number of species and reactions for an user-specified error instead of the minimisation of the error for a fixed number of species. The above formulation has been employed by Maurya *et al.* [96] for the reduction of mechanisms in the context of biochemical networks and by Elliott *et al.* [73, 74] for the combustion of aviation fuels using a fixed number of species. An interesting extension was recently proposed by Sikalo *et al.* [92] in which the fitness function also accounts for the speed of solution.

GA are flexible tools in the sense that they allow for reducing chemical schemes for any type of conditions without specific knowledge on the combustion kinetics. However, the primary disadvantage with such optimisation-based methodologies is associated to the number of functional evaluations to perform which increases to a non-negligible extent the computational expense.

3.3.7 Species lumping

Chemical lumping has been largely studied in the literature and an important amount of publications is found on the subject. Whatever the methodology, the key aspects to be considered for species lumping are (1) to classify which chemical species are to be lumped together, (2) to quantify the contribution of a species to the lumped group and (3) to estimate the thermodynamic parameters for the lumped species and for the associated reactions. Depending on the approach, these steps for lumping are either based on chemical [97–99] or algorithmic considerations. For the latter, the selection of the groups for lumping and the definition of the associated reaction rates may be addressed by solving for a linear [100, 101] or a non-linear [80] system that may also rely on the chemical timescales analysis. Interestingly, all of these approaches may be performed in addition to one of the above reduction methods. It is reported that the quality of the results is fairly insensitive to the order into which the lumping methodology and the other reduction approaches are performed. The present section is not intended to provide a detailed description of these techniques for lumping. Such an analysis may be found in a recent review proposed by Turányi and Tomlin [61]. Only the work published by Pepiot *et al.* [102] for the lumping of isomer species is presented here, since a similar approach is employed for large mechanisms reduction in this thesis.

3.3.7.1 An automatic linear lumping procedure for isomers

The model proposed by Pepiot-Desjardins and Pitsch [102] is now introduced:

- **Lumped species concentration:** An initial set of N_{sp} chemical species referred as \mathcal{S} is considered. This set of species is sub-divided into N_{L_s} lumped groups annotated $\mathcal{L}_{\text{L}_s}^{\mathcal{S}}$. A new chemical species representative of the lumped group is defined from a linear combination of the concentrations $[X_k]$ of the species of the group through the formulation:

$$[X_{\text{L}_s}] = \sum_{k \in \mathcal{L}_{\text{L}_s}^{\mathcal{S}}} [X_k]. \quad (3.26)$$

- **Rate of reactions containing lumped species:** The relative contribution of species k to its lumped group is measured from α_k using:

$$\alpha_k = \frac{[X_k]}{[X_{\text{L}_s}]}. \quad (3.27)$$

The formulation:

$$\dot{Q}_j = K_{fj} \prod_{k=1}^{N_{\text{sp}}} [X_k]^{\nu'_{kj}}, \quad (3.28)$$

initially presented in Equation 2.39 is rewritten with the lumped variables using the relative contribution of each chemical species of the group selected for lumping and using the associated lumped concentrations. For simplification, only the forward rate is considered although the same formulation also applies to the backward chemical rates. The corrected formulation now reads:

$$\dot{Q}_j = K_{fj} \prod_{k=1}^{N_{\text{sp}}} (\alpha_k [X_{\text{L}_s}])^{\nu'_{kj}} = K_{fj} \prod_{k=1}^{N_{\text{sp}}} \alpha_k^{\nu'_{kj}} \prod_{\text{L}_s=1}^{N_{\text{L}_s}} [X_{\text{L}_s}]^{\nu'_{\text{L}_s j}}, \quad (3.29)$$

where $\nu'_{\text{L}_s j}$ refers to the stoichiometric coefficient of the lumped species L_s in the reactants of the j^{th} reaction.

- **Rate of lumped reactions:** Most of the reactions that become identical after the lumping procedure on the chemical species may also be lumped together. The set of \mathcal{R} reactions is now subdivided into N_{L_r} groups of reactions to be lumped and are referred as $\mathcal{L}_{L_r}^{\mathcal{R}}$. The new formulation for the reaction rate of the lumped reactions reads:

$$\dot{Q}_{L_r} = \sum_{j \in \mathcal{L}_{L_r}^{\mathcal{R}}} \dot{Q}_j = K_{fL_r} \prod_{L_s=1}^{N_{L_s}} [X_{L_s}]^{\nu'_{L_s L_r}}, \quad (3.30)$$

where K_{fL_r} refers to the reformulated Arrhenius term in relation 3.29:

$$K_{fL_r} = \sum_{j \in \mathcal{L}_{L_r}^{\mathcal{R}}} K_{fj} \prod_{k=1}^{N_{sp}} \alpha_k^{\nu'_{kj}}. \quad (3.31)$$

The transformation that is proposed is exact only if the evolution of the α_k terms are known in terms of space and time for $k \in [1 : N_{sp}]$. Because this is never the case, Pepiot and Pitsch introduce a model based on an Arrhenius formulation to represent the Arrhenius term K_{fL_r} .

$$f^{K_{fL_r}}(T) = \mathcal{A}_{L_r} T^{\beta_{L_r}} \exp\left(\frac{-E_{L_r}}{\mathcal{R}T}\right). \quad (3.32)$$

The constant of the model \mathcal{A}_{L_r} , β_{L_r} and E_{L_r} are adapted to fit with the reference computed with the detailed chemistry using a least-square regression algorithm. Using this definition, the relative contributions α_k of each species k are now expressed as functions of temperature.

In the formulation proposed by Pepiot-Desjardins and Pitsch, only isomer species are selected into lumped chemical groups. First simulations are performed using the detailed chemistry. Statistics are extracted from these computations in terms of isomers relative contribution and temperature, each point being weighted by the DRGEP coefficient of the isomer species. This DRGEP correction ensures that the contributions for unimportant regions of the state space are dumped. The selection of a group defines the list of reactions to be lumped together. The lumping procedure depicted in the above paragraphs is then applied.

There has been many discussions in the literature in regard to the definition of the thermodynamic properties of the lumped species. In the present case, the relative contribution of each isomer is averaged over the full range of temperature and the thermodynamic coefficients are computed as a weighted average of the species thermodynamic properties.

3.4 Reduction based on analytical expressions

Analytical expressions are derived either from the introduction of partial equilibrium (PEA) or quasi-steady state (QSS) approximations. Very few information is found on the use of the partial equilibrium assumption and from author's knowledge, no automatic methodology to implement this approach exists. On the contrary, the quasi-steady state assumption has been extensively studied and its automatic implementation is reported in several widely recognised publications including papers derived from the seminal work of Chen [103] and Lu and Law [104]. It is therefore decided to focus only on a review of the concepts derived for the implementation of the QSS hypothesis.

Several problems arise from the use of the quasi-steady state assumption. For instance, it appears difficult to select all the species that respect the QSS hypothesis and that, at the same time, remain free from the stiffness introduced by the discontinuities or the non-convergence of the obtained non-linear set of analytic expressions. Furthermore, the high costs associated to the iterative methods used for the resolution of the deduced non-linear system have brought people to think about the linearisation of the system and about its simplification accounting for the large number of null elements present within the matrix to be solved. A review of the existing solutions is proposed within this section.

3.4.1 Selection of QSS species

Regarding the QSS assumption, it is possible to sort the chemical species into three categories, a first category of species which definitely respects the QSS characteristics, one category for the species which are definitely not adapted to this assumption and a category in between for which it is hard to say if the species should be added or not to the QSS list. Most of the existing criteria easily handle the two

Definitely in	Definitely out
• Low concentration	• High concentration
• Low life time	• High life time
• The system is insensitive to it	• The system is sensitive to it

Table 3.1: Categories of species in regards to the QSS characteristics

extreme cases, and thus the selection of the definitely in and definitely out species is straightforward. Difficulty arise when it comes to the choice of whether or not a species from the remaining set should be algebraically expressed through the QSS assumption. Indeed, depending on the used criterion, the list of species selected within this intermediate category can be very different.

3.4.1.1 Comparison of creation and destruction rates

Apart from iterative tests, the first approach employed for the selection of QSS species was based on the definition of the error ϵ_k introduced by assuming species k to be in steady state [103]. $\dot{\omega}_k^C$ and $\dot{\omega}_k^D$ are respectively the rates of creation and destruction of species k and X_k represents its mole fraction.

$$\epsilon_k = X_k \frac{|\dot{\omega}_k^C - \dot{\omega}_k^D|}{\max(|\dot{\omega}_k^C|, |\dot{\omega}_k^D|)} \quad (3.33)$$

More recently, a similar criterion has been proposed by Zamboni *et al.* [105]. For each potential chemical species, an analysis of the creation and destruction molar rates is performed to establish whether or not it respects (within a certain limit) the criteria $\dot{\omega}_k^C \simeq \dot{\omega}_k^D$ necessary to satisfy the QSS approximation. An index $\mathcal{I}_{\text{QSS},k}$ is thus defined, where $\delta_{\text{QSS},k}$ is used to avoid numerical problems and represents the smallest threshold value allowable for the estimation of the index.

$$\mathcal{I}_{\text{QSS},k} = \frac{\max(\dot{\omega}_k^D, \delta_{\text{QSS},k})}{\max(\dot{\omega}_k^C, \delta_{\text{QSS},k})} \quad (3.34)$$

This $\delta_{\text{QSS},k}$ is estimated for each chemical species considering the maximum value in time or space on both forwards and backwards coefficients.

$$\delta_{\text{QSS},k} = \epsilon_{\text{cut}} \max(\max(\dot{\omega}_k^C), \max(\dot{\omega}_k^D)) \quad (3.35)$$

	Validity of the QSSA				
	5%	10%	15%	20%	25%
H ₂	-	-	-	-	-
H	-	-	-	-	-
O	-	★	★	★	★
O ₂	-	-	-	-	-
OH	-	★	★	★	★
H ₂ O	-	-	-	-	-
HO ₂	-	★	★	★	★
CH ₂ (S)	★	★	★	★	★
CH ₃	-	-	-	-	★
CH ₄	-	-	-	-	-
CO	-	-	-	-	-
CO ₂	-	-	-	-	-
HCO	★	★	★	★	★
CH ₂ O	-	-	-	★	★
Total QSS species	2	5	5	6	7

Table 3.2: Validity of the QSS assumption for the most important species appearing within a stoichiometric premixed methane-air flame computed at atmospheric conditions with the GRI-1.2 [106, 107]. Using the criterion proposed by Zambon *et al.* [105]

A cutoff parameter ϵ_{cut} is introduced. It is not explicitly written within Zambon's paper but from experience, it seems that $\epsilon_{\text{cut}} = 0.2$ would be an acceptable value. The k^{th} chemical species is assumed to satisfy the quasi-steady state approximation if the criterion 3.36 is respected over all the studied points (in time or space).

$$|\mathcal{I}_{\text{QSS},k} - 1| < \epsilon_{\text{QSS}} \quad (3.36)$$

This criterion has been studied here for a stoichiometric methane-air flame at atmospheric conditions. The validity of the quasi-steady state assumption (ϵ_{QSS}) is shown within table 3.2 using a skeletal mechanism build on a set of 14 chemical species. It is observed that the QSS assumption is valid within a reasonable limit for 7 chemical species i.e. O, OH, HO₂, CH₂(S), CH₃, HCO and CH₂O. To get an insight of what is measured by this criterion, the creation, destruction and net rates of two chemical species is represented within the figure 3.5 with the grey line representing a cutoff value of 0.2. Within these species, O is one species that totally fit the QSS assumption, and CO is one species that should definitely not be set to a QSS. Although it is consistent with the definition of the QSS approximation, this criterion is questionable in its ability to provide the best list of QSS species for a few reasons [108]. First, it does not account for the reduction of the stiffness of the system. Second, some species are strongly linked and should ideally be added or removed together from the list of species assumed in QSS (this is not something considered when simply using a cutoff point). This is explained by the fact that if the concentration of one of these species is calculated through an analytic expression, the small error introduced through the QSS assumption may have a strong impact on the source term of the other species and may hinder the convergence of the entire system.

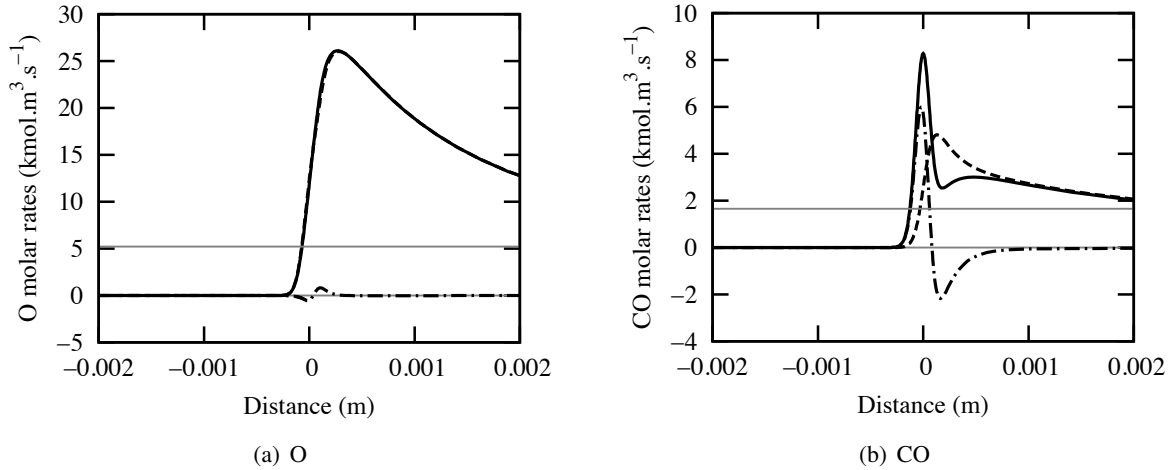


Figure 3.5: Species chemical rates computed with the GRI-1.2 [106, 107]. Net rate (dashed-dotted line), creation rate (solid line), destruction rate (dashed line).

3.4.1.2 Time scale analysis

Approaches based on the calculation of times scales are used to identify the fast and slow chemical species. The goal is here to estimate how fast a given chemical species is consumed after it is produced. Species with a short life time are potential QSS species. On the other hand, species with large life times cannot be set into quasi-steady state since these would lead to large instantaneous errors. This kind of approach has been extensively used over the past and are at the basis of ILDM and CSP reductions. The *life time* of a species is varying in time and space since the species concentrations and the reaction rates vary in time and space. The life time analysis appears to give good results when performed at the maximum concentration of the species [109]. The characteristic times are estimated from the diagonal elements J_{kk} of the Jacobian matrix which can be seen as the ratio of the concentration of the studied species k by the sum of the consuming reactions of this chemical species.

$$\tau_k = -\frac{1}{J_{kk}} = -\frac{1}{\frac{\partial \dot{\omega}_k}{\partial [X_k]}} = \frac{[X_k]}{\sum_{j=1}^{N_r} \nu_{kj} \dot{Q}_j} \quad (3.37)$$

Diffusion has a non-negligible impact on the concentration of the species present within flames. Hence, the chemical time scales estimated for each species should be compared to their respective diffusion timescales. To account for this, Løvas [110] proposed a diffusion weighted species lifetime τ_k^{CW} that is estimated by multiplying the species characteristic time by the ratio of the diffusion coefficient of species k divided by the diffusion coefficient of the inert species N_2 .

$$\tau_k^{CW} = \tau_k \frac{D_k}{D_{N_2}} \quad (3.38)$$

A normalisation of τ_k^{CW} with the characteristic flame time τ_f (computed from the ratio of the flame thickness by the unburned gas velocity i.e. S_L for a perfectly premixed flame) is performed, thus providing a measure that is valid for all flames in the considered range of conditions.

$$\tau_f = \frac{l_f}{S_L} \quad (3.39)$$

$$\vartheta_k = \frac{\tau_k^{CW}}{\sqrt{(\tau_k^{CW})^2 + (\tau_f)^2}} \quad (3.40)$$

This ratio tends to unity when the chemical time scale of the considered species is much larger than the flame time. On the contrary it becomes very low if the chemical time scale is short.

3.4.1.3 LOI - Sensitivity

	Long Life Time	Short Life Time
High sensitivity	High LOI <i>non-appropriate QSS species</i>	Medium LOI <i>hard to classify</i>
Low sensitivity	Medium LOI <i>hard to classify</i>	Low LOI <i>appropriate QSS species</i>

A sensitivity analysis consists of determining the influence of a parameter on another selected one. In the present case, this analysis is performed to quantify the effects induced by a change in a species concentration (the error introduced by the assumption of QSS) on another species concentration or on the temperature of the system. For instance, the effect of a concentration variation of species A on the concentration of a species B is quantified by;

$$S_B^A = \frac{\partial[B]}{\partial[A]} . \quad (3.41)$$

The Level Of Importance approach [110] is a combination of a lifetime analysis with a sensitivity measure. The LOI index for a species k with a sensitivity taken with respect to a quantity Q is;

$$(\text{LOI})_k^Q = \tau_k S_k^Q , \quad (3.42)$$

where τ_k stands for the time scale of species k and S_k^Q for the sensitivity of species k when varying the quantity Q.

3.4.1.4 LTC - Concentration

Whenever a chemical species is added to the QSS list, it is removed from the ODE system. This means that the element mass fraction of all the species with atoms identical to the excluded one will increase so as to compensate for the removed species and thus still fulfil the atom conservation, that reads:

$$\sum_{k=1}^{N_{\text{sp}}} \eta_k^E Y_k = \text{const} , \quad (3.43)$$

where η_k^E stands for the number of E elements contained within species k . In turns, from the introduction of the QSS assumption, the chain of events affects also the temperature through the enthalpy and internal energy conservation. Moreover, a species with a large concentration is a more frequent collisional partner than one with a low concentration. The conclusion is that species with a high mass fraction (i.e. concentration) have a non-negligible effect on the system of ODE and shouldn't therefore be assumed as quasi-steady state species.

A coupling of the Life Time analysis and of the measure of the species concentration is proposed through the LTC approach. This parameter simply corresponds to the product of a species characteristic time with its concentration.

$$(\text{LTC})_k = \tau_k [X_k]. \quad (3.44)$$

	Long Life Time	Short Life Time
High concentration	High LTC <i>non-appropriate QSS species</i>	Medium LTC <i>hard to classify</i>
Low concentration	Medium LTC <i>hard to classify</i>	Low LTC <i>appropriate QSS species</i>

3.4.1.5 Selecting the optimum QSS set using optimisation

As stated earlier, the existing criteria are not perfect and usually fail to properly sort the species when these do not either perfectly match the QSS characteristics or do not match those characteristics at all. To ensure a proper selection, Montgomery [108] proposed a procedure based on a genetic algorithm for the selection of the optimum set of QSS species. Within this approach, the genetic algorithm seeks to minimise the error calculated between the reduced analytic scheme and the reference detailed mechanism based on simple reactor calculations. The algorithm receives as inputs: the parameters of the reduced mechanism to be optimised (number of chemical species, definitely in and definitely out species) and the operating conditions (temperatures, pressures and equivalence ratios). In the present case, a chromosome (a potential solution to the problem) is a given combination of quasi-steady state species.

The optimisation procedure is resumed in four steps. (1) The algorithm is initiated with a random population. Each chromosome is obtained by selecting random species up to the defined number of non-QSS species. Promising QSS combinations can be added to the initial population. (2) Each chromosome is tested through a reactor calculation for each defined conditions and the total error is estimated in comparison to the trajectories of the detailed mechanism that serves as reference.

$$\epsilon = \frac{|\mathcal{O}_{det} - \mathcal{O}_{red}|}{\max\{\delta, \min[\max(\mathcal{O}_{det}, 0), \max(\mathcal{O}_{red}, 0)]\}}, \quad (3.45)$$

where \mathcal{O}_{det} and \mathcal{O}_{red} respectively stands for results from the detailed and the reduced mechanism (either mole fractions, temperature or ignition delay time) and δ refers to a small value defined to avoid achieving large relative errors for very small quantities. (3) A pair of parents (chromosomes) is then selected with respect to a user's defined law in order to produce one child. This new chromosome is created by selecting all the species present within the two parents and then randomly picking species within the remaining pool up to the required number. (4) Step 3 is repeated until a population of chromosome of the same size is obtained.

The procedure employed to create a child is different from the typical crossover approach. A classic approach would indeed define chromosomes which contain as many digits as there are species to be tested. Then it would randomly define a cutoff point defining the part that is exchanged between the parents. The typical approach does not guarantee that the number of QSS species are the same between parents and children. The employed approach enables the algorithm to test many more combinations which is especially beneficial when the procedure is close to convergence.

Note that to improve the performance of the method, the species from the initial mechanism are first sorted into three groups. As explained earlier, some of the species are categorised into a definitely transported group and a group of species which is definitely set into analytic expressions. The remaining set of species is the one that is optimised since it is harder to treat.

3.4.2 Implementing the QSS assumption

Automated approaches have been developed [103, 111] to write subroutines able to solve the algebraic equations obtained through the QSS assumption. These solutions provide the concentration of the non-transported species which are used to either estimate directly the chemical source terms of the transported species or in a more complex way the rates of a created set of global reactions.

3.4.2.1 Output global reaction rates

The following lines review the computer-code implementation of the quasi-steady state assumption which has first been proposed by Chen [103]. All the implementations of the QSS hypotheses that have been proposed later are based on similar operations. The output of the presented implementation are the rates of some created global reactions that are constructed from the initial full set of reactions.

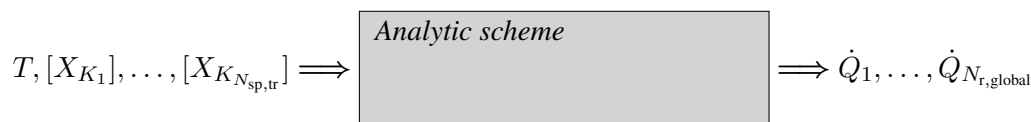


Figure 3.6: Illustration of the analytic file inputs and global reaction rates outputs.

The initial chemistry description links the chemical source terms of the species to the entire set of chemical reactions from the detailed mechanism through the relation $\underline{\dot{\omega}} = \underline{A} \underline{\dot{Q}}$. First, from the list of species selected for the application of the QSS assumption, a decomposition of the species net production rates into transported terms $\underline{\dot{\omega}}_{tr}$ and terms that should be algebraically solved $\underline{\dot{\omega}}_{QSS}$ is performed, leading to the relations:

$$\underline{\dot{\omega}}_{QSS} = \underline{A}_{QSS} \underline{\dot{Q}} \simeq 0, \quad (3.46)$$

$$\underline{\dot{\omega}}_{tr} = \underline{A}_{tr} \underline{\dot{Q}}. \quad (3.47)$$

The underlying principle of the QSS assumption is to filter out the fast reaction steps in order to remove the small time scales from the system to be solved. The fast reactions are selected from the ranking of the associated reaction rates. The selected fast reactions are then grouped together into a contracted vector $\underline{\dot{Q}}_{fast}$ and the remaining steps regrouped into the vector $\underline{\dot{Q}}_{slow}$. The formulations 3.46 and 3.47 are then rewritten, leading to the following relations:

$$\underline{\dot{\omega}}_{QSS} = \underline{A}_{QSS,fast} \underline{\dot{Q}}_{fast} + \underline{A}_{QSS,slow} \underline{\dot{Q}}_{slow} \simeq 0, \quad (3.48)$$

$$\underline{\dot{\omega}}_{tr} = \underline{A}_{tr,fast} \underline{\dot{Q}}_{fast} + \underline{A}_{tr,slow} \underline{\dot{Q}}_{slow}. \quad (3.49)$$

Expressing $\underline{\dot{Q}}_{fast}$ from the relation 3.48 (which formulates the algebraic equations) and substituting it within the equation 3.49 provides an expression which directly links the chemical source terms of the transported species $\underline{\dot{\omega}}_{tr}$ to the rates of the slow reactions. Introducing the term:

$$\underline{B}_{tr,slow} = -\underline{A}_{tr,fast} \underline{A}_{QSS,fast}^{-1} \underline{A}_{QSS,slow} + \underline{A}_{tr,slow}, \quad (3.50)$$

the following relation is therefore obtained,

$$\dot{\omega}_{\text{tr}} = \underline{\underline{B}}_{\text{tr,slow}} \dot{\underline{Q}}_{\text{slow}} \quad (3.51)$$

This last expression is sufficient to compile the chemical source terms of the transported species however it is of interest to compact the reaction rate vector $\dot{\underline{Q}}_{\text{slow}}$ to a global reaction vector $\dot{\underline{Q}}_{\text{global}}$, hence giving;

$$\dot{\omega}_{\text{tr}} = \underline{\underline{B}}_{\text{tr,global}} \dot{\underline{Q}}_{\text{global}} \quad (3.52)$$

This global reaction rate vector is correlated to the rate of the slow reactions through the relation 3.53, where the transfer matrix $\underline{\underline{R}}_{\text{global,slow}}$ is estimated by reducing $\underline{\underline{B}}_{\text{tr,slow}}$ into a row echelon form using a Gauss elimination and by removing the last N_{el} rows which contains only zero elements (since atom conservation introduces new constraints for the system of elementary reactions).

$$\dot{\underline{Q}}_{\text{global}} = \underline{\underline{R}}_{\text{global,slow}} \dot{\underline{Q}}_{\text{slow}} \quad (3.53)$$

Finally the matrix $\underline{\underline{B}}_{\text{tr,global}}$ is estimated by equating both right terms of 3.51 and 3.52 and by using the expression for $\dot{\underline{Q}}_{\text{global}}$ in equation 3.53.

$$\underline{\underline{B}}_{\text{tr,global}} = \underline{\underline{B}}_{\text{tr,global}} \underline{\underline{R}}_{\text{global,slow}}^T \left(\underline{\underline{R}}_{\text{global,slow}} \underline{\underline{R}}_{\text{global,slow}}^T \right)^{-1} \quad (3.54)$$

This leads to a set of $N_{\text{r,global}} = N_{\text{sp}} - N_{\text{sp,QSS}} - N_{\text{el}}$ global reactions whose stoichiometric coefficients are deduced from the transpose of the matrix $\underline{\underline{B}}_{\text{tr,global}}$.

3.4.2.2 Output chemical source terms

As stated within the previous subsection it is not necessary to go through the creation of a reduced set of global reactions. Indeed, in most cases, the output of the system are directly the source terms of the transported chemical species $\dot{\omega}_{\text{tr}}$ estimated from the relation 3.51.

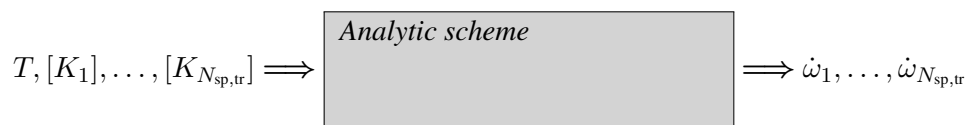


Figure 3.7: Illustration of the analytic file inputs and species source terms outputs.

One should note that a non-linear coupling of the concentrations to be solved through the algebraic relations is often observed (see next section for more details) thus explicit relations cannot be deduced and the solving of the system needs special attention.

3.4.3 Non-linearity of the algebraic system

As stated earlier, the algebraic equations to be solved are usually non-linear in regard to the concentration of the QSS species since there are often reactions which contain more than one QSS reactant. This results in a non-linearity of the associated rate \dot{Q}_{fj} (and \dot{Q}_{rj} for two QSS products).

3.4.3.1 Iterative procedure to solve a non-linear set of equations

The initial approach employed by Chen [103] relied on a non-linear procedure to solve for the coupled non-linear set of algebraic equations. Functional or Newton-based iteration schemes were used. The iteration procedure stopped when all the species were satisfying the following convergence criteria:

$$\max_k \left(\frac{|[X_k]^{n+1} - [X_k]^n|}{\max([X_k]^{n+1}, [X_k]^n)} \right) \leq \epsilon \quad (3.55)$$

where $[X_k]$ refers to the concentration of the k^{th} species, and the superscripts n and $n + 1$ respectively stands for the solution at previous and present iteration. The default setting for ϵ was 10^{-5} .

3.4.3.2 Truncation of the non-linear direct or reverse part of the reactions

A truncation procedure has been developed by Peters and Rogg [112] and employed by Zambon and Chelliah [105]. A similar approach proposed by Lu and Law is [111] shown here. The concentrations of the QSS species are in general small such that the collision frequency of two QSS species is small. As a consequence the reactions with more than one QSS reactants (mostly two) may be unnecessary in most cases. Moreover QSS species are known to be negligible in the third body concentration and in the other correction terms of the Arrhenius expressions. The normalised contribution of the non-linear terms to the destruction of species k and to its creation is computed to assess the importance of these non-linear terms using:

$$\alpha_k = \frac{\sum_{j=1}^{N_r} \nu'_{kj} \dot{Q}_j \delta_j}{\dot{\omega}_k^D} \quad \beta_k = \frac{\sum_{j=1}^{N_r} \nu''_{kj} \dot{Q}_j \delta_j}{\dot{\omega}_k^C} \quad (3.56)$$

$$\text{where } \delta_j = \begin{cases} 1 & \text{if reaction } j \text{ has more than one QSS reactants} \\ 0 & \text{otherwise} \end{cases} \quad (3.57)$$

The same should be applied to the products when dealing with reverse reactions. The non-linear terms are removed from the QSS relations if $\alpha_{\max} < \epsilon$ and $\beta_{\max} < \epsilon$ with

$$\alpha_{\max} = \max_{k=1,N}(\alpha_k) \quad \beta_{\max} = \max_{k=1,N}(\beta_k) \quad (3.58)$$

where ϵ is a threshold value defined by the user. If this condition is satisfied for all the reaction states, the non-linear terms can all be removed from the QSS expressions. then the system is approximated by a set of linear equations. The obtained linear set of equations can be resolved with Gaussian elimination. Note that the time complexity to solve for this matrix is a cubic function of the number of QSS species. The computation is facilitated by deriving an analytical solution based on the sparse coefficient matrix.

3.4.3.3 Lower the number of QSS species to linearise the system

To avoid non-linear coupling of the system of equations, Pepiot [113] simply removes the species which do not allow a proper fulfilment of this criterion. This is adapted to her method, since after the DRGEP reduction she removes all the unnecessary reactions (see chapter 3.3.4). This includes the ones that contains two QSS species as reactants that have a low probability of collision i.e. the ones detected by using the criteria proposed by Lu and Law described within the previous subsection. This would not properly work with the entire initial set of reactions since the number of species that can be put into QSS would be considerably limited.

3.4.4 QSS matrix simplification

Once linearity is ensured, it is of interest to minimise the number of steps necessary to inverse the system to be solved. The matrix associated to the system of equations obtained for the calculation of the QSS species is said to be sparse since a majority of its elements are zeros. To minimise the number of operations, the matrix is re-ordered by swapping columns and rows so as to get as close as possible to a lower or upper triangular matrix. This re-ordering of the matrix corresponds to a different ordering of the species concentration vector.

3.4.4.1 Optimisation procedure to diagonalise sparse matrices

An optimisation approach based on a simulated annealing algorithm has been proposed by Arvidsson *et al.* [109] to lower the number of operations associated to the resolution of a sparse matrix. First, the place of two randomly selected species is changed within the concentration vector to be solved. This is illustrated on Figure 3.8. The number of operations necessary to solve the obtained matrix is calculated

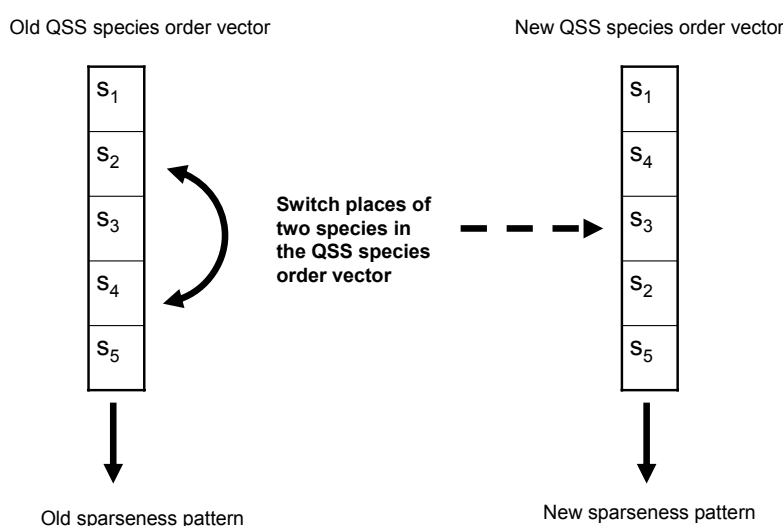


Figure 3.8: Illustration of the procedure to test new sparseness patterns. Two species in the QSS list are switched giving a new pattern. Extracted from Arvidsson [109].

for both elimination and back substitution. The difference in the number of operations between the old concentration vector and the new one is computed (Δ_O). If this difference is less than zero, the new vector is accepted. If not, a Metropolis algorithm¹ is used to accept or decline the new QSS vector relying on the computation of the following probability function.

$$P(\Delta_O, \mathcal{P}_T) = \exp\left(-\frac{\Delta_O}{\mathcal{P}_T}\right) \quad (3.59)$$

The value for \mathcal{P}_T is decreased before the next iteration which is an essential feature of the simulated annealing methods. Through this, the algorithm is expected to first cover a wide array of the function landscape and ignore small features present within the research area. While the parameter \mathcal{P}_T decreases, the algorithm should drift towards deep minima and in the end, simply move downhill when \mathcal{P}_T reaches zero.

¹A Metropolis algorithm is a methodology proposed to randomly select an element from a normal distribution.

3.4.4.2 Identification of inter-dependent chemical species

An algorithm to re-order linear systems of equations has been derived by Lu and Law [111]. The proposed methodology relies on a directed graph to divide the QSS list of species in several subgroups. The

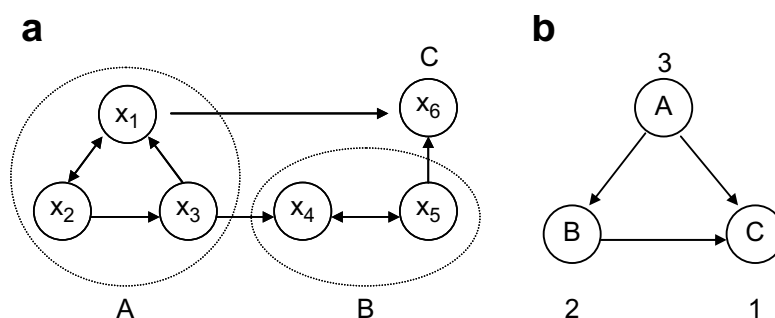


Figure 3.9: Scheme of the QSS graph (QSSG) approach illustrating: (a) the presence of strongly connected components (SCC) and (b) the relation graph derived from (a). The numeration given in (b) indicates the order of the sequence to solve for the problem. Extracted from Lu and Law [104]

species inside a subgroup are strongly connected components (SCC) i.e. cyclically or implicitly related. On the contrary the subgroups are weakly connected to each other and may be explicitly solved. The list of QSS species can then be reordered so that the system is solved explicitly group after group. The concept for the creation of the subgroups is illustrated on Figure 3.9. In this example, six chemical species are to be solved using the QSS assumption. These species are coupled cyclically into three subgroups referred as $g_A = (x_1, x_2, x_3)$, $g_B = (x_4, x_5)$ and $g_C = (x_6)$. The species inside each subgroup require the information about the other species of the group, thus there is no specific order to solve for them. On the other hand, some of the subgroups do not require any information about the other subgroups which may therefore be solved in an explicit manner. In the present case the groups are to be solved in the sequence g_C, g_B, g_A . Finally, within the implicitly coupled subgroups, a spectral method is employed to solve the species by variable elimination through substitution. The approach first eliminates the species which are weakly related, so that the matrix remain as sparse as possible.

The approach proposed by Lu has been extensively validated. A simplification of the sparse matrix using a similar methodology is illustrated on Figure 3.10 for a problem solved by Pepiot [113] and composed of 6 QSS relations. After optimising the order in which the species are solved, the matrix

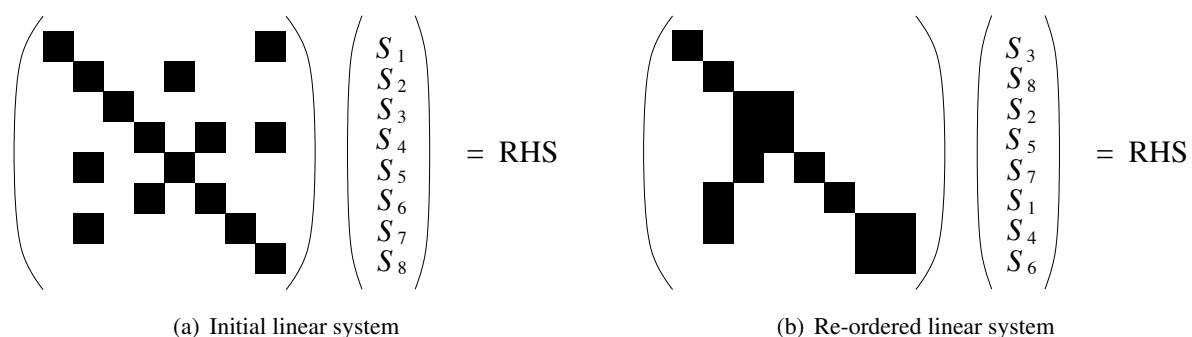


Figure 3.10: Illustration of the linear system of equations to be solved so as to get the QSS species concentrations. Black squares represent non-zero entries. Extracted from Pepiot [113].

becomes block triangular, hence it requires less operations to be inverted.

3.5 Application: Methane-air combustion modelling

It is now decided to illustrate the most employed methodologies by presenting the development found on the oxidation of methane since the first works on the kinetics of methane back in the seventies up to recent publications. The idea is to give the basic information about the type of mechanisms developed up to now and about the associated performances.

3.5.1 The history of methane chemistry modelling for flame simulation

During the seventies, pioneer works paved the way for simulating numerically the physical properties of turbulent flames under the hypothesis of fast or very fast chemistry [115–125]. At that time, aside from a few attempts [126–129], the introduction of finite chemical rates into the modelling of turbulent flames

#	Reaction	Oxidising pathway
1	$\text{CH}_4 + \text{OH} \rightleftharpoons \text{CH}_3 + \text{H}_2\text{O}$	
2	$\text{CH}_4 + \text{H} \rightleftharpoons \text{CH}_3 + \text{H}_2$	$\text{CH}_4 \rightarrow \text{CH}_3$
3	$\text{CH}_4 + \text{O} \rightleftharpoons \text{CH}_3 + \text{OH}$	
4	$\text{CH}_3 + \text{O} \rightleftharpoons \text{CH}_2\text{O} + \text{H}$	
5	$\text{CH}_3 + \text{O} \rightleftharpoons \text{CH}_2\text{O} + \text{H}$	$\text{CH}_3 \rightarrow \text{CH}_2\text{O}$
6	$\text{CH}_3 + \text{O}_2 \rightleftharpoons \text{CH}_2\text{O} + \text{OH}$	
7	$\text{CH}_3 + \text{O}_2 \rightleftharpoons \text{CH}_2\text{O} + \text{OH}$	
8	$\text{CH}_2\text{O} + \text{M} \rightleftharpoons \text{CO} + \text{H}_2 + \text{M}$	
9	$\text{CH}_2\text{O} + \text{OH} \rightleftharpoons \text{HCO} + \text{H}_2\text{O}$	$\text{CH}_2\text{O} \begin{cases} \nearrow \text{CO} \\ \searrow \text{HCO} \rightarrow \text{CO} \end{cases}$
10	$\text{CH}_2\text{O} + \text{O} \rightleftharpoons \text{HCO} + \text{OH}$	
11	$\text{CH}_2\text{O} + \text{H} \rightleftharpoons \text{HCO} + \text{H}_2$	
12	$\text{HCO} + \text{O}_2 \rightleftharpoons \text{CO} + \text{HO}_2$	
13	$\text{HCO} + \text{OH} \rightleftharpoons \text{CO} + \text{H}_2\text{O}$	
14	$\text{HCO} + \text{O} \rightleftharpoons \text{CO} + \text{OH}$	
15	$\text{HCO} + \text{M} \rightleftharpoons \text{CO} + \text{H} + \text{M}$	
16	$\text{CO} + \text{OH} \rightleftharpoons \text{CO}_2 + \text{H}$	$\text{CO} \rightarrow \text{CO}_2$
17	$\text{CO} + \text{O} + \text{M} \rightleftharpoons \text{CO}_2 + \text{M}$	
18	$\text{HO}_2 + \text{O} \rightleftharpoons \text{O}_2 + \text{OH}$	Hydrogen oxidation
19	$\text{HO}_2 + \text{OH} \rightleftharpoons \text{O}_2 + \text{H}_2\text{O}$	
20	$\text{HO}_2 + \text{H} \rightleftharpoons 2 \text{OH}$	
21	$\text{HO}_2 + \text{H} \rightleftharpoons \text{O}_2 + \text{H}_2$	
22	$\text{H} + \text{O}_2 + \text{M} \rightleftharpoons \text{HO}_2 + \text{M}$	
23	$\text{H} + \text{O}_2 \rightleftharpoons \text{OH} + \text{O}$	
24	$\text{O} + \text{H}_2 \rightleftharpoons \text{OH} + \text{H}$	
25	$\text{OH} + \text{H} \rightleftharpoons \text{H}_2\text{O} + \text{H}$	
26	$2 \text{OH} \rightleftharpoons \text{H}_2\text{O} + \text{O}$	
27	$\text{H} + \text{OH} + \text{M} \rightleftharpoons \text{H}_2\text{O} + \text{M}$	
28	$\text{O} + \text{H} + \text{M} \rightleftharpoons \text{OH} + \text{M}$	
29	$2 \text{H} + \text{M} \rightleftharpoons \text{H}_2 + \text{M}$	
30	$2 \text{O} + \text{M} \rightleftharpoons \text{O}_2 + \text{M}$	

Table 3.3: The first detailed chemistry for atmospheric methane-air combustion in a premixed regime. Proposed by Smoot *et al.* [114] in 1976.

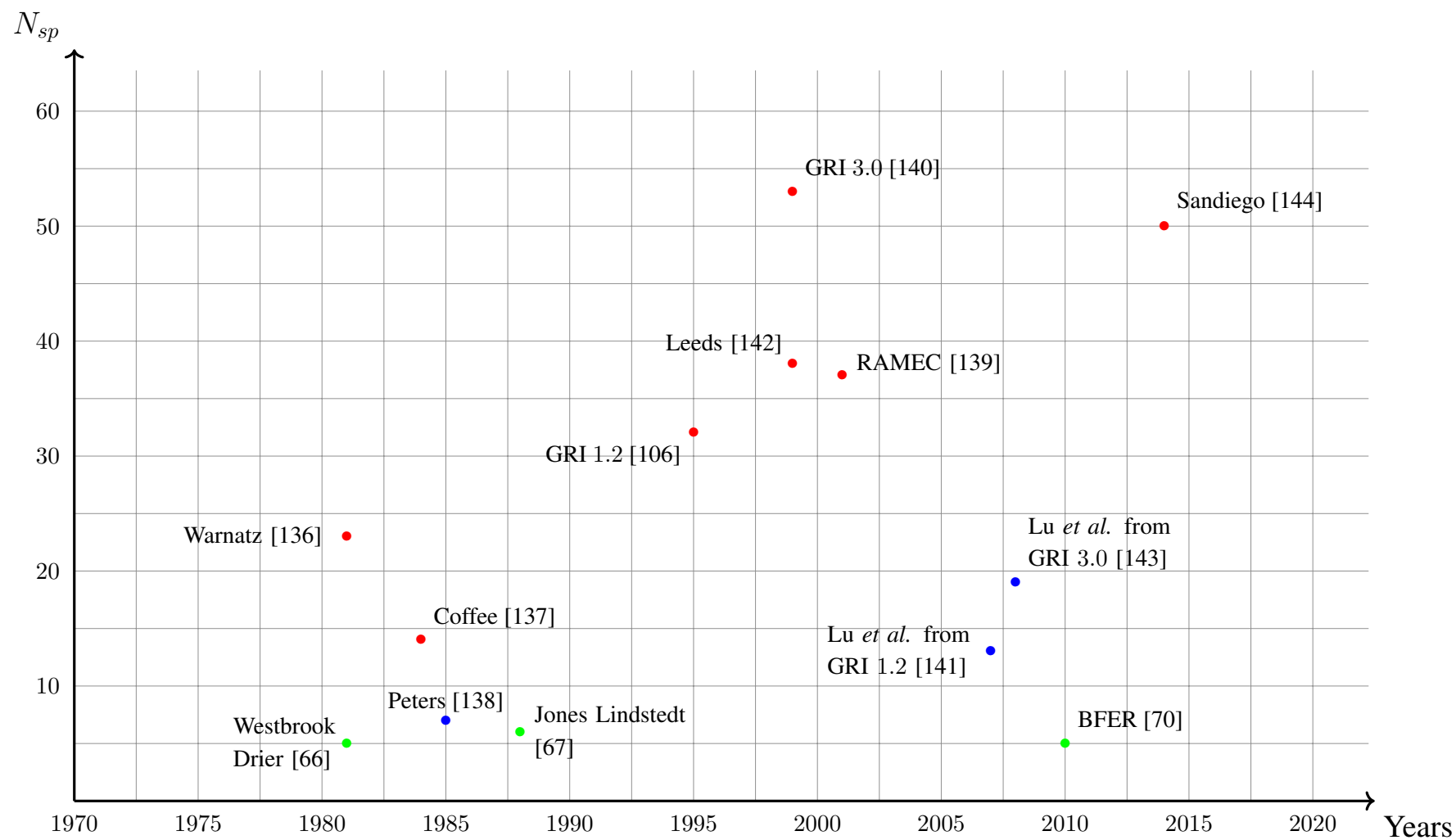


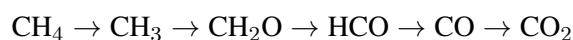
Figure 3.11: Evolution of the size of methane combustion mechanisms over the past five decades. (●): Detailed mechanisms. (●): Analytically reduced mechanisms. (●): Global mechanisms.

was carefully avoided. Indeed, chemical schemes were not that reliable and introducing the asymptotic limit of infinitely fast chemistry appeared as a safer choice. The gap between turbulent flame simulations and finite rate chemistry was, however, soon closed thanks to further works providing predictive chemical models to progress in the simulation of turbulent flames [130, 131], along with strategies to model the reaction zones in the case of unresolved fluctuations of species and temperature [132–135].

In the light of this situation, the oxidation of methane turned out to be a canonical problem in which the great majority of the combustion research groups positioned their efforts. Accordingly, the number of methane combustion schemes available today in the literature exceeds by far the number of mechanisms found for any other molecule which still makes it, one of the most relevant species to study, theoretically. Figure 3.11 provides an overall idea about the evolution from 1970 up to now of the size of the methane combustion mechanisms; reported here as the number of chemical species involved. This figure is discussed in the next sections considering respectively detailed and reduced chemistries.

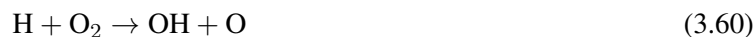
3.5.1.1 Detailed kinetics

The earliest detailed kinetics governing premixed laminar, one dimensional methane-air flames were introduced by Smoot *et al.* [114] in 1976 and by Tsatsaronis [145] in 1978. Both mechanisms were composed of 13 species interacting together over respectively 30 and 29 chemical reactions. The mechanism by Smoot *et al.* is given in Table 3.3 along with the associated oxidation pathways. Overall the mechanism is developed so that methane is oxidised along the standard pathway:



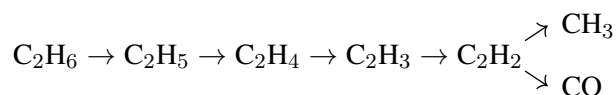
It is constructed from a well known set of hydrogenated steps to which carbonated reactions are added from an extended literature survey of possible pathways. For each reaction, the rate constants were adapted on the basis of comparisons between the predicted trajectories and the available experimental data for the flame velocity, the temperature and species profiles.

From this early work, it is already known that the concentrations of the radical species O, H and OH were primary factors in the reproduction of the flame characteristics associated to the combustion of hydrocarbons. Increasing their concentrations eventually lead to an increase of the flame speed. It is also reported that hydrocarbons flames behave similarly in terms of flame speed, in terms of normalised profiles and also in terms of reactants and main products essentially because of the predominant influence of the two chemical paths:



which are non specific reactions for the hydrocarbon considered.

A few years later, Warnatz proposed a mechanism with 23 species and 50 reactions [136] introducing the C₂ species which he claimed were important for the modelling of flames in rich and near stoichiometric conditions. Dixon-Lewis and Islam [146] also agreed with Warnatz on the introduction of C₂ chemistry and proposed another mechanism including 18 species. Both schemes were relying on the following oxidation pathway for the C₂ chemistry:



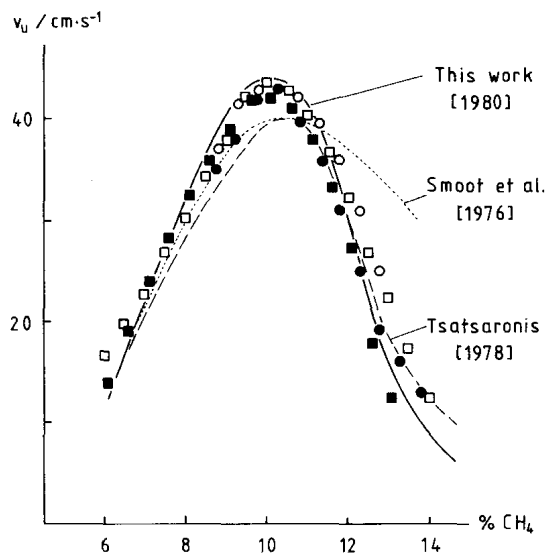


Figure 3.12: Flame velocities in CH_4 -air mixtures at atmospheric conditions. Points: measurements by Lindow [147], Reed *et al.* [148], Andrews and Bradley [149] and Günther and Janish [150]. Solid line: Warnatz [136]. Broken lines: calculations by Smoot *et al.* [114] and by Tsatsaronis [145].

Figure 3.12 gives a comparison of the flame speed as a function of the equivalence ratio obtained for the three chemical mechanisms of Smoot *et al.* [114], Tsatsaronis [145] and Warnatz [136]. The importance of the introduction of the C_2 chemistry for the reproduction of the flame speed in the rich region is here, readily understandable. The mechanism proposed by Warnatz has been largely employed in the following years. In 1984, Coffee [137] proposed two new models relying on the same assumptions and based respectively on 14 chemical species and 38 reactions; and on 20 species with 63 reactions including the C_2 chemistry. Both of the chemistries proposed by Coffee also served as reference for the next years.

By that time, the main reaction paths for the detailed chemical modelling of methane combustion were introduced. The next step became related to the improvement of the existing mechanisms. Since then, a tremendous amount of larger combustion schemes have been proposed relying on more and more intermediate species and reactions which are added to the set of chemical species introduced in the above discussion. Indeed, the primary target of combustion kinetic specialists aimed and still aims at enlarging the range of conditions to which the schemes apply including a wider variety of temperatures, pressures and equivalence ratios but also expanding the capabilities of the mechanisms to the prediction of other flames properties, as for instance, the auto-ignition delays.

It is beyond the scope of this thesis to provide an exhaustive list of publications for the detailed modelling of methane combustion. Yet, the detailed mechanisms that are used in the manuscript for the description of methane-air combustion are: the UC San Diego mechanism [144] released in 2014, the GRI-1.2 mechanism [106, 107] as well as the GRI-3.0 chemical scheme [140] which are two extensively used versions of the mechanisms funded by the Gas Research Institute, the RAMEC mechanism [139] which is an extension of the GRI-1.2 mechanism designed for high pressures and finally the Lindstedt mechanism [151].

3.5.1.2 Reduced kinetics

As for detailed chemistry, it would be too long to provide an exhaustive list of the reduced chemical schemes designed for the combustion of methane with air. Therefore, only, the major release for methane-air combustion are now given.

#	Reaction	\mathcal{A}^*	β	E^*	n_1	n_2
1	$\text{CH}_4 + 1.5\text{O}_2 \rightarrow \text{CO} + 2\text{H}_2\text{O}$	5.000e11	0.00	47800	0.70	0.80
2	$\text{CO} + 0.5\text{O}_2 \rightleftharpoons \text{CO}_2$	2.240e12	0.00	40700	-	-

Table 3.4: Arrhenius coefficients for the two steps chemical scheme [66] proposed by Westbrook and Dryer in 1981. *Units are mol, s, cm³, cal and K.

Westbrook and Dryer two steps global scheme The first global scheme for the oxidation of methane ready for CFD was proposed by Westbrook and Dryer [66] in 1981 and relying on 5 chemical species and 2 global steps constructed from the slow CO oxidation limit of premixed combustion. The reaction parameters of the mechanism were especially chosen to fit with the flame speed measurements. These coefficients are given in Table 3.4 along with the reactions they are associated to.

Jones and Lindstedt four steps global scheme In 1988, Jones and Lindstedt published a different global scheme for methane-air premixed and diffusion flames at atmospheric conditions (300 K, 1 atm). The chemical scheme is constructed this time with 4 chemical steps [67] and introduces a relevant intermediate species for hydrocarbon combustion, namely H₂. The mechanism relies on the assumption that the flame structure comprises two reaction zones. The first one operates the oxidation of methane CH₄ to produce CO and H₂ and the second reaction zone enables the production of the final products CO₂ and H₂O. The oxidation of species CH₄ is achieved through reaction 1 for premixed flame and through the reaction 2 for flames piloted by diffusion. The present scheme demonstrates that global reactions involving only the major species can provide quite a reasonable prediction as the species and temperature equilibrium values are well reproduced.

#	Reaction	\mathcal{A}^*	β	E^*	n_1	n_2
1	$\text{CH}_4 + 0.5\text{O}_2 \rightarrow \text{CO} + 2\text{H}_2$	4.400e14	0.00	30000	0.5	1.25
2	$\text{CH}_4 + \text{H}_2\text{O} \rightarrow \text{CO} + 3\text{H}_2$	3.000e11	0.00	30000	-	-
3	$\text{H}_2 + 0.5\text{O}_2 \rightleftharpoons \text{H}_2\text{O}$	6.800e18	-1.00	40000	0.25	1.5
4	$\text{CO} + \text{H}_2\text{O} \rightleftharpoons \text{CO}_2 + \text{H}_2$	2.750e12	0.00	20000	-	-

Table 3.5: Arrhenius coefficients for the four steps chemical scheme proposed by Jones-Lindstedt [67]. *Units are mol, s, cm³, cal and K.

Peters analytic scheme Another major release in the field of reduced chemistry came from Peters which introduced the coupling between a reduced number of elementary steps and an analytical part in which a large number of intermediate species are expressed from those transported with the flow via quasi-steady state and equilibrium hypotheses [130]. The approach he depicted forms the basis of a

number of methodologies employed today in chemistry reduction including the one proposed in this thesis. The main lines of the paper he published in 1985 are therefore given in the present section.

- **Selection of key reactions** A complete picture of the methane oxidation requires the introduction of approximately a hundred elementary reactions including the C₂ branching. However, a "short mechanism" relying on about a dozen of elementary reactions and using only the C₁ hydrocarbon species may be sufficient to capture the basic information about lean methane-air flames including the flame extinction, the flame speed, the maximum of temperature and the major species profiles. To build such a reduced scheme, Peters first examined numerical solutions of a stoichiometric methane-air flame, hence deducing the major reacting steps for methane oxidation. The results of the analysis are depicted within the following lines;

1. The CH₄ breakup into CH₃ occurs primarily from the elementary steps:



The reaction $\text{CH}_4 + \text{O} \rightarrow \text{CH}_3 + \text{OH}$ appears negligible in comparison to those with H and OH radicals. Moreover, fuel dissociation $\text{CH}_4 + \text{M} \rightarrow \text{CH}_3 + \text{H} + \text{M}$ is rather insignificant in premixed flames.

2. Reaction R₃ continues the C₁-chain with the formation of formaldehyd CH₂O;



The reactions of recombination $\text{CH}_3 + \text{CH}_3 \rightarrow \text{products}$ are the one associated to the production of C₂-species which are important in the rich region. Because the present reduction aims at solving for lean and stoichiometric conditions this path is not retained.

3. Formaldehyd then reacts with radical species H and OH to form HCO from the reactions:



Again, the reaction with the radical species O is comparatively negligible.

4. The HCO is then converted into CO from the relations:



The reaction of dissociation R₇ prevails at high temperature.

5. The predominant reaction for the oxidation of the carbon monoxide CO is;



with a non negligible reverse reaction rate. Reactions of CO with radical O and species O₂ are neglected. The reaction R₉ is known to be one of the key steps describing premixed combustion. The slow rate to which it is associated indeed determines the slow oxidation of the product CO₂ through which the majority of the flame energy is released.

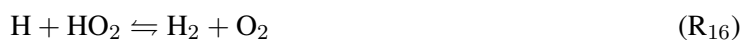
6. The oxygen consumption is attached to the reaction R₁₀. This step is essential as a chain branching since it provides more radical species than it consumes. The remaining three other steps are also important reactions for radicals production.



7. The last steps are for the recombination which leads to the production of water either directly from the radicals H and OH or through the intermediate HO₂.



The hydroperoxyl HO₂ produced from the reaction R₁₄ is then consumed through the chemical paths given by:



This set of 18 reactions is complete in the sense that the oxidation of CH₄ leads to the creation of the stable products CO₂ and H₂O. Interestingly, the important reactions deduced here from a larger mechanism compare very well with the ones first introduced by Smoot *et al.* [114] and by Tsatsaronis *et al.* [145] from experimental considerations. Within these 18 steps, Peters tried to remove the maximum number of fast reactions using the steady state assumption. The slow ones were preserved because they are rate-determining.

- **The Steady State Assumption** As explained earlier, this assumption applies when the reactions that form an intermediate species are slower than the reactions by which the species is consumed. In that case the concentration of the intermediate is small and the associated source term is low in comparison to the reaction rates. From an analysis of the species mole fractions, Peters selected species OH, O, HO₂, CH₃, CH₂O and HCO to be good candidates for the steady state assumption. He then formally expressed the source terms of the transported species from a recombination of reaction rates.

$$\dot{\omega}_{\text{H}} = -2\dot{Q}_1 - 2\dot{Q}_2 - 2\dot{Q}_6 - 2\dot{Q}_8 + 2\dot{Q}_{10} - 2\dot{Q}_{14} + 2\dot{Q}_{16} - 2\dot{Q}_{15}, \quad (3.62)$$

$$\dot{\omega}_{\text{H}_2} = 4\dot{Q}_1 + 4\dot{Q}_2 + \dot{Q}_6 + \dot{Q}_8 + \dot{Q}_9 - 3\dot{Q}_{10} + \dot{Q}_{14} - 3\dot{Q}_{16} + \dot{Q}_{15}, \quad (3.63)$$

$$\dot{\omega}_{\text{O}_2} = -\dot{Q}_{10} - \dot{Q}_{16}, \quad (3.64)$$

$$\dot{\omega}_{\text{H}_2\text{O}} = -\dot{Q}_1 - \dot{Q}_2 - \dot{Q}_9 + 2\dot{Q}_{10} + 2\dot{Q}_{16}, \quad (3.65)$$

$$\dot{\omega}_{\text{CO}} = \dot{Q}_1 + \dot{Q}_2 - \dot{Q}_9, \quad (3.66)$$

$$\dot{\omega}_{\text{CO}_2} = \dot{Q}_9, \quad (3.67)$$

$$\dot{\omega}_{\text{CH}_4} = -\dot{Q}_1 - \dot{Q}_2. \quad (3.68)$$

A further analysis led to a set of 4 global steps computed from the rate of nine elementary reactions. The other reaction rates being transformed into analytical expressions thanks to the steady state formulation. These analytical formulations are required for the computation of the concentrations of species OH, O, HCO and HO₂ that are present in most of the reactions R₁-R₁₆. From the steady state assumption for species CH₃ and CH₂O, the relation $\dot{\omega}_{\text{CH}_3} = \dot{\omega}_{\text{CH}_2\text{O}} = 0$ gives:

$$k_1[\text{CH}_4][\text{H}] + k_2[\text{CH}_4][\text{OH}] = k_6[\text{HCO}][\text{H}] + k_7[\text{HCO}][\text{M}] + k_8[\text{HCO}][\text{O}_2], \quad (3.69)$$

$$k_8[\text{HCO}][\text{O}_2] + k_{14}[\text{H}][\text{O}_2] = (k_{16} + k_{17})[\text{HO}_2][\text{H}] + k_{18}[\text{HO}_2][\text{OH}]. \quad (3.70)$$

The global steps are given in Table 3.6 along with the associated rates. After the analytical reduction, the chemistry may be solved by transporting only 8 chemical species (including the non reacting species N₂).

#	Reaction	Rate
I	$\text{CH}_4 + 2\text{H} + \text{H}_2\text{O} \rightarrow \text{CO} + 4\text{H}_2$	$\dot{Q}_I = \dot{Q}_1 + \dot{Q}_2$
II	$\text{CO} + \text{H}_2\text{O} \rightleftharpoons \text{CO}_2 + \text{H}_2$	$\dot{Q}_{II} = \dot{Q}_9$
III	$2\text{H} + \text{M} \rightleftharpoons \text{H}_2 + \text{M}$	$\dot{Q}_{III} = \dot{Q}_6 + \dot{Q}_8 + \dot{Q}_{14} + \dot{Q}_{15}$
IV	$\text{O}_2 + 3\text{H}_2 \rightleftharpoons 2\text{H} + 2\text{H}_2\text{O}$	$\dot{Q}_{IV} = \dot{Q}_{10} + \dot{Q}_{16}$

Table 3.6: Peters reduced scheme [130].

- **Equilibrium Assumption** The rates expressions in which species OH and O are involved appear to be related to other steady state species. This render the system of algebraic equations non-linear hence complicating the procedure for its solving. To address this issue, Peters observed that in the burned gases region of the flame, the forward and backward rates of reaction R₁₁ to R₁₃ are at equilibrium despite their large values. Assuming partial equilibrium, he then expressed the concentrations of species OH and O from the linear algebraic relations:

$$[\text{OH}] = [\text{H}] \frac{[\text{H}_2\text{O}]}{[\text{H}_2]K_{C12}}, \quad [\text{O}] = \frac{[\text{H}][\text{OH}]}{[\text{H}_2]K_{C11}} = \frac{[\text{H}]^2[\text{H}_2\text{O}]}{[\text{H}_2]^2K_{C11}K_{C12}}. \quad (3.71)$$

where K_{C11} and K_{C12} are expressed from Arrhenius relations. Introducing the concentrations of species OH and O computed from 3.71 into the relations 3.69 and 3.70 allows for solving the entire problem, hence deducing the source terms of the transported species.

BFER two steps with functions of corrections The global mechanism developed by Franzelli *et al.* [70] and published in 2012 is now introduced. The chemical steps employed for its computation are the same as the one proposed by Westbrook and Dryer (see Table 3.4). Methane is first oxidised in a thin layer within which CO and H₂O are produced. Then, a slow oxidation of CO into CO₂ is achieved within a thicker flame layer. The equations for the computation of both reaction rates are given below:

$$K_{f1} = \mathcal{A}_1 f_1(\phi) \exp\left(-\frac{E_1}{\mathcal{R}T}\right) [\text{CH}_4]^{0.5} [\text{O}_2]^{0.65} \quad (3.72)$$

$$K_{f2} = \mathcal{A}_2 f_2(\phi) T^{0.7} \exp\left(-\frac{E_2}{\mathcal{R}T}\right) [\text{CO}][\text{O}_2]^{0.5} \quad (3.73)$$

$$K_{b2} = \frac{\mathcal{A}_2}{K_{eq,2}} f_2(\phi) T^{0.7} \exp\left(-\frac{E_2}{\mathcal{R}T}\right) [\text{CO}_2] \quad (3.74)$$

where $K_{eq,2}$ refers to the equilibrium constant of the second reaction. A Pre-Exponential Adjustment (PEA) approach is proposed to properly recover the flame speed in the rich flame region. This adjustment is performed through the definition of two correction functions $f_1(\phi)$ and $f_2(\phi)$ which depend on the local equivalence ratio.

3.5.2 Assessment of global and analytical reduced methane-air mechanisms

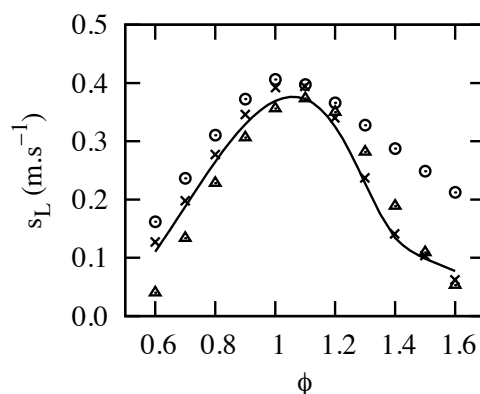


Figure 3.13: Flame speed distribution versus equivalence ratio. Line: detailed chemistry GRI-3.0 [140]. (x): Two-step global mechanism Franzelli *et al.* [70]. (o): Four-step global mechanism Jones and Lindstedt [67]. (▲): Four-step mechanism Peters [138].

Three simplified kinetics of the turbulent combustion literature are first considered for methane-air combustion: the two-step mechanism by Franzelli *et al.* [70], the four-step mechanism by Jones and Lindstedt [67] and the four-step analytical mechanism proposed by Peters [138]. The objective of this section is to illustrate the typical level of accuracy reached with such reduced schemes, which have been widely used in the simulation of turbulent flames.

Five species, CH₄, O₂, CO, H₂O and CO₂ are involved in the two-step mechanism [70]; H₂ is added in the first four-step kinetics, leading to six transported species [67]; one more species H is transported with the flow in the second four-step mechanism, whereas OH, O, HO₂, CH₃, CH₂O and HCO are additional species, which are obtained from quasi-steady state and equilibrium algebraic relationships (analytical part) [138]. Freely propagating methane-air premixed flames are computed at various equivalence ratios with the Cantera [152] chemistry solver. The detailed GRI-3.0 mechanism serves as reference, since it has been optimised under such conditions [140], with 53 species and 325 elementary reactions. In all the simulations of premixed flames, molecular differential diffusion between species and between mass and heat, is included following the Curtiss and Hirschfelder approach [153, 154].

The flame speed response versus equivalence ratio is particularly well-captured with the two-step mechanism (Fig. 3.13). This scheme contains in its rates a correction that is function of the equivalence ratio, to properly follow the flame speed variations and therefore the overall burning rate through the flame. The Jones and Lindstedt four-step mechanism lacks of prediction capabilities for equivalence ratios above unity, while the Peters four-step mechanism reproduces the flame speed over the full range of equivalence ratios. These observations may be put in perspective with the temperature profiles shown in Fig. 3.14 for the stoichiometric condition. Far in the burnt gases, all schemes return the correct equilibrium temperature (not shown in the graphs), however, only the Peters' scheme, which accounts for the H₂/O₂ radicals pool, perfectly matches the specific shape of the profile, with a slowly growing

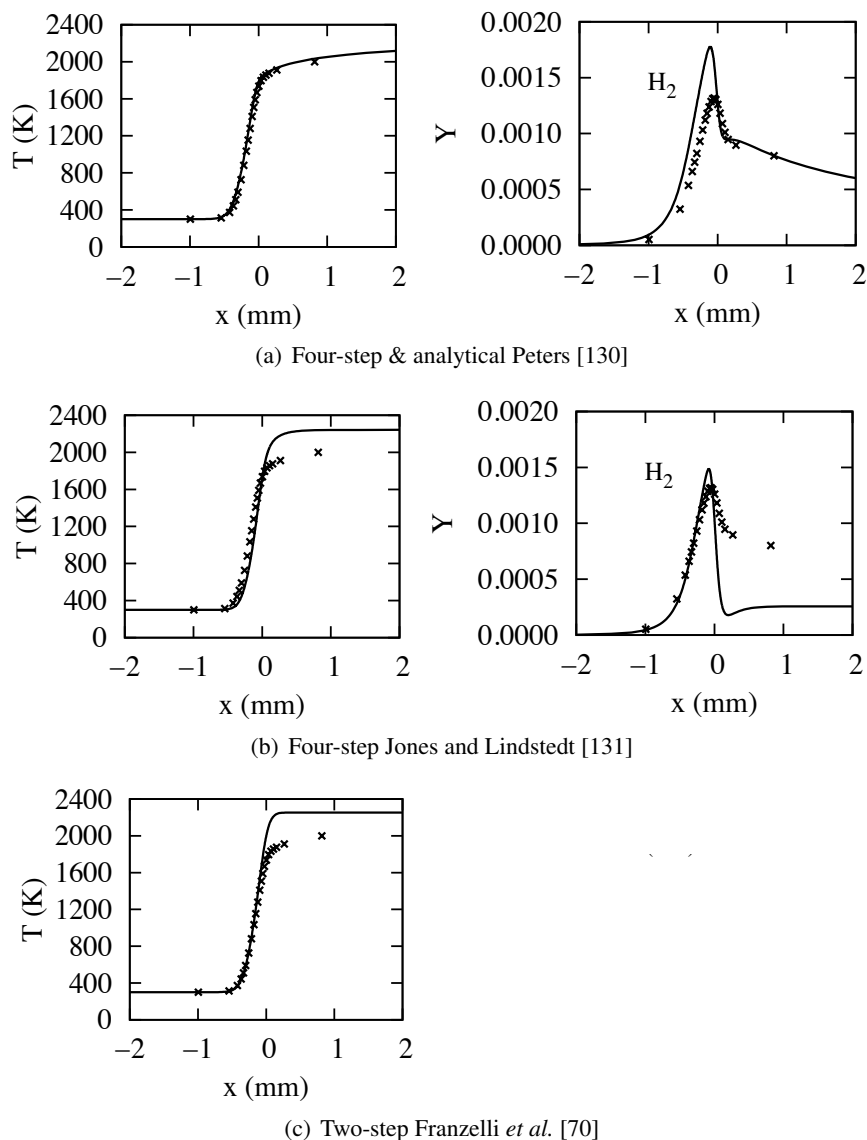


Figure 3.14: Temperature and H_2 profiles in a stoichiometric premixed methane-air flame ($\phi = 1$). (\times): Detailed chemistry GRI-3.0 [140]. (Solid line): Reduced chemistry.

temperature after the strong gradient at the peak heat release, to asymptotically approach the burnt gases temperature.

The H_2 profiles (Fig. 3.14) confirm the importance of the analytical part of the scheme, which provides the proper decay of H_2 towards burnt gases (Fig. 3.14(a)), decay which is overestimated in a global scheme not accounting for intermediates of the H_2/O_2 chemistry (Fig. 3.14(b)). It is seen once more that it may be crucial to keep these intermediate species in the modelling loop of turbulent flames, still without transporting them, when they can be obtained from quasi-steady state assumptions, therefore for a negligible additional computing cost.

In terms of major species, the two-step mechanism captures the fuel (CH_4) and the oxidiser (O_2) responses, but the products, CO , CO_2 are not well predicted (Fig. 3.17). The four-step mechanism by Jones and Lindstedt is accurate on the lean side (Fig. 3.16(a)), but less precise under the stoichiometric condition for CO_2 (Fig. 3.16(b)), in line with the temperature profile (Fig. 3.14(b)). Under rich condition

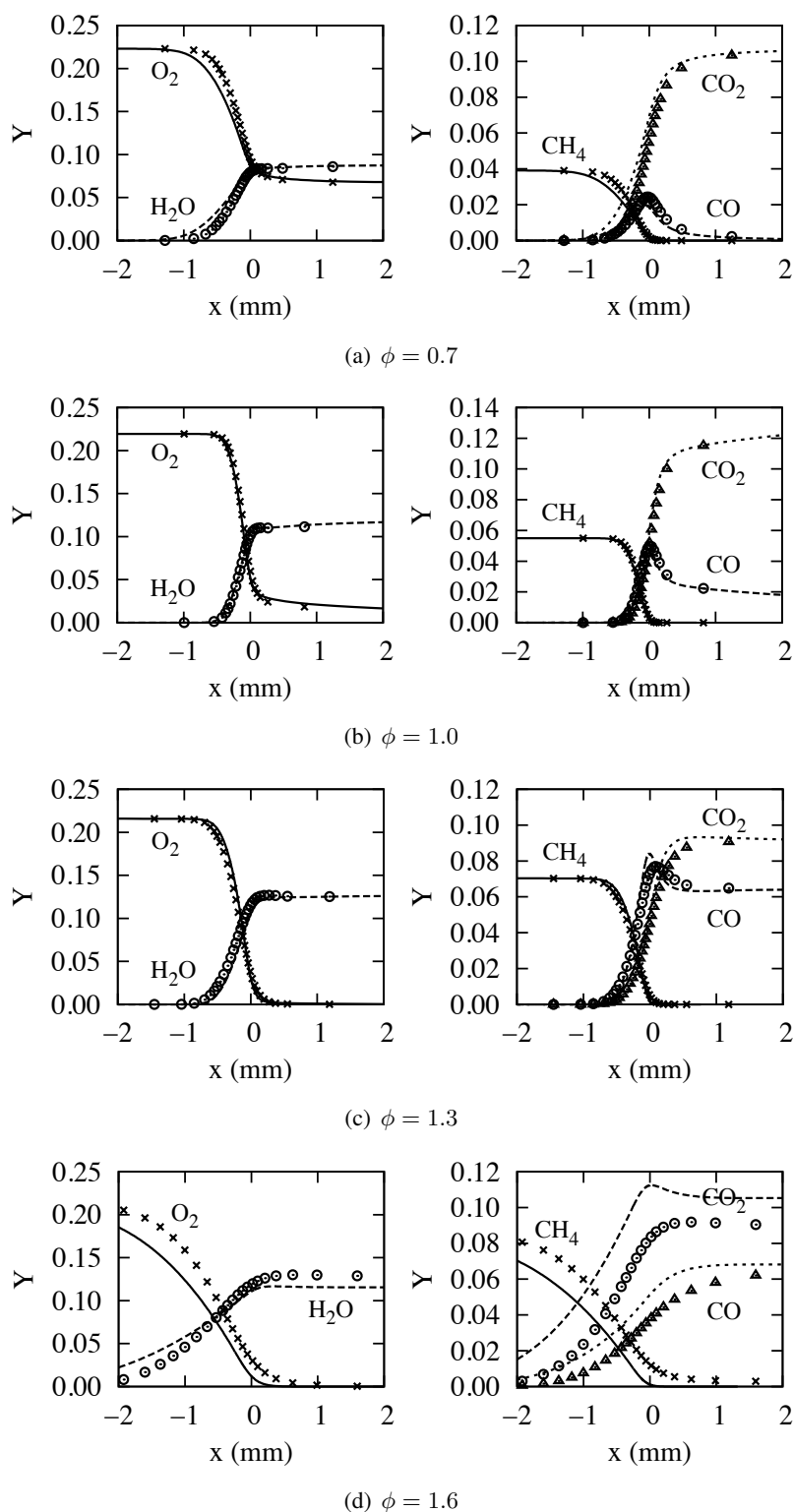


Figure 3.15: Species profiles in freely propagating premixed flame for various equivalence ratios. Line: Detailed chemistry GRI-3.0 [140]. Symbols: Four-step analytical mechanism Peters [138]. In subfigure: Left, solid line and (\times): O_2 , dashed line and (\odot): H_2O . Right, solid line and (\times): CH_4 , dashed line and (\odot): CO , dotted line and (\blacktriangle): CO_2 .

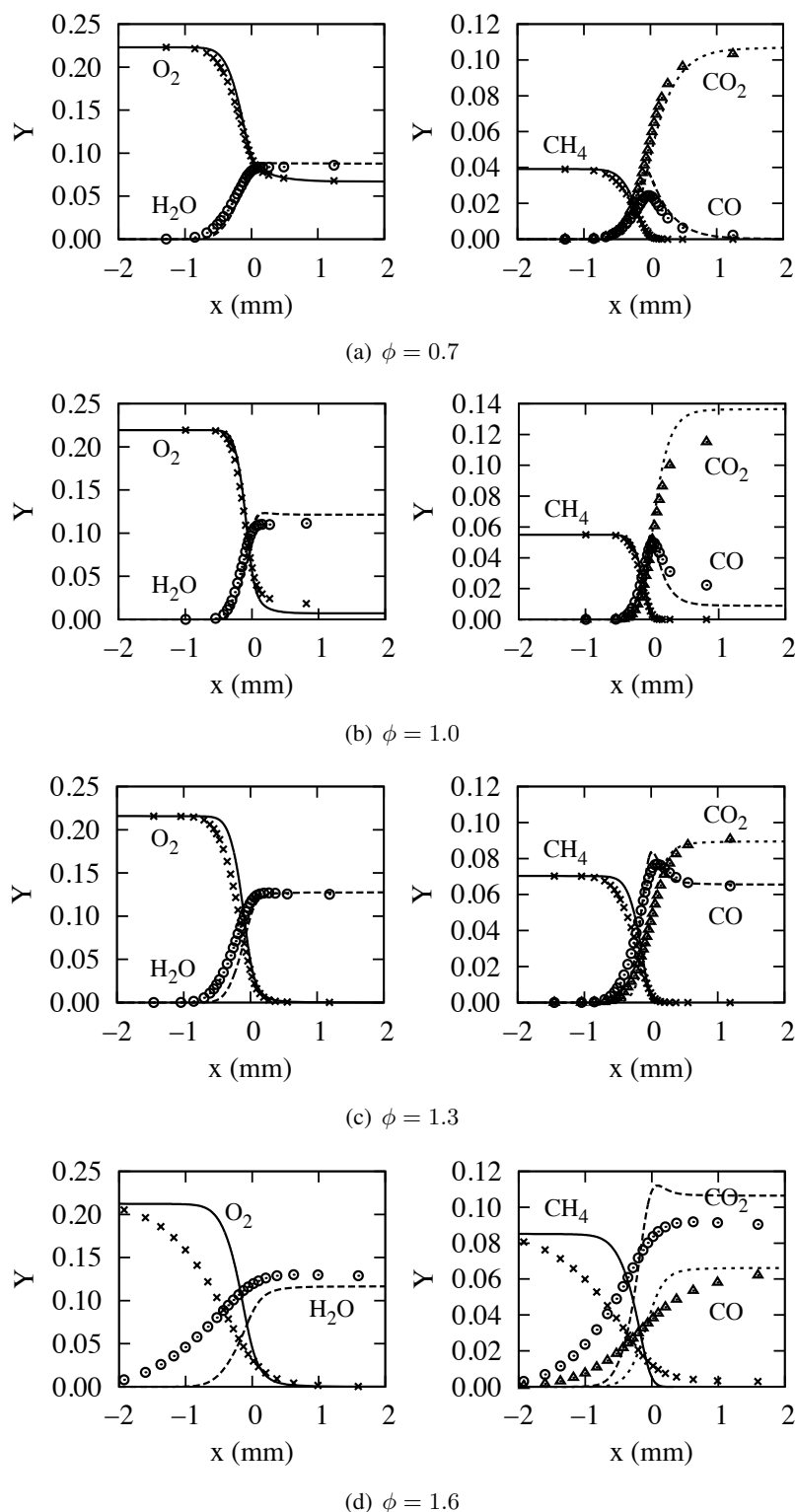


Figure 3.16: Species profiles in freely propagating premixed flame for various equivalence ratios. Line: Detailed chemistry GRI-3.0 [140]. Symbols: Four-step global mechanism Jones and Lindstedt [67]. In subfigure: Left, solid line and (\times): O_2 , dashed line and (\odot): H_2O . Right, solid line and (\times): CH_4 , dashed line and (\odot): CO , dotted line and (\blacktriangle): CO_2 .

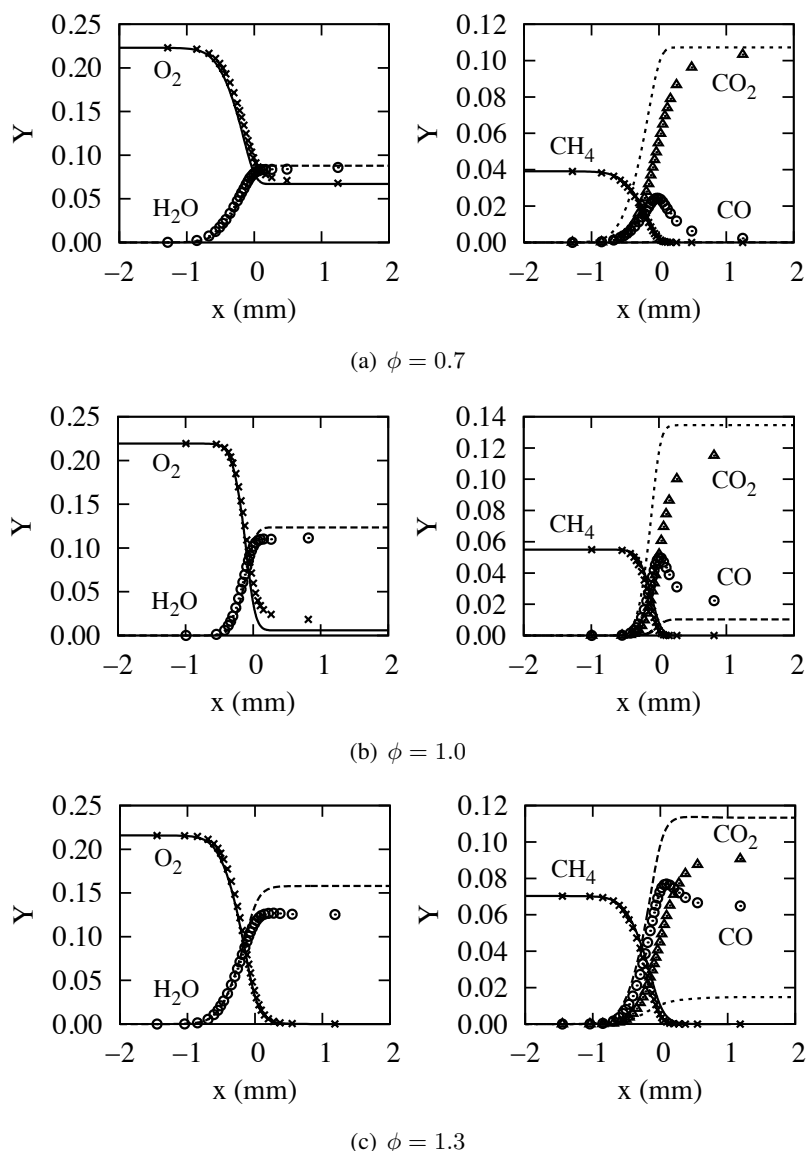


Figure 3.17: Species profiles in freely propagating premixed flame for various equivalence ratios. Line: Detailed chemistry GRI-3.0 [140]. Symbols: Two-step global mechanism Franzelli *et al.* [70]. In subfigure: Left, solid line and (\times): O_2 , dashed line and (\odot): H_2O . Right, solid line and (\times): CH_4 , dashed line and (\odot): CO , dotted line and (\blacktriangle): CO_2 .

$\phi = 1.3$, the temperature profile is better predicted (not shown for brevity), then species are also in better agreement (Fig. 3.16(c)). For higher equivalence ratios, results move away from the reference detailed chemistry solution (Fig. 3.16(d)). The Peters' scheme with its analytical part for intermediates, is overall quite accurate at all equivalence ratios, with an almost perfect reproduction of the detailed scheme up to $\phi = 1.3$ (Fig. 3.15). Far away from the reaction zones, in the burnt gases all schemes deliver the proper equilibrium composition and temperature, whatever the equivalence ratios.

This preliminary exercise illustrates the potential of reduced schemes including an analytical part, which somehow globalises the complex and key role played by intermediates. In order to simplify the development of such reduced schemes for any fuel and flow conditions from well-established detailed

kinetics, it is desirable to design a fully automated procedure, which could easily be integrated as a pre-processing tool in computational fluid dynamics software. The reduced scheme could then be created for the operating conditions under study, in terms of boundary conditions, temperature, pressure, flow residence time and even global intensity of turbulent mixing. In this quest for a reduced scheme, it is reported below that not only the choice of the sets of species and reactions is crucial, but also that an optimisation of the rates is required to reproduce at the same time species profiles, flame speed and quenching point of diffusive-reactive layers.

3.6 Conclusion

Over the last decades, a tremendous amount of chemistry reduction approaches have been developed in order to lower the costs arising from the use of complex mechanisms. In spite of the clear progress on this topic, it appears that there is no straightforward process to create simplified mechanisms, nor is there any unique reduced chemical scheme able to cover all at once a sufficiently wide range of operating conditions. Moreover since reduced chemical schemes directly result from a trade-off between cost and accuracy, they are highly user-dependent. The conclusion to this lack of generic character is that reduced mechanisms must always be derived for specific computational conditions which clearly motivates the need for an automated reduction tool.

The oxidation of hydrocarbon fuels predominantly leads to the creation of water vapour and carbon dioxide through a number of chemical reactions heavily influenced by the operating conditions, the turbulence levels and the fuel to oxidiser ratio at which the combustion takes place. This complex set of reactions can be reduced to a single step or to a few global reactions, however doing so, the informations about key chemical paths are lost. These global schemes have been extensively used due to the very reduced costs to which they are associated. Thanks to the introduction of correction functions, global mechanisms are able to recover a good description of the flame velocity and of the equilibrium temperature over a large range of conditions. As such, they are still interesting today. Nevertheless, the prediction of the pollutants such as CO, NO_x, SO_x and unburned hydrocarbons requires a more detailed description of the chemistry that pilots the reactive process.

For given operating conditions, mechanisms relying on the removal of the unnecessary species and reactions of a detailed chemical scheme (skeletal) and on the introduction of a few kinetic assumptions (analytical) have demonstrated their ability to recover a very detailed description of flames characteristics. Although these chemical descriptions are always much larger than the global schemes, great levels of reduction can be achieved with good accuracy. The levels of the intermediate species are also often well recovered. Figure 3.18 provides a resume of the methodologies available in the literature for the derivation of such mechanisms. The optimised reduced chemistry (ORCh) procedure that is proposed in this thesis relies on the highlighted steps i.e. the approaches employed are (1) the Directed Relation Graph with Error Propagation coupled with the aided-sensitivity analysis, (2) the isomers lumping strategy proposed by Pepiot and Pitsch and (3) the Quasi-Steady State assumption for which species are selected from a comparison of the consumption/production rates and with a linear solving of the QSS expressions.

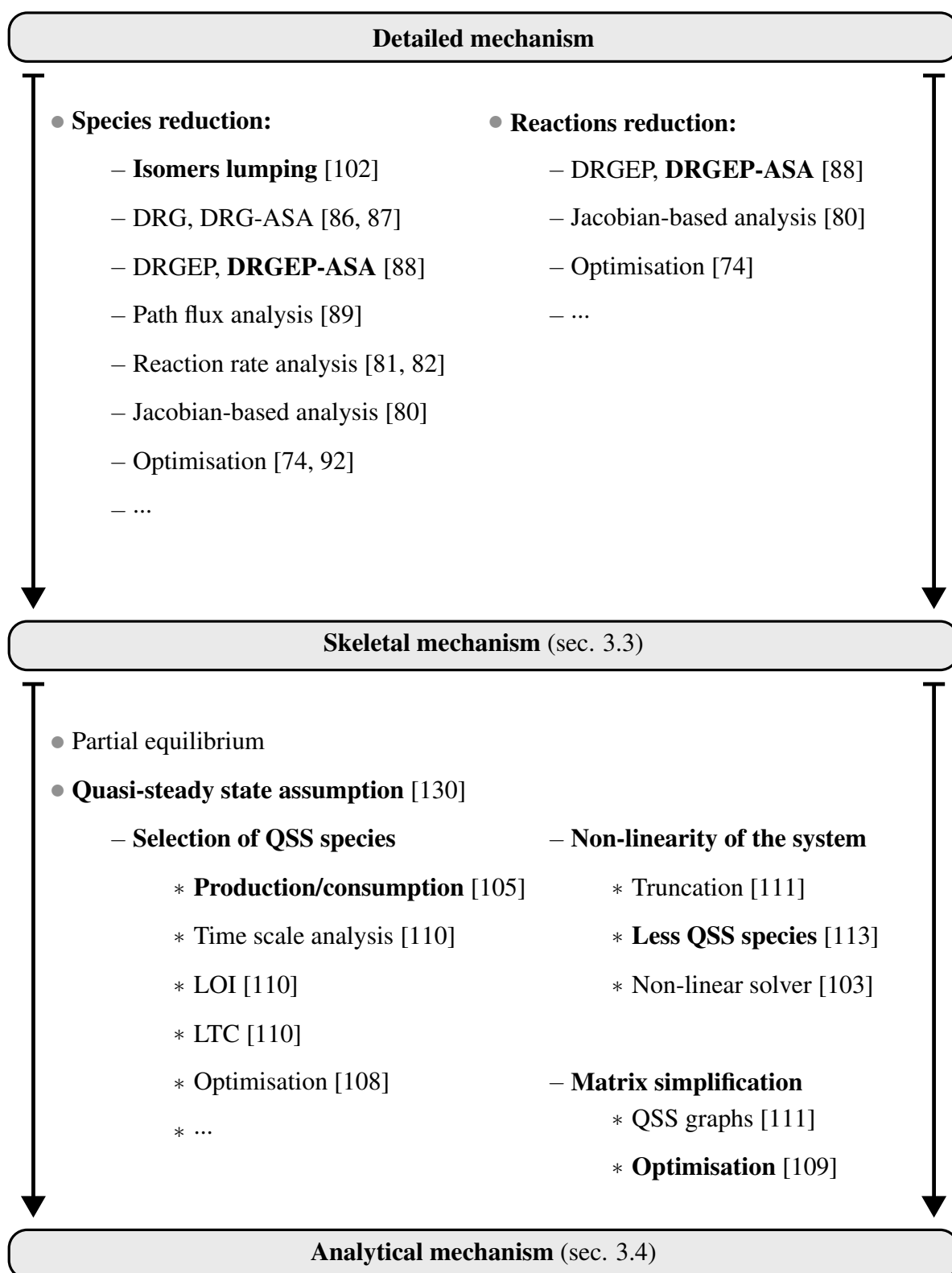


Figure 3.18: A resume of the major methodologies for the reduction of detailed mechanisms to the form of skeletal and analytical schemes.

Chapter 4

A reduction and optimisation strategy applied to premixed methane-air flames

Contents

4.1	Introduction	101
4.2	Optimisation strategy	102
4.2.1	Single-step optimisation methodology	102
4.2.2	Genetic algorithm	104
4.3	Global chemistry for methane-air flames	108
4.3.1	Optimisation of a 3-step mechanism	108
4.3.2	Optimisation of a mechanism with 11 reactions	109
4.4	Skeletal and analytical chemistry for methane-air flames	113
4.4.1	DRGEP for species removal	113
4.4.2	DRGEP for reactions removal	114
4.4.3	Quasi-steady state assumption	114
4.4.4	Application	114
4.5	Conclusion	117

4.1 Introduction

This chapter is intended to assess the relevance of some of the methodologies presented in the literature review for the reduction of chemical mechanisms. First a procedure is proposed for the optimisation of the Arrhenius constants of global systems. The suggested approach relies on two methodologies: (1) the reactions of a given mechanism are optimised separately using a gradient-based algorithm, to restrict the initial research area and then (2) a genetic algorithm is employed to refine the values of the Arrhenius constants considered all together for the full set of reactions.

The proposed optimisation procedure is tested in the simple case of a global mechanism proposed in 1988 by Jones and Lindstedt [67]. This optimisation is performed to check whether or not an automatic optimisation of this global scheme is capable of giving a better description than with the *ad hoc* coefficients initially proposed by the authors. Although the gradient-based procedure performs very well for the coefficients associated to the carbonated reactions of the global mechanism, a limitation is found on

the description of the H₂-O₂ chemical interactions. To address this problem, the single hydrogenated step considered in the global scheme proposed by Jones and Lindstedt is replaced with a more detailed chemistry including a few relevant intermediate species such as H, O and OH. The same optimisation procedure is applied. This results in an 11 steps mechanism capable of accurately predicting the levels of major species, the temperature profile and the flame velocity of atmospheric premixed methane-air flames over a range of equivalence ratios from lean conditions ($\phi = 0.6$) up to stoichiometry.

Although the procedure is established for lean/stoichiometric conditions, the selection of the reacting paths is not straightforward. Therefore the extension of the present mechanism to rich conditions and to the prediction of pollutants levels is hardly conceivable, and the derivation of mechanisms for other fuels necessitates to restart the procedure from scratch. For this reason, it is decided to assess the relevance of the DRGEP method for the removal of unnecessary species and reactions and of the QSS assumptions for the reduction in the number of transported species. Interestingly, the discrepancy introduced by pushing the limits of the threshold levels of both DRGEP and QSS approaches is easily corrected with optimisation of the remaining reactions Arrhenius constants. This is further demonstrated on a methane-air stoichiometric flame.

4.2 Optimisation strategy

Optimisation is a branch of mathematics and of computer sciences that serves to estimate the solution or the group of solutions that best satisfies a user defined quantitative objective while eventually respecting specific constraints. It is employed in the present context to modify a reduced chemical mechanism so that its physical and chemical behaviours get as close as possible to the one of a detailed chemistry that is used as reference.

4.2.1 Single-step optimisation methodology

Automatic tools for the definition of Arrhenius constants for global schemes and for large ranges of operating conditions have been widely discussed in the literature using various optimisation based approaches. Among those, Polifke [71] first proposed a genetic algorithm strategy directly using the chemical sources distribution as targets for optimisation. This approach is further explored in this section.

4.2.1.1 Target profiles and chemical sources

Freely propagating one-dimensional premixed flames are simulated at various equivalence ratios with detailed chemistry, to provide reference species mass fractions profiles, $Y_k^*(x)$. The Hirschfelder and Curtiss approximation [5] is used to estimate the transport coefficients.

Formally, N_{sp} species are involved in the detailed mechanism and $n_{sp} < N_{sp}$ in the reduced one, which represent the large majority of the mass involved through the detailed computation. Target species source terms $\dot{\omega}_k^\circ$ are reconstructed for the reduced scheme from $Y_k^*(x)$ for the n_{sp} species, to ensure that mass budgets are properly closed for the reduced number of transported species:

$$\dot{\omega}_k^\circ = \frac{\partial \rho Y_k^*}{\partial t} + \frac{\partial}{\partial x_i} (\rho (u_i + V_{k,i}^*) Y_k^*) , \quad (4.1)$$

where the density ρ of the mixture corresponding to the reduced scheme is computed from the equation

of state and the velocity u_i associated to the n_{sp} species is corrected to verify mass conservation,

$$\rho = \frac{P}{\mathcal{R} \sum_{k=1}^{n_{sp}} (Y_k^*/W_k) T^*}, \quad (4.2)$$

$$u_i = \frac{\rho^*}{\rho} u_i^*. \quad (4.3)$$

The diffusion velocity reads:

$$V_{k,i}^* = -\frac{D_k^H}{X_k^*} \frac{\partial X_k^*}{\partial x_i} + V_{c,i}^*. \quad (4.4)$$

where the exponent $*$ refers to terms computed with the reference chemistry. As for the detailed chemistry simulation, a diffusive velocity correction noted $V_{c,i}^*$ is used in Eq. (4.1). It is expressed through the relation:

$$V_{c,i}^* = \sum_{k=1}^{n_{sp}} D_k^H \frac{W_k}{W} \frac{\partial X_k^*}{\partial x_i} \quad (4.5)$$

The reaction rate \dot{Q}_j of the j^{th} reaction reads:

$$\dot{Q}_j = \mathcal{A}_j T^{\beta_j} \exp\left(-\frac{E_j}{\mathcal{R}T}\right) [\text{A}]^{n_{1j}} [\text{B}]^{n_{2j}}, \quad (4.6)$$

with \mathcal{A}_j the pre-exponential factor, E_j the activation energy, the temperature exponent β_j , and, the exponent of concentrations n_{1j} and n_{2j} . $[\text{A}]$ and $[\text{B}]$ denote the concentration of the species involved in the chemical reaction step. Given the high values associated to the pre-exponential factor, $a_j = \log \mathcal{A}_j$ is defined to conduct the optimisation process.

The number of reactive steps involved with global chemistry is usually smaller than the number of species, therefore the problem is overdetermined in terms of reference reaction rates (\dot{Q}_j°) to be determined from the chemical rates of the n_{sp} species ($\dot{\omega}_k^\circ$), known from Eq. (4.1). In the following, a number of species equals to the number of reaction steps n_r to be optimised, are selected to compute the reaction rates \dot{Q}_j° from:

$$\dot{\omega}_k^\circ = W_k \sum_{j=1}^{n_r} \nu_{k,j} \dot{Q}_j^\circ, \quad (4.7)$$

where the exponent $^\circ$ is given to terms associated to the global mechanism and where $\nu_{kj} = \nu_{kj}'' - \nu_{kj}'$ expresses the difference between the backward and forward stoichiometric coefficients (see section 2.2.1) of the k^{th} species in the j^{th} reaction rate. This implies that we formulate at this stage the hypothesis that the reaction rates obtained while reproducing $n_r = n$ selected species, are not so different from the rates that would be obtained while trying to fairly distribute the error over all the species. At the end of this preliminary step a set of species profiles $Y_k^*(x)$ and of reaction rates $\dot{Q}_i^\circ(x)$ are available.

4.2.1.2 Fitness function definition

The error between the reference rate \dot{Q}° and the rate to be optimised \dot{Q} is calibrated as:

$$E_1(x_i; c^p) = \left| \ln(\dot{Q}(x_i; c^p)) - \ln(\dot{Q}^\circ(x_i)) \right|. \quad (4.8)$$

where x_i denotes a point of the target profiles and c^p , a given set of the chemical Arrhenius parameters. (The j^{th} indice in \dot{Q}_j , denoting the reaction number, is omitted in this section for sake of clarity.) A

fitness function is defined cumulating the error over the N_G points of the profiles:

$$\begin{aligned}
 f_1(c^p) &= \sum_{i=1}^{N_G} E_1(x_i; c^p), \\
 &= \sum_{i=1}^{N_G} (-1)^{\sigma(x_i; c^p)} \left[a(c^p) \ln(10) + \beta(c^p) \ln(T^*(x_i)) - \frac{E(c^p)}{\mathcal{R}T^*(x_i)} \right. \\
 &\quad \left. + n_1(c^p) \ln([A]^*(x_i)) + n_2(c^p) \ln([B]^*(x_i)) - \ln(\dot{Q}^\circ(x_i)) \right].
 \end{aligned} \tag{4.9}$$

Where the temperature is computed from the local enthalpy and species concentration. The function $\sigma(x_i; c^p)$ is introduced to ensure summation of the errors, $\sigma(x_i; c^p) = 0$ if $\dot{Q}(x_i; c^p) > \dot{Q}^\circ(x_i)$ and $\sigma(x_i; c^p) = 1$ otherwise.

4.2.1.3 Uncorrelated reactions solving

A preliminary estimation of all the parameters of the reaction scheme is obtained by considering every reaction step independently. As illustrated on figure 4.1, the source term fitness function given by (4.9) behaves linearly versus $a(c^p)$, $\beta(c^p)$, $E(c^p)$, $n_1(c^p)$ and $n_2(c^p)$, with a constant slope that changes its sign according to $(-1)^\sigma$. Within this context, a direct approach based on a Newton algorithm is suitable

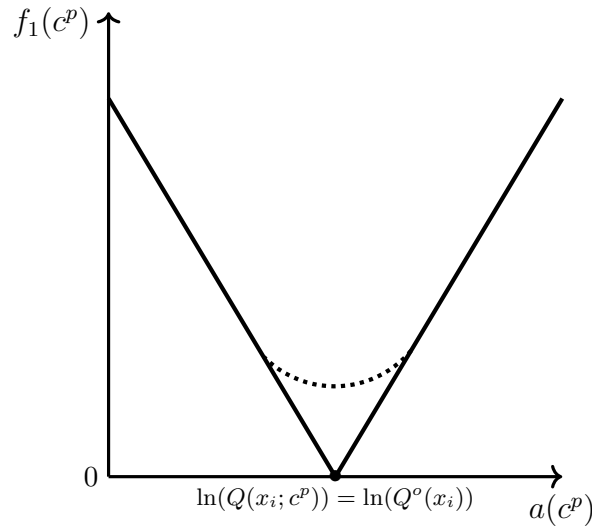


Figure 4.1: Theoretical evolution of the $f_1(c^p)$ error function. Solid line: Profile of the error function for a perfect solution. Dotted line: Profile of the error function for a non-perfect solution.

to obtain a set of parameters for the reduced chemical rates.

4.2.2 Genetic algorithm

A genetic algorithm applies the principles of natural selection and of evolution so as to look for the optimal solution of a problem initialised by a population of potential solutions. Although it is associated to a random research, it uses the informations present in the group of potential solutions to move towards the zone where the performance is the highest. Deterministic methods have the tendency to get stuck in local optimums and are therefore not adapted to solve problems linked to a fitness function which is

non-monotonic. On the contrary, genetic algorithms (GA) do not require hypothesis on the monotony or continuity of the studied functions. Moreover, GA have proven their reliability for solving problems for which classical methods fail to find a converged solution because an initial guess which lies into the radius of convergence of the algorithm is hard to find. The early numerical and theoretical works on genetic algorithms are attributed to Holland [155] which initiated it in the middle of the 60's. The methods he and his colleagues developed are based on a binary description. Most recent works on the subject are known as evolutionary algorithms which defer from GA by their ability to automatically adjust themselves to the problem.

The terms ‘gene’, ‘chromosome’ and ‘population’ are introduced for the optimisation of the Arrhenius parameters. For simplicity in the notation, only one a , one β and one E are considered in the following, see Fig. 4.2. In practice, the procedure is applied to all parameters of all reactions at once. In this section, a given triplet of parameters values (a , β , E) constitutes a chromosome, while a gene is

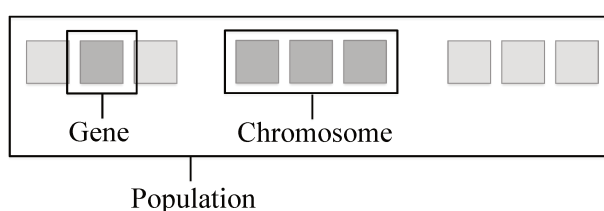


Figure 4.2: Structure of the population

the value taken by one of these parameters (Fig. 4.2). The population is composed of a set of potential solutions, *i.e.* a set of chromosomes.

For every parameter, a range of values is defined allowing a variation of $\pm 2\%$ centred on the condition of the detailed chemistry, a^1 , β^1 and E^1 . For a desired precision Δa in the binary description on the parameter a , the number of required binary digits (bits) reads:

$$N_{bits}(a) \geq \frac{\ln\left(\frac{a_{\max} - a_{\min}}{\Delta a}\right)}{\ln(2)}, \quad (4.10)$$

$N_{bits}(\beta)$, $N_{bits}(E)$ are defined similarly. The gene corresponding to the smallest value a_{\min} (resp. the upper bound a_{\max}) is constructed setting all the bits to ‘0’ (resp. ‘1’) (Table 4.1).

During the evolution algorithm, real values of the parameters must be obtained from binary genes, in order to test them in flame simulations. Every gene is transformed into, $(a)_{10}$, a decimal number and then back into its real value (Table 4.1):

$$a = \frac{(a)_{10}(a_{\max} - a_{\min})}{2^{N_{bits}} - 1} + a_{\min}. \quad (4.11)$$

	$(a)_2$	$(a)_{10}$	a
min	00000	→ 0	→ 3.92
	01011	→ 11	→ 3.97
max	11111	→ 31	→ 4.08

Table 4.1: Translation of one parameter from imposed minimum and maximum values $a \in [3.92, 4.08]$.

Using these tools, the following procedure is applied to find the best parameters for a given reduced chemistry:

1. M chromosomes (*i.e.* a population corresponding to a set of parameters values) are constructed by randomly selecting the values ‘0’ or ‘1’ for the $N_{bits}(a) + N_{bits}(\beta) + N_{bits}(E)$ bits of every chromosome (Fig. 4.3).

$$\begin{array}{|c|c|c|} \hline a & \beta & E_a \\ \hline \end{array} \quad 01011 \ 10010 \ 00100$$

Figure 4.3: Chromosome.

2. M flames are computed with the sets of chemical parameters (chromosomes), leading to $Y_k(x_j; c^p)$, $T(x_j; c^p)$, $u(x_j; c^p)$ for $p = 1, \dots, M$.
3. The fitness function $f(c^p)$ (Eq. 5.23) is computed for every chromosome c^p . One of the objectives is to enhance in the solution evolution the influence of the parameters value having the highest fitness, therefore providing flame solutions the closest to the reference one. To do so, the chromosomes are simply stored in M boxes according to growing order of their fitness, the integer $I_b(c^p) \in [1, M]$ denotes the box position of the p -th chromosome. Then, a linear ranking procedure is applied to the chromosomes according to their fitness. The normalised rank $r(c^p)$ of the p -th chromosome reads:

$$r(c^p) = \frac{\sum_{\ell=1}^p \mathcal{N}(c^\ell)}{\sum_{m=1}^M \mathcal{N}(c^m)}, \quad (4.12)$$

with

$$\mathcal{N}(c^p) = 2 - S_P + 2(S_P - 1) \frac{I_b(c^p) - 1}{M - 1}, \quad (4.13)$$

where a selective pressure $S_P = 2$ was chosen [156].

4. The population is advanced in time, in other words a new set of M chemical parameters (chromosomes) is built, according to three sub-steps:
 - (i) First, a crossover procedure is applied. $M/2$ pair of chromosomes are chosen. A random real number $\xi \in [0, 1]$ is generated and the p -th chromosome is selected if $\xi \in]r(c^\ell), r(c^p)]$, where the ℓ -th chromosome is ranked just below the p -th one (*i.e.* $I_b(c^p) - 1 = I_b(c^\ell)$). This procedure ensures that the chromosomes having a higher fitness are more likely to be selected. Once a given pair is selected, it has a probability of 30% to be left unchanged and a probability of 70% to undergo the crossover operation, in which two sets of parameters exchange a portion of their digits so as to create two new chromosomes (Table 4.2). The crossover point in the chromosome is also randomly selected.

1 cutoff point	0101100	1001000	0010010	→	0101100	1000001	0100101
	1100110	1100001	0100101	→	1100110	1101000	0010010
2 cutoff points	0101100	1001000	0010010	→	0101110	1100000	0010010
	1100110	1100001	0100101	→	1100100	1001001	0100101
3 cutoff points	0101100	1001000	0010010	→	0100110	1001001	0100101
	1100110	1100001	0100101	→	1101100	1100000	0010010

Table 4.2: Crossover operation with multiple cutoff points.

- (ii) Second, a random mutation is applied. Every bit of every chromosome may undergo a switch of its value (0→1) or (1→0), with a probability of 0.2%.

Mutation	1100110	1100001	0100101	→	1110111	1100001	0000101
----------	---------	---------	---------	---	---------	---------	---------

Table 4.3: Mutation operation on 2 binary digits.

(iii) Third, to avoid damaging the best solution during these processes, an elitism operation is applied that consists of simply copying the best solution (*e.g.* $I_b(c^p) = M$ and also called ‘elite’) to the next generation.

A new set of chemical parameter is then available, which is used to repeat the process from point 2. The normalised variance of the fitness,

$$S_f = \frac{\sum_{p=1}^M f^{+2}(c^p) - \frac{1}{M} \left(\sum_{p=1}^M f^+(c^p) \right)^2}{4 \sum_{p=1}^M f^+(c^p) \left(1 - \frac{1}{M} \sum_{p=1}^M f^+(c^p) \right)}, \quad (4.14)$$

where $f^+ = (f - f_{\min}) / (f_{\max} - f_{\min})$ is monitored and the solution is considered converged when its variation between two iterations is below a few percent.

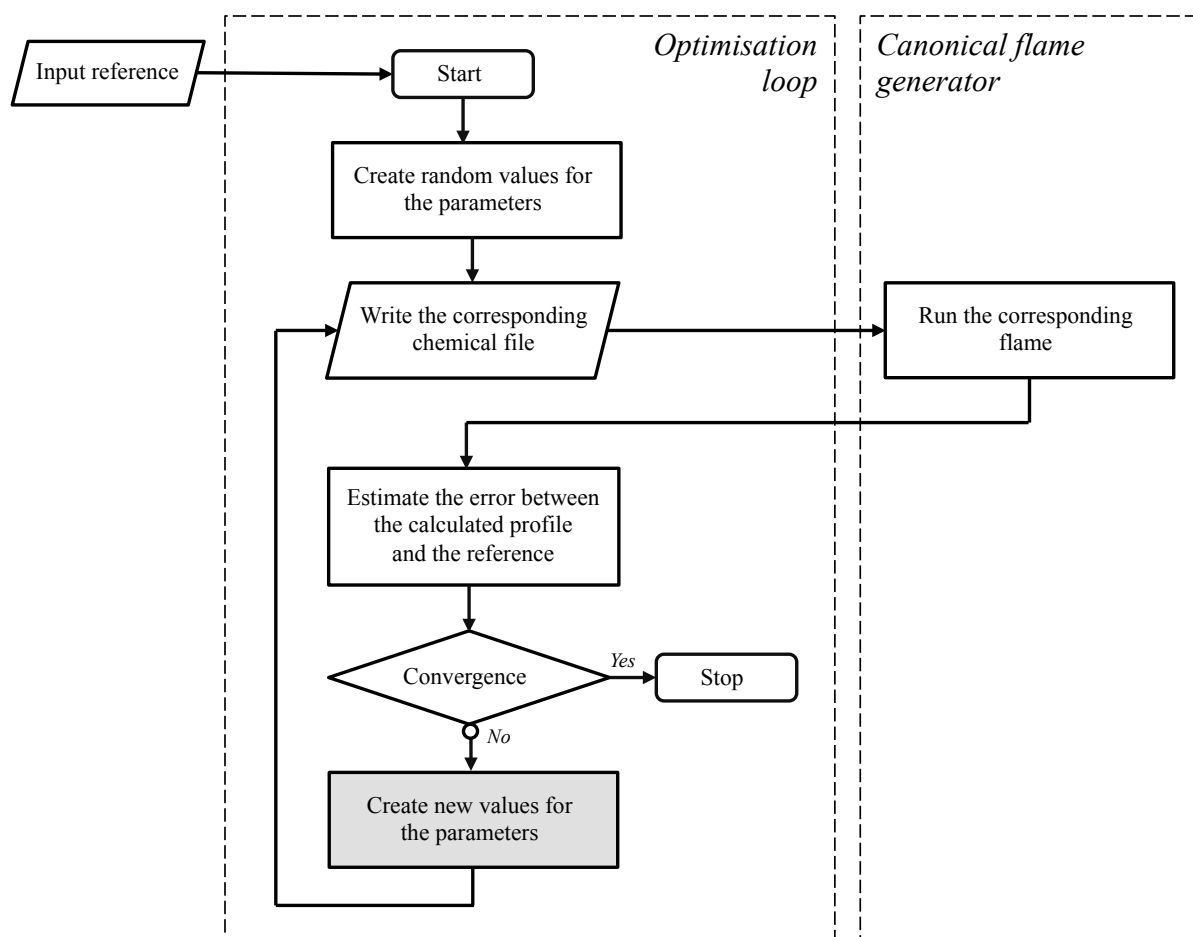


Figure 4.4: Flowchart of the genetic algorithm-based procedure for the optimisation of the Arrhenius constants of any set of reactions. The optimisation procedure is coupled with a canonical flame generator to assess the relevance of the potential solutions.

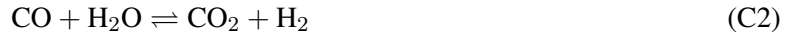
The full procedure is illustrated on Figure 4.4 which provides a flowchart of the optimisation loop. In the present thesis the flame canonical generator is CANTERA. Although the procedure is illustrated in this section with premixed flames, any canonical problem may be used as reference. This point will be addressed in the next chapter.

4.3 Global chemistry for methane-air flames

As a first approach for optimisation, it is decided to study global combustion mechanisms. Two cases are here considered for methane-air combustion.

4.3.1 Optimisation of a 3-step mechanism

A first attempt to improve the global 3 steps Jones and Lindstedt mechanism [67] for the simulation of premixed stoichiometric methane-air flames is here presented using the strategy depicted within the previous section. The three steps considered for the optimisation are:



To illustrate the selection of the chemical targets for a separated optimisation of the steps, the relations between the species source terms and the rates of the three chemical reactions are given from equation 4.15 to equation 4.20.

$$\dot{\omega}_{\text{H}_2} = 2W_{\text{H}_2}\dot{Q}_1 - W_{\text{H}_2}\dot{Q}_2 + W_{\text{H}_2}\dot{Q}_3 \quad (4.15)$$

$$\dot{\omega}_{\text{O}_2} = -0.5W_{\text{O}_2}\dot{Q}_1 - 0.5W_{\text{O}_2}\dot{Q}_2 \quad (4.16)$$

$$\dot{\omega}_{\text{H}_2\text{O}} = W_{\text{H}_2\text{O}}\dot{Q}_2 + W_{\text{H}_2\text{O}}\dot{Q}_3 \quad (4.17)$$

$$\dot{\omega}_{\text{CH}_4} = -W_{\text{CH}_4}\dot{Q}_1 \quad (4.18)$$

$$\dot{\omega}_{\text{CO}} = W_{\text{CO}}\dot{Q}_1 - W_{\text{CO}}\dot{Q}_3 \quad (4.19)$$

$$\dot{\omega}_{\text{CO}_2} = W_{\text{CO}_2}\dot{Q}_3 \quad (4.20)$$

As introduced earlier, the system of equations appears to be overdetermined since there are 6 equations to be solved for only 3 unknown variables. Using the procedure proposed in Section 4.2.1, a set of 3 species source terms is selected as target, to form a 3×3 system to be inverted for the estimation of the rates of the reactions \dot{Q}_1 , \dot{Q}_2 and \dot{Q}_3 . The following explicit formulation is deduced:

$$\dot{Q}_1 = -\frac{\dot{\omega}_{\text{CH}_4}}{W_{\text{CH}_4}}, \quad \dot{Q}_2 = \frac{\dot{\omega}_{\text{H}_2\text{O}}}{W_{\text{H}_2\text{O}}} - \frac{\dot{\omega}_{\text{CO}_2}}{W_{\text{CO}_2}}, \quad \dot{Q}_3 = \frac{\dot{\omega}_{\text{CO}_2}}{W_{\text{CO}_2}}. \quad (4.21)$$

First a computation of a stoichiometric methane-air flame at atmospheric conditions is performed using the GRI-1.2 mechanism [106, 107] to get reference chemical profiles. These profiles are then used to deduce the reference rates for the three reactions as given by 4.21. The optimisation procedure is

finally applied separately optimising the Arrhenius relations given by:

$$\dot{Q}_1 = \mathcal{A}_1 T^{\beta_1} \exp\left(-\frac{E_1}{\mathcal{R}T}\right) [\text{CH}_4]^{n_{11}} [\text{O}_2]^{n_{21}} \quad (4.22)$$

$$\begin{aligned} \dot{Q}_2 = \mathcal{A}_2 T^{\beta_2} \exp\left(-\frac{E_2}{\mathcal{R}T}\right) [\text{H}_2]^{n_{12}} [\text{O}_2]^{n_{22}} \quad (4.23) \\ - \frac{\mathcal{A}_2 T^{\beta_2} \exp\left(-\frac{E_2}{\mathcal{R}T}\right)}{K_{\text{eq},2}} [\text{H}_2\text{O}] [\text{H}_2]^{1-n_{12}} [\text{O}_2]^{1-n_{22}} \end{aligned}$$

$$\begin{aligned} \dot{Q}_3 = \mathcal{A}_3 T^{\beta_3} \exp\left(-\frac{E_3}{\mathcal{R}T}\right) [\text{CO}]^{n_{13}} [\text{H}_2\text{O}]^{n_{23}} \quad (4.24) \\ - \frac{\mathcal{A}_3 T^{\beta_3} \exp\left(-\frac{E_3}{\mathcal{R}T}\right)}{K_{\text{eq},3}} [\text{CO}_2] [\text{H}_2] [\text{CO}]^{1-n_{13}} [\text{H}_2\text{O}]^{1-n_{23}} \end{aligned}$$

For each reaction, 5 terms are to be optimised, namely the \mathcal{A} s, the β s, the E s, as well as the exponents on the concentrations n_1 s and n_2 s. As explained earlier, a gradient-based approach is employed to find the optimum values since a deterministic approach is more suited to this linear optimisation problem. The results for each of the three reactions are given in Figure 4.5. It is observed that the rate associated to reaction 1 properly captures the effects describing the consumption of CH_4 . The slow oxidation of CO to form the stable product CO_2 is also well captured using the third reaction. It is however observed that reaction 2 is not capable of properly reproducing the H_2O rate. Note that the optimisation is here performed using the temperature profile of the detailed chemistry. The difference observed in the optimisation of the rate of reaction 2 indicates that the reference temperature evolution cannot be reproduced. This explains why the temperature profile obtained with the Jones and Lindstedt mechanism provided on Figure 3.14(b) for similar conditions is much stiffer than the reference and rapidly reaches equilibrium.

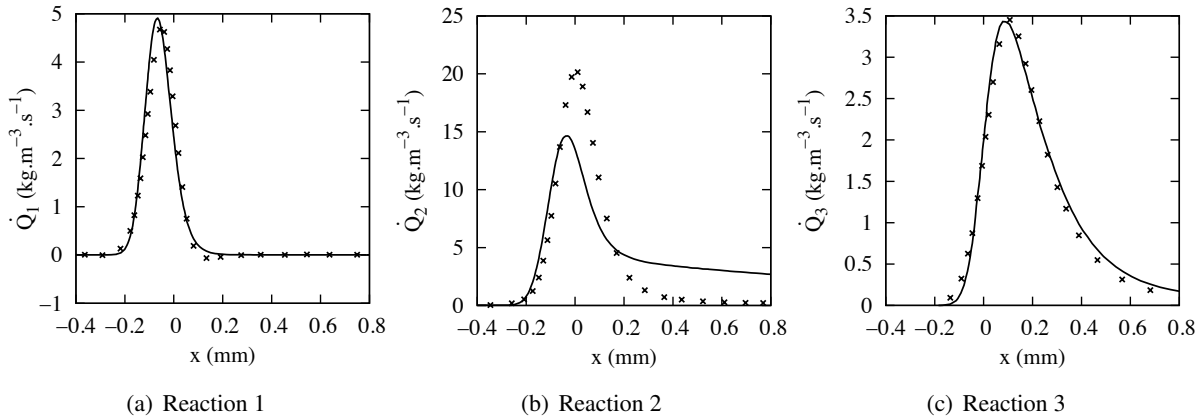


Figure 4.5: Comparison of the rates of the 3 reactions for a stoichiometric methane-air premixed flame. Solid lines: Optimised. (×): Reference obtained from the source terms of species CH_4 , H_2O and CO_2 computed with the GRI-1.2 mechanism [106, 107].

4.3.2 Optimisation of a mechanism with 11 reactions

Because the second step of the global mechanism studied in the previous section fails to reproduce the $\text{H}_2\text{-O}_2$ interaction, it is decided to use a larger set of reactions for the hydro-oxygenated chemistry.

Compared to the previous mechanism, this set of reactions introduces the H, OH and HO₂ species which are known to have a non-negligible effect on the heat release, and hence on the temperature profile. This new mechanism is reported within Table 4.4. It includes, one oxidation reaction for methane (C1 in Table 4.4), a set of 9 reactions for the description of the hydro-oxygenated combustion (H α in Table 4.4) and a water-gas shift reaction (C2 in Table 4.4).

#	Reaction	\mathcal{A}^*	β	E^*	n_1	n_2	
C1	$\text{CH}_4 + 0.5 \text{O}_2 \rightarrow \text{CO} + 2 \text{H}_2$	2.592e15	-0.50	32099	0.799	0.732	
H1	$\text{H} + \text{O}_2 \rightleftharpoons \text{OH} + \text{O}$	3.520e16	-0.70	17069	-	-	
H2	$\text{H}_2 + \text{O} \rightleftharpoons \text{OH} + \text{H}$	5.060e04	2.67	6290	-	-	
H3	$\text{H}_2 + \text{OH} \rightleftharpoons \text{H}_2\text{O} + \text{H}$	1.170e09	1.30	3635	-	-	
H4	$\text{H} + \text{O}_2 + \text{M} \rightarrow \text{HO}_2 + \text{M}$	k_0	5.750e16	-1.40	0	-	-
		k_∞	4.650e12	0.44	0	-	-
H5	$\text{HO}_2 + \text{H} \rightarrow 2 \text{OH}$	7.080e13	0.00	294	-	-	
H6	$\text{HO}_2 + \text{H} \rightleftharpoons \text{H}_2 + \text{O}_2$	1.660e13	0.00	822	-	-	
H7	$\text{HO}_2 + \text{OH} + \text{M} \rightarrow \text{H}_2\text{O} + \text{O}_2 + \text{M}$	k_0	7.000e09	0.00	-1094	-	-
		k_∞	4.500e14	0.00	10929	-	-
H8	$\text{H} + \text{OH} + \text{M} \rightleftharpoons \text{H}_2\text{O} + \text{M}$	4.000e19	-2.00	0	-	-	
H9	$2\text{H} + \text{M} \rightleftharpoons \text{H}_2 + \text{M}$	1.300e15	-1.00	0	-	-	
C2	$\text{CO} + \text{H}_2\text{O} \rightleftharpoons \text{CO}_2 + \text{H}_2$	3.325e16	-0.60	32914	1.107	1.102	

Table 4.4: Arrhenius coefficients for the reduced scheme. *Units are mol, s, cm³, cal and K. n_1 and n_2 take stoichiometric values in the H α reactions. Three body reactions see [157].

The same strategy is applied, again to build a reduced mechanism for lean methane-air combustion. The parameters for both oxidation and the water-gas shift reactions are optimised. The constants of the H₂-O₂ mechanism (H α in Table 4.4) are directly taken from [157]. To focus on the optimisation of the hydrocarbons reactions, no steady-state hypothesis is introduced in the H₂-O₂ mechanism, hypothesis that could however be used to reduce even more the mechanism size. An initial condition for the chemical parameters is obtained with the procedure reported above as a first guess for the genetic algorithm

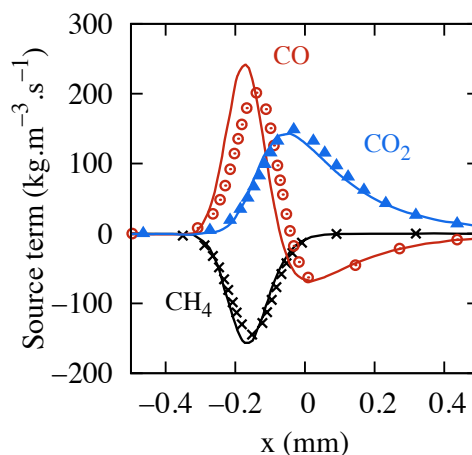


Figure 4.6: Major species burning rates. Stoichiometric flame. Lines: C1 and C2 of Table 4.4 after first guess estimation. Symbols: GRI-mech [140]. (×): CH₄. (⊙): CO. (△): CO₂.

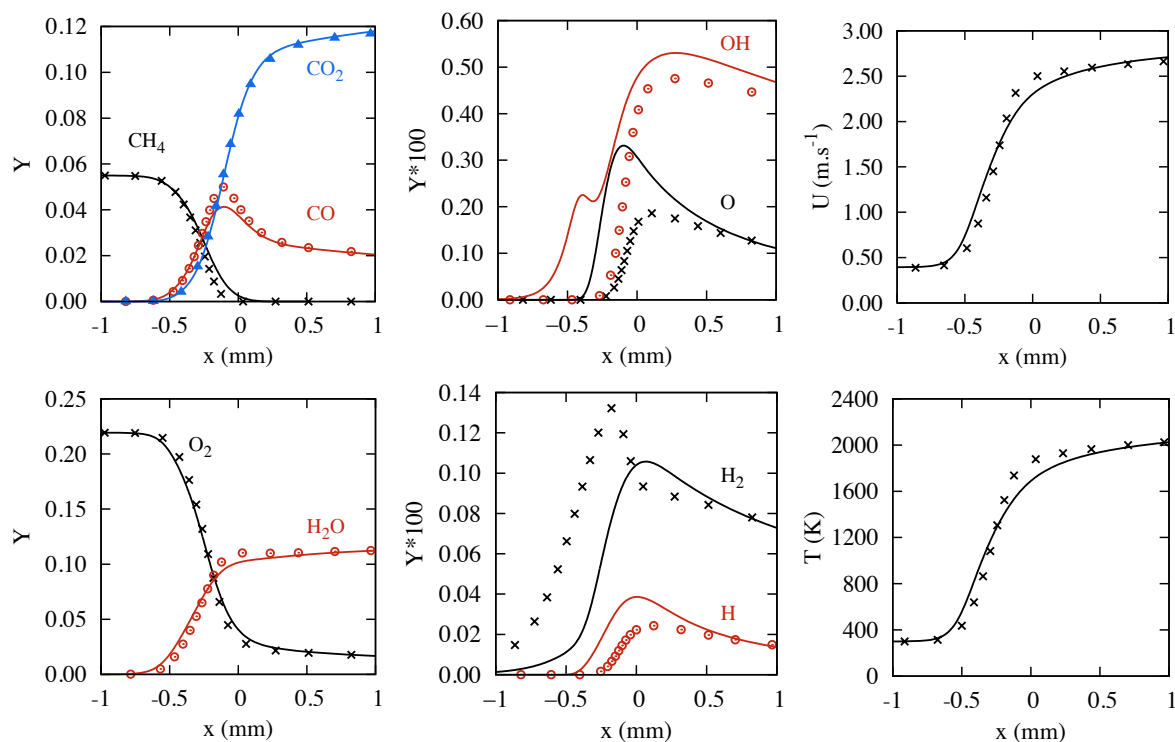
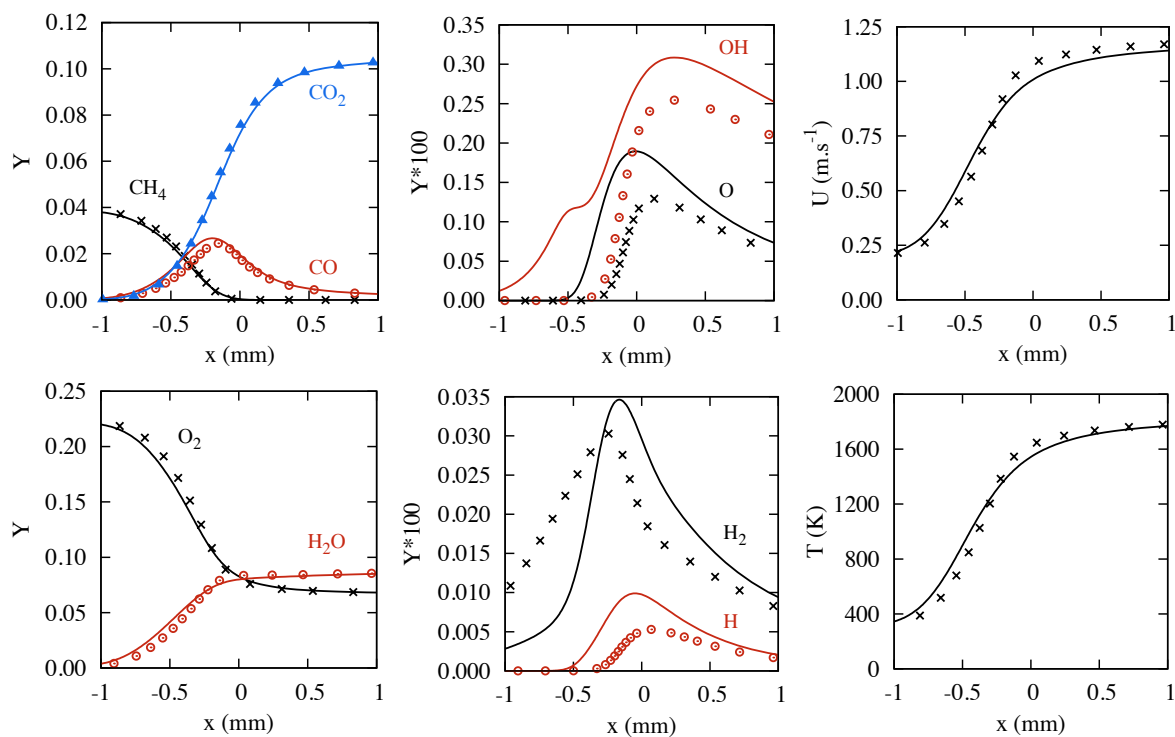
(a) Premixed trajectories $\phi = 1.0$ (b) Premixed trajectories at $\phi = 0.7$

Figure 4.7: Species mass fractions, flame velocity and temperature for equivalence ratios $\phi = 0.7$ and $\phi = 1.0$. Symbols: GRI-mech [140]. Solid lines: Present global 11-step scheme (Table 4.4).

optimisation procedure to be used afterwards. As for the previous study, the source terms of the species CH_4 and CO_2 are used within Eq. (4.7). Figure 4.6 shows that a good match with the detailed mechanism is reached already for chemical sources of major species.

Moving on to the optimisation of the full mechanism using a genetic algorithm coupled with the computation of perfectly premixed flames. A restricted research area is considered and defined from the parameters estimated with the first guess. The number of chromosome is set to $M = 25$ (24 plus one elite). The precision is $\Delta a = \Delta \beta = \Delta n_1 = \Delta n_2 = 0.001$ and $\Delta E = 1$, leading to chromosomes of approximately 100 bits. The method converges after about 15 iterations, which implies the simulations of about 375 flames. The required CPU time is about 1 hour on a laptop.

The profiles of the major species and of the intermediates are given in Fig. 4.7 along with the temperature and flame velocity lines. The magnitude and the slopes of the major species profiles are well captured by the reduced mechanism. Although the description of the temperature evolution is much better than with the Jones and Lindstedt mechanism (see Figure 3.14(b) for comparison), there is still a short difference in the slope of the curves explained by the poor reproduction of the intermediate species profiles. The resulting flame speed response versus equivalence ratio is shown in Fig. 4.8. The reduced scheme appears to properly capture the flame velocity for the range of equivalence ratio considered.

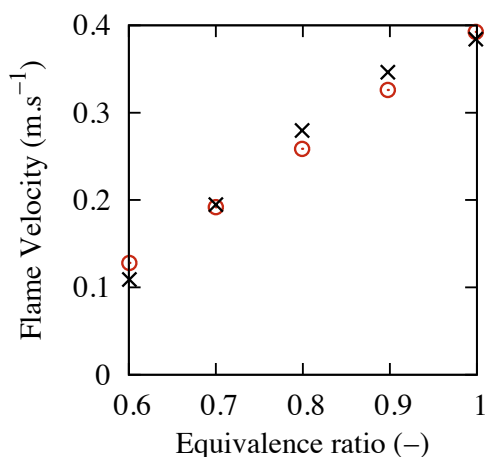


Figure 4.8: Flame speed response versus equivalence ratio. (x): GRI-Mech [140]. (o): Present 11-step mechanism.

As a conclusion, for a target composed of major species profiles and flame speed, no optimal values of the parameters of the chemical rates could be found from automated optimisation, without adding at least 9 elementary steps for the hydro-oxygenated species. Thus jeopardising the option which would consist of simply running an optimisation tool over existing three-step reaction mechanisms, even under a case restricted to premixed flames. An automated approach based on a genetic algorithm has been proposed to obtain chemical parameters from reference detailed chemistry sources and species profiles. The reduced mechanism is based on three parts: a global-step for fuel oxidation, a more detailed sub-mechanism for $\text{H}_2\text{-O}_2$ reactions and a global-step for water-shift. This method will be improved by coupling it with an additional automated approach to generate the reduced mechanism itself, prior to the optimisation of its constants.

4.4 Skeletal and analytical chemistry for methane-air flames

The results obtained with the global approach introduced in the above section are satisfactory regarding the reproduction of the major species, temperature and velocity profiles. Nevertheless, the poor prediction for the intermediates suggests that the use of global chemical schemes is not adapted for capturing the levels of pollutants emissions. Moreover, the derivation of such a scheme requires some basic knowledges about combustion kinetics since the selection of the global steps is not straightforward. As introduced in the review of the literature on chemistry reduction; methodologies relying on the removal of unnecessary species and reactions and on the introduction of a few kinetic simplifications have demonstrated their ability to recover the majority of the flames properties including the capture of intermediate chemical rates. This approach is assessed in the present chapter, again for the modelling of methane-air combustion.

Using the evolution of the species concentrations and temperature from computations performed with the reference detailed chemistry, three steps may be applied to end-up with an optimised and reduced chemical kinetics. The first two are the direct application of well-established procedures available in the literature, in order to reduce the number of species and chemical reactions. The third one is based on the use of the genetic algorithm-based procedure, which was depicted earlier in this chapter. The three steps require the iterative calculation of trajectories with the reduced scheme, up to convergence of the chemical rates.

4.4.1 DRGEP for species removal

The DRGEP procedure is initiated with the selection of a set of target chemical species, for which mass fraction profiles should be well reproduced by the reduced mechanism. As a reminder, the generalised interaction of a species 'C' with a target species 'A' is quantified from the term r_{A-C}^* and the participation of the target species 'A' to the overall atomic balances is given by α_{E-A} . The species are then ranked according to the value of \mathcal{T}_C that is computed from the coupling of the species and of the atoms interactions:

$$\mathcal{T}_C = \max (\alpha_{E-A} r_{A-C}^*) \quad \forall 'E', \quad (4.25)$$

The larger \mathcal{T}_C , the more important the species. The reader is redirected to the literature review and to the paper of Pepiot and Pitsch [88] for more details on the DRGEP approach. In the present thesis, it is decided to systematically recompute the trajectories, progressively removing species starting from the less important ones. $\varphi_k^{N_s}(x)$ denotes the k^{th} thermochemical property at the point x . A trajectory that was obtained with a number N_s of species. $E_k^{N_s}$, a measure of the accumulation of the error along the trajectories for a number N_s of species kept in the kinetics, is defined as:

$$E_k^{N_s} = \left(\frac{\sum_{x=1}^{N_p} (\varphi_k^{\text{Ref}}(x) - \varphi_k^{N_s}(x))^2}{\sum_{x=1}^{N_p} (\varphi_k^{\text{Ref}}(x))^2} \right)^{1/2}, \quad (4.26)$$

where N_p is the number of points along the trajectories, $\varphi_k^{\text{Ref}}(x)$ is the trajectory obtained with the reference detailed chemistry. The mean of the error over all the species are defined for the trajectories with N_s species:

$$E_{\text{mean}}(N_s) = \frac{1}{N_s} \sum_{k=1}^{N_s} E_k^{N_s}. \quad (4.27)$$

A threshold value $E_{s_{\text{mean}}}^{\circ}$ is defined and the number of species N_s is diminished as long as $E_{\text{mean}}(N_s) < E_{s_{\text{mean}}}^{\circ}$. For instance, $E_{s_{\text{mean}}}^{\circ} = 0.05$ would mean that, before optimisation of the constants of the chemical rates, 5% of error in mean in the species mass fraction and temperature is fine. An error that will be reduced by the subsequent optimisation step using a genetic algorithm.

4.4.2 DRGEP for reactions removal

The mechanism is further reduced removing unnecessary reactions. The importance of the j^{th} reaction to the production of the species 'C' linked to the target 'A' is measured with the parameter \mathcal{T}_j from the relation:

$$\mathcal{T}_j = \max(\alpha_{E-A} r_{A-C}^* r_{C,j}), \quad (4.28)$$

As for the number of species, trajectories are systematically re-computed, progressively removing reactions starting from the less important ones (smaller \mathcal{T}_j). The variable $E_k^{N_r}$ representing the cumulated error along the trajectory $\varphi_k^{N_r}(x)$ of the k^{th} species (or temperature) for a number N_r of reactions, is computed from:

$$E_k^{N_r} = \left(\frac{\sum_{x=1}^{N_p} (\varphi_k^{\text{Ref}}(x) - \varphi_k^{N_r}(x))^2}{\sum_{x=1}^{N_p} (\varphi_k^{\text{Ref}}(x))^2} \right)^{1/2}, \quad (4.29)$$

$E_{\text{mean}}(N_r)$ is defined as in (4.27). A number N_r of elementary reactions is kept according to $E_{\text{mean}}(N_r) < E_{r_{\text{mean}}}^{\circ}$, where $E_{r_{\text{mean}}}^{\circ}$ is a threshold value linked to the required precision of the reduced scheme.

4.4.3 Quasi-steady state assumption

The computing cost in reactive flow simulations is mainly controlled by the number of transported species. As discussed above, to avoid carrying on a too large number of species balance equations, an analytical part may be systematically generated in reduced schemes [105, 158]. The concentrations of a subset of species are then obtained from algebraic relations derived from quasi-steady state assumptions. In the present approach, if the integral over the trajectory of the net variation rate of a species is sufficiently small compared to the integral of the maximum between the production rate and the consumption rate of that species, then the species is assumed in quasi-steady state, namely:

$$\mathcal{I}_k = \frac{\left| \int_0^{\infty} \dot{\omega}_k(t) dt \right|}{\max \left(\int_0^{\infty} \dot{\omega}_k^{\text{P}}(t) dt, \int_0^{\infty} \dot{\omega}_k^{\text{C}}(t) dt \right)} < \mathcal{T}_{\text{QSS}}, \quad (4.30)$$

where \mathcal{T}_{QSS} controls the precision of the quasi-steady state assumption that returns linear or non-linear algebraic relations between species concentrations. To avoid the cost of solving iteratively a non-linear system, only the chemical species featuring a linear relationship are assumed in quasi-steady state, others are kept within the transported ones. To preserve the automated character of the method, the algebraic system is cast by the code into a matrix form.

4.4.4 Application

The GRI-1.2 [106, 107] mechanism is used as reference and as a starting point for the present reduction. It is composed of 32 chemical species and 177 reactions. The targets defined to be properly reproduced

by the reduced mechanism are the major species namely O_2 , CH_4 , H_2O , CO and CO_2 . Flame speed and temperature are also properties to be accurately predicted by the reduced scheme.

As described above, the DRGEP approach is first applied to remove the species which are poorly related to the targets. The relation graphs for the 5 targets are given on Figure 4.9, at the point of maximum heat release. For all targets, the interactions of primary importance are with radical species H, O and OH as well as with HCO notably for the production of CO. Obviously, it is observed that CH_4 is strongly related to CH_3 while CO_2 is also strongly connected to the CO species. The error for the reduction is monitored with $E_{\text{mean}}(N_s)$. The mechanism is reduced to 15 species, since $E_{\text{mean}}(15) < 5\%$, while the error goes far above 5% for lower N_s values.

The reactions involving removed species are also eliminated leading to a mechanism composed of 54 reacting steps. It is of interest to further reduce the mechanism in terms of reactions, first because it reduces the calculation time and second because it allows for introducing more quasi-steady state relations while maintaining the system linear, hence easy to solve. To illustrate this last comment, the non-linear interactions between the intermediates of the 54 reactions mechanism are given in Figure 4.10(a). The red numbers refer to a non-linear term introduced because of a concentration exponent different from unity. For instance, the red number for the O-O interaction refers to the forward term of the reaction:



Likewise, the black numbers refer to the non-linear interaction that would appear while introducing quasi-steady state hypotheses for two intermediates coupled within the same forward (or reverse) reaction rate. As another example, the number 1 associated to the HO_2 -HCO interaction within Figure 4.10 corresponds to the right term of reaction:



Because, of this coupling, adding species HO_2 and HCO into quasi-steady state would necessitate the use of a non-linear solver. The error introduced while reducing the number of steps is again controlled so that the mean error stays below 5%. Doing so, the final skeletal mechanism is composed of 15 species and 26 reactions. The list of reactions for this reduced mechanism is given in Table 4.5. The non-linear interactions between the intermediates involved in the 26 reactions mechanism are given in Figure 4.10(b). Interestingly, the number of non-linear limitation is substantially reduced. As introduced by Lu and Law [111], this results from the fact that, because of the low concentrations of the intermediate species, the associated collision frequency is small and the participation of these reactions to the combustion process is often relatively unimportant. Note that, the introduction of quasi-steady state hypotheses requires careful attention, since there are still quite a few restrictions.

The number of transported species is now further reduced, using the quasi-steady state hypothesis. The criteria provided in 4.30 is used to assess the relevance of the application of the QSS assumption for each radical species. It states that the consumption rate of species k must equal its production rate. The evaluation for the entire set of intermediates gives for each \mathcal{I}_k : HCO (0.3%), OH (0.9%), O (1.2%), HO_2 (1.2%), CH_3O (2.8%), H (3.7%), H_2 (4.2%), CH_2O (5.6%), CH_3 (19.1%). Three species are selected, namely HCO, HO_2 and CH_3O which respect $\mathcal{I}_k < 5\%$ and which are linearly coupled within the remaining 26 reactions. The final mechanism necessitates the transport of 12 chemical species (including the inert species N_2), which are involved within 26 steps and require the use of 3 QSS relations. The results with this mechanism are given with the dashed lines of Figure 4.11(a) for the stoichiometric condition of the reduction. The trajectories for the major species are properly recovered, there is however a gap in the reproduction of the levels for the intermediates. An optimisation procedure is finally

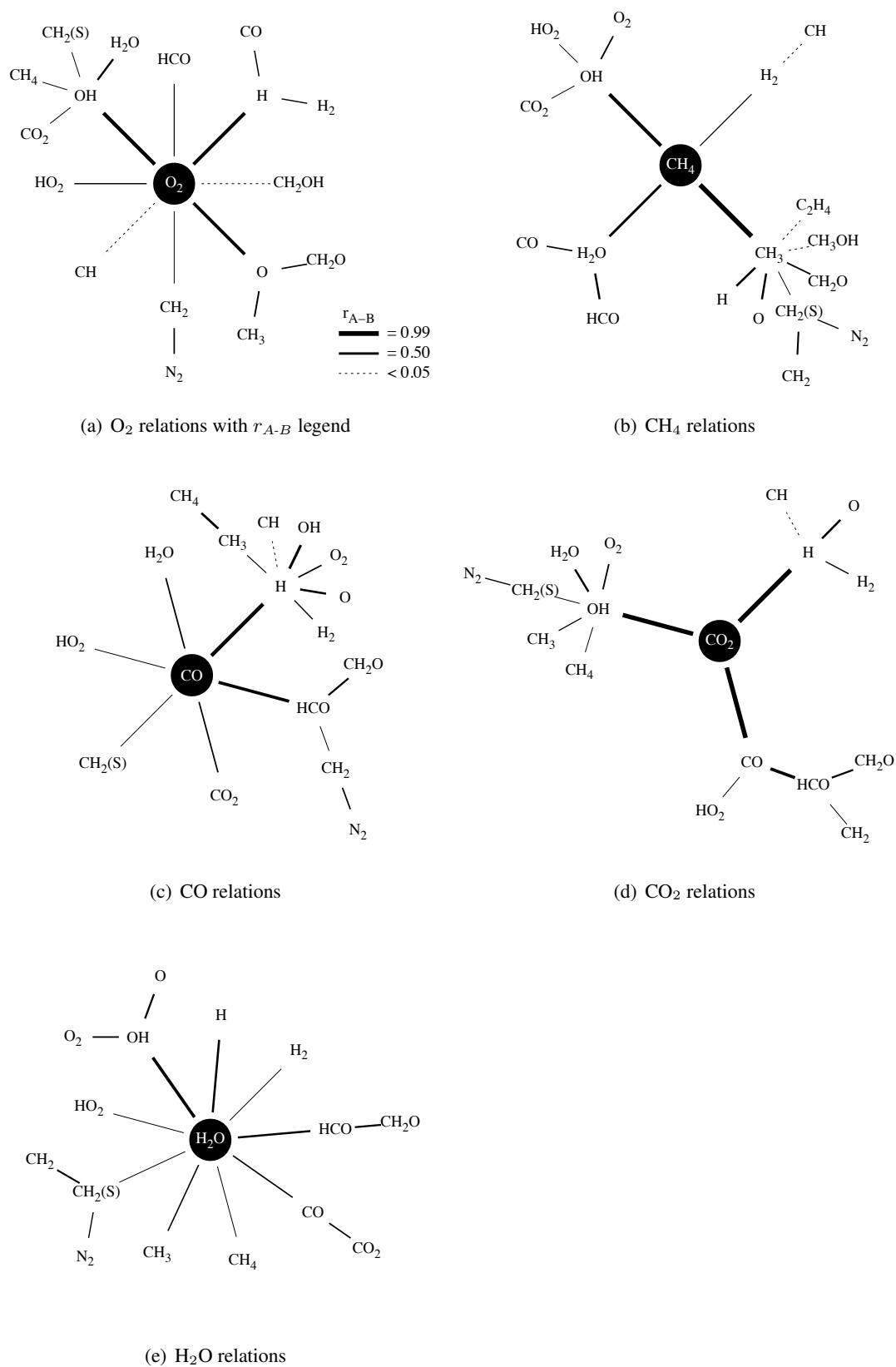


Figure 4.9: Target species relation graphs at maximum heat release. Direct r_{A-B} paths are given according to their amplitude.

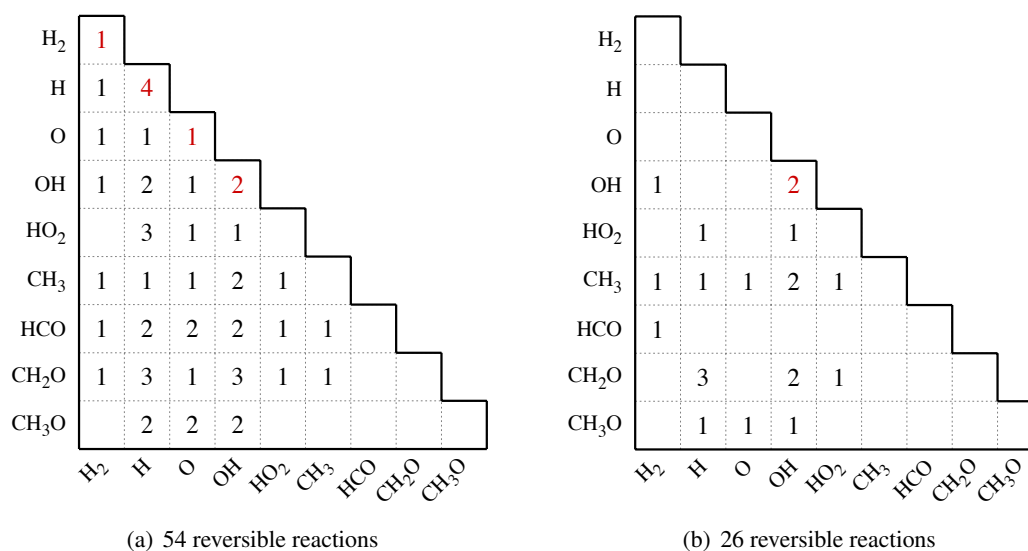


Figure 4.10: Number of non-linear coupling between the intermediate chemical species. Comparison of the interactions before (left) and after (right) the removal of unnecessary reactions.

employed to correct this difference using the Arrhenius terms. The parameters are allowed to vary with $\Delta a_j = \Delta \beta_j = \Delta E_j = 3\%$. The crossover rate is fixed to 75%, the mutation rate to 2%, and a population of 100 chromosomes is considered. The Arrhenius parameters obtained after optimisation are given for each reaction in Table 4.5. The results for the stoichiometric condition used for both reduction and optimisation of the GRI-1.2 mechanism are given with solid lines on Figure 4.11(a). A slightly better reproduction of the major species profiles is now available, while a perfect reproduction of the intermediates is also obtained. Flame velocity along the trajectories and temperature are now also very well reproduced. Although the reduction was performed only for the stoichiometric condition, the properties of a premixed flame at $\phi = 0.7$ are also given in Figure 4.11(b). The profiles for major species and temperature are satisfactory. However, the levels for the intermediates such as H and OH are slightly under predicted hence leading to a lower flame velocity in the burned gases. The equilibrium condition (far from the reactive layer) are nevertheless acceptable.

4.5 Conclusion

By construction, reduced mechanisms cannot be generic and must therefore be created for specific conditions. An attempt to derive a mechanism for premixed methane-air stoichiometric and lean conditions has been proposed to assess the capabilities of some of the methodologies depicted in the literature review. First an optimisation procedure is used to arrange a 3 steps chemical scheme from the literature. No further improvement of the mechanism could be achieved without adding a more detailed chemistry for the interactions with hydro-oxygenated species. Indeed, as reported in the review, the inclusion of the radical species H and OH is of primary importance for recovering the proper flame temperature and velocity. Although the results obtained with this first analysis were encouraging, creating from scratch a reduced mechanism appeared as a complex task. Indeed, selecting the global chemical steps capable of properly describing a process necessitates a detail understanding about kinetics. This is hard to automate. Moreover a poor reproduction of the intermediate species levels was obtained with global

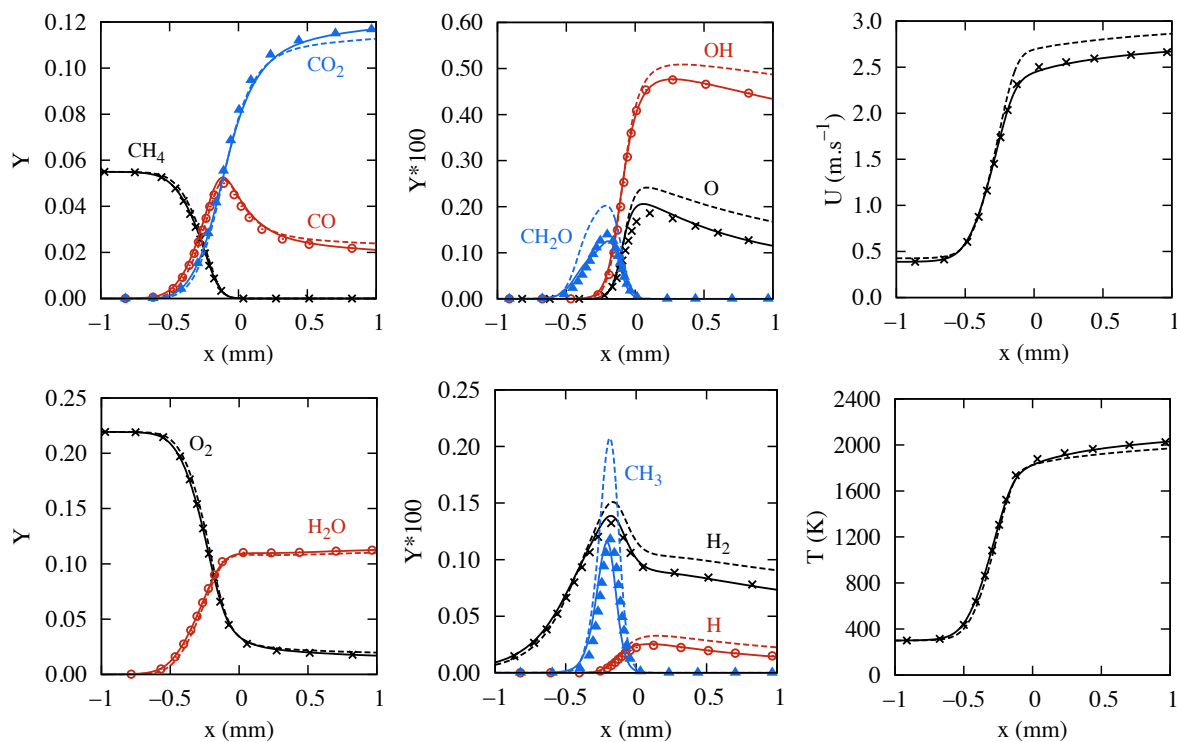
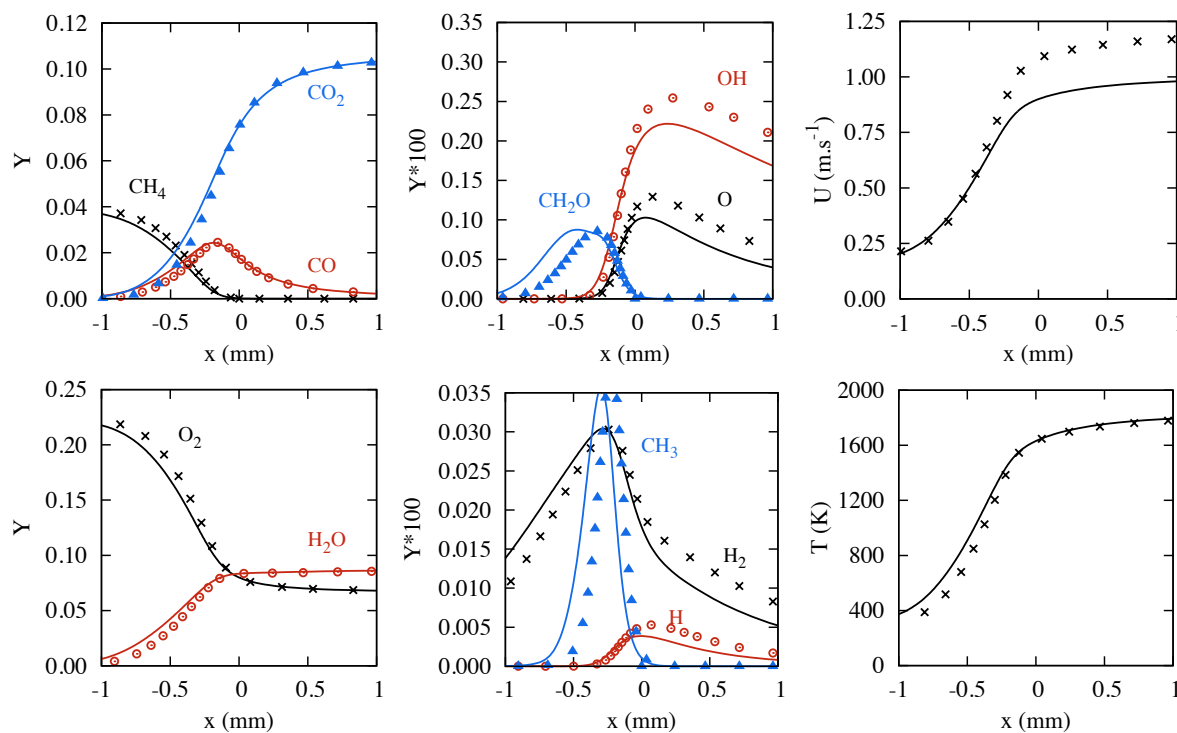
(a) Premixed trajectories $\phi = 1.0$ (b) Premixed trajectories at $\phi = 0.7$

Figure 4.11: Species mass fractions, flame velocity and temperature for equivalence ratios $\phi = 0.7$ and $\phi = 1.0$. Symbols: GRI-1.2 [106, 107]. Dashed lines: Present analytical scheme before optimisation. Solid lines: final analytical scheme (Table 4.5).

#	Reaction		\mathcal{A}^*	β	E^*
1	$\text{O} + \text{CH}_3 \rightleftharpoons \text{H} + \text{CH}_2\text{O}$		1.79e11	0.00	0
2	$\text{O} + \text{CH}_4 \rightleftharpoons \text{OH} + \text{CH}_3$		8.81e05	1.48	8695
3	$\text{H} + \text{O}_2 + \text{M} \rightleftharpoons \text{HO}_2 + \text{M}$		2.40e12	-0.80	0
4	$\text{H} + 2 \text{O}_2 \rightleftharpoons \text{HO}_2 + \text{O}_2$		8.71e13	-1.64	0
5	$\text{H} + \text{O}_2 + \text{H}_2\text{O} \rightleftharpoons \text{HO}_2 + \text{H}_2\text{O}$		1.52e13	-0.69	0
6	$\text{H} + \text{O}_2 + \text{N}_2 \rightleftharpoons \text{HO}_2 + \text{N}_2$		2.03e14	-1.70	0
7	$\text{H} + \text{O}_2 \rightleftharpoons \text{O} + \text{OH}$		8.83e10	0.00	14500
8	$\text{H} + \text{HO}_2 \rightleftharpoons 2 \text{OH}$		1.71e11	0.00	640
9	$\text{H} + \text{CH}_3 (+ \text{M}) \rightleftharpoons \text{CH}_4 (+ \text{M})$	k_0	5.35e13	-0.59	386
		k_∞	2.47e27	-4.76	2440
10	$\text{H} + \text{CH}_4 \rightleftharpoons \text{CH}_3 + \text{H}_2$		7.06e05	1.60	11019
11	$\text{H} + \text{CH}_2\text{O} (+ \text{M}) \rightleftharpoons \text{CH}_3\text{O} (+ \text{M})$	k_0	9.48e08	0.45	2600
		k_∞	2.20e24	-4.80	5560
12	$\text{H} + \text{CH}_2\text{O} \rightleftharpoons \text{HCO} + \text{H}_2$		3.84e07	1.06	3243
13	$\text{H} + \text{CH}_3\text{O} \rightleftharpoons \text{OH} + \text{CH}_3$		3.20e10	0.00	0
14	$\text{OH} + \text{H}_2 \rightleftharpoons \text{H} + \text{H}_2\text{O}$		2.07e05	1.53	3435
15	$2 \text{OH} \rightleftharpoons \text{O} + \text{H}_2\text{O}$		3.70e01	2.40	-2055
16	$\text{OH} + \text{HO}_2 \rightleftharpoons \text{O}_2 + \text{H}_2\text{O}$		5.00e10	0.00	-503
17	$\text{OH} + \text{CH}_4 \rightleftharpoons \text{CH}_3 + \text{H}_2\text{O}$		9.46e04	1.57	3238
18	$\text{OH} + \text{CO} \rightleftharpoons \text{H} + \text{CO}_2$		4.26e04	1.21	70
19	$\text{OH} + \text{CH}_2\text{O} \rightleftharpoons \text{HCO} + \text{H}_2\text{O}$		4.35e06	1.17	-447
20	$\text{HO}_2 + \text{CH}_3 \rightleftharpoons \text{OH} + \text{CH}_3\text{O}$		1.32e10	0.00	0
21	$\text{CH}_3 + \text{O}_2 \rightleftharpoons \text{O} + \text{CH}_3\text{O}$		2.35e10	0.00	29441
22	$\text{CH}_3 + \text{O}_2 \rightleftharpoons \text{OH} + \text{CH}_2\text{O}$		5.12e07	0.00	8580
23	$\text{HCO} + \text{H}_2\text{O} \rightleftharpoons \text{H} + \text{CO} + \text{H}_2\text{O}$		2.60e15	-0.97	17187
24	$\text{HCO} + \text{M} \rightleftharpoons \text{H} + \text{CO} + \text{M}$		6.06e14	-0.94	17336
25	$\text{HCO} + \text{O}_2 \rightleftharpoons \text{HO}_2 + \text{CO}$		7.02e09	0.00	403
26	$\text{CH}_3\text{O} + \text{O}_2 \rightleftharpoons \text{HO}_2 + \text{CH}_2\text{O}$		4.28e-16	7.66	-3640

Table 4.5: Skeletal mechanism with the Arrhenius coefficients optimised to reproduce trajectories computed with the GRI-Mech 1.2 [106, 107]. *Units are mol, s, cm³, cal and K. The Chaperon efficiencies of the GRI-1.2 are preserved for both three-body and fall-off reactions.

chemistry, hence limiting the capabilities of prediction for specific pollutants such as NO_x, and soots.

For these reasons, a strategy to create first skeletal and then analytical schemes was proposed following the conclusions provided in the literature review. A few details about the criterion to select the necessary species and to choose the ones to set into quasi-steady state was then given. To push the reduction further ahead, the limits of traditional DRGEP and QSS approaches were extended. Indeed, it is proposed to correct the introduced error using optimisation. This approach was tested over the same application, and the results showed very good agreement with the reference for both major species, intermediates, flame speed and temperature. This strategy is retained for the rest of the thesis to end up with Optimised Reduced Chemistries (ORChs).

Chapter 5

A new canonical problem for turbulent combustion

Contents

5.1	Introduction	121
5.2	Formalism	122
5.2.1	Lagrangian framework	122
5.2.2	Stochastic mixing of elementary particles	122
5.2.3	Evaporation	123
5.2.4	Deterministic closure	124
5.3	Test under the conditions of a methane-air jet flame in vitiated coflow	125
5.3.1	Problem settings	125
5.3.2	Impact of mixing time and number of particles	126
5.3.3	Global mechanism tests	127
5.3.4	Automated reduction with optimisation of the chemical rates	129
5.3.5	Results in stochastic micro-mixing, premixed and strained diffusion flame	133
5.4	Application to a four-inlet methane/vitiated-air/hydrogen-air/steam problem	140
5.5	Conclusion	141

5.1 Introduction

To set up an automated reduction procedure for chemistry, the reference detailed chemistry must be probed over evolutions from fresh to burnt gases conditions. As already discussed in the literature review, this is usually done following the time or space evolution of the chemical composition in the simulation of homogeneous reactors, one-dimensional premixed or diffusion flames. A slightly different approach is proposed in this chapter, in which it is formally possible to accommodate an unlimited number of inlets and boundary conditions, to cover a wide range of temperatures, equivalence ratios and flow chemical compositions. A stochastic methodology is proposed to generate simulation-relevant trajectories in composition space to be used for both model reduction and validation of the resulting reduced models. This is done aside from any flow simulation.

5.2 Formalism

5.2.1 Lagrangian framework

At initial time, the total mass flow rate \dot{Q}_m is broken down to N_p stochastic particles, each corresponding to an elementary mass flow rate \dot{q}_m .

$$\dot{Q}_m = \dot{q}_m N_p \quad (5.1)$$

Within this representative set of particles, N_{p_j} ones are initiated to the local chemical composition and temperature of the j^{th} inlet according to the mass flow rate \dot{Q}_{m_j} of the inlet j .

$$N_{p_j} = \frac{\dot{Q}_{m_j}}{\dot{q}_m} \quad (5.2)$$

Moreover, some particles are set at the stoichiometric conditions, or other conditions representative of recirculating burnt gases to secure ignition and/or mimic dilution by burnt gases.

Using a Lagrangian framework, the composition of a fluid particle in terms of mass fractions Y_k and sensible enthalpy h_s evolves according to:

$$\frac{d\rho Y_k^L(t)}{dt} = \nabla \cdot \left(\frac{\lambda_{th}}{C_p Le_k} \nabla Y_k^L \right) + \rho \dot{\omega}_k^L \quad \forall k, \quad (5.3)$$

$$\frac{d\rho h_s^L(t)}{dt} = \nabla \cdot (\lambda_{th} \nabla T^L) + \rho \dot{\omega}_{h_s}^L, \quad (5.4)$$

where for each Lagrangian particle, λ_{th} represents the thermal diffusivity, C_p the heat capacity, Le_k and $\dot{\omega}_k^L$ are respectively the Lewis number and the chemical source term of species k and $\dot{\omega}_{h_s}^L$ is the heat source term.

5.2.2 Stochastic mixing of elementary particles

In a turbulent environment, this Lagrangian formalism can take different forms depending on how the molecular diffusion fluxes are modelled. A stochastic modelling of the diffusion fluxes is first introduced, considering a set of particles for each of the j^{th} inlet. It is illustrated on figure 5.1 in which N_f fuel particles are mixed with N_o oxidiser particles and N_b burned gases ones introduced to secure ignition.

The time evolution of the composition of each stochastic particle is piloted by equations (5.5) and (5.6) obtained defining a stochastic turbulent micro-mixing closure referred thereafter as MIX, and parameterised by τ_t , a characteristic turbulent mixing time.

$$\frac{dY_k^p(t)}{dt} = \text{MIX}_k^p(\tau_t) + \dot{\omega}_k^p \quad \forall k, \quad (5.5)$$

$$\frac{dh_s^p(t)}{dt} = \text{MIX}_{h_s}^p(\tau_t) + \dot{\omega}_{h_s}^p. \quad (5.6)$$

In a first attempt the micro-mixing term is modelled using the Curl closure [159]. A pair of particles is selected randomly and their concentrations and enthalpies are estimated from the mean values, i.e.

$$\phi^{p1} = \phi^{p2} = \frac{\phi^{p1} + \phi^{p2}}{2}. \quad (5.7)$$

Molecular differential diffusion effects are thus not accounted for in these equations.

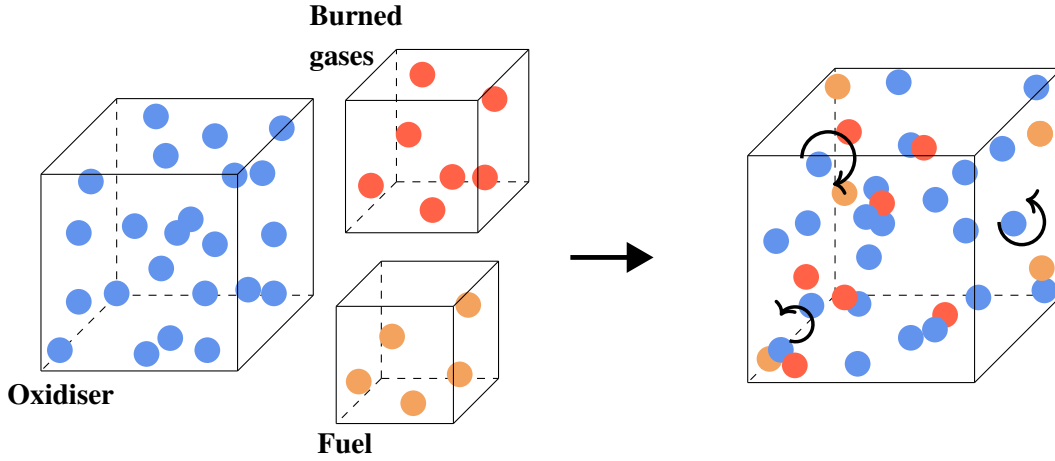


Figure 5.1: Illustration of the stochastic particles distribution and initialisation.

5.2.3 Evaporation

To account for the impact of liquid fuel injection on chemistry reduction, the elementary mass flow rate \dot{q}_m associated to the p^{th} particle may be decomposed into a liquid and a gas phase following Farcy *et al.* [160] so that,

$$\dot{q}_m = \dot{q}_{m_L}^p(t) + \dot{q}_{m_G}^p(t). \quad (5.8)$$

The liquid mass flow rate $\dot{q}_{m_L}^p(t_0) = 0$, for a particle initiated to the conditions of a gaseous inlet while the gas mass flow rate $\dot{q}_{m_G}^p(t_0) = 0$, for a particle corresponding to the spray inlet. $\dot{\omega}_{\nu_k}^p$ is introduced to account for the contribution of the spray evaporation to the increase in the gaseous mass while $\dot{\omega}_{\nu_{h_s}}^p$ quantifies the evaporation source of heat.

$$\frac{dY_k^p(t)}{dt} = \text{MIX}_k^p(\tau_t) + \dot{\omega}_k^p + \dot{\omega}_{\nu_k}^p \quad \forall k, \quad (5.9)$$

$$\frac{dh_s^p(t)}{dt} = \text{MIX}_{h_s}^p(\tau_t) + \dot{\omega}_{h_s}^p + \dot{\omega}_{\nu_{h_s}}^p. \quad (5.10)$$

The Curl closure introduced through equation 5.7, now accounts for the mass of gas mixed, hence species mass fractions and enthalpies after mixing are such that:

$$\phi^{p1} = \phi^{p2} = \frac{\dot{q}_{m_G}^{p1} \phi^{p1} + \dot{q}_{m_G}^{p2} \phi^{p2}}{\dot{q}_{m_G}^{p1} + \dot{q}_{m_G}^{p2}}. \quad (5.11)$$

The spray going through a liquid inlet j is assumed to be composed of \dot{n}_j spherical droplets initiated to the same diameter $d_j(t_0)$. The amount of droplets \dot{n}_j carried by each stochastic particle is deduced from the elementary mass flow rate \dot{q}_m , so that:

$$\dot{q}_m = \dot{n}_j \rho_L \frac{\pi}{6} d_j^3(t_0), \quad (5.12)$$

where ρ_L stands for the liquid density. Droplets are assumed to be above the liquid boiling point, hence the decrease in diameter is computed through the d^2 -law [161] using a characteristic time τ_{v_j} which depends on droplets size and composition and on the ambient conditions.

$$d_j(t) = d_j(t_0) \left[1 - \frac{t}{\tau_{v_j}} \right]^{\frac{1}{2}}. \quad (5.13)$$

Using the d^2 -law, the initial size of a droplet defines its lifetime. Each droplet has been given the same initial size. This may be improved in the future by studying the impact of the size of the droplets on the obtained trajectories, and reduced mechanism. A Probability Density Function may also be used to get a more realistic distribution of the size of the particles. It is however expected that this would have a low impact on the results and therefore it is not considered in this first approach.

The balance between the liquid and the gaseous mass flow rates for the particle p is expressed as a function of the phase change for all the transported species:

$$\dot{q}_{m_G}^p(t + \delta t) = \dot{q}_{m_G}^p(t) + \sum_{k=1}^{N_{sp}} \dot{n}_j \dot{W}_{\nu_k}^p(t) \delta t, \quad (5.14)$$

$$\dot{q}_{m_L}^p(t + \delta t) = \dot{q}_{m_L}^p(t) - \sum_{k=1}^{N_{sp}} \dot{n}_j \dot{W}_{\nu_k}^p(t) \delta t, \quad (5.15)$$

where $\dot{W}_{\nu_k}^p(t)$ represents the mass of liquid of the k^{th} component that is released during δt . It is expressed from the variation of the volume of the droplets, through the relation:

$$\dot{W}_{\nu_k}^p(t) = Y_{k,L}^p(t) \rho_L \frac{\pi}{6} \left[\frac{d_j^3(t) - d_j^3(t + \delta t)}{\delta t} \right]. \quad (5.16)$$

For each p^{th} particle associated to the j^{th} inlet, the source term of gas release for the species k and for the enthalpy are respectively expressed through the relations 5.17 and 5.18 (for more details, see [160]):

$$\dot{\omega}_{\nu_k}^p(t) = \frac{1}{\delta t} \left[\frac{\dot{q}_{m_G}^p(t) Y_{k,G}^p(t) + \dot{n}_j \dot{W}_{\nu_k}^p(t) \delta t}{\dot{q}_{m_G}^p(t + \delta t)} - Y_{k,G}^p(t) \right], \quad (5.17)$$

$$\dot{\omega}_{h_s}^p(t) = \frac{1}{\delta t} \left[\frac{\dot{q}_{m_G}^p(t) h_s^p(t) + \sum_{k=1}^{N_{sp}} \dot{n}_j \dot{W}_{\nu_k}^p(t) [h_k(T_B) - \mathcal{L}_{\nu_k}] \delta t}{\dot{q}_{m_G}^p(t + \delta t)} - h_s^p(t) \right]. \quad (5.18)$$

where T_B refers to the boiling temperature of the liquid considered and \mathcal{L}_{ν_k} is the corresponding latent heat of evaporation.

5.2.4 Deterministic closure

The optimisation of a reduced chemistry over all the stochastic particles considered is not an option because of obvious computing time limitations. Another model problem may be obtained from equations (5.3) and (5.4) after expressing the diffusive budget with a deterministic micro-mixing closure, as the linear relaxation model (IEM or LMSE), parameterised with τ_t [126, 162]:

$$\frac{dY_k^L(t)}{dt} = \frac{\langle Y_k \rangle(t) - Y_k^L(t)}{\tau_t} + \dot{\omega}_k^L, \quad (5.19)$$

$$\frac{dh_s^L(t)}{dt} = \frac{\langle h_s \rangle(t) - h_s^L(t)}{\tau_t} + \dot{\omega}_{h_s}^L, \quad (5.20)$$

where $\langle \cdot \rangle(t)$ denotes a mean value seen at time 't' by the traveling particles. When the time evolving mean values are known, the deterministic chemical trajectories are obtained, starting from each inlet and ending at the equilibrium condition ($t \rightarrow \infty$). The time evolution of the mean gaseous composition of the flow surrounding the deterministic reference trajectories is obtained by solving for the ensemble

of stochastic particles. This mean composition is computed for each species mass fraction and for the enthalpy considering only the gaseous phase. The subsequent relations are used:

$$\langle Y_k \rangle (t) = \frac{\sum_{p=1}^{N_P} \dot{q}_{m_G}^p(t) Y_k^p(t)}{\sum_{p=1}^{N_P} \dot{q}_{m_G}^p(t)}, \quad (5.21)$$

$$\langle h_s \rangle (t) = \frac{\sum_{p=1}^{N_P} \dot{q}_{m_G}^p(t) h_s^p(t)}{\sum_{p=1}^{N_P} \dot{q}_{m_G}^p(t)}. \quad (5.22)$$

In the following, the two systems of equations, (5.19) to (5.20) for the reference trajectories, and, (5.5) to (5.6) for the stochastic particles, are thus coupled through the relations (5.21) to (5.22) to be simultaneously advanced in time. Varying the inlet properties and the time evolution of the mean values, a large range of operating conditions may be covered at once by chemical trajectories.

5.3 Test under the conditions of a methane-air jet flame in vitiated coflow

5.3.1 Problem settings

The building of the chemical trajectories are illustrated under the conditions of the Cabra *et al.* non-premixed jet flame [163] (see Table 5.1), therefore in the simple form of a two-inlet single phase problem to begin with. Two trajectories are obtained starting from a rich ($\phi = 4.4$) premixed methane-air mixture at 320K, and, the burnt products of a lean hydrogen/air combustion at 1350 K. The trajectory issued from the fuel stream will cover an equivalence ratio range decreasing from $\phi = 4.4$ to $\phi = 1$, and the one from the vitiated-air stream an equivalence ratio increasing from $\phi = 0$ to $\phi = 1$. This choice of the two streams evolving up to the stoichiometric condition was made to focus on the dynamics of fluid particles that would travel from the fuel and the co-flow streams to mix and react in the vicinity of the flame surface. At initial time, to secure ignition, particles are added at the chemical equilibrium

	T (K)	Y _{O₂}	Y _{N₂}	Y _{H₂O}	Y _{CH₄}
Fuel jet	320	0.194	0.589	0.00211	0.214
Coflow	1350	0.142	0.757	0.100	0.000178

Table 5.1: Conditions for the methane-air jet flame in vitiated coflow study [163]. T: Temperature, Y_k : Species k mass fraction.

condition at $\phi = 1$, for a number of particles of about 4% of the total number N_P . Varying this number up to 8% of N_P does not affect the results. Figure 5.2(a) depicts this initial composition of the particles in a temperature versus mixture fraction diagram. The time evolution of the stochastic particles and of the associated deterministic trajectories is then showed on plots 5.2(b)-5.2(d) following respectively Eqs. (5.5) to (5.6) for the particles and Eqs. (5.19) to (5.20) for the reference trajectories. Both the theoretical mixing and the equilibrium lines appear to be followed by the stochastic particles. Figure 5.3 shows the scatter plots of major species and temperature built from the stochastic particles. These scatter plots contain particles sampled every millisecond. As also reported experimentally [163], the particles undergo a large variety of equivalence ratios, flow composition and temperature.

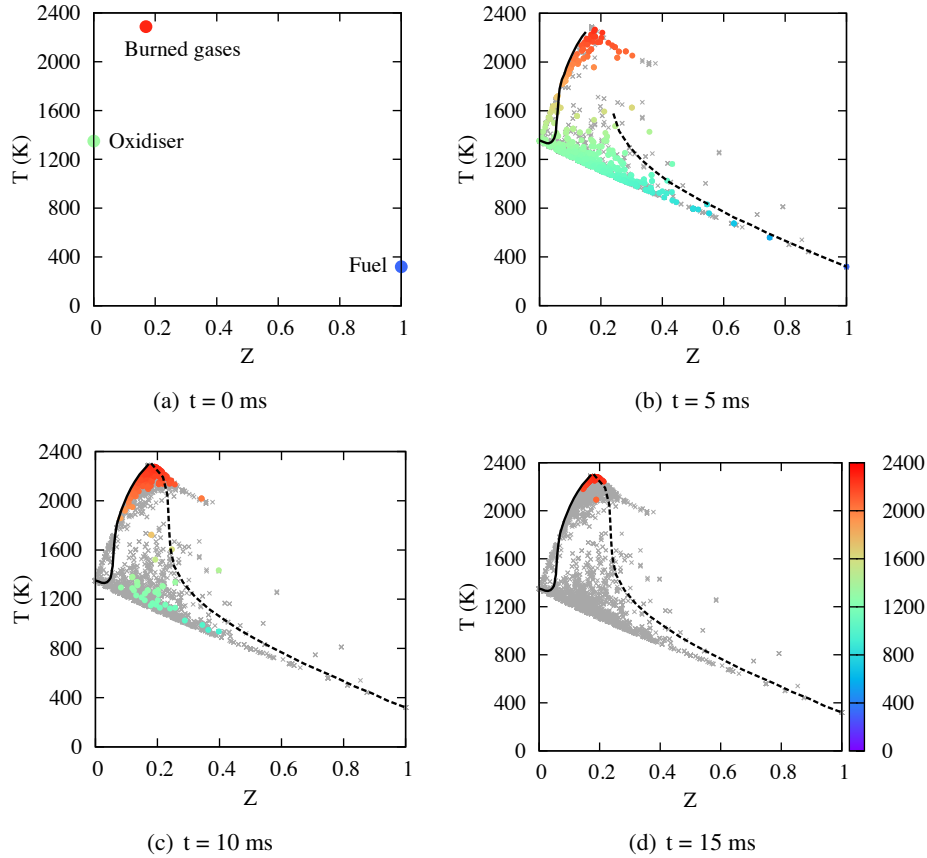


Figure 5.2: Time evolution of the particles (Eqs. (5.5) to (5.6)) coloured by temperature and of the associated deterministic trajectories (Eqs. (5.19) to (5.20)). Both are expressed in a temperature versus mixture fraction diagram. Solid line: oxidiser trajectory. Dashed line: fuel trajectory. GRI-3.0 mechanism, non-premixed methane vitiated-air conditions of Table 5.1. Grey crosses show the history of the conditions faced by the particles.

5.3.2 Impact of mixing time and number of particles

Information on the time-history of turbulent micro-mixing has been extracted from previous LES of the same burner [164], leading to an average value of the micro-mixing time $\tau_t = 2$ ms. The impact of varying the value of the mixing time is shown in Fig. 5.4, for representative trajectories issued from the fuel-jet. As expected, decreasing the mixing time leads to faster ignition. Nevertheless, the major ingredient for chemistry reduction, *i.e.* the range of values covered by the species concentrations, weakly varies with τ_t . In the following, the value $\tau_t = 2$ ms is retained for performing the chemistry reduction. It is subsequently verified that varying this value does not impair the prediction of the reduced scheme, when compared to the detailed one. The number of stochastic particles has also been varied, it is shown in Fig. 5.5 that above 500 particles, increasing further the number of particles does not impact much on the results, this value is then retained.

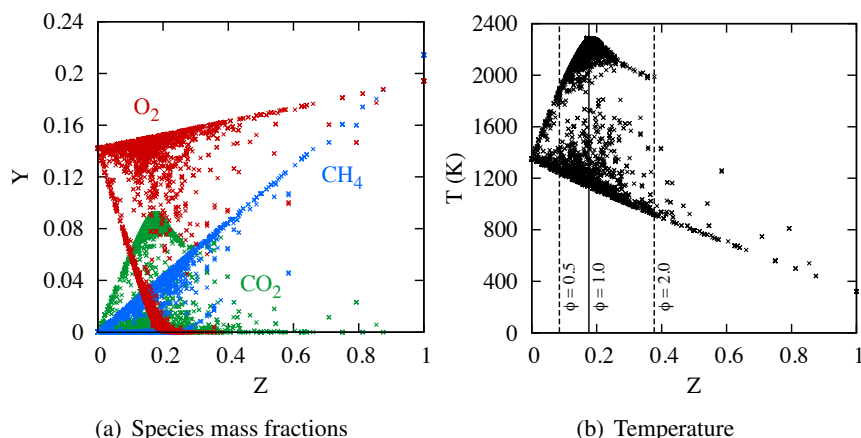


Figure 5.3: Scatter plots of major species mass fractions and temperature versus mixture fraction (Eqs. (5.5) and (5.6)). GRI-3.0 mechanism, non-premixed methane vitiated-air conditions of Table 5.1. ϕ : Equivalence ratio.

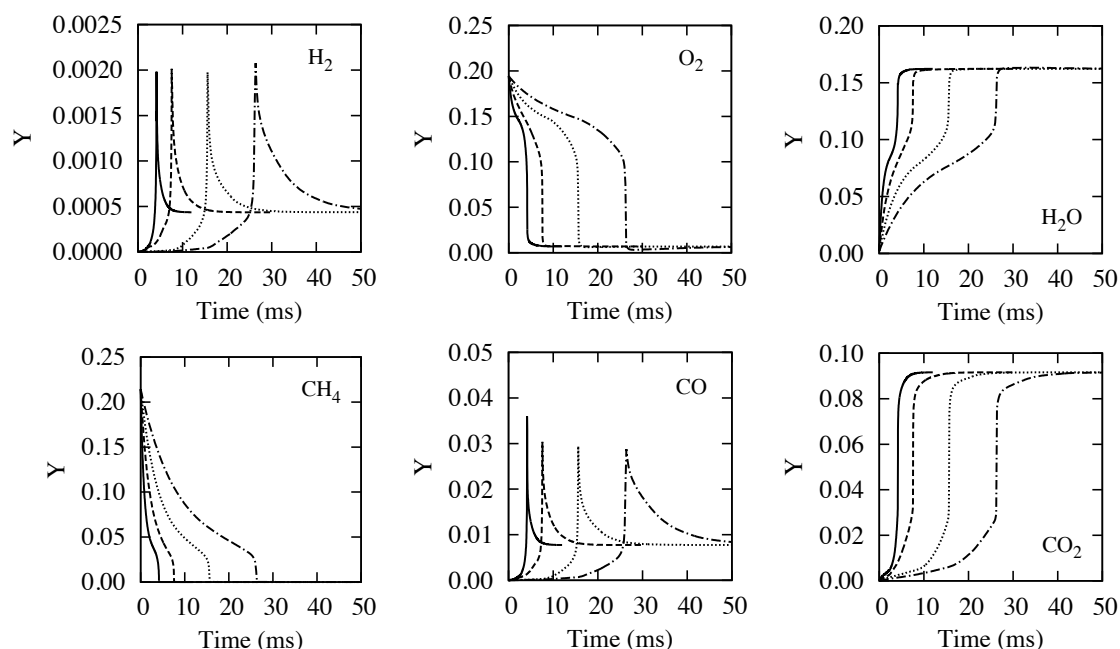


Figure 5.4: Trajectories mass fractions vs time issued from fuel-jet (Eqs. (5.19) to (5.20)). Solid line: $\tau_t = 0.8\text{ms}$. Dashed line: $\tau_t = 2\text{ms}$. Dotted line: $\tau_t = 4\text{ms}$. Dashed-dotted lines: $\tau_t = 8\text{ms}$.

5.3.3 Global mechanism tests

The evolution of major species are presented in Fig. 5.6 for the reference detailed mechanism [140] and the four-step global mechanism by Jones and Lindstedt [67], both trajectories issued from fuel-jet and vitiated-air are displayed. Interestingly, this global mechanism, which was performing quite well in the one-dimensional premixed flame (Fig. 3.16), loses its prediction capabilities along the trajectories. In particular, for CO and CO₂, the trajectories which should be very close to each other, due to micro-mixing effects (bottom of Fig. 5.6), become separated due to too early ignition. This could be expected, since this mechanism was calibrated against laminar premixed flames. Moreover, with the four-step

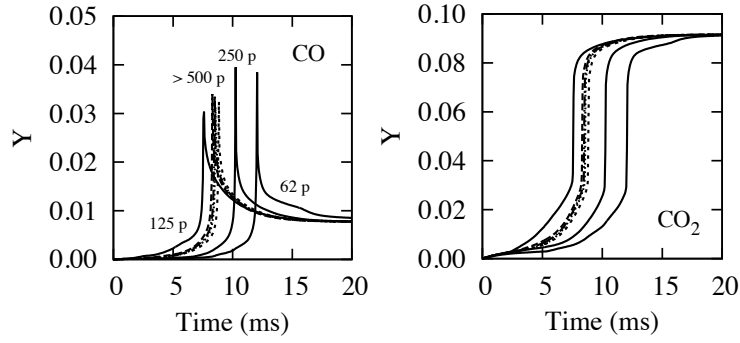


Figure 5.5: CO (left) and CO₂ (right) mass fractions vs time issued from fuel-jet (Eqs. (5.19) and (5.20)) for various N_T (Eqs. (5.5) and (5.6)), GRI-3.0 detailed mechanism. Solid lines: $N_P = 62$ up to $N_P = 250$ particles. Dashed lines $500 < N_P < 1500$. $\tau_t = 2$ ms.

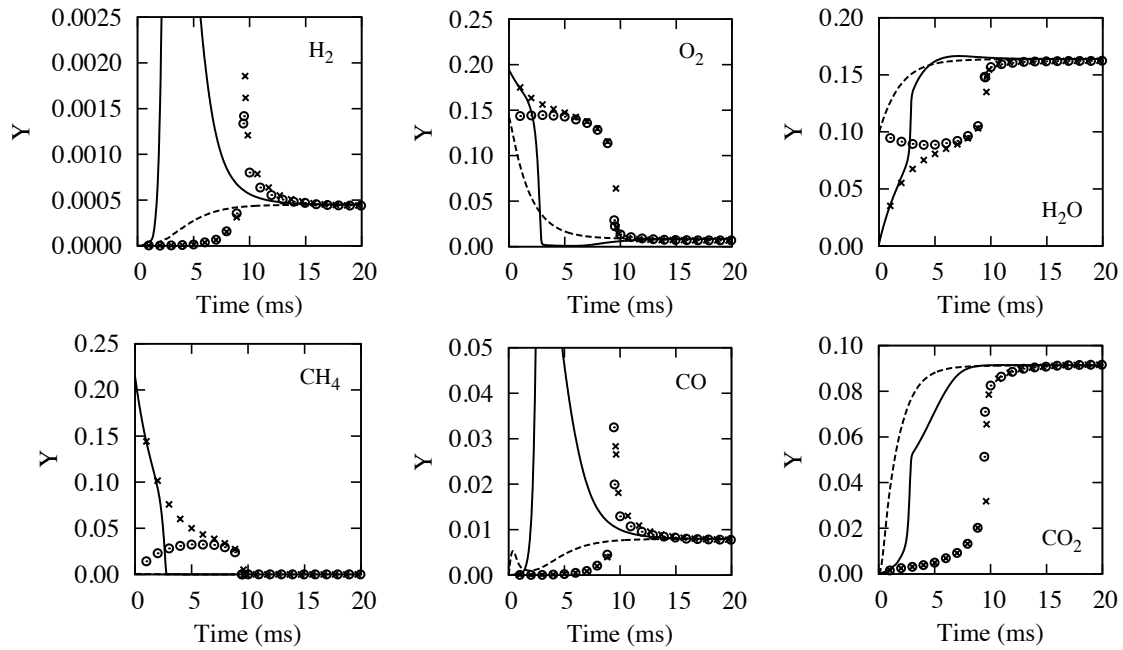


Figure 5.6: Trajectories (Eqs. (5.19) and (5.20)), four-step Jones and Lindstedt [67] and GRI-3.0 detailed mechanism [140]. Fuel-jet trajectory, solid-line: Four-step, (x): GRI-3.0. Coflow-jet (vitiated-air) trajectory, dashed-line: Four-step, (o): GRI-3.0.

mechanism by Peters considered in the literature review [138], along the trajectories, it was found that the concentration in H radical present in the quasi-steady state relations was always too small, leading to spurious quenching. Hence, it is legitimate to wonder:

1. Whether a reduced mechanism could be derived fitted on such trajectories, which intend to be representative of the interaction between turbulent-mixing and reaction?
2. How the resulting mechanism would respond applied back to the simulation of the same trajectories?
3. How the resulting mechanism would respond applied to the simulation of laminar premixed flames, for fresh gases at various equivalence ratios?

4. How the resulting mechanism would respond applied to the simulation of laminar diffusion flames, in counter-flowing jets of methane against vitiated-air and for various strain rates, up to diffusion-flamelet quenching?
5. In the case of departure from the reference premixed flame or/and micro-mixing solutions, is it possible to automatically optimise the rate of the reduced scheme, to match the detailed chemistry response?

These five questions are now addressed.

5.3.4 Automated reduction with optimisation of the chemical rates

Starting from the detailed mechanism and the evolution of the species concentrations and temperature as defined above, three steps are now performed to end-up with an optimised and reduced chemical kinetics. DGREP and QSS are applied to the one-dimensional trajectories only ((Eqs. 5.19) and (5.20)), but during the re-computation of the trajectories with less and less species and reactions and also during the optimisation loop discussed thereafter, the reduced model is applied to all the stochastic particles ((Eqs. 5.5) and (5.6)), which drive the deterministic trajectory. For large reductions, in the case of lack of convergence of the optimisation loop, it is observed that the chemistry is in fact not adapted for a too large number of the considered N_P stochastic particles.

5.3.4.1 Application of DRGEP and QSS

Once defined a set of target chemical species, whose concentrations should be well approximated by the reduced scheme, the Directed Relation Graph with Error Propagation approach (DRGEP) is applied. To stay within the context of the chemical schemes discussed so far, the target species retained here are: CH₄, O₂, CO, CO₂, H₂O and H₂. Figure 5.7 illustrates the behavior of the r_{A-B} coefficients by displaying the species related to CH₄ at two representative times. Whatever the starting point of the trajectory (fuel-jet or vitiated-air), it is seen that the species in the first layer of interaction are the same, *i.e.* OH, H₂O and CH₃. While the relative position of other species, such as HCO, moves between $t = 2.5$ ms and $t = 5$ ms, from an outer layer (*i.e.* a weak interaction zone, $r_{A-B} < 0.05$ in Fig. 5.7(c)) to an intermediate layer of interaction ($r_{A-B} \approx 0.1$ in Fig. 5.7(d)).

The two steps (DRGEP and QSS) are applied to the chemical response along the trajectories (Equations (5.19) and (5.20) with $E_{\text{mean}}(N_S) = 8\%$, $E_{\text{mean}}(N_R) = 4\%$ and $\mathcal{T}_{\text{QSS}} = 7\%$), leading to a reduced scheme with 16 species, among which 13 are transported with the flow: the six target species, CH₄, O₂, CO, CO₂, H₂O and H₂, to which H, O, OH, CH₃, CH₂O and C₂H₆, N₂ are added; while HO₂, HCO and CH₃O are obtained from analytical relationships. These species participate to 46 elementary reactions, which are given in Table 5.2. At this stage, the constants of the rates are still those of the GRI-3.0 mechanism. Figures 5.8(a) and 5.8(b) (dotted line) compare the chemical trajectories obtained with this preliminary reduced scheme (DRGEP+QSS) against the detailed chemistry response (symbols). The reduced scheme overestimates the ignition delay and peak values of intermediates are not captured, see dotted lines in Figs 5.9(a) and 5.9(b).

Because high temperature chemistry is correctly described, the very same reduced scheme applied to freely propagating premixed flames, does quite well for the stoichiometric case, as seen in Fig. 5.10(a) (dotted-line). The fresh gases composition of these flames results from the premixing of the two, methane and vitiated-air, inlet conditions. Lean cases are not considered for premixed flames because of the

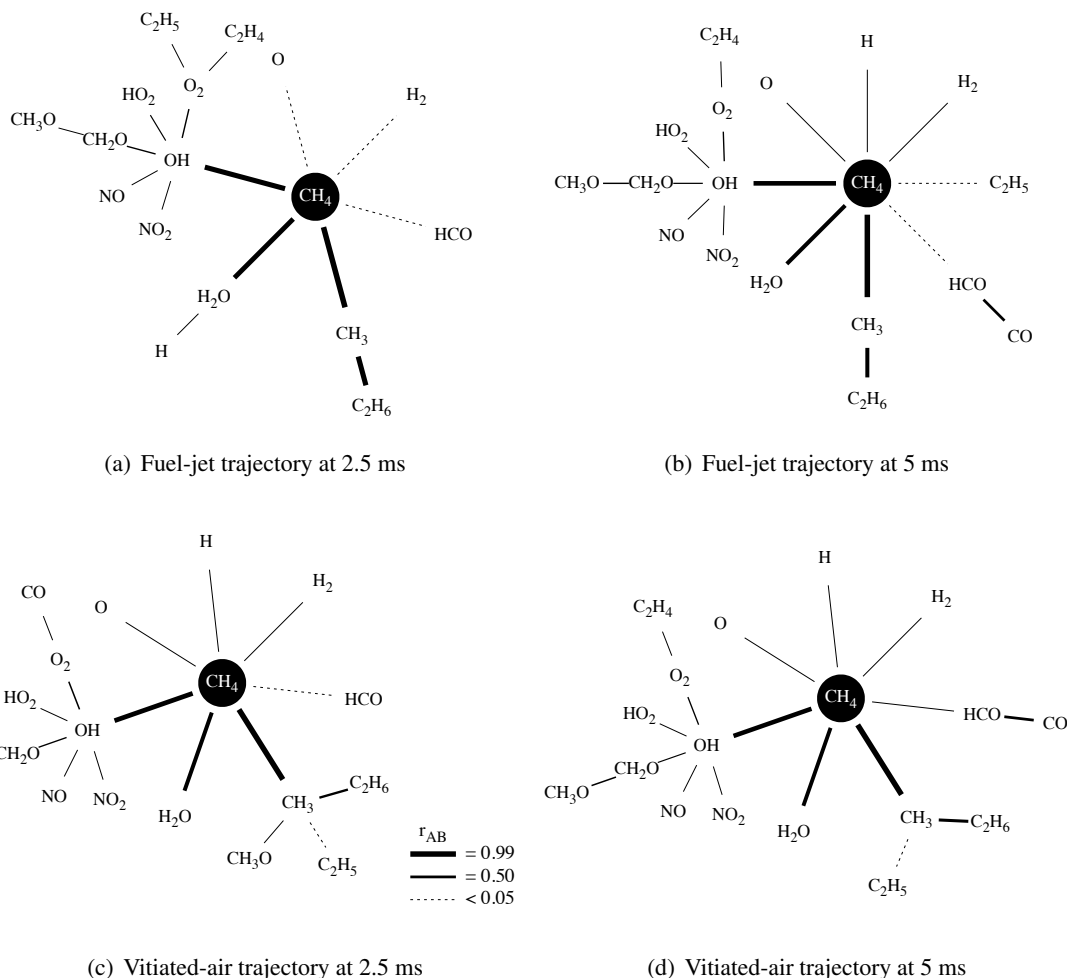


Figure 5.7: Visualisation of species interrelations for the two trajectories. Direct r_{A-B} paths are plotted according to their amplitude.

occurrence of fast auto-ignition with vitiated-air. However, for larger equivalence ratios, the departure is more pronounced, see for instance dotted line in Fig. 5.10(c) for major species and in Fig. 5.11 for the minor ones. Moreover, the velocity profiles through the flame, and thus the flame speed, are not captured by this preliminary scheme, see dotted line in Fig. 5.10. Indeed, there is nothing in the species trajectories based on the turbulent micro-mixing closures to account for the existence of an eigenvalue giving the speed of propagation of the laminar flame into the unburned gases.

Diffusion flames are shown in Fig. 5.13 for the same reduced kinetics. The simulation of counter-flowing jets of methane against vitiated-air is performed with the one-dimensional flame solver REGATH [165]. A very low level of strain rate $a_T = 20 \text{ s}^{-1}$, corresponding to an almost unstrained diffusion flame, and, a higher level $a_T = 769 \text{ s}^{-1}$, are considered. Quite good predictions are already reported with this preliminary mechanism, with only some departure on the max level of CO (Fig. 5.13).

This suggests that the stochastic problem with micro-mixing, covering a large range of equivalence ratios and temperatures, and the prediction of the flame speed are more demanding than the counter-flowing diffusion flamelets, at least for these methane/vitiated-air conditions. An additional optimisation step is thus required, to perfectly match the detailed chemistry response, in terms of flame speed and for

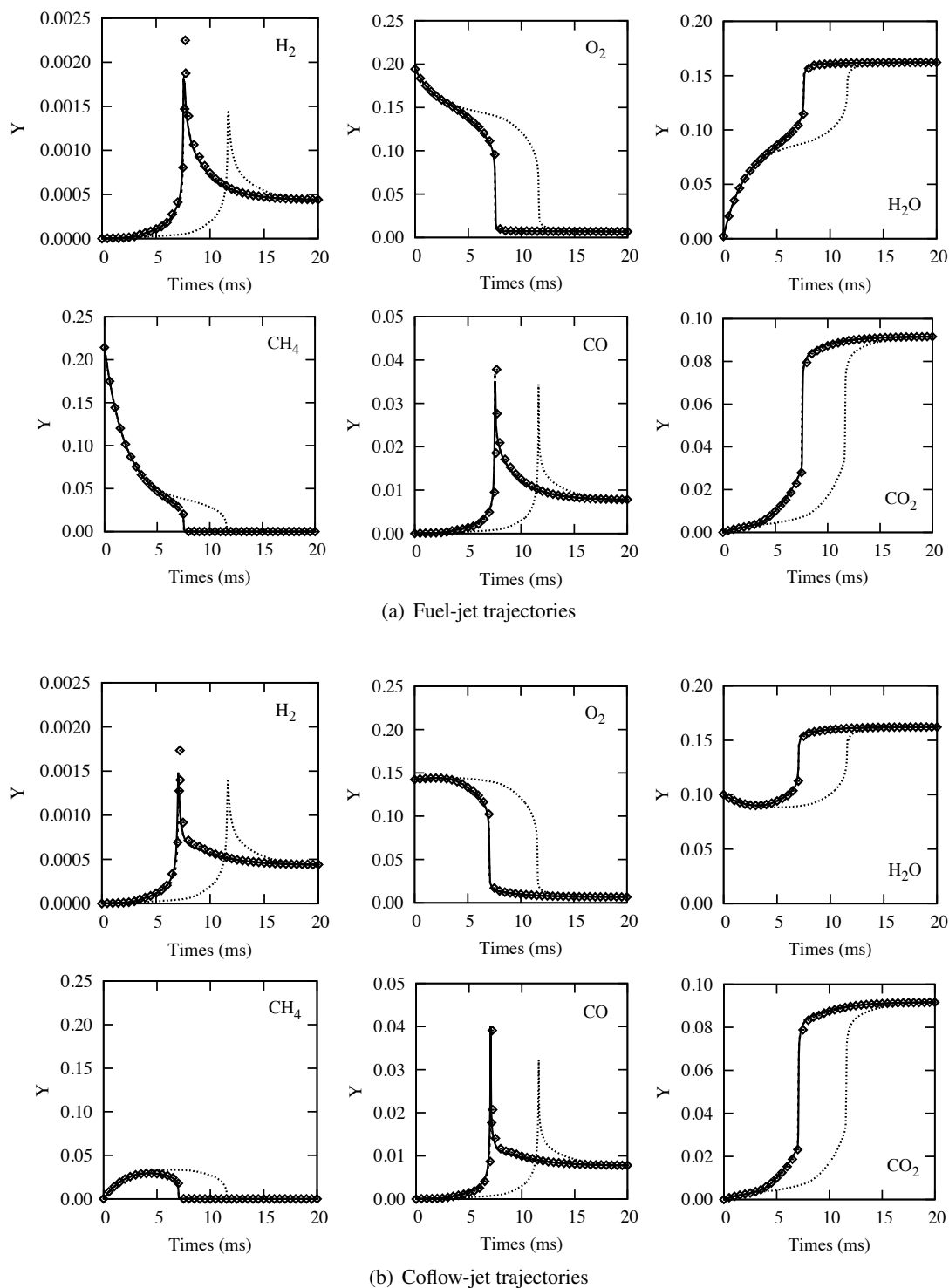
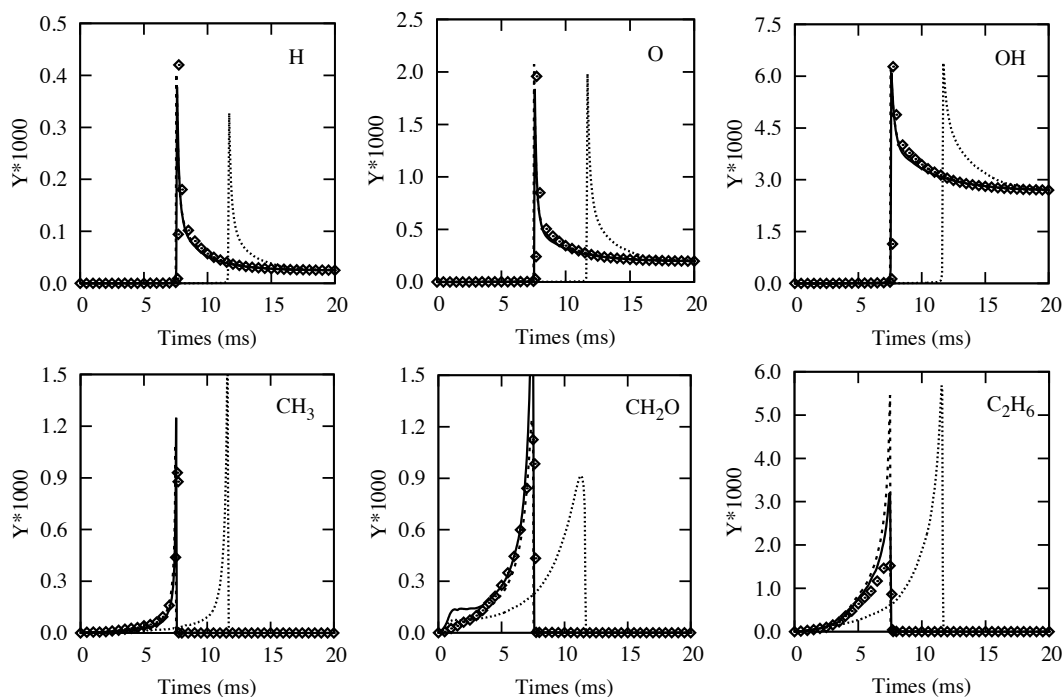
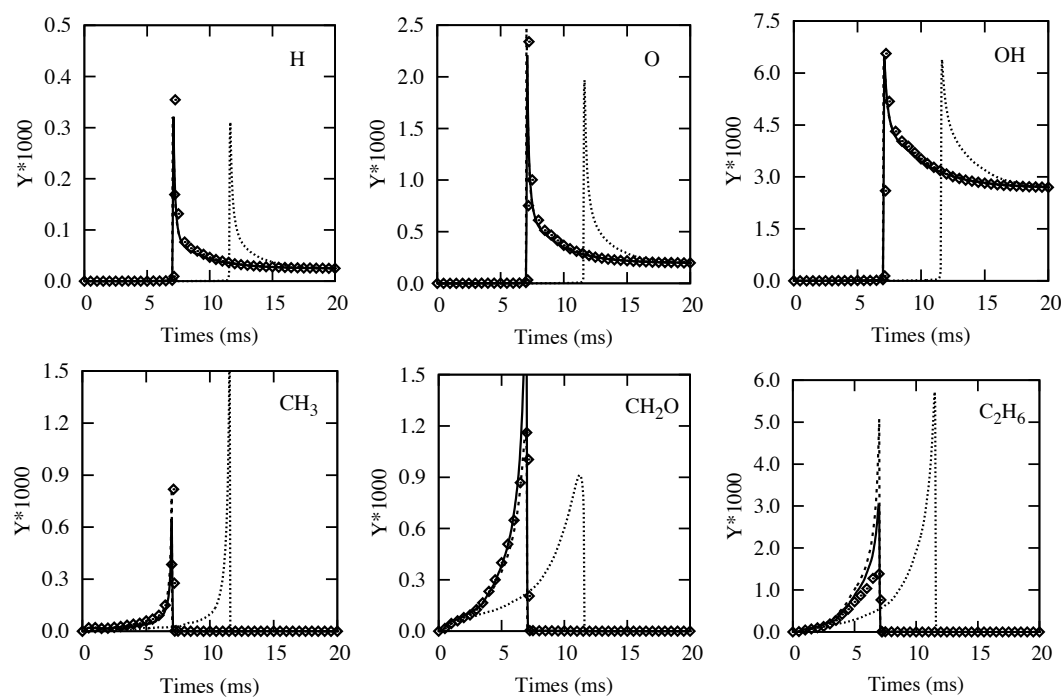


Figure 5.8: Deterministic trajectories (Eqs. (5.19)-(5.20)). $\tau_t = 2$ ms. Major species. Symbols: Detailed reference (GRI-3.0). Dotted-line: Preliminary reduced mechanism (DRGEP+QSS). Dashed-line: Micro-mixing optimised (DRGEP+QSS+GA micro-mixing trajectories). Line: Fully optimised (DRGEP+QSS+GA micro-mixing trajectories+premixed flames, Table 5.2).



(a) Fuel-jet trajectories



(b) Coflow-jet trajectories

Figure 5.9: Deterministic trajectories (Eqs. (5.19)-(5.20)). $\tau_t = 2$ ms. Minor species. Symbols: Detailed reference (GRI-3.0). Dotted-line: Preliminary reduced mechanism (DRGEP+QSS). Dashed-line: Micro-mixing optimised (DRGEP+QSS+GA micro-mixing trajectories). Line: Fully optimised (DRGEP+QSS+GA micro-mixing trajectories+premixed flames, Table 5.2).

all the conditions of the micro-mixing trajectories. This optimisation step is now completed using the genetic algorithm approach depicted earlier.

5.3.4.2 Optimisation of the chemical rates

The optimisation of the parameters of the chemical rates (\mathcal{A}_j , β_j and E_{a_j} in relation (4.6)) is now applied to the scheme of Table 5.2 derived after DRGEP and QSS. For the micro-mixing optimised scheme (DRGEP+QSS+GA micro-mixing trajectories), the reference solution is composed of the two micro-mixing trajectories obtained above with the GRI-3.0 mechanism (see symbols in Figs. 5.8(a) and Fig. 5.8(b)). For the fully optimised scheme (DRGEP+QSS+GA micro-mixing trajectories+premixed flames), the premixed flame profiles (species, temperature and velocity) are added (symbols in Figs. 5.10).

The fitness function

$$f(\mathcal{C}^m) = - \sum_{n=1}^{n_I} \sum_{\ell=1}^{N_\ell} \left[\sum_{k=1}^{N_v} \left| \frac{\varphi_k^{\text{Ref}}(t^\ell, n) - \varphi_k(t^\ell; \mathcal{C}^m, n)}{\varphi_k^{\text{Ref}}(t^\ell, n)} \right| \right], \quad (5.23)$$

is computed for every chromosome \mathcal{C}^m , where $\varphi_k(t^\ell)$ denotes the values of N_v variables (concentrations, enthalpy, or any useful quantity) computed in the model problem and that should be reproduced by the reduced scheme. In the present case, the parameters entering the fitness function are the mass fractions and the temperatures along the micro-mixing trajectories, to derive a first micro-mixing optimised reduced scheme (DGREP+QSS+GA micro-mixing trajectories). The species and the velocity profiles across the premixed flames are then added to the fitness function, to generate a second and fully optimised scheme (DGREP+QSS+GA micro-mixing trajectories+premixed flames). For these premixed flames, x^ℓ , the position through the flame replaces t^ℓ in above equations. (The diffusion flame profiles are not included.) φ_k^{Ref} are the detailed chemistry reference values.

5.3.5 Results in stochastic micro-mixing, premixed and strained diffusion flame

The genetic algorithm is parallelised and it takes about 2 hours to get a perfectly converged solution on an IBM iDataPlex type machine using 96 processors. The number of chromosomes equals the number of processors, $M = 96$, and for this case $2M$ trajectories are computed simultaneously over M processors.

5.3.5.1 Application to the two-inlet methane/vitiated-air problem

The application of the genetic algorithm to optimise the rates of the reduced scheme derived from directed relation graph with error propagation and quasi-steady state leads to the values of the chemical parameters given in Table 5.2, when both the micro-mixing trajectories and the premixed flames are included as target of the genetic algorithm. As already indicated above, another scheme was also derived without including the premixed flames as target. These simplified chemistries reproduce well the two trajectories from the fuel-jet and vitiated-air inlets (dashed and solid lines in Figs. 5.8(a) and 5.8(b)). Intermediate radical species, which were not included as target species during the reduction nor in the fitness function (relation 5.23), are also reasonably captured, as seen in dashed and solid lines of Figs. 5.9(a) and 5.9(b).

The reduction and optimisation procedure was conducted for a fixed value $\tau_t = 2$ ms. It is therefore necessary to test the obtained chemical kinetics with a different mixing time, this is done in Fig. 5.12 for $\tau_t = 8$ ms. For this four times larger mixing time, the two trajectories issued from the fuel and vitiated-air inlets behave differently. The mixing time being larger, the relative influence of micro-mixing is lessened and the trajectories stay separated longer in time, but all species are still very well reproduced.

#	Reaction	\mathcal{A}^*	β	E^*
1	$\text{O} + \text{H}_2 \rightleftharpoons \text{H} + \text{OH}$	4.1065e+04	2.685	6166.28
2	$\text{O} + \text{HO}_2 \rightleftharpoons \text{OH} + \text{O}_2$	3.3374e+13	0	0
3	$\text{O} + \text{CH}_3 \rightleftharpoons \text{H} + \text{CH}_2\text{O}$	1.3273e+14	0	0
4	$\text{O} + \text{CH}_4 \rightleftharpoons \text{OH} + \text{CH}_3$	5.3275e+08	1.449	8356.70
5	$\text{O} + \text{HCO} \rightleftharpoons \text{OH} + \text{CO}$	2.4038e+13	0	0
6	$\text{O} + \text{HCO} \rightleftharpoons \text{H} + \text{CO}_2$	5.7415e+13	0	0
7	$\text{O} + \text{CH}_2\text{O} \rightleftharpoons \text{OH} + \text{HCO}$	3.9937e+13	0	3687.39
8	$\text{O} + \text{CH}_3\text{O} \rightleftharpoons \text{OH} + \text{CH}_2\text{O}$	1.2294e+13	0	0
9	$\text{O}_2 + \text{CH}_2\text{O} \rightleftharpoons \text{HO}_2 + \text{HCO}$	5.2658e+13	0	41441.70
10	$\text{H} + \text{O}_2 + \text{M} \rightleftharpoons \text{HO}_2 + \text{M}$	5.2064e+18	-0.819	0
11	$\text{H} + 2 \text{O}_2 \rightleftharpoons \text{HO}_2 + \text{O}_2$	9.1249e+18	-1.252	0
12	$\text{H} + \text{O}_2 + \text{H}_2\text{O} \rightleftharpoons \text{HO}_2 + \text{H}_2\text{O}$	6.4145e+18	-0.700	0
13	$\text{H} + \text{O}_2 + \text{N}_2 \rightleftharpoons \text{HO}_2 + \text{N}_2$	8.1196e+18	-1.198	0
14	$\text{H} + \text{O}_2 \rightleftharpoons \text{O} + \text{OH}$	2.7173e+16	-0.638	16837.10
15	$\text{H} + \text{OH} + \text{M} \rightleftharpoons \text{H}_2\text{O} + \text{M}$	3.2807e+22	-1.953	0
16	$\text{H} + \text{HO}_2 \rightleftharpoons \text{O} + \text{H}_2\text{O}$	2.3618e+12	0	677.85
17	$\text{H} + \text{HO}_2 \rightleftharpoons \text{O}_2 + \text{H}_2$	4.1616e+13	0	1073.36
18	$\text{H} + \text{HO}_2 \rightleftharpoons 2 \text{OH}$	9.3909e+13	0	630.28
19	$\text{H} + \text{CH}_3 (+\text{M}) \rightleftharpoons \text{CH}_4 (+\text{M})$	1.5329e+16	-0.489	517.21
20	$\text{H} + \text{CH}_4 \rightleftharpoons \text{CH}_3 + \text{H}_2$	6.9485e+08	1.627	10518.70
21	$\text{H} + \text{HCO} \rightleftharpoons \text{H}_2 + \text{CO}$	7.2434e+13	0	0
22	$\text{H} + \text{CH}_2\text{O} (+\text{M}) \rightleftharpoons \text{CH}_3\text{O} (+\text{M})$	9.0024e+11	0.441	2564.83
23	$\text{H} + \text{CH}_2\text{O} \rightleftharpoons \text{HCO} + \text{H}_2$	7.9533e+07	1.887	2806.22
24	$\text{OH} + \text{H}_2 \rightleftharpoons \text{H} + \text{H}_2\text{O}$	2.3163e+08	1.557	3375.07
25	$2 \text{OH} \rightleftharpoons \text{O} + \text{H}_2\text{O}$	3.6103e+04	2.374	-2190.14
26	$\text{OH} + \text{HO}_2 \rightleftharpoons \text{O}_2 + \text{H}_2\text{O}$	2.1018e+13	0	-499.91
27	$\text{OH} + \text{CH}_4 \rightleftharpoons \text{CH}_3 + \text{H}_2\text{O}$	8.5838e+07	1.629	3069.97
28	$\text{OH} + \text{CO} \rightleftharpoons \text{H} + \text{CO}_2$	3.9376e+07	1.241	68.97
29	$\text{OH} + \text{HCO} \rightleftharpoons \text{H}_2\text{O} + \text{CO}$	2.1461e+13	0	0
30	$\text{OH} + \text{CH}_2\text{O} \rightleftharpoons \text{HCO} + \text{H}_2\text{O}$	6.0662e+09	1.188	-448.27
31	$\text{OH} + \text{CH}_3\text{O} \rightleftharpoons \text{H}_2\text{O} + \text{CH}_2\text{O}$	6.5742e+12	0	0
32	$\text{HO}_2 + \text{CH}_3 \rightleftharpoons \text{O}_2 + \text{CH}_4$	9.8826e+11	0	0
33	$\text{HO}_2 + \text{CH}_3 \rightleftharpoons \text{OH} + \text{CH}_3\text{O}$	6.9779e+13	0	0
34	$\text{HO}_2 + \text{CO} \rightleftharpoons \text{OH} + \text{CO}_2$	1.2290e+14	0	23365.70
35	$\text{CH}_3 + \text{O}_2 \rightleftharpoons \text{O} + \text{CH}_3\text{O}$	8.9666e+13	0	30530.50
36	$\text{CH}_3 + \text{O}_2 \rightleftharpoons \text{OH} + \text{CH}_2\text{O}$	1.4800e+12	0	20758.90
37	$2 \text{CH}_3 (+\text{M}) \rightleftharpoons \text{C}_2\text{H}_6 (+\text{M})$	1.0249e+17	-1.121	657.91
38	$\text{CH}_3 + \text{HCO} \rightleftharpoons \text{CH}_4 + \text{CO}$	7.7865e+12	0	0
39	$\text{CH}_3 + \text{CH}_2\text{O} \rightleftharpoons \text{HCO} + \text{CH}_4$	3.0030e+03	2.737	5598.00
40	$\text{HCO} + \text{H}_2\text{O} \rightleftharpoons \text{H} + \text{CO} + \text{H}_2\text{O}$	3.1001e+17	-0.948	17111.00
41	$\text{HCO} + \text{M} \rightleftharpoons \text{H} + \text{CO} + \text{M}$	4.6278e+16	-0.959	17305.40
42	$\text{HCO} + \text{O}_2 \rightleftharpoons \text{HO}_2 + \text{CO}$	2.6664e+13	0	397.03
43	$\text{CH}_3\text{O} + \text{O}_2 \rightleftharpoons \text{HO}_2 + \text{CH}_2\text{O}$	4.2800e-13	7.597	-3351.89
44	$\text{O} + \text{CH}_3 \rightarrow \text{H} + \text{H}_2 + \text{CO}$	9.5832e+13	0	0
45	$\text{OH} + \text{HO}_2 \rightleftharpoons \text{O}_2 + \text{H}_2\text{O}$	6.1266e+15	0	17622.10
46	$\text{OH} + \text{CH}_3 \rightarrow \text{H}_2 + \text{CH}_2\text{O}$	1.1982e+10	0.501	-1730.78

Table 5.2: Units are mol, s, cm³, cal and K. Reduction by DRGEP and QSS and parameters of rates optimised by genetic algorithm over micro-mixing trajectories and premixed flames. The Chaperon efficiencies of the GRI-3.0 mechanism are preserved for both three-body and fall-off reactions.

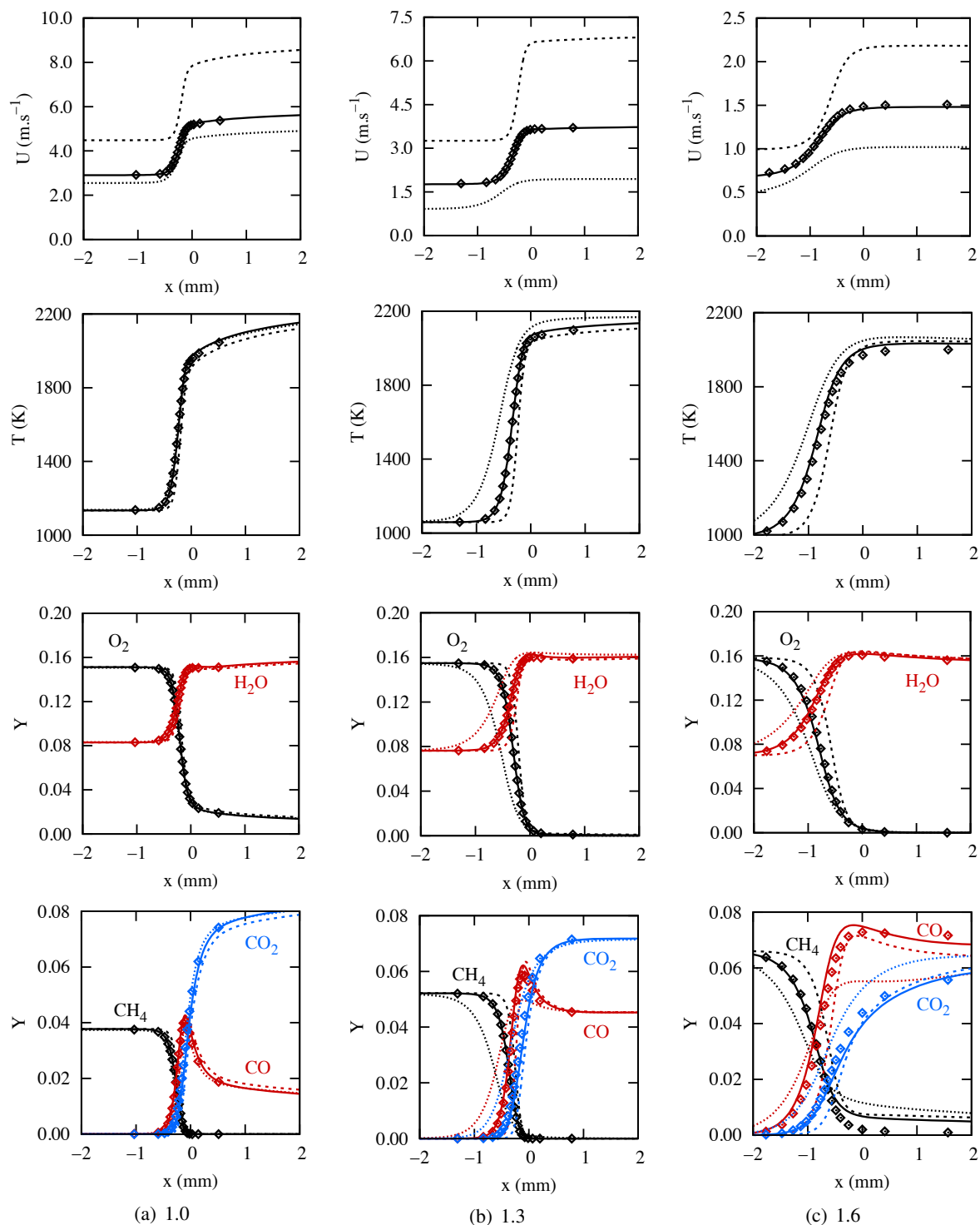


Figure 5.10: Freely propagating premixed flames. Velocity, temperature and major species. Symbols: Detailed reference (GRI-3.0). Dotted-line: Preliminary reduced mechanism (DRGEP+QSS). Dashed-line: Micro-mixing optimised (DRGEP+QSS+GA micro-mixing trajectories). Line: Fully optimised (DRGEP+QSS+GA micro-mixing trajectories+premixed flames, Table 5.2).

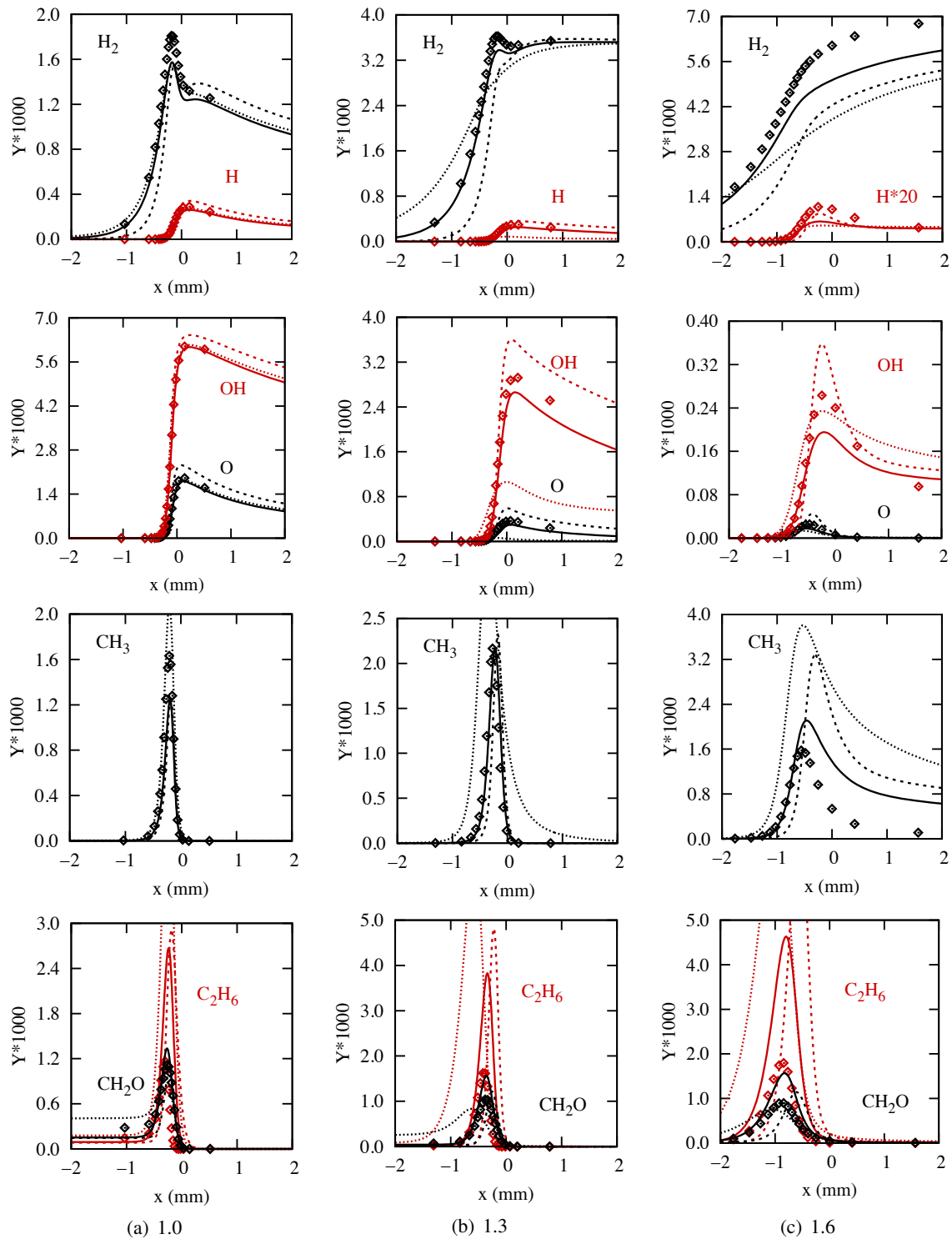


Figure 5.11: Freely propagating premixed flames. Minor species. Symbols: Detailed reference (GRI-3.0). Dotted-line: Preliminary reduced mechanism (DRGEP+QSS). Dashed-line: Micro-mixing optimised (DRGEP+QSS+GA micro-mixing trajectories). Line: Fully optimised (DRGEP+QSS+GA micro-mixing trajectories+premixed flames, Table 5.2).

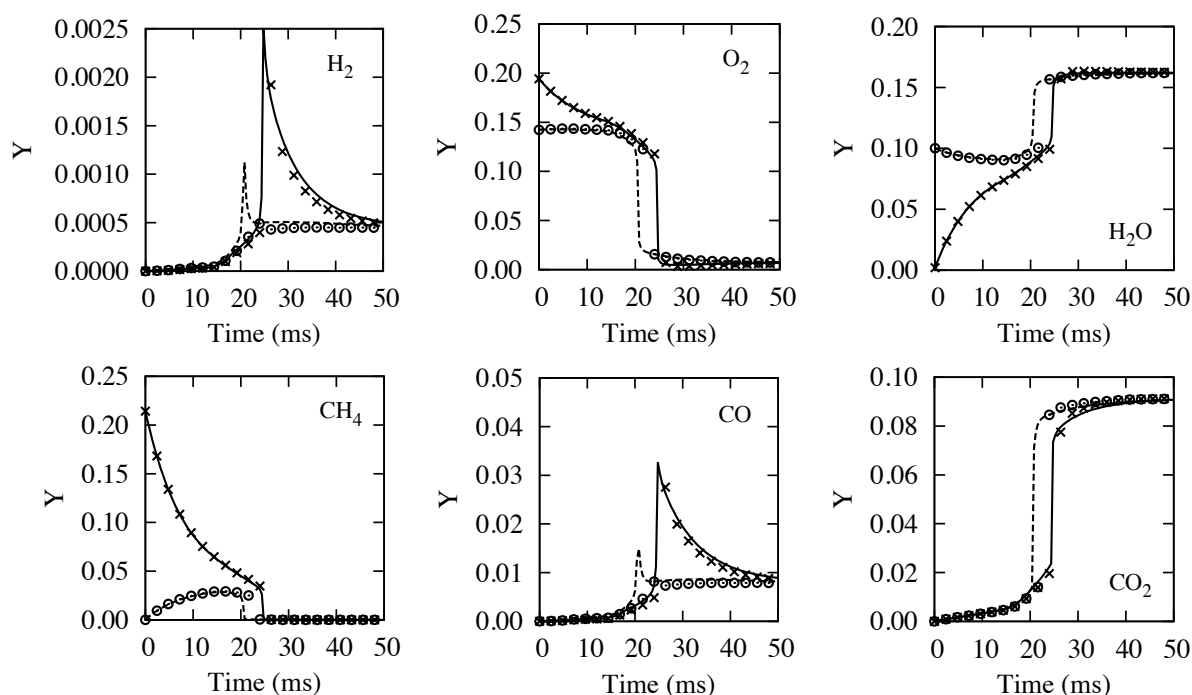


Figure 5.12: Trajectories (Eqs. (5.19)-(5.20)). $\tau_t = 8$ ms. Fuel-jet trajectory. Line: Micro-mixing optimised (DRGEP+QSS+GA micro-mixing trajectories). \times : GRI-3.0. Coflow-jet trajectory (vitiated-air). Dashed-line: Micro-mixing optimised. \odot : GRI-3.0.

The predictions, already acceptable before optimisation in the case of the stoichiometric premixed flame (dotted line Fig 5.10(a)), are left unaffected by the optimisation of the rates (solid line in Fig. 5.10(a)). After optimisation, other equivalence ratios are now properly captured by the reduced scheme (solid line in Fig. 5.10), along with the temperature and velocity profiles (and therefore flame speed) under various equivalence ratios (solid line in the upper part of Fig. 5.10). The minor species are shown in Fig. 5.11. Overall, the approximation of OH and O radicals, as also CH₃ to a lesser extent, are reasonable, with a departure growing on the rich side. Would one intermediate species be essential for the simulation of a specific physical phenomena, as for instance soot production, it could be added as an additional target in the optimisation loop.

In the configuration of the counter-flowing jets of methane against vitiated-air, the impact of the optimisation of the chemical rates with the genetic algorithm lies in the improvement of the peak CO prediction. Indeed, in Fig. 5.13 showing the major species distribution before optimisation, the peak CO was underestimated. The optimised chemical rates provide a better approximation of CO, as seen in Fig. 5.14, in particular for the high level of strain-rate (Fig. 5.14(b)). For intermediate species in the diffusion flamelet, overall the scheme performs better at high-strain (Fig. 5.15), but for C₂H₆ that is overestimated, even at high-strain.

The maximum temperature in the diffusion flamelet versus strain-rate up to quenching, hence the upper part of the S-curve [117], is reported in Fig. 5.16. Before reaching the quenching limit, the error in the maximum temperature within the flamelet stays below 2%. It is important to note that the diffusion flame was not included in the optimisation loop. The preliminary reduced scheme (DRGEP+QSS) underestimates the quenching limit (dotted line in Fig. 5.16). With the scheme optimised over the micro-mixing trajectories, the quenching point value gets above the reference one (dashed line). The addition

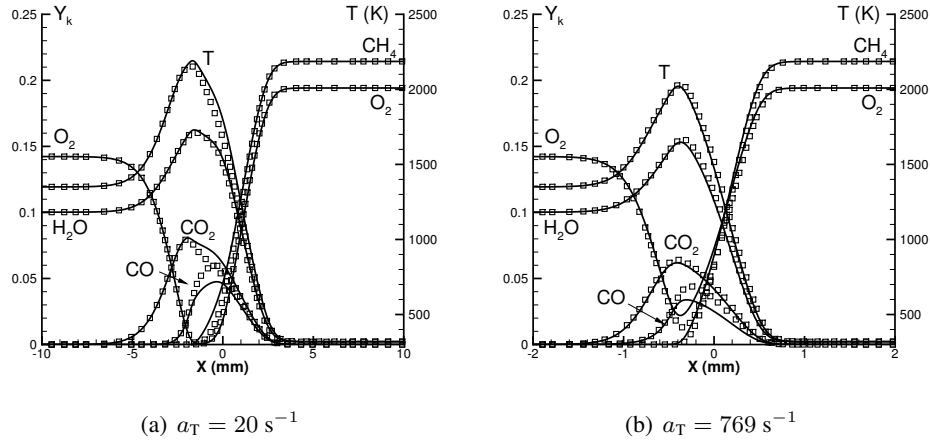


Figure 5.13: Major species and temperature distribution in diffusion-flamelets for two strain-rate levels. Solid-line: preliminary reduced mechanism (DRGEP+QSS). Symbols: GRI-3.0.

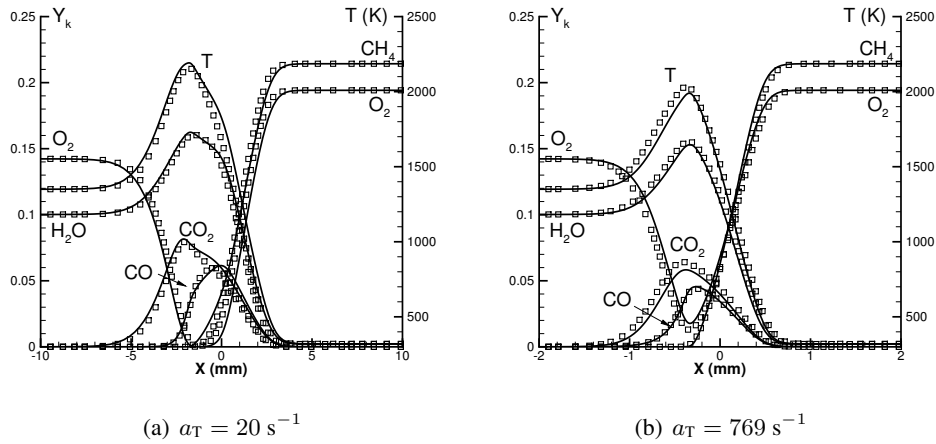


Figure 5.14: Major species and temperature in diffusion-flamelets for two strain-rate levels. Symbols: GRI-3.0. Solid-line: Fully optimised (DGREP+QSS+GA micro-mixing trajectories+premixed flames).

of the premixed flames in the optimisation loop leads to an analytical reduced chemistry that reproduces the response of temperature at quenching (solid line in Fig. 5.16). Hence, it is observed that a scheme featuring the correct laminar flame speed also provides the quenching point of the corresponding diffusive-reactive layer, which is not the case with a scheme only optimised against micro-mixing. This observation may be put in perspective with the derivation by Norbert Peters of a relation between, χ_q , the quenching scalar dissipation rate and S_L , the flame speed [166, 167]:

$$\chi_q \approx \frac{Z_s^2(1 - Z_s)^2}{D/S_L^2}, \quad (5.24)$$

where D denotes a mean molecular diffusion coefficient. This relation demonstrates the intricate links between the time scale imposed by the flow to the diffusion flame (calibrated by χ_q) and the time scale of the premixed laminar flame D/S_L^2 , both interacting with the chemical time scale driven by the same

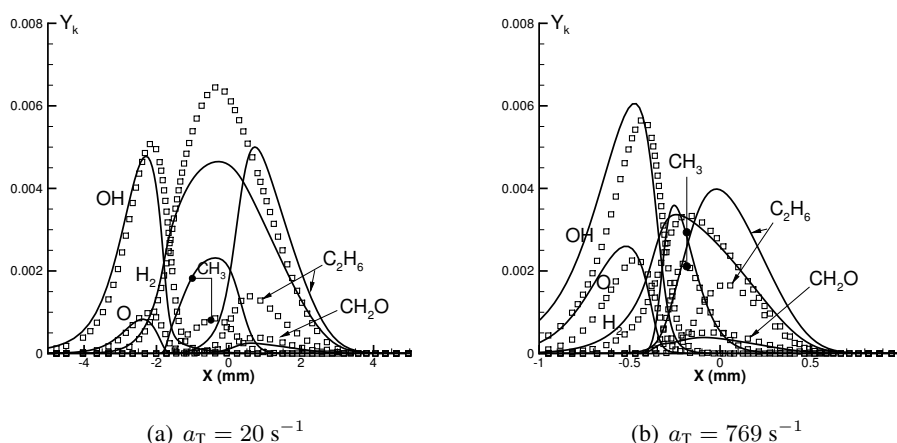


Figure 5.15: Minor species in diffusion-flamelets for two strain-rate levels. Symbols: GRI-3.0. Solid-line: Fully optimised (DGREP+QSS+GA micro-mixing trajectories+premixed flames).

kinetics. Relation (5.24) was extended to diffusion edge-flame quenching in [168].

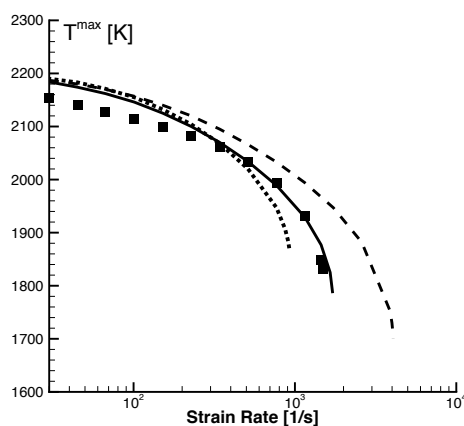


Figure 5.16: Response of the maximum temperature versus strain-rate up to diffusion flamelet quenching. Symbols: Detailed reference (GRI-3.0). Dotted-line: Preliminary reduced mechanism (DRGEP+QSS). Dashed-line: Micro-mixing optimised (DRGEP+QSS+GA micro-mixing trajectories). Line: Fully optimised (DRGEP+QSS+GA micro-mixing trajectories+premixed flames, Table 5.2).

The pre-exponential factor $\log(\mathcal{A}_j)$, the temperature exponent β_j and the activation energy E_{a_j} have thus been optimised for every reaction in the context of the reduced scheme and the operating conditions, leading to the values of Table 5.2. It is important to note that one should not expect any physics behind a specific response of the elementary reactions to the optimisation process, other than the need to counterbalance the loss of many other elementary reactions and species. Also, modifying the operating conditions may lead to a fully different set of optimised parameters. The need for non-trivial, and somehow not based on any first principal, adjustments to match the various canonical problems, underlines the importance of relying on fully automated approaches for chemical scheme reduction and optimisation, in view of their application to turbulent flow simulations.

5.4 Application to a four-inlet methane/vitiated-air/hydrogen-air/steam problem

Adding inlets to the automated method discussed above is straightforward, since the representation of the inlets is achieved through the initial conditions of the stochastic particles. A group is defined from particles having the same initial conditions, then N groups of particles at initial time leads to the simulation of a N -inlet problem. As required in the combustion chambers with secondary cooling air-injection, or in furnaces with recirculating burnt gases that have undergone cooling in wall boundary layers.

In order to demonstrate the potential of the method for addressing a multiple-inlet practical case, the automated reduction method is applied to a four-inlet problem. To the two-inlet considered above, two more are added, which inject stoichiometric H_2 /Air mixture and steam, respectively. These conditions and the corresponding mass flow rates, all being arbitrary chosen here for demonstrating the method, are summarised in Table 5.3. At initial times, the particles are distributed over the inlet according to their

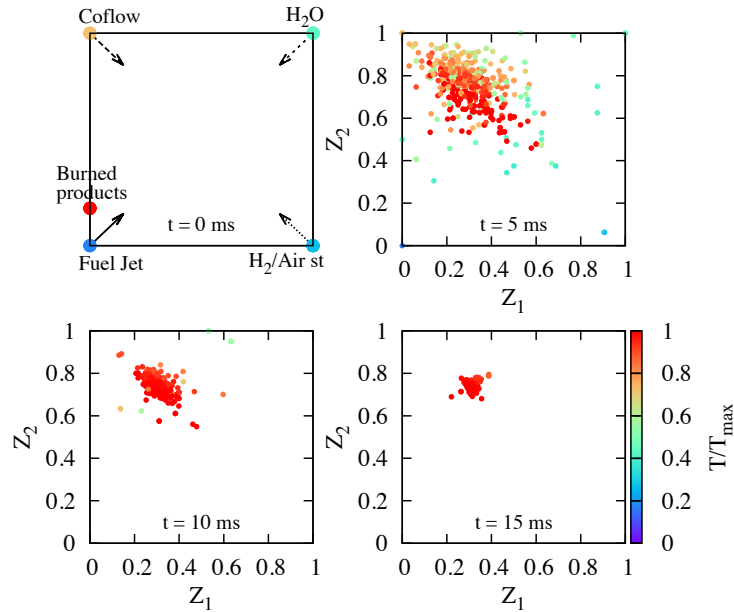


Figure 5.17: Scatter plot of particles position in mixture fraction space in a four-inlet problem (Table 5.3) coloured by normalised temperature. Four times: $t = 0, 5, 10, 15$ ms.

mass flow rate and, as previously, to secure ignition 20 particles are added at the chemical equilibrium conditions for $\phi = 1$. Figure 5.17 shows a representative evolution of the particles in mixture fraction space coordinates (where Z_1 and Z_2 are mixture fractions initially set to unity respectively in the inlet 1 and 2 and set to zero in the other inlets), for $\tau_t = 2$ ms.

Inlet	$R_{\dot{Q}_m}$ in %	T (K)	Y_{O_2}	Y_{N_2}	Y_{H_2O}	Y_{CH_4}	Y_{H_2}
Inlet 1	8.00	320	0.194	0.589	0.00211	0.214	0.926
Inlet 2	60.00	1350	0.142	0.757	0.100	0.000178	0.240
Inlet 3	15.19	500	0.1478	0.5562	0.0	0.0	0.2958
Inlet 4	16.81	800	0.0	0.0	1.0	0.0	0.0

Table 5.3: Conditions for methane-air combustion in vitiated coflow with four inlets. T: Temperature, Y: Mass fraction. $R_{\dot{Q}_m}$: fraction of total mass flow rate.

First, four reference trajectories are computed using the GRI-3.0 detailed mechanism. In a first approach it is tried to proceed from the reduced scheme derived with only two-inlet and to further optimise the chemical parameters according to the four-inlet trajectories. Therefore, the optimised scheme of Table 5.2 is used as a starting point, to apply the genetic algorithm to the four-inlet case of Table 5.3. A new set of chemical parameters is obtained (not given for brevity). Results are presented in Fig. 5.18, a good agreement is seen for major species. Some departure exists for the peak of CO along the trajectory issued from the pure steam inlet, possibly the result of the direct application of the genetic algorithm without revisiting the chemical scheme through the DRGEP and QSS steps for this particular trajectory. This demonstrates, once more, the need to reduce the chemical schemes in line with the burner conditions targeted. However, other species and trajectories are perfectly captured (Fig. 5.18) and the results confirm the feasibility of the automated method to derive reduced chemical schemes fit for the simulation of real combustion systems.

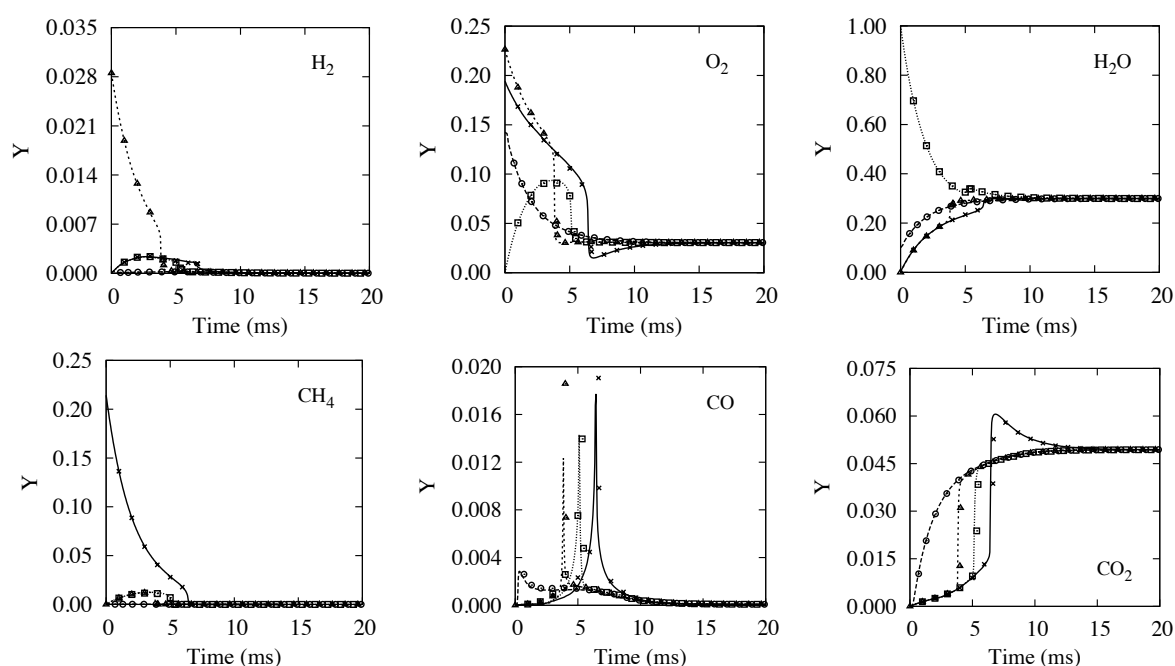


Figure 5.18: Species mass fractions in a four-inlet problem. Lines: reduced mechanism. Symbols: GRI-3.0. Solid-line and (×): Inlet 1. Long-dashed-line and (○): Inlet 2. Short-dashed-line and (▲): Inlet 3. Dotted-line and (□): Inlet 4. (See Table 5.3).

5.5 Conclusion

To systematically cover the full range of chemical compositions observed downstream of flow injection, reference composition space trajectories are obtained with a detailed chemistry, prior to any flow simulation. These trajectories, issued from the various inlets of the combustion system, are computed combining a stochastic mixing closure with a deterministic approach, to follow a set of paths in composition space. Along these trajectories, the reduction and optimisation approach depicted in Chapter 4 may be used to obtain a reduced chemical scheme.

The method is applied to the conditions of a methane/vitiated-air burner [163], with a good reproduction of the major species along the reference trajectories and also in one-dimensional premixed and

strained diffusion flames for the same fresh gases compositions. The response up to the flame quenching point is also examined for the latter. These one-dimensional flames are simulated before and after applying the genetic algorithm, with or without including premixed flames as target of this optimisation loop (they are not considered in the first reduction steps based on the micro-mixing trajectories only).

In terms of rate optimisation to get as close as possible to the detailed chemistry response of chemical species, for this case with vitiated-air, it is seen that the one-dimensional flames are less demanding than the composition-space trajectories, at least up to an equivalence ratio of 1.3 for the premixed flame. But the optimisation based on the micro-mixing trajectory only, does not allow for reproducing the flame speed. Adding the flame speed as target of the genetic algorithm provides a scheme performing well for all canonical problems, including the quenching point of diffusion flames (upper part of the so-called ‘S-curve’), as expected from flame theory [166, 167].

Many combustion systems operate with staged air-injection, as gas turbines, or with numerous inlets at various compositions, as in gas production units based on methane reforming. To demonstrate the potential of the proposed strategy, the rates of the reduced chemical scheme are further optimised after adding two more inlets: another fuel (hydrogen), and, a separated steam flux, thus considering a four-inlet problem.

Potential improvements of the method exist, for instance most advanced micro-mixing closures [169–171] could be considered in the construction of the reference composition-space trajectories. A distribution of mixing-times [172] could also be introduced in the reduction/optimisation loop.

Chapter 6

Reduced kinetics for the partial oxidation part of an auto-thermal reformer

Contents

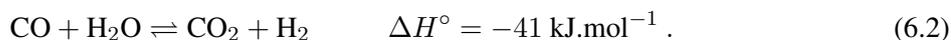
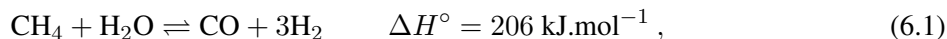
6.1	Introduction	143
6.1.1	Syngas production	143
6.1.2	Canonical modelling of the flow in an ATR reactor	145
6.1.3	Mechanisms reduction	145
6.2	Conditions for the study and for the reduction	145
6.2.1	Flow composition	145
6.2.2	Preliminary equilibrium study	146
6.3	Reduced mechanisms for ATR reactors	149
6.3.1	Reduction of the RAMEC	149
6.3.2	Other reductions	152
6.4	Reduced schemes assessment using RANS simulations	158
6.5	Conclusion	159

6.1 Introduction

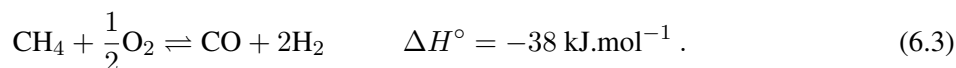
6.1.1 Syngas production

Syngas or synthesis gas is a gaseous mixture primarily composed of CO and H₂ and very often of some CO₂ that serves in a variety of petrochemical and metallurgical industries. For instance, syngas is essential to process many chemicals, as methanol or ammonia, and it is at the core of one of the options for converting natural gas into liquid fuels. While the production of syngas relies on numerous strategies [173–177], the usual processes being used to manufacture it are steam methane reforming (SMR), non-catalytic partial oxidation (POX) and auto-thermal reforming (ATR). Steam reforming [176] consists of a preheated mixture of natural gas and steam that travels through a series of tubes filled with catalyst and immersed within a fired-heater. While travelling through the tubes of the reformer, the mixture is catalytically converted into hydrogen, carbon monoxide and carbon dioxide undergoing reactions that

can be summarised through two global steps, the endothermic reforming reaction 6.1 and the slightly exothermic water gas shift reaction 6.2:



Overall the SMR results from an endothermic conversion, heat being provided by external burners. With non-catalytic partial oxidation [178], steam is replaced by pure oxygen to oxidise the natural gas from mixing and burning conditions achieved by creating a turbulent diffusion flame. The exothermic global reaction describing a partial oxidation process is:



Auto-thermal reforming [179] combines both partial oxidation and adiabatic steam reforming in a single reactor. Figure 6.1 provides an illustration of the ATR reactor. A mixture of natural gas, steam and oxygen first reacts into a combustion zone and the burned products then travel through a catalyst bed where reforming reactions occur. Table 6.1 provides orders of magnitudes of the range of temperature

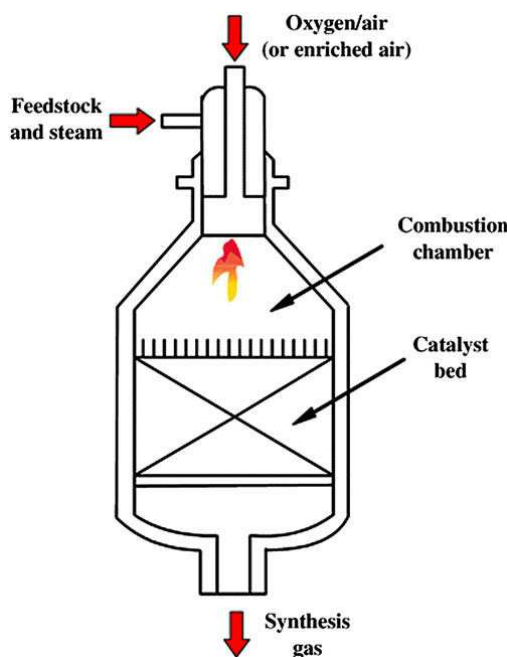


Figure 6.1: Illustration of an ATR reactor [180].

and pressure covered for each process as well as the standard H_2/CO ratio of the exiting mixture. Typical ATR reactors operate above the atmospheric pressure (up to 40 bar) and feature characteristic length of

Method	Operating conditions		H_2/CO
	Temperature (K)	Pressure (bar)	
SMR	1000 - 1200	15 - 40	3.0 - 5.0
POX	1100 - 1300	20 - 150	1.6 - 1.8
ATR	1500 - 1800	20 - 40	1.6 - 2.6

Table 6.1: Characteristics of syngas production processes

many meters. The high levels of temperature reached within the combustion area is a critical parameter for the design of the equipments in ATR systems and for their durability. The main elements concerned by this thermal load are: the burner, the refractory vessel and the catalyst bed.

6.1.2 Canonical modelling of the flow in an ATR reactor

One-dimensional laminar flames are usual model configurations on which the development, calibration and validation of detailed and reduced chemistry is based [158, 167]. However in the ATR case, for at least three reasons, this canonical problem may not be the most relevant one. Firstly, one-dimensional flames are one- (premixed) or two- (diffusion) inlet problems and ATR burners have at least three inlets carrying three different flow compositions. Very intense mixing occurs between these three streams right downstream of injection, which jeopardises the concept of a sequential pattern of two-inlet mixing problems (*e.g.* methane would first mix with steam and then the resulting mixture would react with oxygen). Secondly, one-dimensional flames are not well suited to study reacting flows featuring large residence times. The ATR chemical process is a combination of fast and slow reactions, fuel oxidation occurs close to the burner with short time scales, whereas the reactions typical of syngas productions are slower and develop in a convective mode over much larger time scales. Thirdly, ATR operates at about 40 bar in the presence of very intense micro-mixing, with burnt products recirculating in a swirling flow motion in the stabilisation zone of the flame, thus in a regime which is most probably far from a one-dimensional laminar diffusive/reactive layer.

The coupled stochastic and deterministic approach depicted in the previous chapter allows for covering a large variety of inlet conditions which may also include recirculating burned products, hence allowing for the creation of reference trajectories representative of the mixture composition faced by ATR systems. Moreover, the use of elementary particles interacting together over a defined mixing time scale τ_t enables to account for the sequential structure of the reactive flow. In this context, the introduced new canonical approach is applied in this chapter to the reduction of a chemical mechanism for the auto-thermal reforming of methane.

6.1.3 Mechanisms reduction

The stability of the reaction zones where combustion starts in the turbulent flow, and the overall efficiency of the chemical processes involved in ATR systems, strongly depend on the complex interaction between the turbulent flow fluctuations and the non-linear chemical response. The application of numerical simulations to systems of large dimensions is a rapidly growing field [181, 182] leading to a modelling framework useful to progress in the design of industrial processes involving strong interactions between chemistry and turbulence. However, the existence of a chemical scheme of moderate size is mandatory to perform any of these simulations.

6.2 Conditions for the study and for the reduction

6.2.1 Flow composition

The present study focuses on the development of a reduced mechanism able to account for the principal chemical behaviour faced by the partial oxidation (POX) part of an auto-thermal reforming system. The studied POX reactor is illustrated on Figure 6.2. It is made up of a three-inlet concentric burner composed of (1) oxygen plus steam (2) steam and (3) methane plus steam. The flow rates and compositions of the

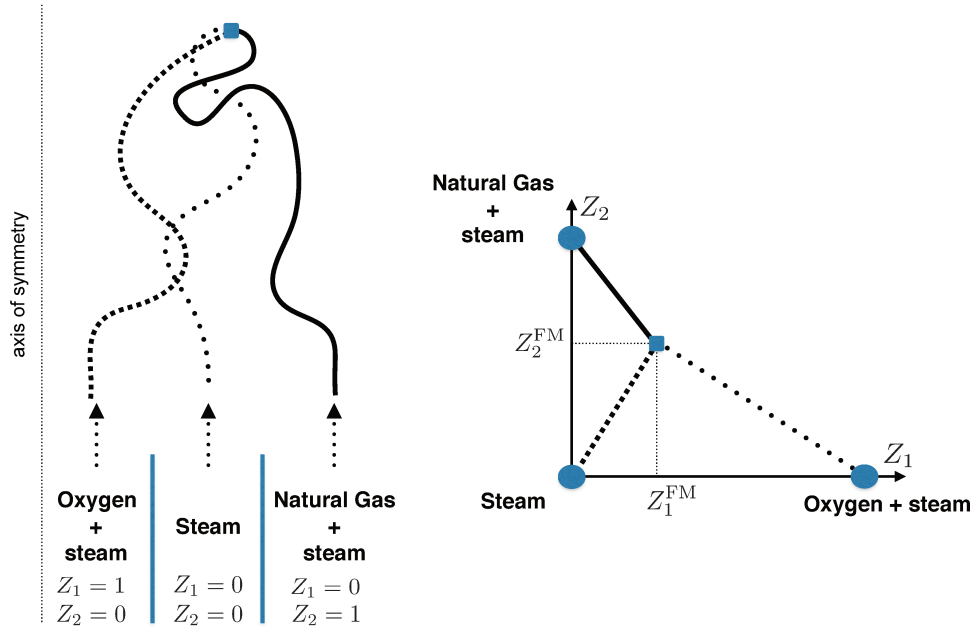


Figure 6.2: Sketch of the three-inlet ATR composition space formulation. Left: Physical space trajectories. Right: Mixture fractions evolution.

inlets are summarised within table 6.2 corresponding to an equivalence ratio of $\phi_o = 3.35$ (see [183] for such ATR conditions). The combustion products at chemical equilibrium are mainly composed of: H_2 (7% in mass), CO (36%) and CO_2 (18%), H_2O (diluent+product) (38%) and some CH_4 left (1%).

Inlet	Flow rate (kg/s)	Temperature (K)	Mass fraction			Passive scalar	
			Y_{CH_4}	Y_{O_2}	Y_{H_2O}	Z_1	Z_2
1	0.0917	512	0	0.909	0.090	1	0
2	0.0193	548	0	0	1	0	0
3	0.1403	867	0.498	0	0.501	0	1

Table 6.2: Operating conditions of the ATR system.

The mixing of the three inlets of an ATR burner (Table 6.2) may be monitored with two passive scalars Z_1 and Z_2 (Figure 6.2). In the Z_1 - Z_2 composition space, the mixing between the three streams leads to three lines, each starting from an inlet and ending at the fully mixed condition Z_1^{FM} - Z_2^{FM} , which is determined from \dot{Q}_{m_G} the inlet mass flow rates: $Z_\ell^{FM} = \dot{Q}_{m_G} / (\sum_{g=1}^3 \dot{Q}_{m_g})$, where G denotes the inlet where the ℓ th passive scalar is set to unity.

6.2.2 Preliminary equilibrium study

First, to get a general idea of the conditions faced by the studied ATR reactor, auto-ignition calculations are presented in Figure 6.3. The proposed graphs provide an analysis in the Z_1 - Z_2 mixture fraction space for a variety of flow compositions obtained with different mixing proportions of the inlets 1, 2 and 3. Graph 6.3(a) shows the corresponding compositions. The blue solid lines provide the equivalence ratio of the obtained mixture and the red lines delineate the percentage of dilution by inlet 2. The other subfigures depict the equilibrium state reached by perfectly stirred reactors that would be initiated to the

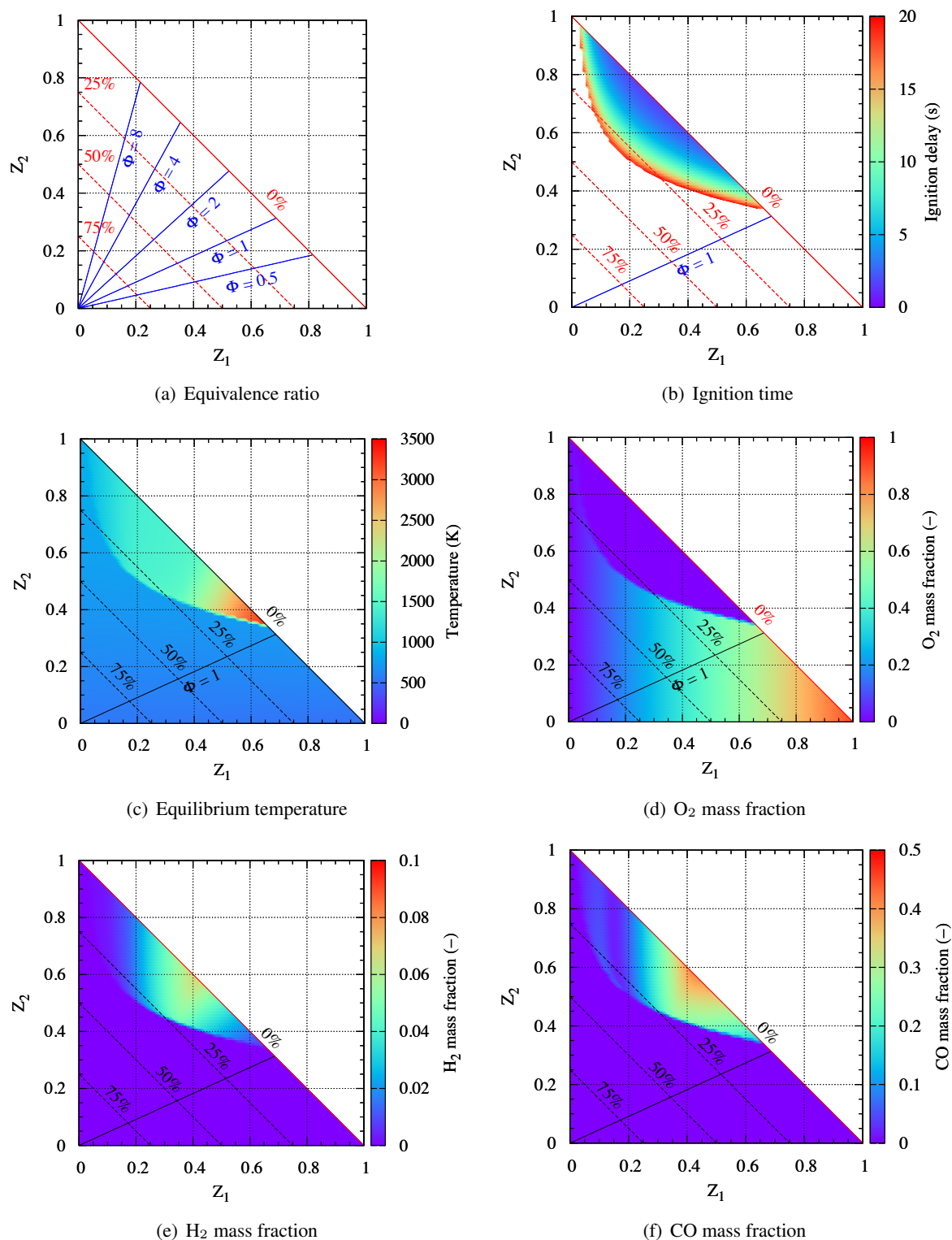


Figure 6.3: Equilibrium analysis performed for different compositions obtained through the mixing of the three inlets of the ATR system. The temperature, ignition delay and main species mass fractions are expressed in a mixture fraction space. The computations are made from perfectly stirred reactors.

fresh conditions of the associated Z_1 and Z_2 mixtures. The RAMEC mechanism [139] is employed for this preliminary analysis.

The results should be tempered by the fact that in the real system, the ignition is greatly accelerated by the mixing with the burned gases. Yet, using this simple representation, it is observed that overall, the compositions that properly ignite correspond to dilution levels by inlet 2 that are lower than 25%. It also appears that because of the high rate of H_2O dilution in the fuel mixture entry i.e. inlet 1, the burning limit is for equivalence ratios greater than 1. As already reported, overall the system operates at $\phi_o = 3.35$ which appear to be in the region of maximum H_2 levels. Regarding the temperature, the maximum levels are achieved close to stoichiometry with values of the order of 3500 K. The temperature in the region of interest is of approximately 2000 K.

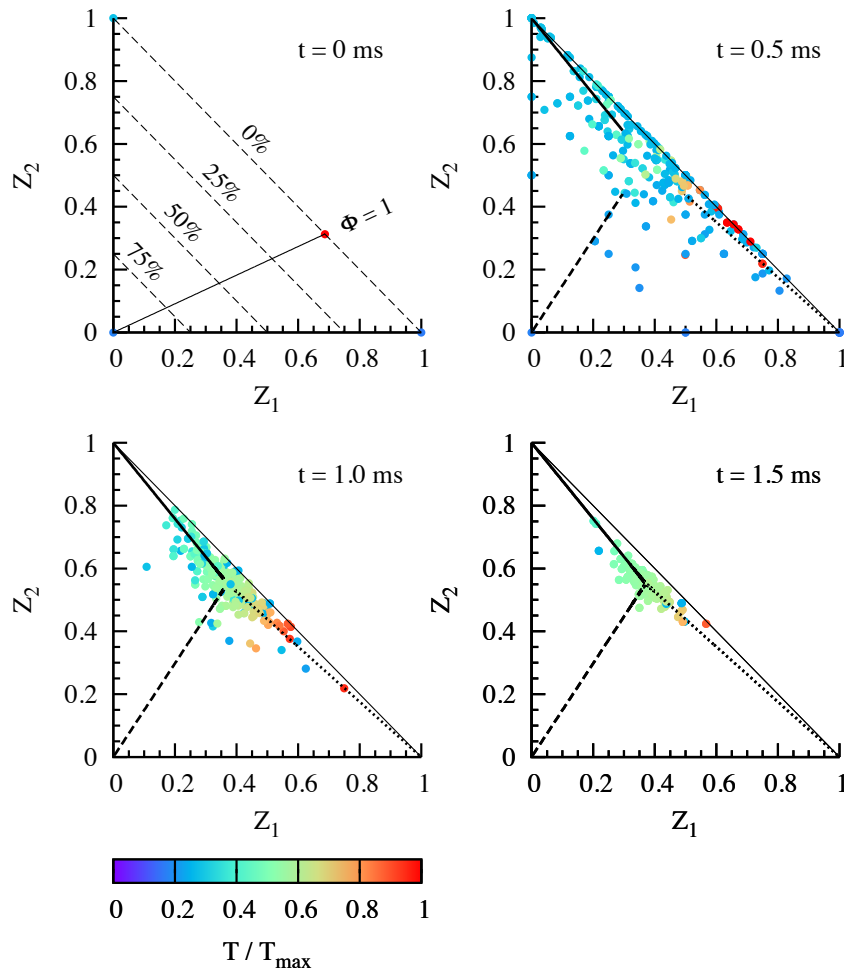


Figure 6.4: Time evolution of the N_T stochastic particles (Eqs. 5.19-5.20) coloured by temperature normalised by its adiabatic value under stoichiometric conditions. Top left: Line delineating in % the degree of dilution by Inlet 2 (Inlet 1: $Z_1 = 1$, Inlet 3: $Z_2 = 1$, Table 6.2) and particles at $t = 0$ (red and blue circles), $\phi = 1$: Stoichiometric condition. Other graphs: particles at $t > 0$ and projection of trajectories in Z -space. Dotted line: Inlet 1. Dashed line: Inlet 2. Solid line: Inlet 3.

6.3 Reduced mechanisms for ATR reactors

To serve as target for both reduction and optimisation, it is proposed to construct composition-space trajectories of species mass fraction following the formulations proposed in 5.19-5.20. As a reminder, a stochastic model problem is first designed to probe the dynamical response of a detailed chemical scheme, over a large range of chemical compositions of the mixture. Reference composition space trajectories are built, featuring turbulent micro-mixing governed by a characteristic time τ_t suited to the studied ATR system and reactions.

6.3.1 Reduction of the RAMEC

To authors knowledge, no detailed mechanisms have been validated under ATR conditions. The RAMEC chemical scheme has been retained for a first reduction attempt. It is composed of 35 species in the case of oxy-combustion (without N_2 , He and Ar) and 186 elementary reactions [139]. Its validation involved shock tube experiments for several methane-air mixtures with equivalence ratios between 0.4 and 6, pressures from 40 to 260 bar and temperatures ranging between 1040 K and 1500 K.

6.3.1.1 Reference trajectories

The time evolution of a set of $N_T = N_P + N_B$ stochastic particles is considered to compute for the deterministic trajectories that will be used for both reduction and optimisation. At initial time, the N_P particles are divided into three groups, according to the relative contribution of the mass flow rates of the three inlets i.e. $N_{P_G} = N_P \times \dot{Q}_{m_G} / \sum_{g=1}^3 \dot{Q}_{m_g}$ for $G = 1,2,3$. In each of these groups, at $t = 0$, the particles take the concentration and enthalpy of their respective inlet. To this, N_B particles are added

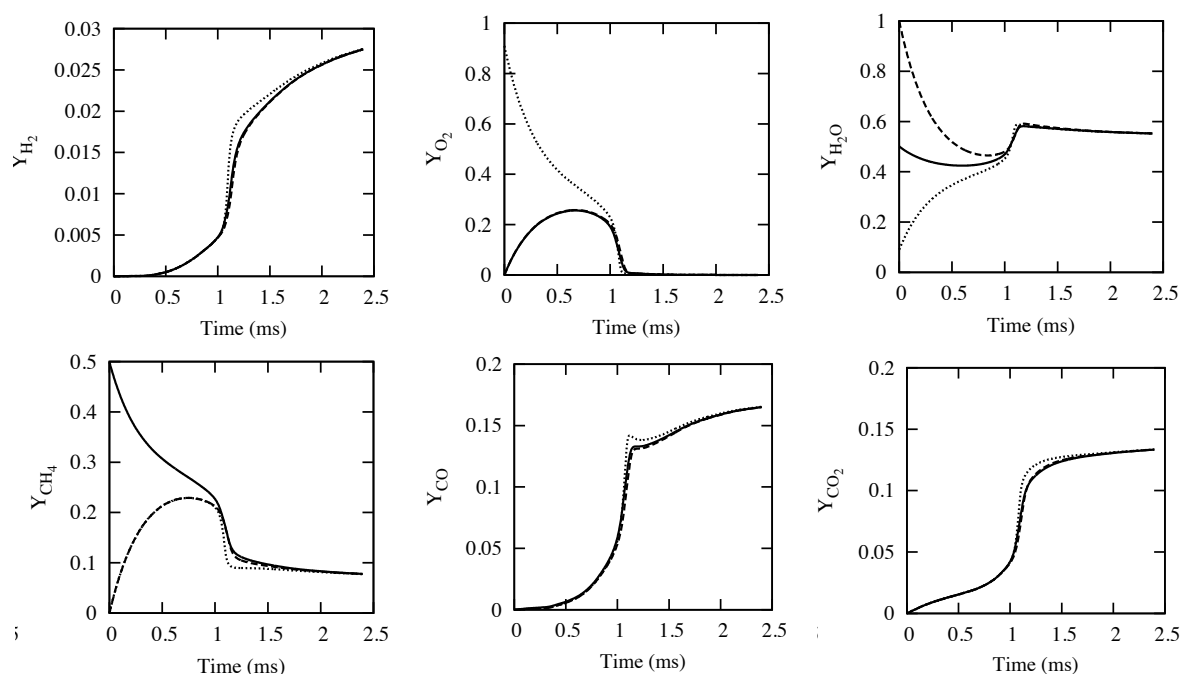


Figure 6.5: Representative reference trajectories mass fractions vs. time (Eqs. 5.19-5.20). Dotted line: Inlet 1. Dashed line: Inlet 2. Line: Inlet 3.

which are taken at chemical equilibrium and under the stoichiometric condition (6.4 top left). These additional particles represent the effect of some stoichiometric burned gases recirculating in the swirling flow and contributing to the ignition of the mixture. All these particles are allowed to evolve in time.

Various values of turbulent micro-mixing time τ_t have been tested in the interval [0.01 ms, 0.3 ms]. The initial part of the trajectories slightly varies with τ_t , but the variations with τ_t of the parameters of the chemical mechanism derived stay below a few %, because in all cases, by construction of the model problem the full range of equivalence ratios and dilution by the steam flux are covered and contribute to the optimisation process. All the results are then presented for $\tau_t = 0.3$ ms, corresponding to typical characteristic micro-mixing times for burners of large dimensions (*i.e.* $\tau_t \approx 0.5\ell_t/u'$, with a turbulent Reynolds number $Re_t = u'\ell_t/\nu \approx 2000$, the integral length scale $\ell_t \approx 5$ mm and velocity fluctuations $u' \approx 7 \text{ m}\cdot\text{s}^{-1}$), values confirmed by Reynolds Average Navier Stokes Simulation (RANS) of the burner configuration [184]. Varying N_p , the total number of stochastic particles, it was found that increasing it above $N_p = 80$ has a negligible impact on the trajectories, the value $N_p = 100$ was then selected. $N_B = 4$ was found sufficient to ignite the reference problem.

Figure 6.4 shows the evolution of the particles in time and illustrates the large range of equivalence ratios and temperatures covered at once by the model problem, *i.e.* by the three trajectories which are given in Fig. 6.5. Ignition occurs in the flammability region that is depicted within Figure 6.3. The diffusion of the energy provided by the burned gases particles appears to be the dominant effect for the ignition of the rest of the particles. After $t = 2.0$ ms, the set of particles appears to be well mixed, hence showing a mixture that tends to the global point of equilibrium of the burner.

6.3.1.2 DRGEP and QSS reduction

As for the other cases studied, the skeletal/analytical reduction strategy is used. First the chemical response is examined in order to reduce the number of species and elementary reactions to be transported with the flow. The DRGEP approach is employed to recover the proper mass fractions for the species CH_4 , O_2 , CO , CO_2 , H_2O and H_2 . Figure 6.6 illustrates the relation graph analysis for methane at $t = 1$ ms for the inlet 3 trajectory. Again, the interrelations between species are displayed according

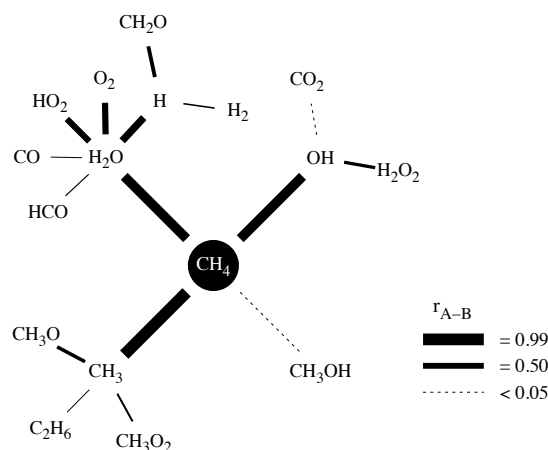


Figure 6.6: Visualisation of species relations at $t = 1$ ms for the Inlet 3 trajectory. Direct r_{A-B} paths are plotted according to their amplitude.

to the ratio r_{A-B} , measuring the amplitude of the rate of variation of species 'A' when 'B' is involved, relatively to the total rate of variation of species 'A'. It is seen that the relation coefficient $r_{\text{CH}_3-\text{CH}_4}$

#	Reaction	A^*	β	E_a^*
1	$O_2 + CH_2O \rightarrow HO_2 + HCO$	9.08e+13	0.0	39331
2	$H + O_2 + H_2O \rightleftharpoons HO_2 + H_2O$	1.10e+16	-0.76	0
3	$H + O_2 \rightleftharpoons O + OH$	7.37e+13	0.0	14087
4	$H + CH_3 \rightleftharpoons CH_4$	7.98e+29	-4.75	2448
5	$H + CH_4 \rightleftharpoons CH_3 + H_2$	6.03e+08	1.58	10912
6	$H + CH_2O \rightleftharpoons CH_3O$	8.51e+26	-4.77	5588
7	$H + C_2H_2 \rightleftharpoons C_2H_3$	9.41e+36	-7.29	7248
8	$H + C_2H_4 \rightleftharpoons C_2H_5$	3.81e+38	-7.63	6952
9	$H + C_2H_6 \rightleftharpoons C_2H_5 + H_2$	1.09e+08	1.85	7554
10	$H + CH_2CO \rightleftharpoons CH_3 + CO$	1.14e+13	0.0	3375
11	$OH + H_2 \rightleftharpoons H + H_2O$	2.17e+08	1.47	3362
12	$2 OH \rightleftharpoons H_2O_2$	6.93e+14	-0.90	-1693
13	$2 OH \rightleftharpoons O + H_2O$	3.50e+04	2.35	-2129
14	$OH + HO_2 \rightarrow O_2 + H_2O$	1.95e+13	0.0	-512
15	$OH + H_2O_2 \rightleftharpoons HO_2 + H_2O$	1.60e+12	0.0	317
16	$OH + H_2O_2 \rightarrow HO_2 + H_2O$	5.58e+14	0.0	9157
17	$OH + CH_3 \rightleftharpoons CH_2 + H_2O$	5.98e+07	1.60	5384
18	$OH + CH_4 \rightleftharpoons CH_3 + H_2O$	9.79e+07	1.57	3120
19	$OH + CO \rightleftharpoons H + CO_2$	4.64e+07	1.21	69
20	$OH + CH_2O \rightleftharpoons HCO + H_2O$	3.18e+09	1.18	-441
21	$OH + C_2H_2 \rightarrow H + CH_2CO$	2.18e-04	4.54	-979
22	$OH + C_2H_4 \rightleftharpoons C_2H_3 + H_2O$	3.49e+06	2.00	2492
23	$OH + C_2H_6 \rightleftharpoons C_2H_5 + H_2O$	3.34e+06	2.09	874
24	$2 HO_2 \rightarrow O_2 + H_2O_2$	1.37e+11	0.0	-1630
25	$2 HO_2 \rightarrow O_2 + H_2O_2$	5.20e+14	0.0	11653
26	$HO_2 + CH_3 \rightarrow OH + CH_3O$	1.68e+13	0.0	0
27	$HO_2 + CO \rightarrow OH + CO_2$	1.22e+14	0.0	24165
28	$HO_2 + CH_2O \rightarrow HCO + H_2O_2$	8.55e+11	0.0	8070
29	$CH_2 + O_2 \rightarrow OH + HCO$	1.06e+13	0.0	1504
30	$CH_2 + CH_3 \rightarrow H + C_2H_4$	4.50e+13	0.0	0
31	$CH_2 + CH_4 \rightleftharpoons 2 CH_3$	2.35e+06	2.04	8136
32	$CH_2 + CO \rightleftharpoons CH_2CO$	7.43e+29	-5.09	7042
33	$CH_3 + O_2 \rightarrow O + CH_3O$	2.97e+13	0.0	28315
34	$CH_3 + O_2 \rightarrow OH + CH_2O$	3.83e+10	0.0	8866
35	$CH_3 + OH \rightarrow CH_2O + H_2$	8.66e+12	0.0	0
36	$CH_3 + H_2O_2 \rightleftharpoons HO_2 + CH_4$	2.40e+04	2.48	5198
37	$2 CH_3 \rightleftharpoons C_2H_6$	4.06e+46	-9.69	6216
38	$2 CH_3 \rightarrow H + C_2H_5$	6.64e+12	0.10	10312
39	$CH_3 + CH_2O \rightarrow HCO + CH_4$	3.00e+03	2.81	5906
40	$CH_3 + C_2H_4 \rightleftharpoons C_2H_3 + CH_4$	2.34e+05	1.98	8909
41	$CH_3 + C_2H_6 \rightleftharpoons C_2H_5 + CH_4$	6.38e+06	1.74	10209
42	$HCO + H_2O \rightleftharpoons H + CO + H_2O$	1.71e+18	-0.98	17029
43	$HCO + M^\dagger \rightleftharpoons H + CO + M^\dagger$	1.53e+17	-1.00	17056
44	$C_2H_3 + O_2 \rightarrow HCO + CH_2O$	4.87e+12	0.0	-241

Table 6.3: Reduced scheme. Transported species: H_2 , O_2 , OH , H_2O , HO_2 , CH_3 , CH_4 , CO , CO_2 , C_2H_2 . Quasi-steady state: H , O , H_2O_2 , CH_2 , HCO , CH_2O , CH_3O , C_2H_3 , C_2H_4 , C_2H_5 , C_2H_6 , CH_2CO . *Units are mol, s, cm^3 , cal and K. \dagger Chaperon efficiencies are 2.0 for H_2 , 0.0 for H_2O , 2.0 for CH_4 , 1.5 for CO , 2.0 for CO_2 and 3.0 for C_2H_6 .

is close to unity and species CH_3 , OH and H_2O are present within the first layer of the CH_4 relation graph. The error is monitored again with the threshold values $E_{\text{smean}}^{\circ} = E_{\text{rmean}}^{\circ} = 10\%$. Reduction is also performed ensuring that the equilibrium is conserved for all trajectories allowing the profiles to deviate in the reacting layer. As a result, 13 species (C , CH , $\text{CH}_2(\text{S})$, CH_2OH , CH_3OH , C_2H , HCCO , HCCOH , CH_3O_2 , $\text{CH}_3\text{O}_2\text{H}$, $\text{C}_2\text{H}_5\text{O}$, $\text{C}_2\text{H}_5\text{O}_2$, $\text{C}_2\text{H}_5\text{O}_2\text{H}$) and 142 reactions are removed with this first step. The first guess of the reduced mechanism contains 22 species (H_2 , H , O , O_2 , OH , H_2O , HO_2 , H_2O_2 , CH_2 , CH_3 , CH_4 , CO , CO_2 , HCO , CH_2O , CH_3O , C_2H_2 , C_2H_3 , C_2H_4 , C_2H_5 , C_2H_6 , CH_2CO) and a total of 44 reactions from which 17 are non-reversible (including 1 three-body).

Regarding the introduction of QSS assumptions, in the present ATR case for $\mathcal{T}_{\text{QSS}} = 0.10$, species H , OH , O , HO_2 , H_2O_2 , CH_3 , CH_2 , CH_2O , HCO , CH_3O , C_2H_3 , C_2H_4 , C_2H_5 , C_2H_6 and CH_2CO may be assumed in quasi-steady state. However species OH , HO_2 and CH_3 must be kept within the transported species, for the algebraic QSS system to be linear versus all species, leading to a mechanism with 10 transported species: H_2 , O_2 , OH , H_2O , HO_2 , CH_3 , CH_4 , CO , CO_2 and C_2H_2 . The results obtained with this preliminary mechanism are illustrated in Figures 6.7(c) for the trajectory issued from inlet 3. Because of the reduction in the number of species and reactions, and because of the introduction of the QSS hypothesis, the chemical rates of the transported species do not match those of the detailed mechanism, then the Arrhenius coefficients for the remaining 44 reactions are optimised.

The number of chemical parameters is $3 \times 44 = 132$. A set of $M = 96$ chromosomes (potential solutions) is built with an allowed variation of $\pm 5\%$ for \mathcal{A} , the pre exponential factor, $\pm 3\%$ for β , the temperature exponent and for E , the activation energy. The M trajectories are computed simultaneously over M processors with the set of equations 5.19-5.20 and the departure from the detailed chemistry response is measured with a fitness function based on species mass fractions. The population is advanced in time according to the genetic algorithm procedure depicted in Chapter 4 and the process is repeated up to convergence (minimisation of the fitness function). The rates of the resulting optimal mechanism are given in Table 6.3.

Running each of the three steps, it takes less than 8 hours to get a perfectly converged solution on an IBM iDataPlex type machine. Figures 6.7(a), 6.7(b) and 6.7(d) are showing comparisons between the responses obtained with the detailed mechanism and the reduced one for the target species H_2 , O_2 , H_2O , CH_4 , CO , CO_2 . The maximum difference is observed on the trajectories of CH_4 with an error of about 3% in the prediction of methane consumption.

6.3.2 Other reductions

Other mechanisms have been reduced from the GRI-3.0 [140] and the Lindstedt [151] chemical schemes following the procedure employed for the RAMEC mechanism. The only modification for the creation of the reduced schemes regards the definition of the composition of the burned gases. These are here initiated to the equilibrium condition for the perfect mixing of the three inlets instead of being set to the equilibrium of the stoichiometric condition. This new assumption appears more realistic for the simulation of the ATR system. Table 6.1 resumes the list and the size of the mechanisms reduced for the conditions of the ATR process.

Figures 6.8 and 6.9 provide a comparison of the target species mass fractions between the three detailed mechanisms, GRI-3.0, Lindstedt and RAMEC and their respective reduced versions for the conditions of the ATR system. The results of inlets 1, 2 and 3 presented on these figures are obtained considering a larger set of burned gases initiated with the composition corresponding to the equilibrium of the perfect mixing for the three inlets. Since the GRI-3.0 and the RAMEC mechanisms are both

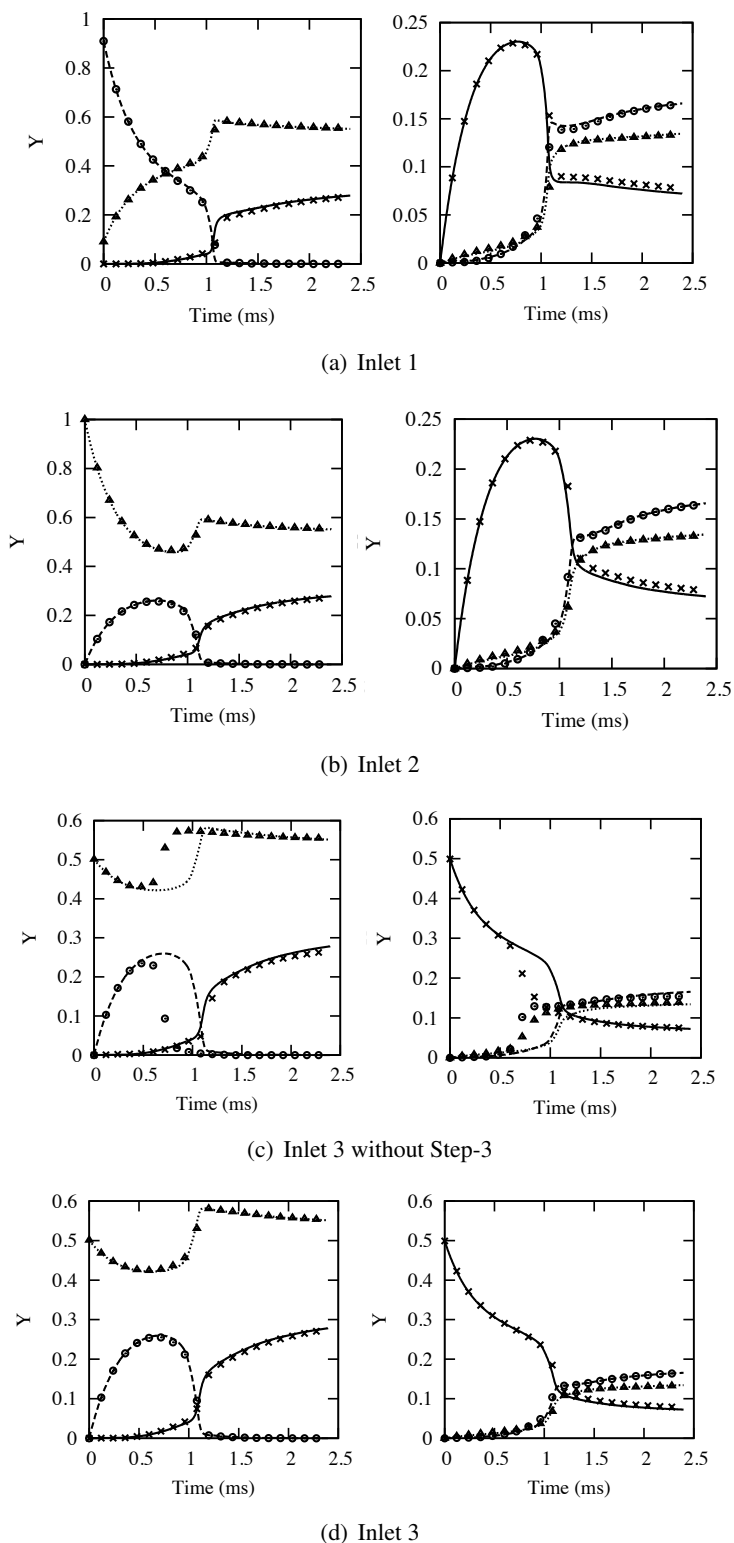
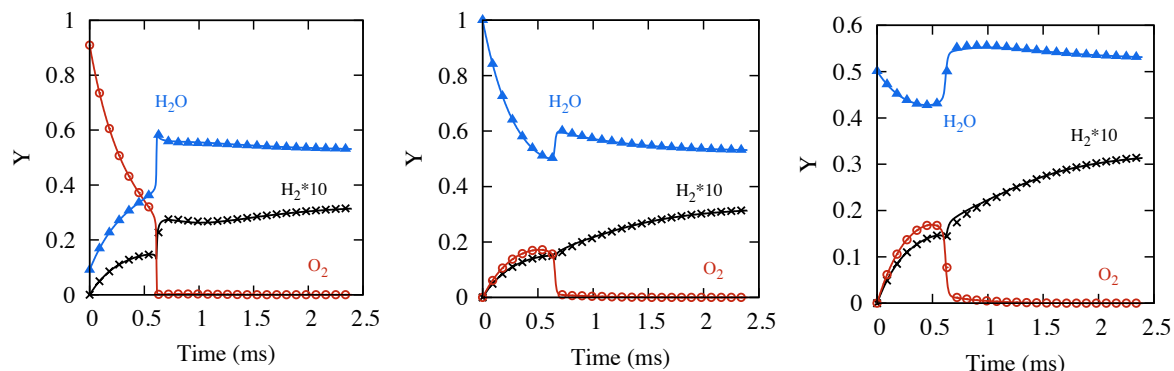
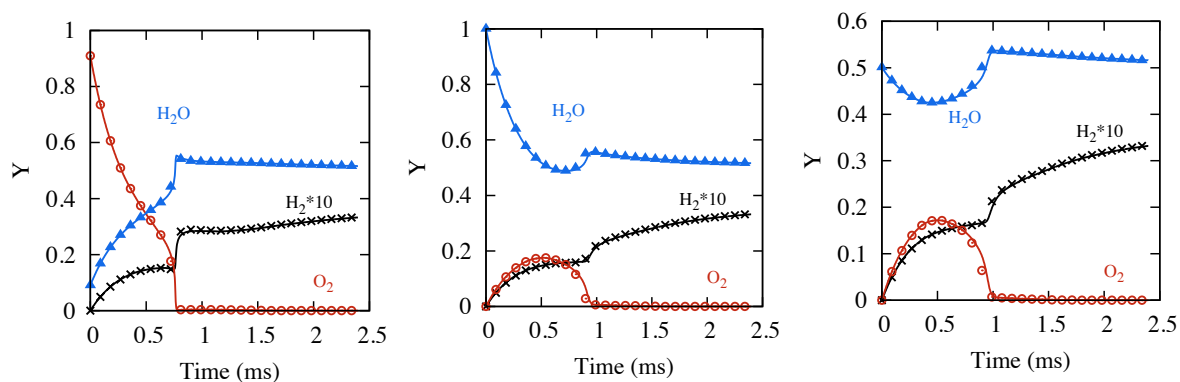


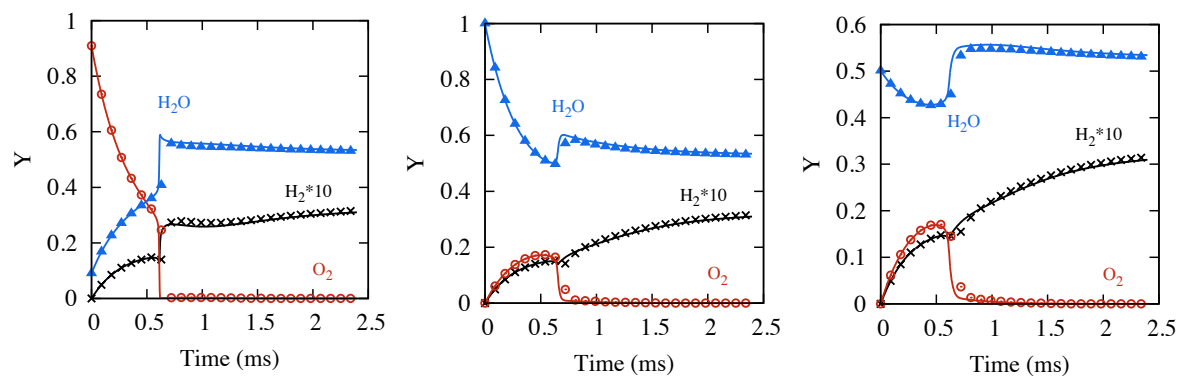
Figure 6.7: Mass fraction trajectories. Lines: Reference detailed mechanism [139]. Symbols: Reduced mechanism. Left plots: Line and (\times): $H_2 \cdot 10$, Dashed line and (\odot): O_2 , Dotted line and (\blacktriangle): H_2O . Right plots: Line and (\times): CH_4 , Dashed line and (\odot): CO , Dotted line and (\blacktriangle): CO_2 .



(a) Symbols: GRI-3.0 detailed mechanism [140]. Lines: Analytical mechanism derived from the GRI-3.0 with 17 species and 95 reactions. Left plot: inlet 1, centre plot: inlet 2, right plot: inlet 3.

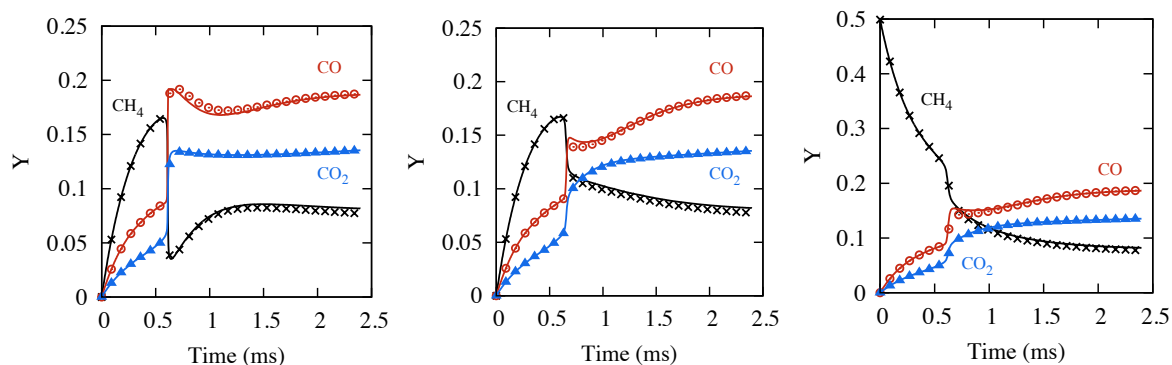


(b) Symbols: Lindstedt detailed mechanism [151]. Lines: Analytical mechanism derived from the Lindstedt with 16 species and 68 reactions. Left plot: inlet 1, centre plot: inlet 2, right plot: inlet 3.

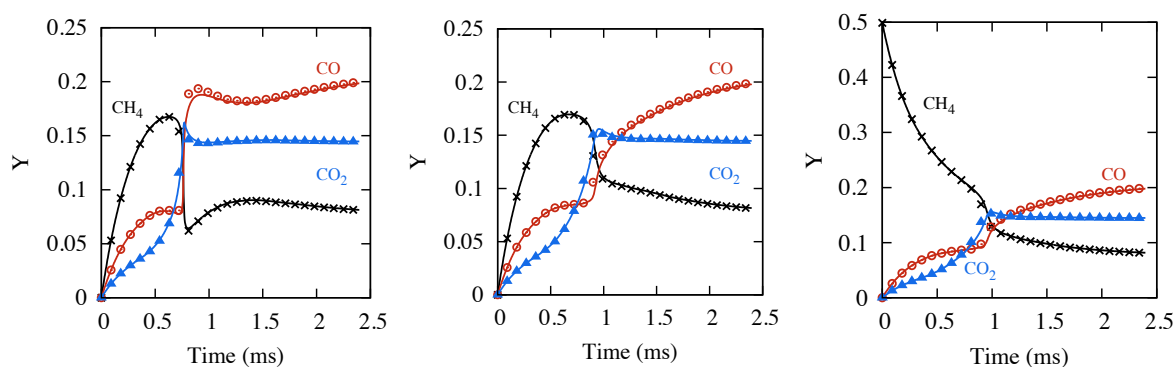


(c) Symbols: RAMEC detailed mechanism [139]. Lines: Analytical mechanism derived from the RAMEC with 16 species and 44 reactions. Left plot: inlet 1, centre plot: inlet 2, right plot: inlet 3.

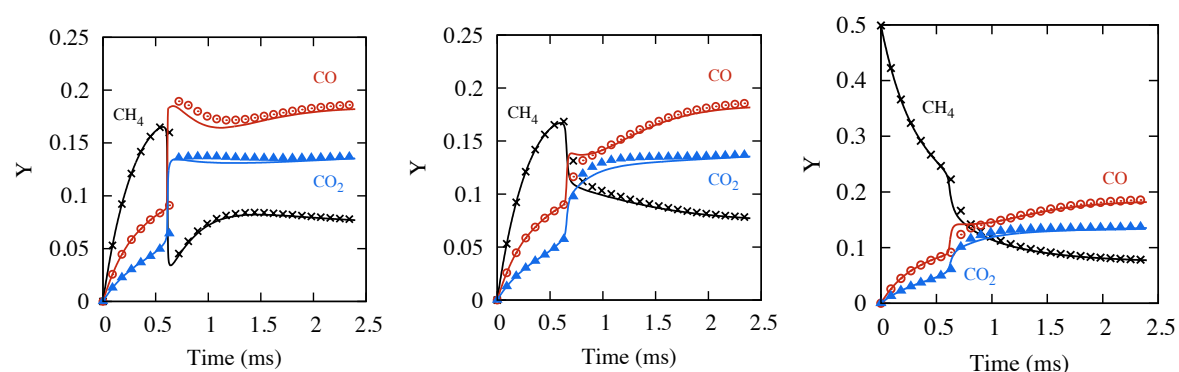
Figure 6.8: Comparison of the mass fraction trajectories for inlets 1, 2 and 3. Computations are performed using the GRI-3.0, Lindstedt and RAMEC mechanisms and their respective reduced versions. Symbols: Reference detailed mechanisms. Lines: Reduced mechanisms. Line and (\times): H_2^*10 , Dashed line and (\odot): O_2 , Dotted line and (\blacktriangle): H_2O .



(a) Symbols: GRI-3.0 detailed mechanism [140]. Lines: Analytical mechanism derived from the GRI-3.0 with 17 species and 95 reactions. Left plot: inlet 1, centre plot: inlet 2, right plot: inlet 3.

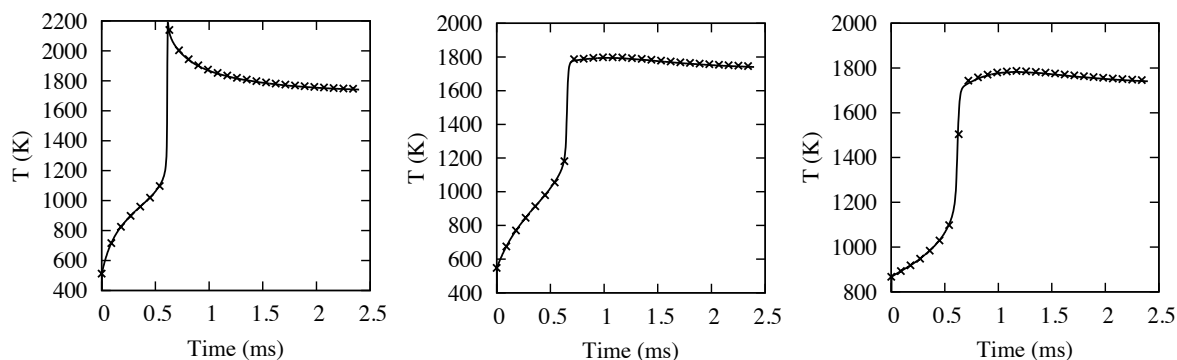


(b) Symbols: Lindstedt detailed mechanism [151]. Lines: Analytical mechanism derived from the Lindstedt with 16 species and 68 reactions. Left plot: inlet 1, centre plot: inlet 2, right plot: inlet 3.

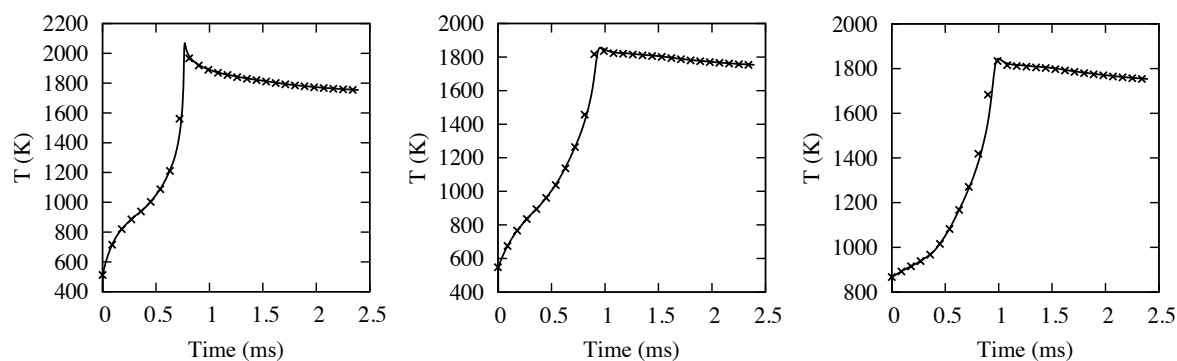


(c) Symbols: RAMEC detailed mechanism [139]. Lines: Analytical mechanism derived from the RAMEC with 16 species and 44 reactions. Left plot: inlet 1, centre plot: inlet 2, right plot: inlet 3.

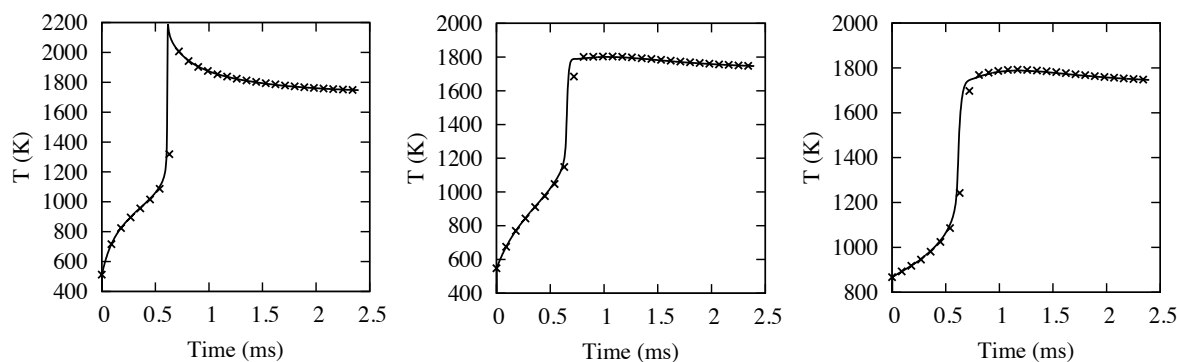
Figure 6.9: Comparison of the mass fraction trajectories for inlets 1, 2 and 3. Computations are performed using the GRI-3.0, Lindstedt and RAMEC mechanisms and their respective reduced versions. Symbols: Reference detailed mechanisms. Lines: Reduced mechanisms. Line and (\times): CH_4 , Dashed line and (\odot): CO , Dotted line and (\blacktriangle): CO_2 .



(a) Symbol: GRI-3.0 detailed mechanism [140]. Line: Analytical mechanism derived from the GRI-3.0 with 17 species and 95 reactions. Left plot: inlet 1, centre plot: inlet 2, right plot: inlet 3.



(b) Symbol: Lindstedt detailed mechanism [151]. Line: Analytical mechanism derived from the Lindstedt with 16 species and 68 reactions. Left plot: inlet 1, centre plot: inlet 2, right plot: inlet 3.



(c) Symbol: RAMEC detailed mechanism [139]. Line: Analytical mechanism derived from the RAMEC with 16 species and 44 reactions. Left plot: inlet 1, centre plot: inlet 2, right plot: inlet 3.

Figure 6.10: Comparison of the temperature trajectories for inlets 1, 2 and 3. Computations are performed using the GRI-3.0, Lindstedt and RAMEC mechanisms and their respective reduced versions. Symbols: Reference detailed mechanisms. Lines: Reduced mechanisms.

created from the same mechanism, it appears that their trajectories are very similar. The ones computed with the Lindstedt slightly differ from the ones obtained with the two other mechanisms especially in terms of ignition delay, although the equilibrium appears to be the same for the trajectories computed with the three mechanisms. Figure 6.10 provides same comparisons but for the temperature profiles. Again, the trajectories computed with the RAMEC and the GRI-3.0 appear to coincide while the temperature profile of the Lindstedt differs from the two others.

For every mechanism, the trajectories computed with the reduced schemes match accurately the ones obtained with the associated detailed mechanism. There is however a short delay in the trajectories of the reduced RAMEC compared to the reference on Figures 6.8(c), 6.9(c) and 6.10(c). This may be due to the assumption that was formulated for the burned gases composition employed for the derivation of this reduced mechanism.

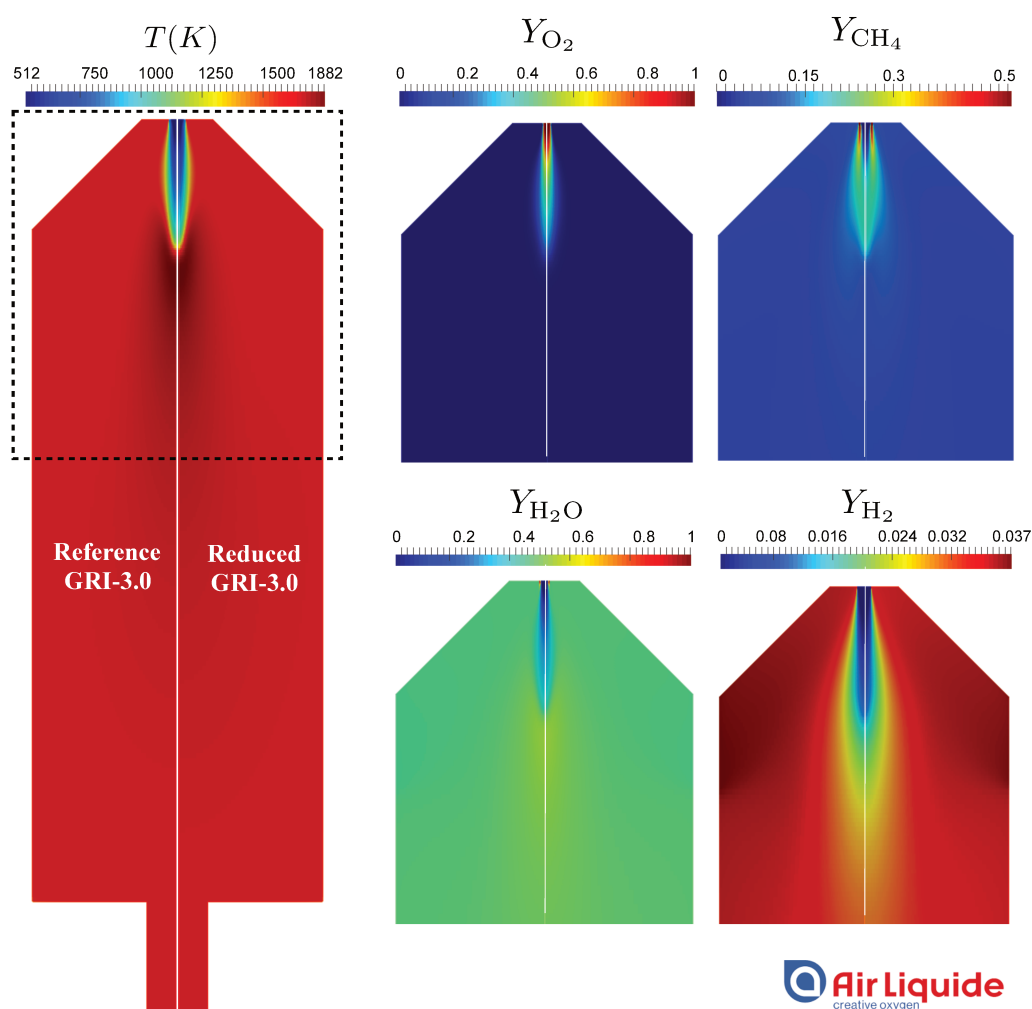


Figure 6.11: RANS simulation of an ATR reactor. Computations are performed with Fluent using as a reference the GRI-3.0 mechanism [140] with 35 species and 217 reactions (left images) and the skeletal version of the GRI-3.0 mechanism with 26 species and 95 reactions (right images).

6.4 Reduced schemes assessment using RANS simulations

The mechanisms derived from the GRI-3.0, Lindstedt and RAMEC detailed schemes have all been assessed with RANS computations of an ATR reactor. For each reduction, three computations have been performed: (1) a calculation with the detailed scheme for comparison, (2) a calculation with the skeletal mechanism and (3) a calculation with the analytical routine. The simulations have been performed by R. Xin in the Air Liquide's premises and under the supervision of G. Lodier and B. Labégorre. The flow solver Fluent is used with EDC modelling [185, 186] for the turbulent flame. This model is based on a description where the fine structures with Kolmogorov characteristic size are folded by the largest turbulent structures. The Eddy-Dissipation Concept introduced by Magnussen states that molecular mixing and chemical reactions take place within these small structures. Within each computational cell, the proportion of fine structures is quantified from a mass fraction of the total flow modelled in accordance with the ratio of kinetic energy between these two regions. These small structures exchange mass and energy with the surrounding environment according to a transfer rate, and reaction is solved within these fine scales for a modelled residence time and using a PSR description. The details about the implementation are not given in the present lines. Only the performances of the reduced chemistries are assessed in comparison to the reference used for the reduction.

Table 6.4 gives the computational time associated to a direct integration of the species source terms for each mechanism tested. Note that only 6 QSS expressions are used for the RAMEC analytical mechanism. Indeed, the convergence of the RANS simulations was not reached with the 12 QSS relations formulated earlier, a point that must be clarified in the near future. Figures 6.11 and 6.12 provide a com-

Combustion mechanism	N_{sp}	N_r	N_{QSS}	Computational time	Decrease (%)
GRI-3.0 [140]	35	217	-	34.2s/it	-
GRI-3.0 skeletal	26	95	-	13.9s/it	59.3
GRI-3.0 analytical	17	95	9	10.5s/it	69.3
Lindstedt [151]	29	141	-	14.0s/it	-
Lindstedt skeletal	22	68	-	8.0s/it	42.8
Lindstedt analytical	16	68	6	5.4s/it	61.4
RAMEC [139]	35	186	-	21.3s/it	-
RAMEC skeletal	22	44	-	7.6s/it	64.3
RAMEC analytical	16	44	6	5.4s/it	74.6

Table 6.4: Mechanisms reduced for the auto-thermal reforming of methane.

parison of the simulations respectively for the GRI-3.0 and RAMEC with their deduced skeletal versions. The computational results for the Lindstedt are not given. It is observed that the difference introduced with the skeletal mechanism derived from the GRI-3.0 is almost imperceptible. Same applies for the reduced mechanisms achieved with the Lindstedt mechanism (not shown). Interestingly the variation with the introduction of the QSS assumptions is negligible in all cases. The largest discrepancy observed is for the RAMEC mechanism (Figure 6.12). Two effects may explain these differences (1) the reduction in the number of species and reactions has been pushed towards larger extent than for the GRI-3.0 and Lindstedt mechanisms and (2) the reduction of the RAMEC was performed with a composition of the burned gases based on the stoichiometric mixing of the three inlets of the burner, instead of respecting the rich mixing composition corresponding to Z_1^{FM} and Z_2^{FM} .

6.5 Conclusion

The chemistry reduction/optimisation methodology ORCh depicted earlier was assessed in the present chapter, for a complex industrial system employed in the field of syngas production. The auto-thermal reforming of methane (ATR) is studied focusing on the region of partial oxidation (POX). Methane, oxygen and steam are separately injected into the combustion chamber of an ATR system. The flow reacts under the influence of an intensive turbulent mixing between the introduced mixtures and a large amount of recirculating burned gases at high temperature.

The new canonical problem proposed in the previous chapter with the stochastic mixing of elementary particles particularly suits the present non-premixed application composed of three different inlets and for which combustion is highly piloted by the recirculating gases. Three detailed mechanisms from the literature have been reduced for those conditions to skeletal and analytical forms ending to at least a 50% reduction in the number of species and reactions. The trajectories of Figure 6.7 for the RAMEC mechanism, those of Figures 6.8(a), 6.9(a) and 6.10(a) for the GRI-3.0 mechanism and the profiles of Figures 6.8(b), 6.9(b) and 6.10(b) for the Lindstedt mechanism demonstrated a perfect reproduction of

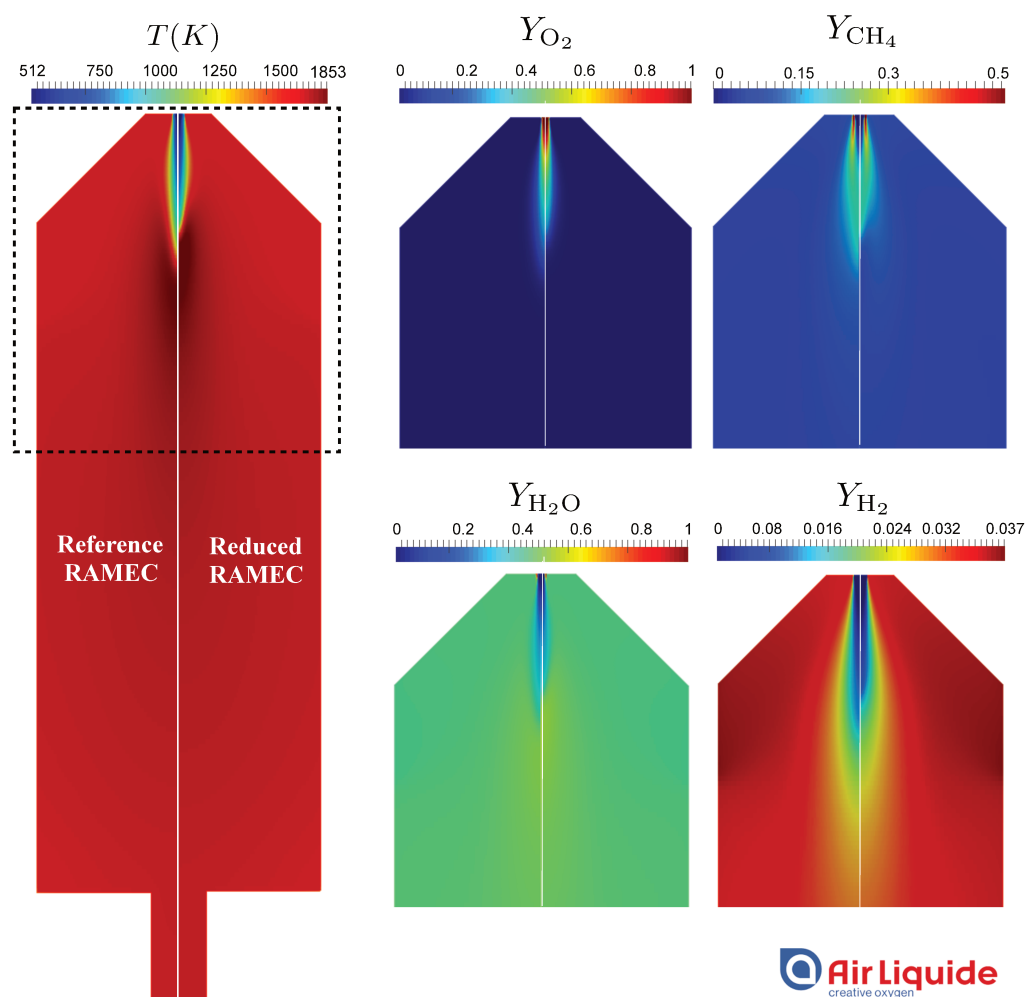


Figure 6.12: RANS simulation of an ATR reactor. Computations are performed with Fluent using as a reference the RAMEC mechanism [139] with 35 species and 186 reactions (left images) and the skeletal version of the RAMEC mechanism with 22 species and 44 reactions (right images).

the reference species and temperature profiles for the conditions of the reduction. The impact of the composition selected for the definition of the burned gases particles appeared to have a non-negligible impact on the reduced chemistry. It led to differences for the mechanisms reduced with the RAMEC (see Figures 6.8(c), 6.9(c) and 6.10(c)) which was initially studied with a stoichiometric composition.

The derived mechanisms have been studied by Air Liquide using RANS simulations of an ATR reactor. Depending on the mechanisms, the skeletal schemes demonstrated a 40% to 60% reduction in computational time while adding analytical expressions led to a further 30% reduction. In terms of precision, the mechanisms derived with the GRI-3.0 and Lindstedt mechanisms did not show much difference with the reference computed with the same simulations parameters. The simulations performed with the skeletal RAMEC showed a short discrepancy although this difference should again be tempered by the different composition for burned gases particles.

Although the 1D simulations performed with CANTERA allowed for the introduction of 12 QSS relations, no more than 6 QSS assumptions could be employed with Fluent. The same applied for the other schemes but to a lower extent i.e. even though the criteria $\mathcal{I}_k < 10\%$ appeared to work in 1D computations for the setting of the species under the assumption that production equals consumption, with the RANS simulations no convergence could be achieved for $\mathcal{I}_k > 5\%$. This point must be further investigated.

Chapter 7

Application to kerosene-air combustion: CO and NO_x levels prediction

Contents

7.1	Introduction	161
7.1.1	Combustor design	162
7.1.2	Pollutants emissions	162
7.1.3	LEMCOTEC project	167
7.2	Studied configuration	167
7.2.1	Multipoint injection	168
7.2.2	Previous LES study	168
7.3	Reduced chemical schemes for kerosene combustion	169
7.3.1	Kerosene oxidation detailed mechanisms	169
7.3.2	ORCh for kerosene	169
7.3.3	Mechanism reduction	171
7.3.4	QSS species and optimisation	176
7.3.5	Results and comparison between a surrogate composition and n-decane	178
7.3.6	Reduction limits	180
7.4	Large-Eddy Simulation of an ultra-low NO_x combustor	183
7.4.1	Numerical settings	183
7.4.2	Simulation	186
7.5	Conclusion	190

7.1 Introduction

This chapter presents an application of the reduction methodology to the conditions of an aeronautical combustion chamber designed in the context of NO_x reduction. A detailed chemical mechanism is first reduced for the operating conditions of the study using the full surrogate composition and accounting for the description of both CO and NO_x levels in diffusion and premixed regimes. The mechanism is then further reduced by introducing a simplification in the composition of the studied fuel. To assess

the capabilities of the reduction methodology, the approach is pushed towards its limits trying to capture only the concentrations of CO while maintaining reasonable equilibrium temperature and flame velocity profiles. The settings of a Large-Eddy Simulation (LES) performed to predict the levels of pollutants associated to the studied multipoint injection system installed inside a mono-sector are then presented along with a qualitative analysis of the results and a comparison with experimental measurements at the exit of the combustor.

7.1.1 Combustor design

The development of aero-engines raises many issues. Each of these constraints need to be addressed very carefully to provide a safe, economic and long-term operation of the engine. Current major challenges for the design/conception of aeronautical combustion chambers are related to; **(1) the geometry:** design of the inlet and outlet interface, definition of the combustor length, **(2) the operability:** capabilities regarding the ground ignition, in-flight re-ignition, the combustion stability for both standard operating conditions and under extreme circumstances such as water, ice, sand and/or accidental birds injection, **(3) the performances:** estimation of the combustor efficiency, of the thermal map, prediction of both pollutants and smokes emissions, adaptation to other types of fuel and **(4) the thermo-mechanical behaviour:** thermal resistance of the combustion chamber, vibration resistance, lifetime analysis. The present chapter is looking towards performances and more precisely towards the estimation of the pollutants levels.

7.1.2 Pollutants emissions

7.1.2.1 Certifications

The International Civil Aviation Organisation (ICAO) is an ONU body set up to elaborate the norms and the regulations to standardise international aeronautic transportation. The Committee on Aviation Environmental Protection (CAEP) is a technical entity of the ICAO council which aims at studying and developing proposals to lower the impact of aviation on the environment. New aircrafts are required to meet the ICAO engine certification standards that impose limits for aero-engines emissions seen separately in terms of local air quality (LAQ) and global emissions. This includes the definition of goals for

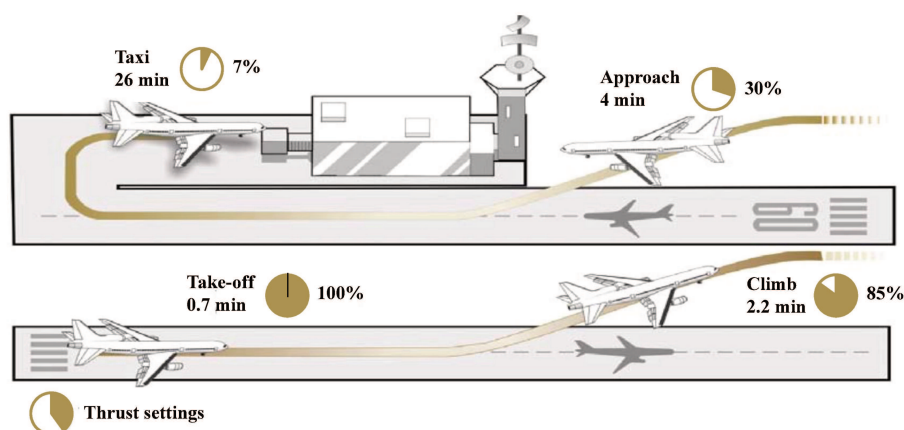


Figure 7.1: Illustration of ICAO emissions certification procedure; landing take-off cycle [187].

the emissions of NO and NO₂ (commonly referred as NO_x), carbon monoxide and unburned hydrocarbons (HC) for a standard landing take-off (LTO) cycle (see Figure 7.1).

Each engine certification is performed on a test bed going through the thrust settings given in Figure 7.1 to collect the fuel flow and pollutants emissions for the defined standard modes. Table 7.1 provides the 2006 ICAO standard values for the certification of an aero-engine when burning 1 kg of jet fuel. Much of the efforts for future engines are focusing on the NO_x reduction. The CAEP has a target of 45% NO_x reduction for medium term (2016) and a reduction goal of 60% for the long term (2026) compared to the standard emissions of 2006 at a reference operating pressure ratio (OPR) of 30. On another hand,

Emission	Limit	Emission	Limit
CO ₂	3160.0 g	CO	< 0.60 g
H ₂ O	1290.0 g	Particulates	< 0.05 g
NO _x	15.0 g	Hydrocarbons	< 0.01 g
SO _x	1.2 g		

Table 7.1: 2006 ICAO standards for emissions certification of aircraft engines.

the Advisory Council for Aeronautics Research in Europe (ACARE) targets an 80% reduction of the NO_x emissions by 2020 in comparison to the levels of 2000. In addition, ACARE imposed a 20% reduction of the fuel consumption of the engine and of the associated CO₂ emissions.

7.1.2.2 CO formation

The creation of the intermediate species CO happens in the flame region through the interaction with highly reactive precursors such as HCO. It then oxidises to form CO₂ but through slower chemical processes which are initiated in the flame region and ended in the post-flame region far from the reactive layer. Because of this slow recombination, the levels of the CO concentrations at the exit of aeronautical combustion chambers are always above the equilibrium values.

- The higher levels of CO concentrations are found in the **fuel rich regions** of the combustion chambers because the lack of O₂ reduces the rates of the reactions allowing the CO recombination into carbon dioxide CO₂. Rich regions are typically encountered in the non-premixed or partially premixed flames that develop in configurations where the fuel is injected in its liquid form.
- **Flame quenching** close to the walls or because of poor air-cooling design also reduces the rates of the CO recombination, hence locally and globally increasing the CO concentrations [188].
- A **poor combustion efficiency** is also associated to an incomplete oxidation of the carbon monoxide. This is for instance seen in lean blow-off conditions [189].

7.1.2.3 Influence of the operating conditions on the CO levels

A high inlet temperature results in a high flame temperature which has the tendency to provoke more chemical dissociations. In turns, the CO-CO₂ equilibrium is shifted towards CO. In contrast, an increase of the pressure inside the combustor favours the recombination of CO into CO₂. At full power, the CO emissions are far below the restrictions thanks to the high levels of combustion efficiency associated to today's aeronautical chambers. Nevertheless, CO emissions become an issue at low power levels for which a much higher CO production is observed.

7.1.2.4 NO_x formation

The reaction mechanisms describing the formation of NO are commonly split into two families associated to different characteristic times; (1) fast processes relying on the carbon chemistry and (2) slow reactions that appear in post-flame regions where carbonated species have reached chemical equilibrium. The chemical paths proposed in the literature result from recent studies which are still subject to debate.

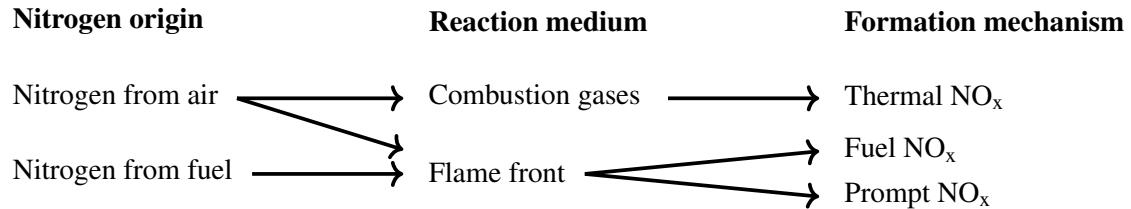
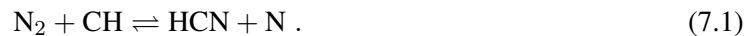


Figure 7.2: NO_x formation paths [190].

• Front flame NO

As introduced in Figure 7.2, two reacting paths have been considered to model the production of nitric oxide within the flame, namely the prompt NO and the fuel NO.

- Fenimore [191] first introduced the **prompt NO** by noticing the presence of high NO concentrations in regions too close to the flame front to be attributed to the slow post-combustion processes. He proposed a mechanism that relies on the N₂ decomposition by combustion radicals such as the intermediate CH. At that time, Fenimore attributed this process to the production of the HCN radical:



Because it provides a satisfactory prediction of the NO formation for several applications, this path has been retained for the derivation of numerous mechanisms including the Luche [65] and the GRI-3.0 [140] schemes used as reference in the present thesis. It is however accepted today that the radical NCN is the proper species to model the prompt NO since unlike radical HCN it agrees with the quantum mechanics principle of spin conservation.



The formation of prompt NO is essentially observed in the flame front of stoichiometric and slightly rich flames due to the higher temperature levels encountered and to larger hydrocarbon radicals concentrations. Typically, the time scale for the prompt NO are of the order of 10⁻⁴ s for a 10 bar combustion and of about 10⁻² s for an atmospheric pressure.

- The **fuel NO** results from the degradation of a fuel which contains azote bonds. For instance, this is encountered for the combustion of coal that contains at least 1% of azote in atomic fraction, even for the purest types. This is however never the case for kerosene or methane which are pure hydrocarbons fuels.

• NO production in the post-flame region

- **Thermal NO** formation essentially happen in the burnt gases. It is described by the extended version of the Zeldovich mechanism [192],



Reaction 7.3 is associated to a high activation energy. As such, it is the rate limiting reaction of the Zeldovich chain. Moreover, the concentration of the species O exponentially depends on the temperature of the gases, so that the rate of the reaction 7.3 becomes significant only for temperatures that are higher than 1800 K. For both reasons the production of NO happens essentially in the burned gases region. It is reported that the level of NO produced with these slow post-flame reactions is of the order of 35% to 70% of the total NO production. This chemical process is slow in comparison to the other reacting mechanisms. The concentration of NO at the exhaust of the combustors are therefore often below equilibrium and the levels of emissions strongly depend on the residence time.

- The **N₂O mechanism** is added to the Zeldovich description through the reactions:



It contributes to a large extent to the formation of NO_x for lean premixed flames at high pressures [193]. Such conditions are typically found in recent gas turbines combustors.

- Two steps are added for the production of NO through the **intermediate species NNH**;



This chemical pathway frequently appears for flames at low temperatures.

- Finally the production of NO via **reactions with NO₂** is given by;



which appears to be obtained for moderate temperatures. The concentrations in NO₂ are usually small at the combustor exit.

7.1.2.5 Influence of the operating conditions on the NO_x production

The impact of the fuel burning conditions (temperature, pressure, mixing, equivalence ratio...) on the production of NO_x has been largely studied in the literature. A few information is given below on this matter:

- **Temperature** significantly impacts the formation of NO_x. Higher inlet temperatures lead to increased flame and post-flame temperatures hence raising to a large extent the production of thermal NO and to a smaller one, the formation of prompt NO.
- **Pressure** is known to significantly influence the production of NO_x however there are large inconsistencies in the literature on its impact depending on the considered formation pathway. It is usually agreed that thermal NO have a square root dependence to pressure $P^{0.5}$. For the other pathways, it is much more difficult to conclude. Some analysis demonstrated a decrease of the NO concentration in the inner flame region for higher pressures and an increase in the post flame zone while results at lean well premixed conditions indicated the contrary and others at very well mixed conditions showed no clear dependence on pressure. As a result, the pressure dependence on the formation of NO_x seems to be largely influenced by the conditions of the study and in particular by the mixing and the overall equivalence ratio.
- **Liquid fuel** plays a major role in the production of NO_x since the evaporation of fuel droplets leads to large inhomogeneities in the flow, as for instance, the creation of rich pockets of fuel-air mixtures. Baessler *et al.* [194] conducted a study of the NO_x levels depending on the pre-vaporisation of the fuel. They demonstrated that there is a clear dependence of the NO_x production on the combustion regime which is driven by the quality of the spray.

7.1.2.6 Constraints

Figure 7.3 illustrates the levels of pollutants emissions as a function of the equivalence ratio. The window for the lowest CO emissions is restricted to lean conditions and centred around $\phi = 0.8$. Unfortunately, the figure shows that there is no ideal condition for the lowering of the pollutants levels i.e. diminishing the NO_x production eventually results in an increase of the CO emissions and vice versa. The best compromise between the production of both CO and NO_x is depicted in the graph 7.3 for very lean conditions

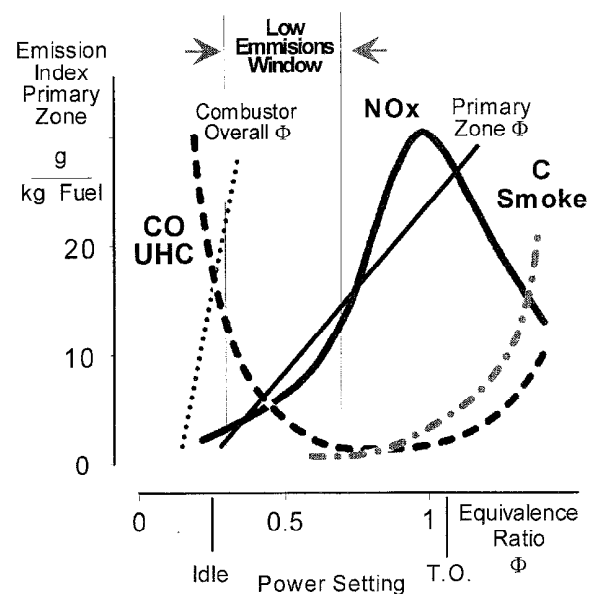


Figure 7.3: Pollutants emissions (NO_x, CO, unburned hydrocarbons, smokes) as a function of the equivalence ratio, for standard combustors [195].

approximately from $\phi = 0.4$ up to $\phi = 0.6$. This observation is at the origin of the development of Lean Partially Premixed (LPP) combustion systems which encompasses the conditions of the present study.

7.1.3 LEMCOTEC project

The design of today's gas turbines points towards an increase of the Overall Pressure Ratio (OPR) which leads to higher pressure and temperature levels. Unfortunately this favours NO_x production, hence novel models are necessary. In this context, the tendency is to move away from stoichiometry, since large reductions in the NO_x emissions are achievable coupling local rich conditions to an overall lean combustion. As a partner of the European project called Low Emissions Core-Engine Technologies (LEMCOTEC), Safran is currently developing a prototype for an ultra-low NO_x combustion chamber. Different designs of the combustor and of the associated components have been proposed and experimentally studied by the company. The present chapter focuses on the simulation of one of the proposed design for the injection system. The performances in terms of overall CO and NO_x emissions are known for different operating conditions.

7.2 Studied configuration

A series of experimental studies have been conducted at Onera to assess the performance of the various designs proposed by Safran for the injection system. They used a test rig that is composed of a mono-sector combustion chamber to discriminate between the different models. The exact operating conditions cannot be described for confidentiality reasons, however the configuration under study is a kerosene-air flame operating under a pressure of the order of 10 bar. Probes are placed at the exit of the combustor to measure the pollutants levels. Unfortunately because of the high pressures and temperatures achieved within the chamber, optical measurements are difficult to perform and quite expensive. In this respect, the use of LES allows for better understanding the phenomena that drive the pollutants formation within the combustion chamber.

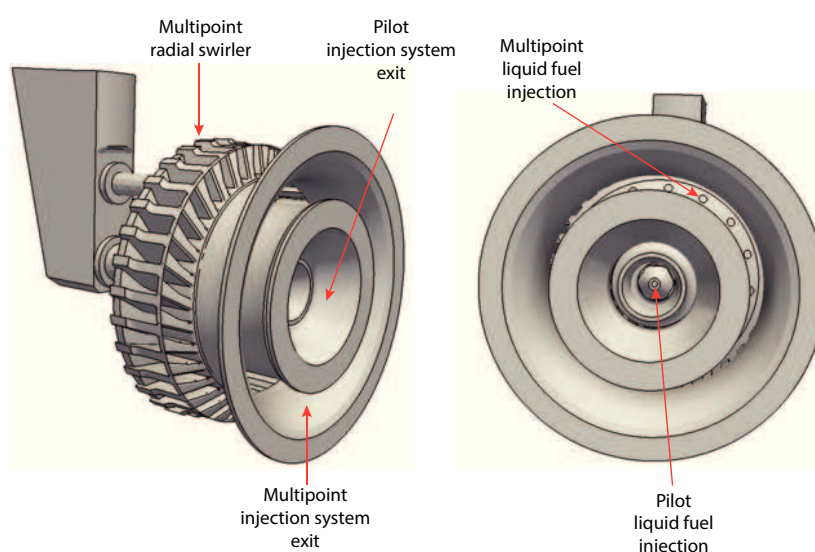


Figure 7.4: LEMCOTEC multipoint injection system. Image extracted from [17].

7.2.1 Multipoint injection

The geometry that is studied in the present chapter is given in Figure 7.4 for two different views. The injection system is divided into two parts that are radially staged: (1) the pilot injection system that is composed of two co-rotating swirlers associated to a hollow-cone central injector and (2) the multipoint injection system that is composed of 16 swirler vanes installed into a radial swirler. The injection of liquid fuel is achieved thanks to 16 plain holes placed in the inner wall.

The principle that lies behind the creation of such a design is illustrated on Figure 7.5. The pilot flame is attached in the centre of the geometry surrounding the Primary Recirculation Zone (PRZ). Its main function is to provide hot combustion gases to allow for a correct stabilisation of the main flame. In addition, the high level of swirling in the multipoint injection system is expected to guarantee a correct atomisation and evaporation of the liquid jets as well as an efficient mixing with the carrying air flow. In principle, this leads to the creation of a lean premixed flame hence allowing for lower NO_x emissions.

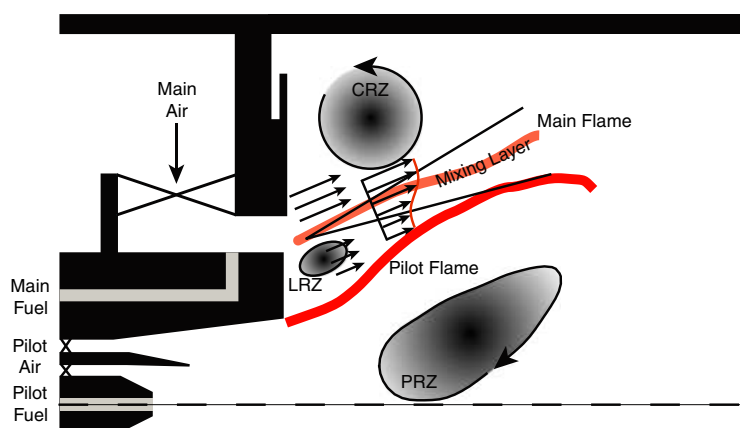


Figure 7.5: Illustration of a multipoint injection system [196].

7.2.2 Previous LES study

The same configuration has been studied at CERFACS by T. Jaravel [17] using the LES code AVBP with a mechanism composed of 27 species and 452 chemical reactions. This mechanism is reduced from the JetSurf chemical scheme composed of 120 species and 977 reactions to which is added the 17 species and 245 reactions that describe NO_x formation in the Luche chemical scheme. The list of species used in his simulation is given in Table 7.2.

Transported species	Analytically resolved species
N ₂ , H, H ₂ , O, OH, O ₂ , H ₂ O, HO ₂ , CO, CH ₂ O, CH ₃ , CO ₂ , CH ₄ , C ₂ H ₆ , C ₂ H ₄ , CH ₂ CO, C ₂ H ₂ , C ₃ H ₆ , C ₄ H ₈ , C ₄ H ₆ , C ₅ H ₁₀ , C ₆ H ₁₂ , NC ₁₂ H ₂₆	H ₂ O ₂ , CH, CH ₂ , CH ₂ (S), HCO, C ₂ H ₅ , C ₂ H ₃ , CH ₃ O, HCCO, C ₂ H, AC ₃ H ₅ , CH ₂ CHO, NC ₃ H ₇ , C ₄ H ₇
NO, NO ₂ , HCN, N ₂ O	N, NH, NCO, NH ₂ , HNCO, HNO

Table 7.2: Species of a n-dodecane (NC₁₂H₂₆) reduced mechanism (by T. Jaravel [17]) composed of 27 transported species associated to 20 QSS relations and 452 reactions.

7.3 Reduced chemical schemes for kerosene combustion

The reduction and optimisation strategy that has been introduced all along this thesis is now applied for the derivation of chemically reduced mechanisms for aeronautical applications. In particular, the methodology is employed for the creation of kinetics for the prediction of the NO_x and CO emissions and of two other schemes further reduced to only apply to CO prediction while maintaining reasonable flame speed and equilibrium temperature profiles for a large range of equivalence ratios.

7.3.1 Kerosene oxidation detailed mechanisms

Several detailed mechanisms are found in the literature for the combustion of kerosene surrogates. A few important releases are the mechanism by Dagaut [197] that is composed of 225 chemical species and 3493 reactions and a version that derives from of this mechanism, developed by Luche [65] accounting for 91 species and 991 reacting steps. Because of its reasonable size in comparison to other detailed schemes for kerosene-air combustion, the Luche mechanism often serves as a standard reference. It is employed as a starting point for both reduction and optimisation in the present chapter. The surrogate composition that is used is the one proposed by Luche [65] and given in Table 7.3.

Name	Formula	Mass fraction	Molar mass (g/mol)
N-decane	NC ₁₀ H ₂₂	0.767388	142.284
Propylbenzene	PHC ₃ H ₇ ¹	0.131402	120.194
Propylcyclohexane	CYC ₉ H ₁₈	0.101210	126.241
Kero Luche	C _{9.73957} H _{20.0542}	1	137.195

Table 7.3: Liquid Kerosene composition as proposed by Luche [65].

7.3.2 ORCh for kerosene

The ORCh strategy is used to derive four chemically reduced mechanisms for a large range of conditions and for various sets of targets and precisions. First, a mechanism that properly gets most of the physic of kerosene-air flames in diffusion and premixed regimes is proposed. It is created to recover the proper equilibrium temperature, the flame speed and the production of CO and NO_x. A second version is derived with the exact same targets but using n-decane (NC₁₀H₂₂) instead of the full kerosene surrogate description. A third mechanism with 22 transported species is achieved by removing the NO_x from the

	N species	N reactions	N QSS	Fuel composition	Targets
Reference mechanism	91	991	-	Surrogate	-
Mechanism A	32	419	27	Surrogate	NO, NO ₂ , CO, T, S _L
Mechanism B	26	338	24	N-decane	NO, NO ₂ , CO, T, S _L
Mechanism C	22	222	14	N-decane	CO, T, S _L
Mechanism D	16	95	7	N-decane	CO, T, S _L

Table 7.4: Description of the characteristics of the four mechanisms reduced from the Luche reference scheme for the conditions of the LEMCOTEC application.

¹PH is a phenyl group; a cyclic group of atoms with the formula C₆H₅.

list of targets. Finally to look for the smallest mechanism possible a further reduction is performed. It is observed that keeping 16 transported species is enough to get a proper description of the diffusion regime and most of the physics that describe perfectly premixed flames.

7.3.2.1 Stochastic particles definition and deterministic trajectories construction

A total amount of 880 particles is divided into three groups, each corresponding to a certain mass of air, of kerosene and of recirculating burned gases. The particles of a given group are initiated to the conditions of the fluid they represent. Kerosene is considered in its liquid form so that the particles that are initiated to the fuel condition represent a certain amount of kerosene droplets that will undergo evaporation. A mixing characteristic time $\tau_t = 0.1$ ms is defined from the ratio k/ϵ of a RANS simulation performed by Safran on the geometry of the LEMCOTEC burner. The initial size of the droplets is estimated from the mean of the Sauter Mean Diameter associated to the studied injection systems (pilot and multipoint). As a first attempt the same diameter is fixed for every droplet and every kerosene particle. The time evolution of the droplets diameter pilots the fuel release. It is computed using the d^2 -law [161]. The problem is solved in time considering mixing, evaporation and reaction according to the equations 5.9-5.10. The deterministic trajectories that will serve for the reduction analysis and for the optimisation are constructed from the computation of the mean properties of the gaseous phase 5.21-5.22 of the particles and from the relaxation to these mean values 5.19-5.20.

7.3.2.2 Impact of the mixing on particles trajectories

It is first necessary to ensure that the size of the equivalence ratio area that is covered by the stochastic problem is large enough i.e. ensure that the particles are facing very rich to very lean conditions, as is the case in the studied combustion chamber. Figure 7.6(a) gives a scatter plot of the kerosene, air and burned gases particles distributed in a temperature vs mixture fraction diagram for a mixing characteristic time $\tau_t = 0.1$ ms. Although a few amount of particles appear to react in the rich region, it is observed that the great majority of the particles are mixed together before reacting. Kerosene particles are therefore rapidly diluted by the large amount of air, hence leading to overall lean reacting conditions. To examine this issue, an analysis of the impact of the mixing time on the range of equivalence ratios covered by

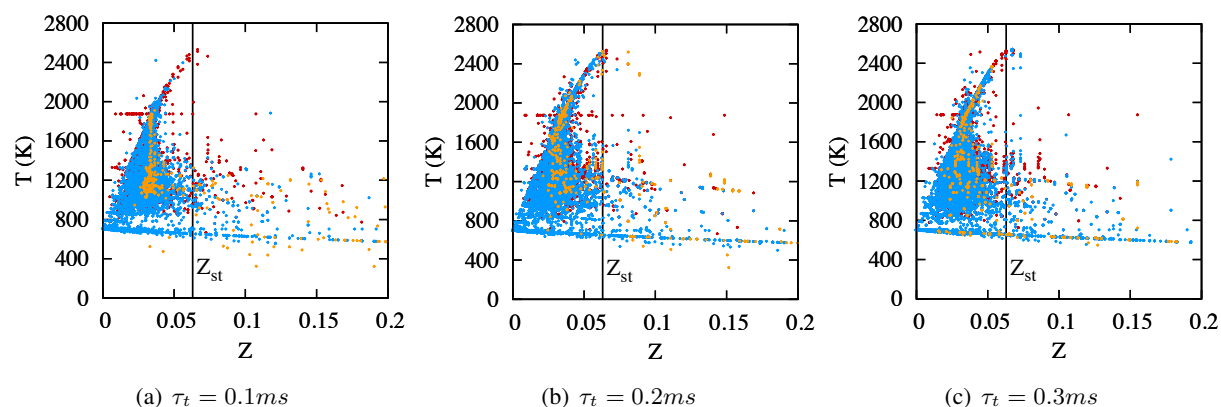


Figure 7.6: Scatter plots of particles temperature as a function of their mixture fraction for several micro-mixing times. Particles are coloured depending on the initial condition they are given: (●): air, (●): kerosene and (●): burned gases.

the particles of the simulated process is proposed on all the plots of Figure 7.6. Although it appears that increasing the mixing characteristic time slightly enlarges the range of equivalence ratios faced by the particles, it does not allow for covering sufficiently the rich region. Therefore, it appears necessary to account for the effects induced by the staged combustion and by the additional air. In principle, more complex mixing laws may be implemented relying, for instance, on separated groups of particles representing the pilot flame region and the conditions faced by kerosene and air particles within the multipoint injection system. These separated groups may be mixed together along with a large quantity of burned gases and of dilution air after a certain time. Such an implementation may be the final extent of the methodology. However, as a first attempt to account for the injection of cooling and dilution air, a simplified approach is employed. At initial time, an arbitrary amount of 60% of the air elementary particles is

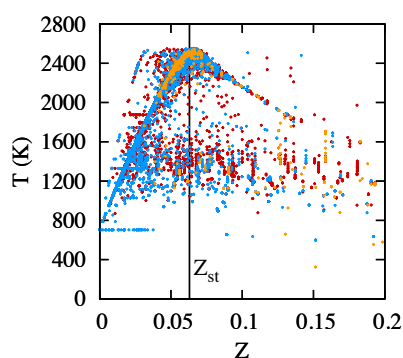


Figure 7.7: Scatter plot of particles temperature as a function of their mixture fraction. The air is progressively allowed to participate in the mixing. Particles are coloured depending on the initial condition they are given: (●): air, (●): kerosene and (●): burned gases.

allowed to mix with the kerosene and burned gases particles, the rest being released progressively along the simulation time. Figure 7.7 illustrates the distribution of the particles in the same diagram using this delayed characteristic. Thanks to the lowering of the initial amount of air, the range of equivalence ratios that is covered by the reacting particles now includes the rich region. Adding the remaining amount of air progressively translate the equilibrium line to the global lean condition of the LEMCOTEC burner.

7.3.3 Mechanism reduction

Figure 7.12(a) shows the deterministic trajectories computed with the Luche [65] reference mechanism for some of the major reactants (namely $\text{NC}_{10}\text{H}_{22}$, O_2), major pollutant products (CO , CO_2) of the kerosene oxidation and for the target species NO and NO_2 . It is possible to distinguish between four zones in the NO profiles for the simulated process. (1) For $t < 0.50$ ms, the hot burned gases are mixed with the fresh air and the fuel. This leads to a large production of thermal NO as described by the Zel'Dovich mechanism, (2) For $t \in [0.50 : 1.20]$ ms], the fuel is decomposed because of the energy provided by the burned gases, this increases furthermore the temperature and provoke the creation of the first intermediates. The temperature level reached leads to a decrease in the concentration of NO through its recombination into NO_2 . (3) The flame front is observed for $t \in [1.20 : 1.30]$ ms]. As expected it is associated to an increase in the NO mass fraction due to the production of prompt NO . (4) Within the post-flame region ($t > 1.30$ ms) there is again a production of NO through the mixing with the remaining air.

As usual, the reduction procedure is initiated with the DRGEP approach. The methodology for

lumping is applied for the first time in this section, because there are some isomers within the Luche mechanism. Again the QSS assumption and the proposed optimisation strategy will be used to end up with a reduced chemistry. Targets are obviously to reproduce the CO and NO_x levels and to recover flame speed and temperature. Both premixed and diffusion regimes are considered.

7.3.3.1 DRGEP analysis

Relation graphs for the production/consumption of NO are given on Figure 7.8 at times $t = 1.25$ ms and $t = 1.50$ ms, and the graph for species CO is given on Figure 7.9 at $t = 1.25$ ms. The number of

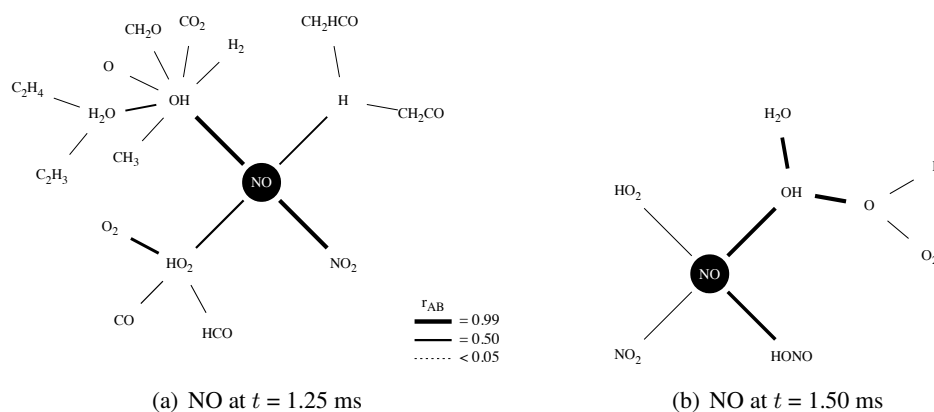


Figure 7.8: Directed relation graphs for species NO at various time of the reacting process. Only interactions greater than $r_{AB} = 0.10$ are represented.

chemical species interacting with species NO reduces significantly in the post-flame region compared to that in the flame layer. Interestingly, although the analysis is done for kerosene-air combustion and using the Luche mechanism, the species strongly related to CO are almost the same as for methane-air combustion.

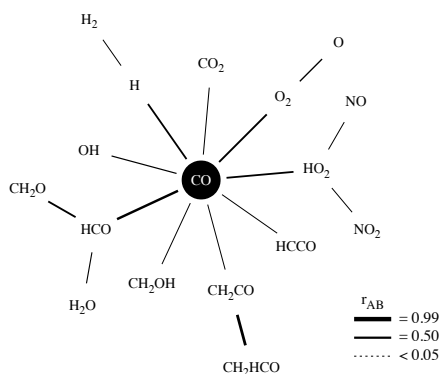


Figure 7.9: Species CO directed relation graph at $t = 1.25$ ms. Only interactions greater than $r_{AB} = 0.10$ are represented.

A small threshold error is first defined so as to remove the most unnecessary species while maintaining a good reproduction of the species profiles $E_{S_{\text{mean}}}^0 = E_{T_{\text{mean}}}^0 = 3\%$. The obtained mechanism is composed of 64 chemical species.

7.3.3.2 Isomers lumping

The present section focuses on the application of the linear lumping procedure proposed by Pepiot and Pitsch [102] that was reported in the review chapter. Large detailed mechanisms are often composed of several species that share the same molecular formula but with a different chemical structure. These groups of species are called isomers. They are given in Table 7.5 for the 64 species mechanism previously reduced with DRGEP. As introduced in the review of the literature, some of these isomers may be cast

Brut	Isomers
C ₁₀ H ₂₁	AC ₁₀ H ₂₁ , CC ₁₀ H ₂₁ , DC ₁₀ H ₂₁ and EC ₁₀ H ₂₁
C ₉ H ₁₇ C	CC ₉ H ₁₇ C, EC ₉ H ₁₇ C and FC ₉ H ₁₇ C
PHC ₃ H ₆	APHC ₃ H ₆ and CPHC ₃ H ₆

Table 7.5: Isomers of kerosene in the Luche mechanism [65].

in the form of a single molecule that is given properties linearly computed from the ones of the species it represents. This relies on the hypothesis that each of the isomers behave similarly. This assumption is verified for the C₁₀H₂₁ isomers on the centre plot of the Figure 7.10 which shows the mass fraction of the involved species normalised by their respective peak value. It appears that each of the normalised isomers fall on the same profile and therefore they may be expressed with a single species involved within similar reactions. All the isomers do not respect this assumption. For instance the normalised profiles

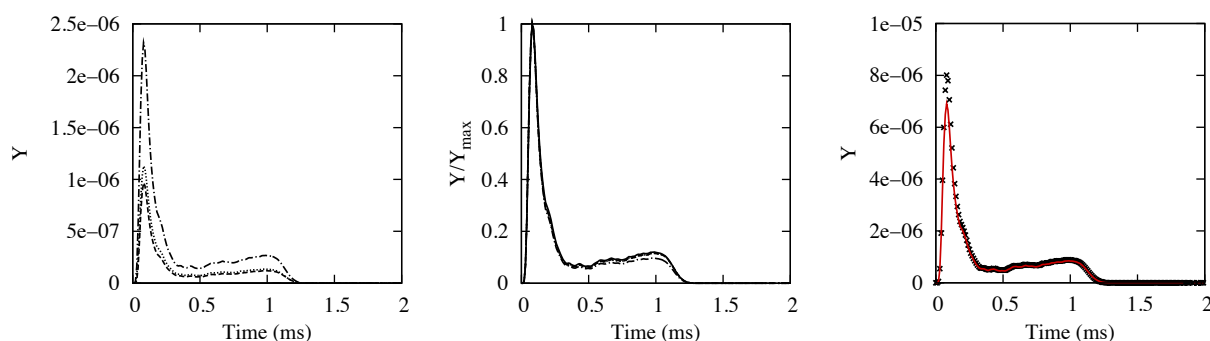


Figure 7.10: Lumping analysis of the C₁₀H₂₁ isomers. Left and centre plots; solid line: AC₁₀H₂₁, dashed: CC₁₀H₂₁, dotted: DC₁₀H₂₁ and dashed-dotted: EC₁₀H₂₁. Right plot; dots: $Y_{AC_{10}H_{21}} + Y_{CC_{10}H_{21}} + Y_{DC_{10}H_{21}} + Y_{EC_{10}H_{21}}$ and solid red line: lumped C₁₀H₂₁(L). Trajectory starting from the air inlet.

for species APHC₃H₆ and species CPHC₃H₆ are given in Figure 7.11. It is observed that these isomers are definitely not self-similar and as such, they cannot be linearly lumped together.

The contribution of an isomer to the lumped chemical species is quantified from the ratio of the concentration of this isomer by the sum of the isomers concentrations. For instance, at time t and for the profile associated to the inlet L , the contribution of species AC₁₀H₂₁ to the lumped chemical species C₁₀H₂₁(L) is given by:

$$\alpha_{AC_{10}H_{21}}^L(t) = \frac{[X_{AC_{10}H_{21}}^L](t)}{[X_{AC_{10}H_{21}}^L](t) + [X_{CC_{10}H_{21}}^L](t) + [X_{DC_{10}H_{21}}^L](t) + [X_{EC_{10}H_{21}}^L](t)} \quad (7.14)$$

Locally, at time t and for the inlet L , the formulation is exact, however small variations are observed

along the profiles, so that the contribution of each isomer is averaged in time and on the inlets i.e.

$$\alpha_{AC_{10}H_{21}} = \sum_{t=1}^{N_t} \sum_{L=1}^{N_L} \frac{\alpha_{AC_{10}H_{21}}^L(t)}{N_t N_L} \quad (7.15)$$

A group of isomers is selected for lumping if the difference in local contribution of the isomer with its averaged contribution stays below an user-defined threshold value \mathcal{T}_l . For instance, the isomer species $AC_{10}H_{21}$ is selected if:

$$\frac{|\alpha_{AC_{10}H_{21}}^L(t) - \alpha_{AC_{10}H_{21}}|}{\alpha_{AC_{10}H_{21}}} < \mathcal{T}_l \quad \forall t, \forall L \quad (7.16)$$

The lumping contribution for the two groups of isomers of the studied mechanism that are linearly linked together are given in Table 7.6. Overall, it is seen that the isomer species participate to the combustion process with a contribution of the same order of magnitude.

Lumped species	Composition of the lumped species			
$C_{10}H_{21}(L)$	18% $AC_{10}H_{21}$	29% $CC_{10}H_{21}$	22% $DC_{10}H_{21}$	31% $EC_{10}H_{21}$
$C_9H_{17}(L)$	29% CC_9H_{17}	41% EC_9H_{17}	30% FC_9H_{17}	

Table 7.6: Lumping groups

The mechanism is now further reduced replacing each isomer species by the associated lumped chemical species. The pre-exponential factor of the reactions within which an isomer involved as a reactant is replaced by its associated lumped species, is corrected according to the formulation 3.29. As an example, the lumping procedure for the isomers of $C_{10}H_{21}$ is now presented considering the sets of reactions 7.17 and 7.20 where the isomer species are respectively involved in the products and in the reactants:

- **Lumped species into products:** The initial set of reactions 7.17 is related to the isomer species $AC_{10}H_{21}$, $CC_{10}H_{21}$, $DC_{10}H_{21}$ and $EC_{10}H_{21}$ that are grouped together to form the single lumped

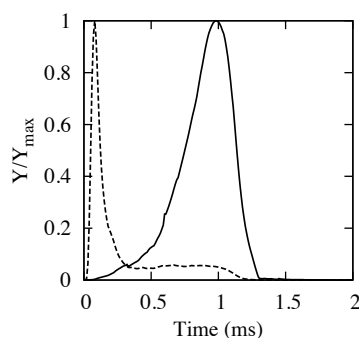
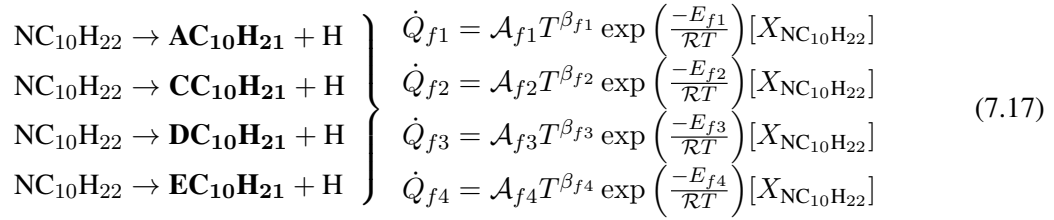
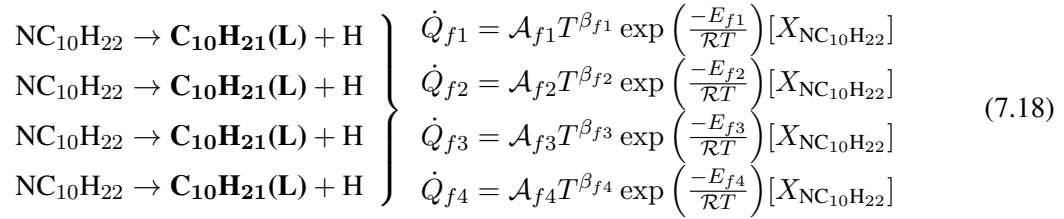


Figure 7.11: Lumping analysis of the PHC_3H_6 isomers. Solid line: $APHC_3H_6$, dashed: $CPHC_3H_6$. Trajectory starting from the air inlet.

species C₁₀H₂₁(L).



Because the lumped species does not participate to the estimation of the rate associated to the four reactions, the Arrhenius relation of each reaction is unchanged, so that:

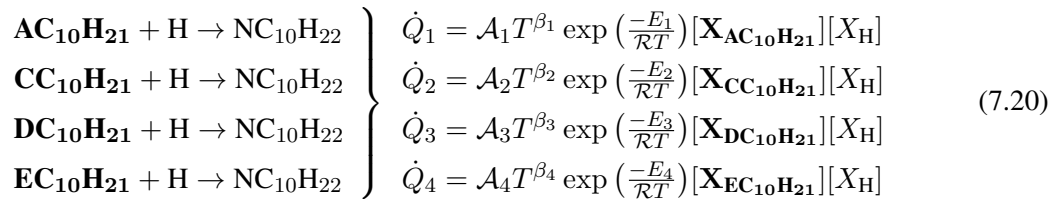


The reactions of the system 7.18 are then lumped together to form a single reaction whose chemical rate equals the sum of the rates of the initial reactions $\dot{Q}_{fL} = \dot{Q}_{f1} + \dot{Q}_{f2} + \dot{Q}_{f3} + \dot{Q}_{f4}$. The problem to be solved is then again non-linear and may not satisfy the equality. It is resolved using the Genetic Algorithm procedure reported above in 4.2.2. Since the concentration of species NC₁₀H₂₂ is involved in each reaction, the optimisation problem is simplified to the minimisation of the error ϵ_{fL} that quantifies the difference between the Arrhenius estimation for the lumped reaction and the sum of the Arrhenius equations of the four initial reactions;

$$\begin{aligned} \epsilon_{fL} = \mathcal{A}_{fL} T^{\beta_{fL}} \exp\left(\frac{-E_{fL}}{\mathcal{R}T}\right) - \mathcal{A}_{f1} T^{\beta_{f1}} \exp\left(\frac{-E_{f1}}{\mathcal{R}T}\right) - \mathcal{A}_{f2} T^{\beta_{f2}} \exp\left(\frac{-E_{f2}}{\mathcal{R}T}\right) \\ - \mathcal{A}_{f3} T^{\beta_{f3}} \exp\left(\frac{-E_{f3}}{\mathcal{R}T}\right) - \mathcal{A}_{f4} T^{\beta_{f4}} \exp\left(\frac{-E_{f4}}{\mathcal{R}T}\right) \end{aligned} \quad (7.19)$$

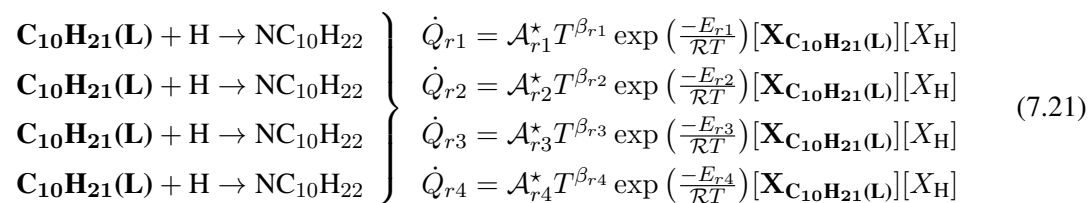
where \mathcal{A}_{fL} , β_{fL} and E_{fL} are respectively the pre-exponential factor, the temperature exponent and the activation energy associated to the lumped chemical reaction.

- **Lumped species into reactants:** As for the above example, the same set of chemical species is studied. In this case, the reverse reactions are considered and the isomers to be lumped are now in the reactants side. Hence the concentrations of the isomers is now involved in the calculation of the reactions rates.



Again, the lumped species C₁₀H₂₁(L) takes the isomers place. The reactions rates must be corrected introducing the contribution of the isomers $\alpha_{\mathbf{AC}_{10}\mathbf{H}_{21}}$, $\alpha_{\mathbf{CC}_{10}\mathbf{H}_{21}}$, $\alpha_{\mathbf{DC}_{10}\mathbf{H}_{21}}$ and $\alpha_{\mathbf{EC}_{10}\mathbf{H}_{21}}$ so

as to account for the higher concentration of the lumped species.



where the introduced pre-exponential terms are

$$\begin{array}{ll} \mathcal{A}_{r1}^* = \alpha_{\text{AC}_{10}\text{H}_{21}} \mathcal{A}_{r1}, & \mathcal{A}_{r2}^* = \alpha_{\text{CC}_{10}\text{H}_{21}} \mathcal{A}_{r2}, \\ \mathcal{A}_{r3}^* = \alpha_{\text{DC}_{10}\text{H}_{21}} \mathcal{A}_{r3}, & \mathcal{A}_{r4}^* = \alpha_{\text{EC}_{10}\text{H}_{21}} \mathcal{A}_{r4}. \end{array} \quad (7.22)$$

Then again, the chemical reactions being similar can now be lumped together. The procedure depicted earlier for isomer species within the products also applies to the present reduction. The coefficients \mathcal{A}_{rL} , β_{rL} and E_{rL} are optimised as well following this procedure.

This procedure is employed to reduce the mechanism through the creation of the lumped species $\text{C}_{10}\text{H}_{21}(\text{L})$ and $\text{C}_9\text{H}_{17}\text{C}(\text{L})$. The mechanism is then further reduced by 5 species. About 60 reactions are also removed. After lumping the mechanism is therefore composed of 59 species involved over 419 reactions. The concentration profile resulting from the lumping of the isomers $\text{C}_{10}\text{H}_{21}$ is given on the right graph of Figure 7.10. The profile that is obtained agrees quite well with the profile that represents the sum of the initial isomer species.

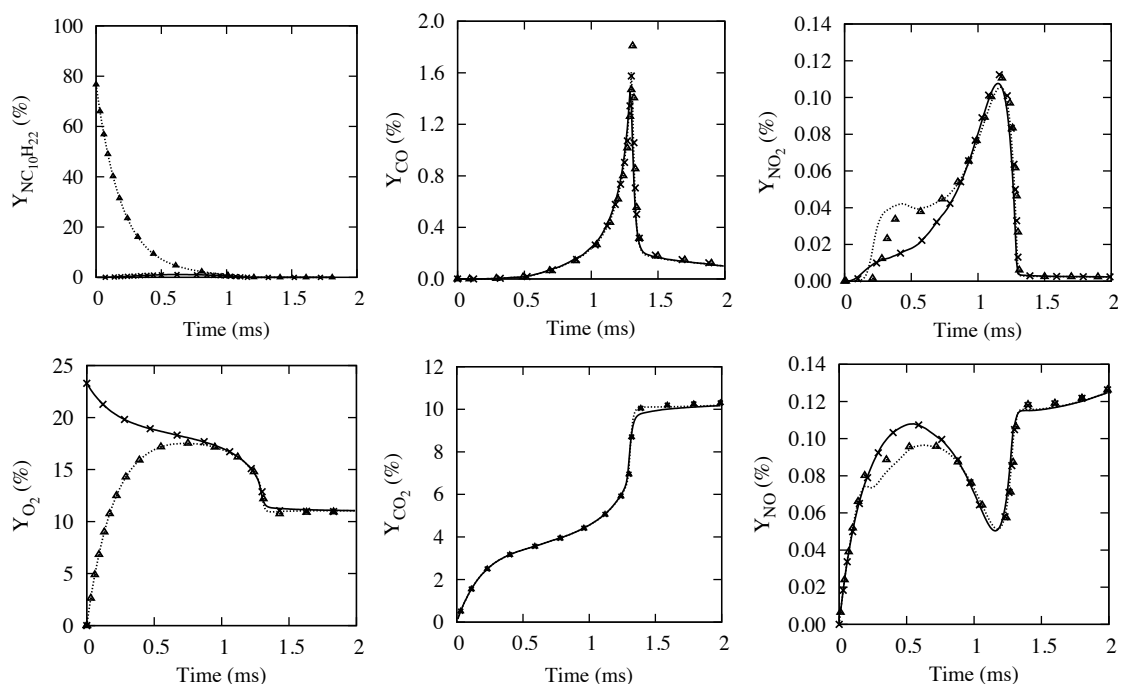
7.3.4 QSS species and optimisation

As usual, the reduction procedure is completed with the use of quasi-steady state relations. Following the same selection methodology as for the other applications proposed in this thesis, 27 species are expressed analytically including 10 species exclusively for capturing the NO_x levels. The list of species that is finally retained is given in the Table 7.7 separated in groups referring to the transported species and to the analytically solved species and subdivided into lists of species including or not, a nitrogen atom and therefore directly involved in the production of NO_x.

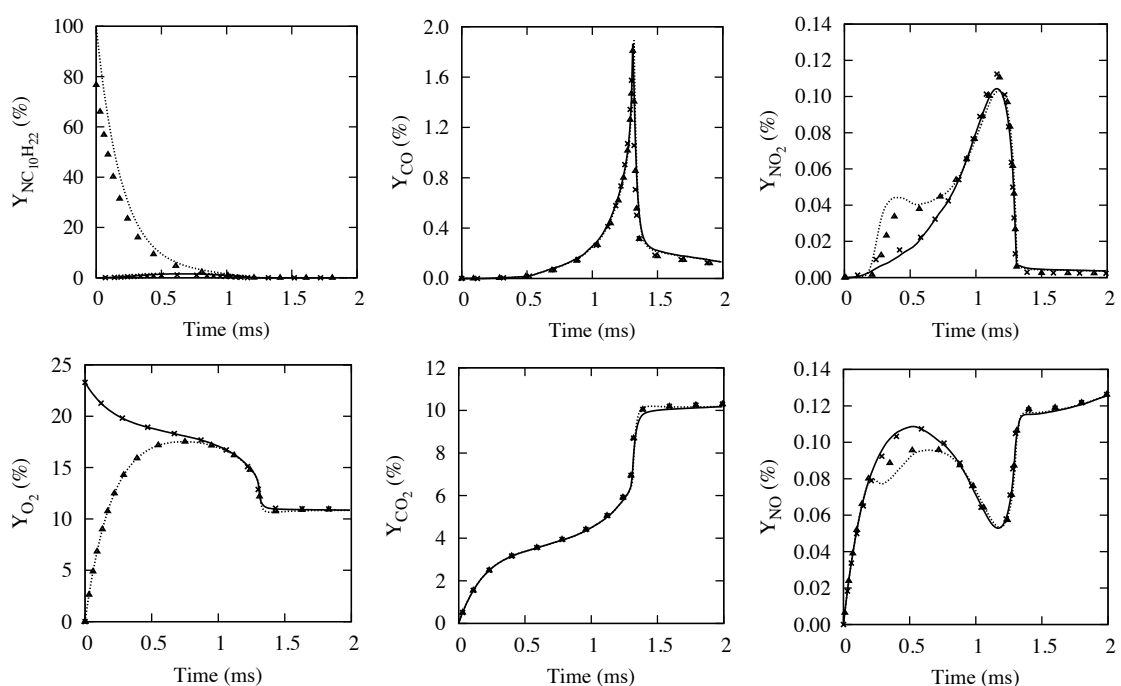
Transported species	Analytically resolved species
H ₂ , O ₂ , CO, CO ₂ , CH ₄ , C ₂ H ₆ , CH ₂ O, C ₂ H ₂ , C ₂ H ₄ , C ₃ H ₆ , C ₄ H ₆ , NC ₁₀ H ₂₂ , PHC ₃ H ₇ , TOLUEN, CYC ₉ H ₁₈ , H, O, OH, HO ₂ , H ₂ O, CH ₃ , C ₃ H ₃ , AC ₃ H ₅ , BC ₆ H ₁₃ , CPHC ₃ H ₆ , PHCH ₂ , C ₆ H ₅ O, N ₂	HCO, CH ₃ OH, C ₂ H ₅ , CH ₃ O, CH ₂ OH, CH ₂ CO, C ₂ H ₃ , CH ₂ HCO, HCCO, NC ₃ H ₇ , PC ₄ H ₉ , AC ₆ H ₁₃ , AC ₈ H ₁₇ , C ₁₀ H ₂₁ (L), APHC ₃ H ₆ , C ₆ H ₅ , C ₉ H ₁₇ (L)
NO, HCN, N ₂ O, NO ₂	HNO, HONO, H ₂ CN, NNH, NH ₂ , NH, N, CN, NCO, HNCO

Table 7.7: **Mechanism A.** Species of a kerosene surrogate (77% NC₁₀H₂₂, 13% PHC₃H₇, 10% CYC₉H₁₈) reduced mechanism composed of 32 transported species associated to 27 QSS relations and 419 reactions.

Again, a genetic algorithm is employed for the optimisation of some of the reactions chemical rates in order to reproduce the targets CO, NO and NO₂ along the stochastic/deterministic trajectories. The reactions involving nitrogen species being almost all conserved after the DRGEP reduction, their Arrhenius constants are maintained to their original values to reduce the size of the research area.



(a) Oxidation of the kerosene surrogate (77% NC₁₀H₂₂, 13% PHC₃H₇, 10% CYC₉H₁₈). Comparison between detailed chemistry computation and reduced chemistry (mechanism **A**) using the species of Table 7.7



(b) Comparison of the oxidation of the kerosene surrogate (77% NC₁₀H₂₂, 13% PHC₃H₇, 10% CYC₉H₁₈) using detailed chemistry with the oxidation of the n-decane (100% NC₁₀H₂₂) computed with the reduced mechanism **B** (Table 7.8).

Figure 7.12: Deterministic trajectories (Eqs. (5.19)-(5.20)). $\tau_t = 0.2$ ms. Target species. Symbols: Detailed reference (Luche [65]). Lines: Preliminary reduced mechanism (DRGEP+Lumping+QSS). Solid-line: Air inlet trajectory. Dotted-Line: Fuel (kerosene or n-decane) inlet trajectory.

7.3.5 Results and comparison between a surrogate composition and n-decane

7.3.5.1 Deterministic trajectories

A comparison of the trajectories computed with the detailed chemical scheme and the obtained reduced and optimised mechanism is given in Figure 7.12(a). Both the kerosene and air inlets are considered for the major reactants i.e. O₂ and n-decane NC₁₀H₂₂ that represents 77% of the kerosene surrogate composition as well as for the major pollutants CO, CO₂ and NO, NO₂. The trajectories computed with the reduced mechanism are in good agreement with the trajectories of the detailed chemical scheme.

The mechanism is constructed to recover the proper description for the production of NO_x which are very sensitive species. As such, it appears that the number of species involved is important. Transporting 32 species is still prohibitive and a further reduction of the mechanism size would be appreciable. Trying to further reduce the mechanism, the initial composition of the fuel is simplified to 100% n-decane NC₁₀H₂₂. The DRGEP procedure is repeated in order to remove unnecessary species and reactions considering this new composition. After reduction, the new mechanism relies on the transport of 26 chemical species and on the solving of 24 quasi-steady state relations involved within 338 reactions.

Transported species	Analytically resolved species
H ₂ , O ₂ , CO, CO ₂ , CH ₄ , C ₂ H ₆ , CH ₂ O, C ₂ H ₂ , C ₂ H ₄ , C ₃ H ₆ , C ₄ H ₆ , NC ₁₀ H ₂₂ , H, O, OH, HO ₂ , H ₂ O, CH ₃ , C ₃ H ₃ , AC ₃ H ₅ , BC ₆ H ₁₃ , N ₂	HCO, CH ₃ OH, C ₂ H ₅ , CH ₃ O, CH ₂ OH, CH ₂ CO, C ₂ H ₃ , CH ₂ HCO, HCCO, NC ₃ H ₇ , PC ₄ H ₉ , AC ₆ H ₁₃ , AC ₈ H ₁₇ , C ₁₀ H ₂₁ (L)
NO, HCN, N ₂ O, NO ₂	HNO, HONO, H ₂ CN, NNH, NH ₂ , NH, N, CN, NCO, HNCO

Table 7.8: **Mechanism B**. Species of a n-decane (NC₁₀H₂₂) reduced mechanism composed of 26 transported species associated to 24 QSS relations and 338 reactions.

The new list of species is given in Table 7.8 and the associated trajectories are displayed on Figure 7.12(b). The impact of the modification of the fuel composition on the trajectories appears negligible since the results, again, well agree with the computations performed with the detailed chemical scheme

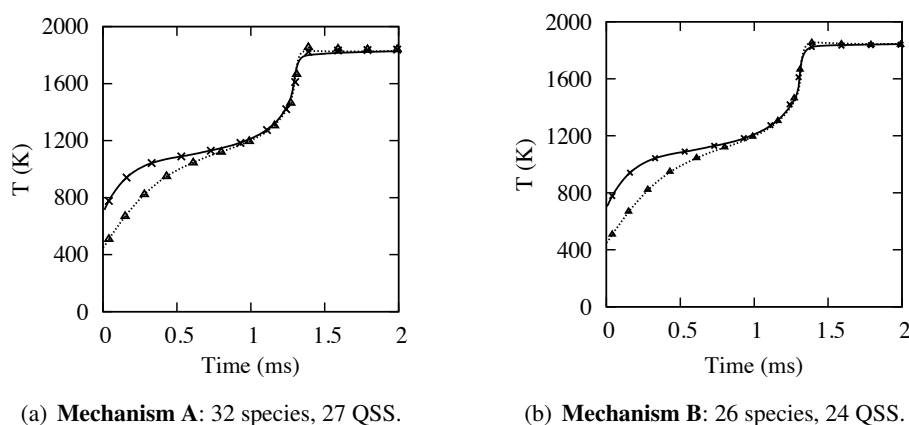


Figure 7.13: Deterministic trajectories (Eqs. (5.19)-(5.20)). $\tau_t = 0.2$ ms. Temperature profiles for 32 transported species and 26 transported species. Symbols: Detailed reference (Luche [65]). Lines: Preliminary reduced mechanism (DRGEP+Lumping+QSS). Solid-line: Air inlet trajectory. Dotted-Line: Fuel (kerosene or n-decane) inlet trajectory.

and considering the full composition of the fuel.

The temperature trajectories associated to the mechanism for the full kerosene description and to the mechanism for the combustion of n-decane are given in Figure 7.13. In both cases and for both air and kerosene deterministic trajectories, no difference is reported in comparison to the trajectories obtained from the initial detailed mechanism.

7.3.5.2 Premixed response

Although the mechanisms are reduced considering only the stochastic problem which, as explained earlier refers to a diffusion combustion regime, it is of interest to verify that the description in a perfectly premixed regime is still correct. For instance, the flame velocity is known to significantly impact on the position of the flame, indeed within aeronautical combustion chambers, many regions are usually subjected to partially premixed conditions. Figure 7.14 provides a comparison of the flame velocity, the equilibrium temperature and the equilibrium levels for species CO and for NO obtained from perfectly premixed kerosene-air flame computations at about 10 bar. A short difference is observed on the estimation of the flame speed S_L for equivalence ratios from $\phi = 1$ up to $\phi = 2$, but overall the description is acceptable. Both reduced mechanisms perfectly capture the equilibrium temperature and equilibrium

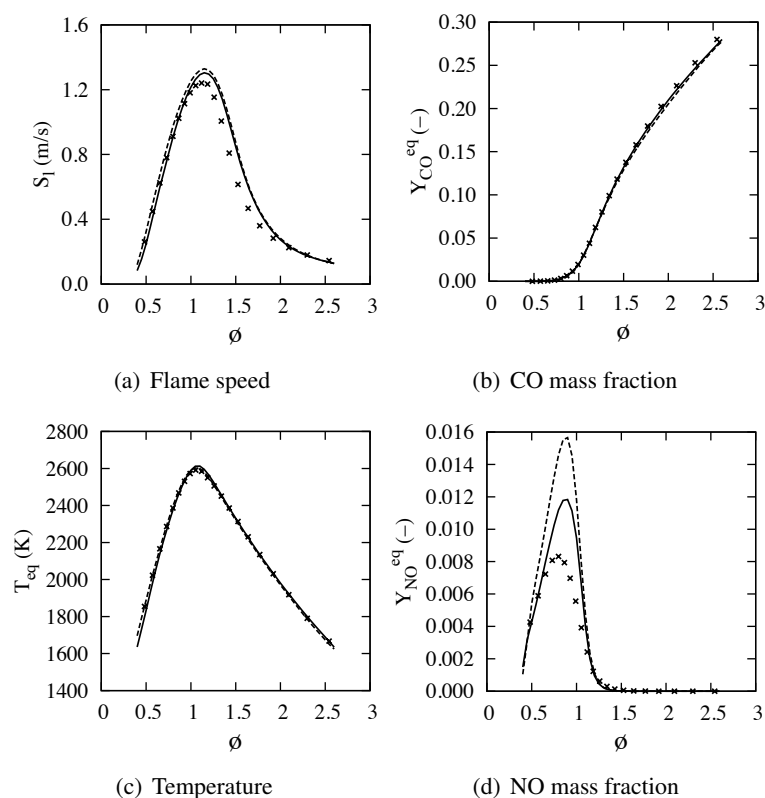


Figure 7.14: Flame speed, temperature and CO and NO equilibrium mass fractions at various equivalence ratios computed from premixed flames (Eqs. (2.54)-(2.56)). Symbols: Detailed reference (Luche [65]). Lines: Reduced mechanism (DRGEP+Lumping+QSS). Solid-line: kerosene oxidation mechanism (A) with 32 transported species (Table 7.7). Dashed-Line: n-decane oxidation mechanism (B) with 26 transported species (Table 7.8).

CO level for every equivalence ratio. A large over prediction of the NO levels is achieved using the reduced mechanisms for conditions around the stoichiometric point. It appears that the mechanisms that have been reduced for the conditions of the stochastic problem are not generic enough to reproduce the levels of NO at very high temperatures as encountered in premixed stoichiometric flames.

7.3.5.3 QSS matrix simplification

As reported in the review of the literature, it may be expensive to solve for the analytical system when a large number of QSS species is involved. Figure 7.13(a) shows the non-zero entries in the matrix that must be inverted to estimate the concentration associated to the 24 species expressed in quasi-steady state. It is estimated that 216 operations are necessary to solve for the problem using a Gaussian Elimination procedure. As observed, there is a great majority of zeros within the system which may easily be simplified by defining a new order for the solving of the concentrations. A procedure similar to that proposed by Arvidsson *et al.* [109] is employed here to lower the number of operations for solving the system. This results in the sorted matrix that is shown on Figure 7.13(b) which only necessitates 85 operations to be solved.

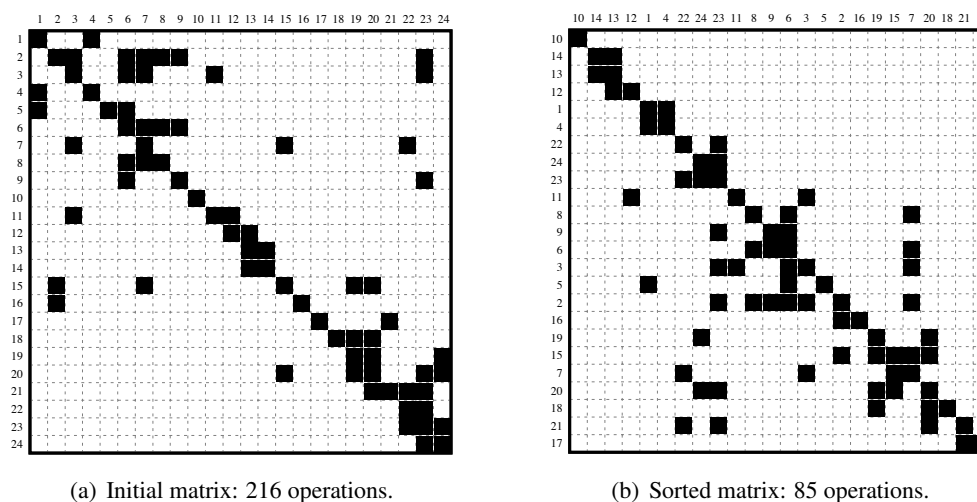
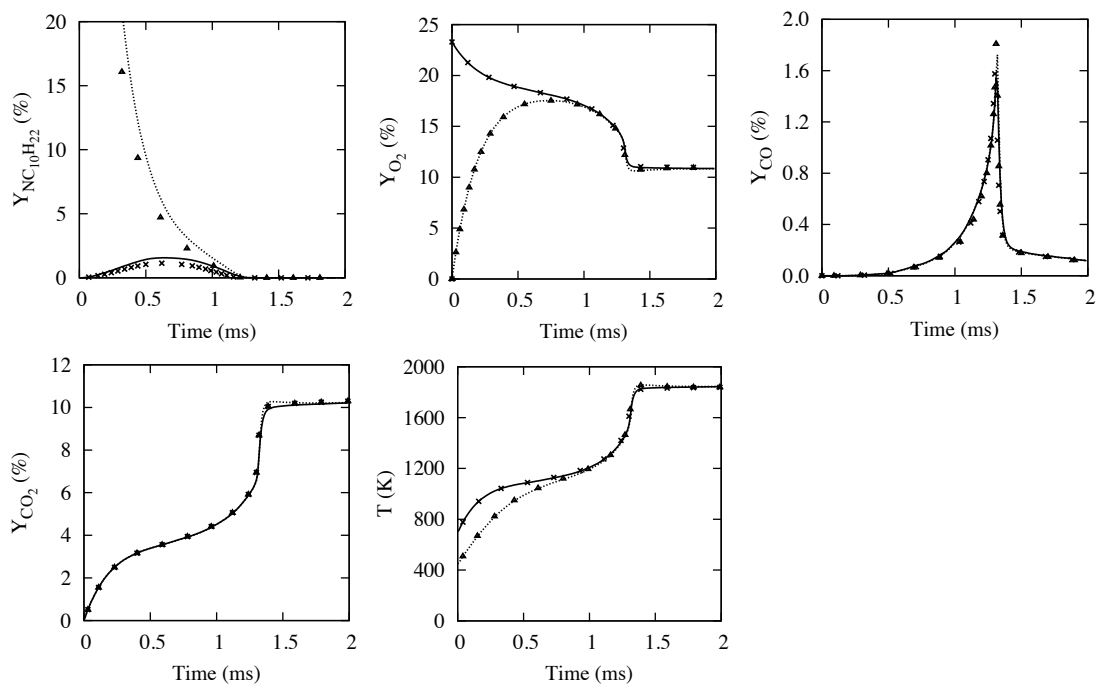


Figure 7.15: Reduction of the number of steps for solving the QSS matrix associated to the mechanism **B** using a Gaussian elimination solving. The reduction is achieved by optimising the order of the species within the matrix [109].

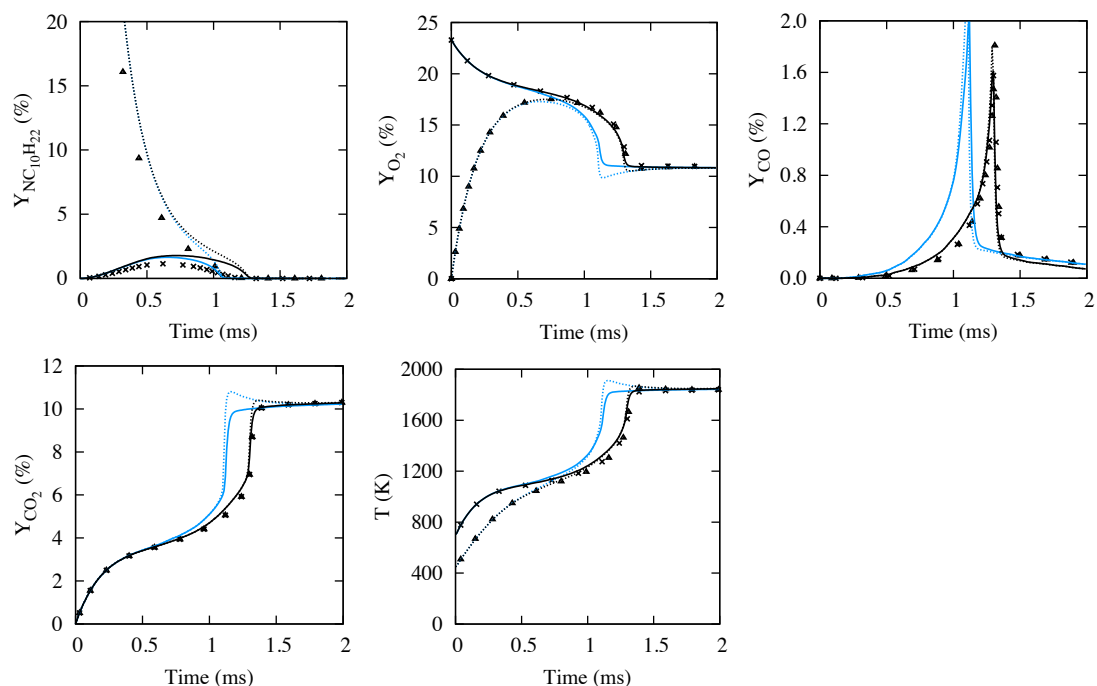
7.3.6 Reduction limits

Transported species	Analytically resolved species
H ₂ , O ₂ , CO, CO ₂ , CH ₄ , C ₂ H ₆ , CH ₂ O, C ₂ H ₂ , C ₂ H ₄ , C ₃ H ₆ , C ₄ H ₆ , NC ₁₀ H ₂₂ , H, O, OH, HO ₂ , H ₂ O, CH ₃ , C ₃ H ₃ , AC ₃ H ₅ , BC ₆ H ₁₃ , N ₂	HCO, CH ₃ OH, C ₂ H ₅ , CH ₃ O, CH ₂ OH, CH ₂ CO, C ₂ H ₃ , CH ₂ HCO, HCCO, NC ₃ H ₇ , PC ₄ H ₉ , AC ₆ H ₁₃ , AC ₈ H ₁₇ , C ₁₀ H ₂₁ (L)

Table 7.9: **Mechanism C**. Species of the reduced mechanism composed of 22 transported species associated to 14 QSS relations and 222 reactions.



(a) Comparison between the reference computations and the results computed with the reduced mechanism (C) of Table 7.9 with 22 transported species, 14 QSS relations and 222 reactions.



(b) Comparison between the reference computations and the results computed with the reduced mechanism (D) of Table 7.10 with 16 transported species before optimisation (blue lines) and after optimisation (black lines).

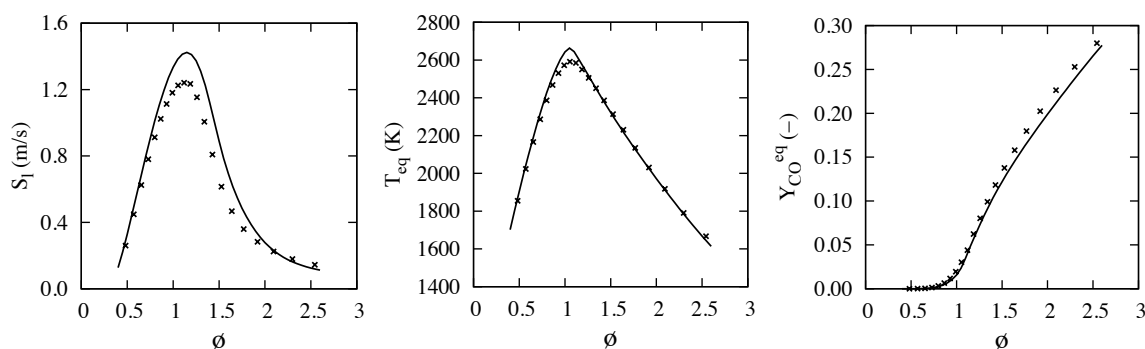
Figure 7.16: Deterministic trajectories (Eqs. (5.19)-(5.20)). $\tau_t = 0.2$ ms. Target species. Symbols: Detailed reference (Luche [65]). Lines: Preliminary reduced mechanism (DRGEP+Lumping+QSS). Solid-line: Air inlet trajectory. Dotted-Line: Fuel (kerosene or n-decane) inlet trajectory.

Transported species	Analytically resolved species
H ₂ , O ₂ , CO, CO ₂ , CH ₂ O, C ₂ H ₄ , C ₃ H ₆ , NC ₁₀ H ₂₂ , H, O, OH, HO ₂ , H ₂ O, CH ₃ , BC ₆ H ₁₃ , N ₂	HCO, C ₂ H ₅ , CH ₃ O, C ₂ H ₃ , NC ₃ H ₇ , AC ₆ H ₁₃ , AC ₈ H ₁₇

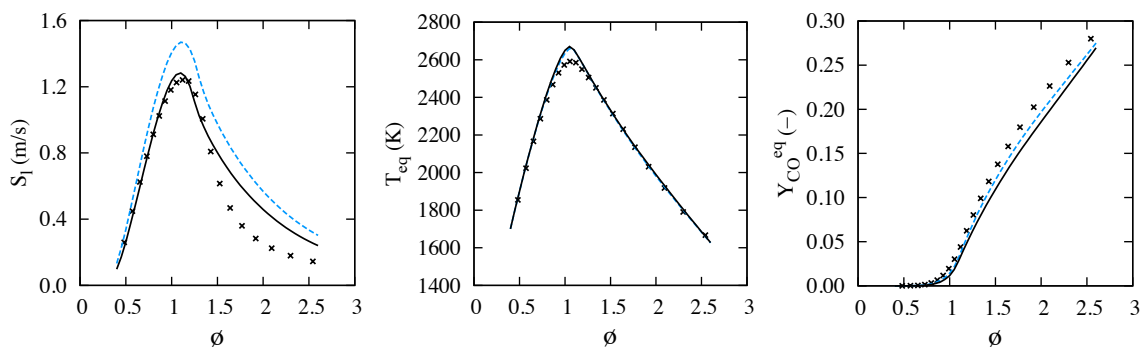
Table 7.10: **Mechanism D**. Species of the reduced mechanism composed of 16 transported species associated to 7 QSS relations and 95 reactions.

To assess the reduction capabilities over such large mechanisms, it is decided to remove the NO_x from the list of target species. Indeed, most day to day simulations do not require the estimation of the pollutants levels but only necessitate to recover the proper flame speed and equilibrium temperature. As reported by Franzelli *et al.* [64], the use of 7 species is enough to capture the proper equilibrium temperature. This list includes as pollutants only the species CO and CO₂. Since CO is part of these necessary species, the 26 species mechanism that was derived in the previous section is now further reduced accounting only for the reproduction of the CO level.

A new reduced version is obtained with 22 species, 14 QSS relations and associated to 222 chemical reactions. The list of species for this reduced chemical scheme is given in Table 7.9. The deterministic trajectories computed with this mechanism are given in Figure 7.16(a) for n-decane NC₁₀H₂₂, O₂ and pollutants CO and CO₂.



(a) Comparison between the reference computations and the results computed with the reduced mechanism (C) of Table 7.9 with 22 transported species, 14 QSS relations and 222 reactions.



(b) Comparison between the reference computations and the results computed with the reduced mechanism (D) of Table 7.10 with 16 transported species before optimisation (blue lines) and after optimisation (black lines).

Figure 7.17: Flame speed, temperature, and CO equilibrium mass fraction at various equivalence ratios computed from premixed flames (Eqs. (2.54)-(2.56)). Symbols: Detailed reference (Luche [65]). Lines: Reduced mechanism (DRGEP+Lumping+QSS).

All the species trajectories are very well reproduced as for the temperature profile also given on Figure 7.16(a). The flame speed, equilibrium temperature and CO level at equilibrium are given in Figure 7.17(a) for a premixed combustion regime. The prediction for the CO level and for the temperature at equilibrium are again well reproduced. Nevertheless, a larger discrepancy regarding the prediction of the flame velocity is observed, again for equivalence ratios around $\phi = 1$.

The reduction is further pushed towards its limitation, looking for the minimum number of species and reactions that still capture the tendency of the analysed properties. The lists of 16 transported species and 7 analytical ones that are given in Table 7.10 correspond to this very reduced version. This higher level of reduction is associated to larger differences with the reference. The introduced error is again corrected with an optimisation procedure. Because the difference for the prediction of the flame velocity also appears important, the fitness function that is used by the genetic algorithm is now constructed with both the trajectories of the stochastic/deterministic problem and premixed one-dimensional flames for several equivalence ratios ranging from 0.5 to 2.5. The results for the deterministic trajectories associated to the target species and to the temperature are given on Figure 7.16(b) before and after the optimisation of the reactions rates constants. Again the reduced chemical scheme appears to provide a correct description of the trajectories constructed with the stochastic problem. Figure 7.17(b) shows that because of the high reduction level, the reduced scheme does not properly capture the flame speed in the rich region of the flame. Although optimisation allows for reducing the gap with the detailed chemistry response in terms of flame speed, this is not sufficient enough to capture the real shape of the profile. Interestingly, temperature and CO equilibrium levels are not so much impacted by either the reduction or the optimisation.

7.4 Large-Eddy Simulation of an ultra-low NO_x combustor

7.4.1 Numerical settings

The domain that is considered for the calculation is showed on Figure 7.18. The injection system is placed in a square cross section combustion chamber with a converging section at the exit allowing for an acceleration of the flow. Approximately 30% of the injected air in terms of mass flow is used for film cooling (see Figure 7.18) to lower the temperature at the walls and at the access windows. The mesh has been provided by Safran Tech. It is composed of about 64 million of cells associated to 11.6 million of

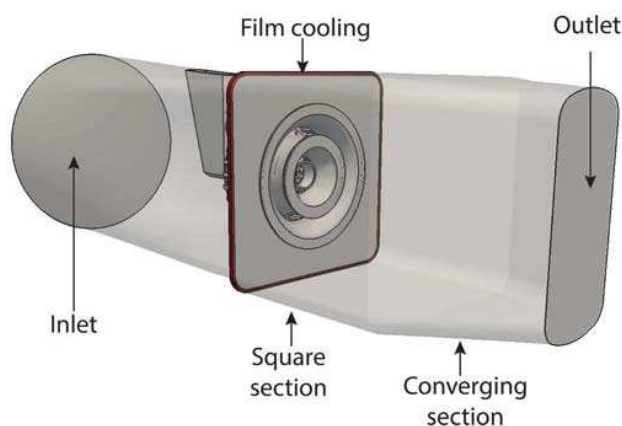


Figure 7.18: Representation of the computational domain. Image extracted from Jaravel [17].

nodes. Figure 7.19 provides an idea about the characteristic size of the mesh that is used. Within the pilot swirler region and the pilot injection system, the size of the mesh is of the order of 200 μm . It increases to about 400 μm in the pilot flame region. The size of the mesh within the swirler of the multipoint injection system is of the order of 400 μm as well. The mesh characteristic size then largely increases towards the exit of the combustor.

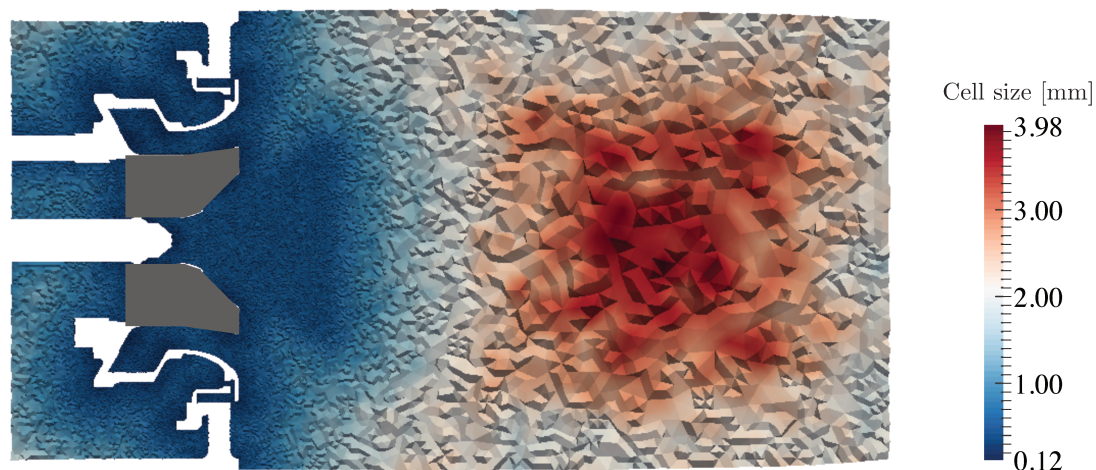


Figure 7.19: Resolution of the mesh with 64 million cells.

A Large-Eddy Simulation (LES) is performed using the low Mach number solver of the code YALES2 with a variable density formulation. The gaseous inlets are all modelled from a mass flow boundary condition without injecting turbulence, the majority of the turbulence being created while transiting through the swirlers. The dynamic Smagorinsky model is employed to account for the sub-grid scale turbulent fluctuations. Regarding the reactive part of the simulation, the mechanism of Table 7.8 that is composed of 26 chemical species interacting with 24 quasi-steady state relations is used so as to account for the production of both CO and NO_x.

7.4.1.1 Modelling of the injection, transport and evaporation of the n-decane droplets

A particular attention must be paid on the modelling of the fuel injection [198]. Indeed, as for the majority of the aeronautical burners, the injection systems of the LEMCOTEC chamber are equipped with swirlers. Thanks to the introduction of the swirl, the sheets of liquid that left the injectors are given a high velocity so that they get destabilised and disintegrated into mists of droplets. The atomisation of a spray is a complex phenomena that cannot be accounted for in the present simulation because the calculation cost would be prohibitive for its modelling into the full geometry. The numerical characteristics defined for both the pilot and the multipoint injection systems are given as follows:

- **Pilot injection:** The model Liquid Injection for Swirled Atomisers (LISA) proposed in the thesis of Guedot [199] is employed for the injection of liquid n-decane droplets in the pilot region. It requires the definition of the liquid mass flow rate, of the spray half angle γ_s and of the radius R_0 corresponding to the exit orifice of the injector as illustrated on Figure 7.20. The Lagrangian particles are injected on a crown with R_0 as outside radius and an inside radius R_A that is estimated from the Risk and Lefebvre [200] correlation:

$$\left(\frac{R_A}{R_0}\right)^2 = \frac{\sin^2 \gamma_s}{1 + \cos^2 \gamma_s}. \quad (7.23)$$

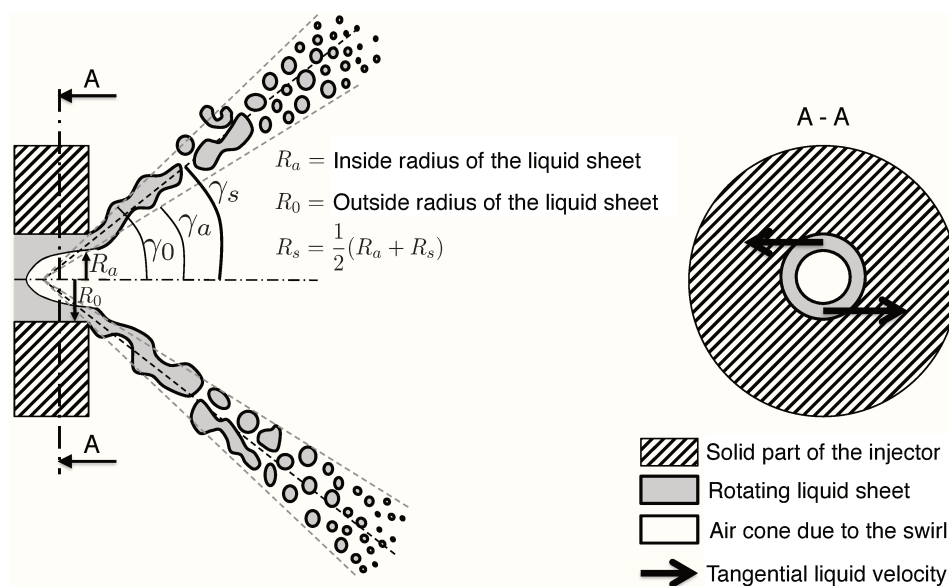


Figure 7.20: Geometrical characteristics of the spray exiting the injector (Guedot [199]).

This relation correlates γ_s , the mean spray angle with (1) the surface of the gaseous inner region with radius R_A that is created by the air recirculating in the centre of the atomiser and (2) the exit orifice with radius R_0 . For each particle, the point of injection is randomly selected on the crown following an uniform distribution. The speed of injection is estimated from the radial position of the particle on the crown by ensuring that the particle respects the defined normal velocity while remaining within $[\gamma_0, \gamma_A]$, the limiting angles defined from R_0 and R_A . The n-decane droplets are injected within the pilot region with an angle $\gamma_s = 30^\circ$. The injection is performed using a Rosin-Rammler distribution centred on a SMD provided by Safran of $12.9 \mu\text{m}$.

- **Multipoint injection:** The system retained by Safran for the multipoint injection respects the jet in crossflow hypothesis. The correlation proposed by Freitag and Hassa [201] is derived for such injection conditions and is therefore employed for the estimation of the droplets SMD in the multipoint injection system. The relation reads:

$$\text{SMD} = 6.9e^{-4} D^{0.2} \left(\frac{P_{\text{dyn}}}{P^{0.45}} \right)^{-0.374}, \quad (7.24)$$

where P is the gas static pressure and P_{dyn} refers to the dynamic pressure of the gas computed from ρu^2 with u the velocity of the carrying phase. Using the correlation, a value $\text{SMD} = 36 \mu\text{m}$ is imposed for the simulation. The Lagrangian droplets are injected on an eulerian boundary with a fixed diameter. The number of droplets injected is computed to respect the normal velocity that is set to $u_{\text{norm}} = 5.96 \text{ m}\cdot\text{s}^{-1}$ considering the liquid mass flow.

In regards to the evolution of the Lagrangian particles, a two-way coupling strategy on the mass, momentum and energy conservation is employed for solving the interactions between the particles and the carrying phase (see section 2.5 for more informations). The evaporation model that was introduced in section 2.5.2.2, is used to account for the production of the gaseous n-decane.

7.4.1.2 TFLES settings

The interactions between the turbulence and the chemistry are accounted for using the dynamic TFLES model. The thickening of the flame is performed following the procedure introduced in section 2.4.6.4 i.e. the thickening is computed from the local mesh size using the relation 2.107 and the Charlette efficiency function [38]. The evolution of the flame thickness depending on the equivalence ratio of the mixture for perfectly premixed conditions is given on the left plot of Figure 7.21. The thickening factor is plotted on the right graph of Figure 7.21 depending on the local size of the LES mesh, with 5 points in the flame layer and assuming $\delta_L^{th} = 100 \mu\text{m}$. The local thickening factor and the efficiency function is

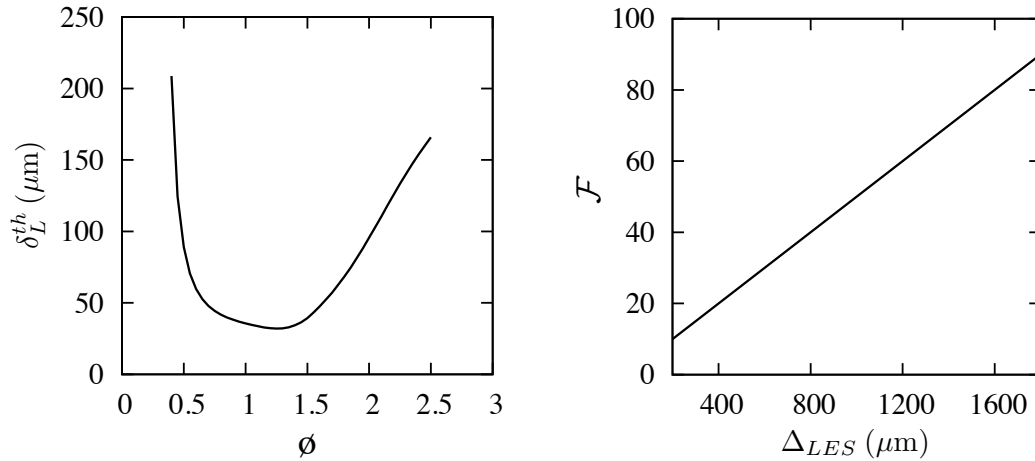


Figure 7.21: Left: Thermal flame thickness computed with the mechanism of Table 7.8 for the conditions of LEMCOTEC combustion chamber as a function of the equivalence ratio. Right: Thickening factor evolution against the cell size for $n = 5$ points within the flame and with $\delta_L^{th} = 100 \mu\text{m}$.

piloted by the flame sensor relying on the source term $\dot{\omega}$ provided with equation 2.117. The threshold $\dot{\omega}_S$ to capture the position of the flame is fixed to 10% of the maximum of $\dot{\omega}$ on the domain. No propagation step is used while 2 filtering steps are employed as illustrated on Figure 2.9.

7.4.2 Simulation

Within this section, the results of the reactive computation are given. First, the flow simulation is initiated with pure air so as to install the velocity field. The liquid n-decane droplets are then added. Evaporation settles itself, because the air entering the combustion chamber is at a higher temperature than the boiling temperature of the n-decane. Combustion is then established introducing 16 ignition kernels distributed around the combustion chamber in front of the injectors of the multipoint system plus a kernel inside of the large recirculation zone created by the swirl in the pilot region. These kernels correspond to an additional source term of enthalpy defined to reach of specified temperature of 2400 K. They are all set during 0.5 ms with a ramping time of 0.1 ms.

7.4.2.1 Characteristic time of the flow

The convective time τ_{conv} is estimated from the flow velocity \bar{u} computed within the largest cross-section of the combustion chamber and from the length of the combustor L_c . It is given below for both the

non-reactive and the reactive simulations.

$$\begin{aligned}\tau_{\text{conv}}^{\text{cold}} &= \frac{L_c}{\bar{u}_{\text{cold}}} = 11.6 \text{ ms} \\ \tau_{\text{conv}}^{\text{hot}} &= \frac{L_c}{\bar{u}_{\text{hot}}} = 3.9 \text{ ms}\end{aligned}\quad (7.25)$$

7.4.2.2 Topology of the reacting two-phase flow within the mono-sector

The flow behaviour within the combustion chamber is analysed qualitatively, here, from instantaneous fields. Figure 7.22 provides an illustration (1) of the turbulence level encountered within the swirler of the pilot region and the swirler of the multipoint zone, (2) of the evaporation of the n-decane droplets injected in both regions, and (3) of the reaction zones, depicted from an iso-surface of the enthalpy source term. An intensive mixing of the droplets with the compressed air going through the injection system is observed, enhancing the evaporation and the reaction within the chamber.

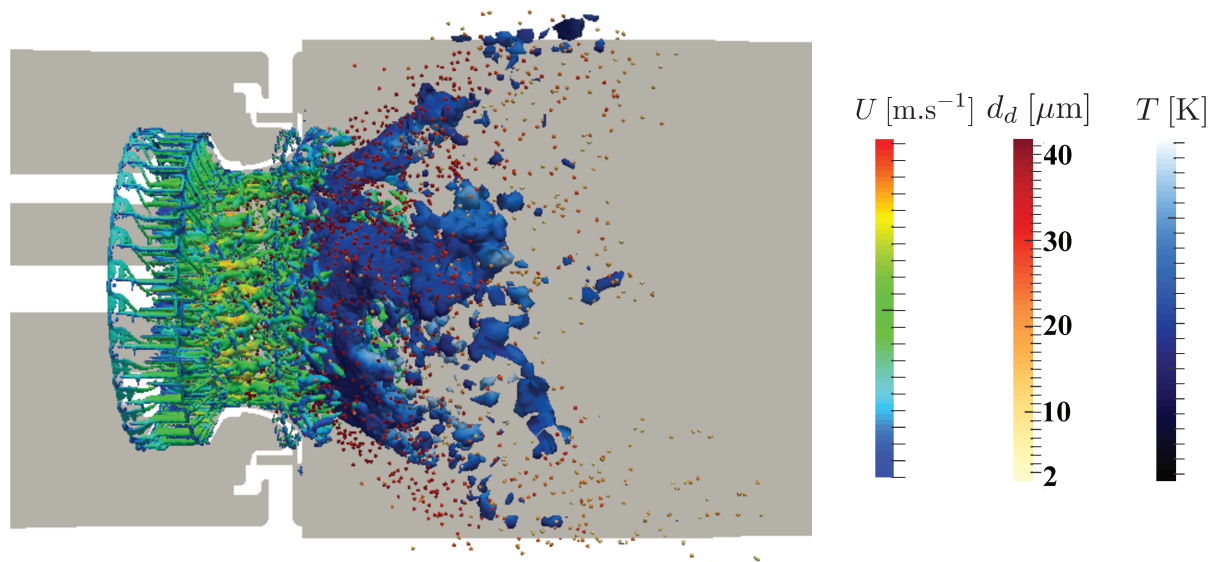


Figure 7.22: Illustration of the turbulence, reaction and evaporation interaction. Isosurface of Q criterion coloured by the velocity, iso surface of the enthalpy source term coloured by temperature, and Lagrangian particles coloured by the droplets diameter.

An instantaneous image of the temperature field in the axis of the combustion chamber is given on Figure 7.23(a). It is observed that the flame is first stabilised at the exit of the pilot injection system exhibiting a M-shape. The increase of the temperature within this inner region provides the energy necessary for the evaporation of the droplets coming from the multi-point injection and of the reaction of the obtained lean mixture. Figures 7.23(b) and 7.23(c) are showing the production rates of respectively species CO and species NO. The CO is produced exclusively within the flame. NO appears to be formed primarily within the flame, the contribution of the post flame NO being much lower. Figure 7.24 provides instantaneous fields of the mixture fraction, temperature and CO, NO mass fraction within the exit plane of the combustion chamber. The mixture fraction shows large inhomogeneities within the exit of the chamber with an inner region that is richer and an overall mixture fraction that is leaner near the wall. This is induced by the large amount of air injected within the multi-point region as well as the air introduced for wall-cooling. These large differences in mixture fraction lead to similar inhomogeneities

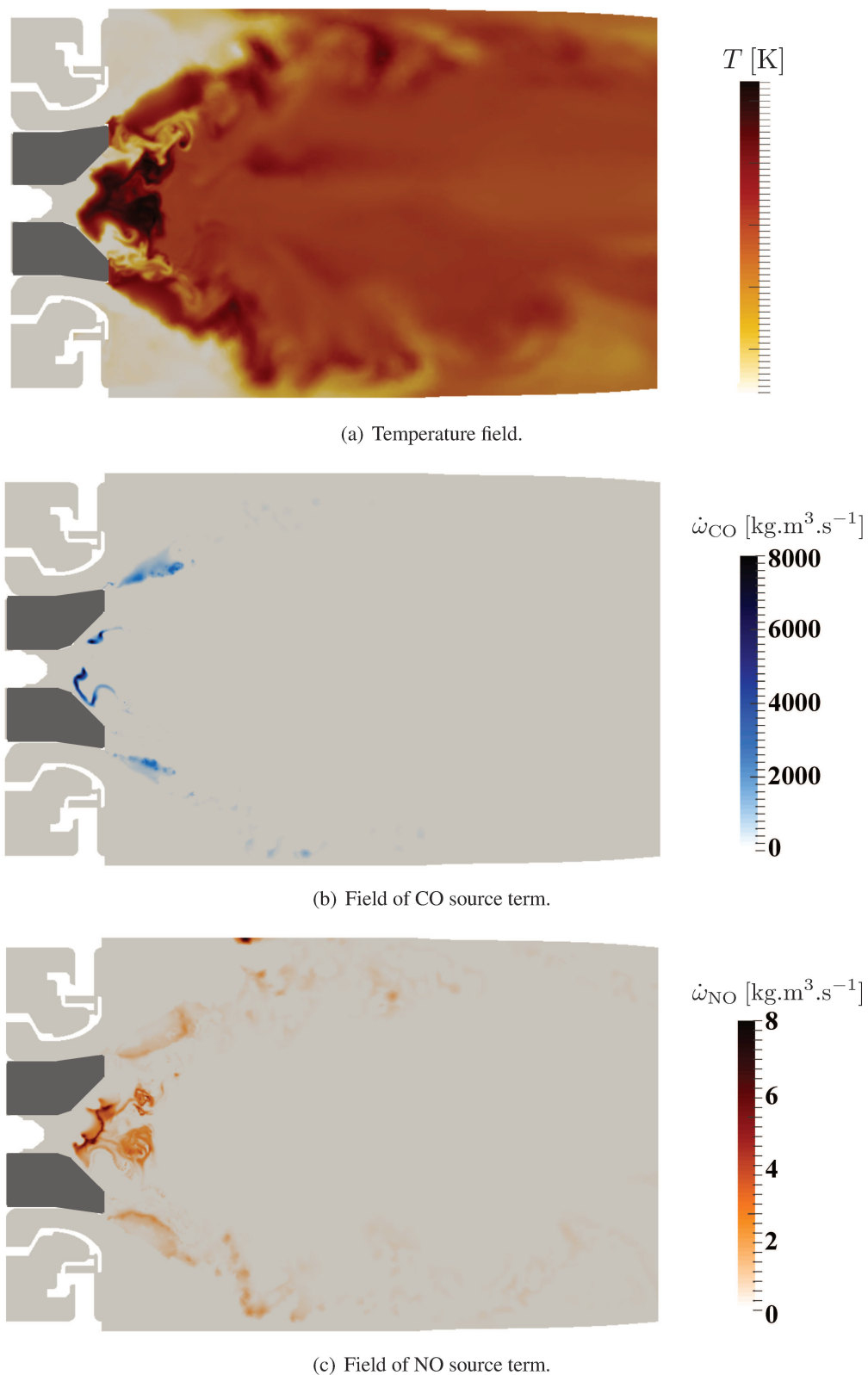


Figure 7.23: Instantaneous LES fields in the middle plane of the mono-sector.

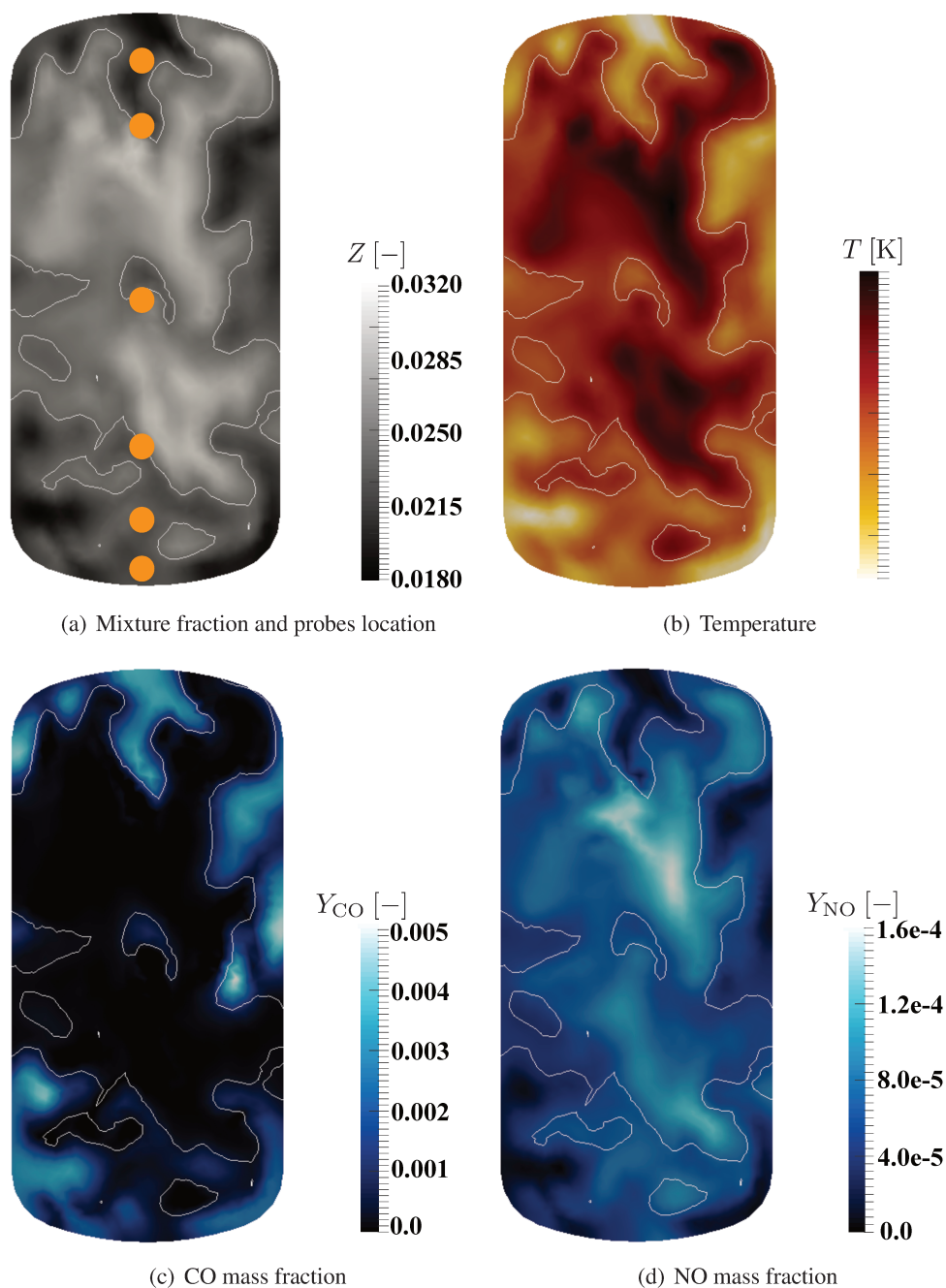


Figure 7.24: Instantaneous LES fields in the exit plane of the combustion chamber. Isocontour of the mixture fraction for conditions corresponding to the global mixing of the burner

in temperature. The field of NO mass fraction is directly correlated to the temperature field showing larger values in the regions of maximum temperature. Regarding the CO mass fraction, the inner region shows mass fractions close to zero corresponding to a state at chemical equilibrium. On the contrary, the lower temperature of the zones close to the wall shows high CO mass fractions obtained from a mixture that is not at equilibrium.

7.4.2.3 Pollutants levels: comparison with experimental measurements

Figure 7.24(a) provides the location of the 6 probes employed for pollutants measurements in an experiment conducted at Onera. Statistics have been accumulated from additional simulations performed by Safran Aircraft Engines (A. Figuer). The emissions in terms of CO, NO and NO_x are evaluated from the LES using respectively, the formulations 7.26, 7.27 and 7.28 averaged over the 6 probes and over the 15 ms used for statistics.

$$\langle \text{IECO} \rangle_{\text{probes}} = \sum_t \frac{\sum_{i=1}^6 Y_{\text{CO}_i}}{\sum_{i=1}^6 Z_i} \quad (7.26)$$

$$\langle \text{IENO} \rangle_{\text{probes}} = \sum_t \frac{\sum_{i=1}^6 Y_{\text{NO}_i}}{\sum_{i=1}^6 Z_i} \quad (7.27)$$

$$\langle \text{IENO}_x \rangle_{\text{probes}} = \sum_t \frac{\sum_{i=1}^6 Y_{\text{NO}_2_i} + \frac{W_{\text{NO}}}{W_{\text{NO}_2}} Y_{\text{NO}_i}}{\sum_{i=1}^6 Z_i} \quad (7.28)$$

The comparison between the experimental results and the averaged LES emissions (in g/kg of fuel) are given in table 7.11. Overall, the CO emissions are well predicted by the simulation, with a relative error of about 7%, while a larger overestimation of the NO and NO_x levels is achieved with the simulation compared to the experimental values.

	Experiment (g/kg of fuel)	LES (g/kg of fuel)	Relative error
$\langle \text{EICO} \rangle_{\text{probes}}$	51.47	55.30	7.4%
$\langle \text{EINO} \rangle_{\text{probes}}$	1.21	2.30	90.0%
$\langle \text{EINO}_x \rangle_{\text{probes}}$	2.85	4.17	46.3%

Table 7.11: Comparison between the experimental and simulated pollutants emission averaged in time and over the 6 probes.

7.5 Conclusion

The stochastic mixing problem introduced earlier is evaluated in the context of pollutants emission for the aeronautical industry. A multi-point injection system is studied on a mono-sector operating at about 10 bar. The system has been derived recently for NO_x reduction in the context of the LEMCOTEC European project. The settings of the evaporation of the liquid droplets is defined and the trajectories are computed considering a separated injection of kerosene and air to which a large amount of particles representing recirculating burned gases is added. Analysing the distribution of the particles in a temperature versus mixture fraction diagram, it is observed that the particles essentially react in a partially premixed lean regime. To increase the range of equivalence ratios covered by the stochastic/deterministic problem, a part of the air is released progressively. This is done to dissociate the combustion air from the introduced cooling air. As a result, the combustion first takes place in a rich/stoichiometric environment and is gradually diluted with air, hence reaching the overall lean condition that characterises the burner condition. Following the constructed deterministic trajectories, several mechanisms are derived from an initial chemical scheme composed of 91 species and 991 reactions. The first mechanism rely on the full kerosene composition and is developed for reproducing the CO and NO_x levels. It is further reduced

simplifying the fuel composition to pure n-decane. To assess the limitation of the proposed reduction methodology, NO_x are then removed from the list of targets. Two new mechanisms are obtained composed respectively of 22 and 16 transported species. Both mechanisms appear to provide an accurate description of the profiles for deterministic trajectories and for the reproduction of the CO and temperature equilibrium against a large range of equivalence ratios in comparison to the levels computed with the initial detailed chemistry. Nevertheless, in the rich region, the flame speed computed with both reduced schemes shows higher levels in comparison to the reference. The input settings of a Large-Eddy Simulation (LES) performed with the LEMCOTEC mono-sector are then provided along with a qualitative analysis of the flow. Finally, a comparison between experimental and numerical data of the CO and NO_x emissions averaged over probes placed in the exit plane of the combustion chamber shows a good reproduction of the CO levels while NO_x levels are overall over predicted.

Chapter 8

Conclusions and perspectives

Contents

8.1	Conclusions	193
8.1.1	Global chemistry assessment	193
8.1.2	Reduction strategy relying on skeletal and analytical formalisms	194
8.1.3	A new canonical problem for reduction	194
8.1.4	Applications	195
8.2	Perspectives	196
8.2.1	Stochastic modelling	196
8.2.2	Reduction methodology	197
8.2.3	Flame-turbulence interaction	197
8.2.4	Other applications	197

8.1 Conclusions

This thesis aims at developing an automated approach for the derivation of reduced chemical mechanisms ready for Computational Fluid Dynamics (CFD) simulations. A wide variety of methodologies is found in the literature for the reduction of detailed combustion schemes. These either rely on the definition of a few global steps or may be derived from the removal of the least important chemical paths and from the introduction of quasi-steady state hypothesis. The work outlined in this manuscript suggests an approach relying on the coupling of existing reduction techniques with optimisation. The procedure is combined with a novel canonical problem customised for turbulent combustion applications featuring multiple inlets. The novel reduction approach is applied to many theoretical and industrial applications and validated over one-dimensional profiles and in computations based on a Reynolds Averaged Navier Stokes (RANS) formulation and on Large-Eddy Simulation (LES).

8.1.1 Global chemistry assessment

First the capabilities of global mechanisms are assessed. Using a genetic algorithm, the chemical constants of a reduced set of reactions for methane-air combustion are optimised in order to capture the correct flame speed, equilibrium temperature, and major species profiles in a perfectly premixed regime.

The limits of a 3 steps chemistry are demonstrated and a solution relying on the introduction of an additional set of reactions for the hydrogenated chemistry is proposed. The results obtained after optimising once again the constants of the global steps are in good agreement with the target profiles that are obtained with the reference mechanism. Nevertheless, intermediate species profiles are poorly reproduced with the proposed set of reactions. Moreover, the selection of the global chemical steps appears not to be a straightforward exercise. It is therefore concluded that global chemistry is not suitable for proposing an automated approach for the derivation of reduced chemistries. This conclusion includes the fact that the obtained reduced mechanisms would not be capable of capturing the correct levels for the radical species of interest in this thesis.

8.1.2 Reduction strategy relying on skeletal and analytical formalisms

Building on the extensive work carried out to date, a reduction methodology relying on the construction of a skeletal mechanism and on the introduction of analytical relations is proposed. The approach is employed for the derivation of another chemical mechanism for methane-air premixed combustion. First the well-known Directed Relation Graph with Error Propagation (DRGEP) method is used for the selection of the species and of the reactions that can be removed without significantly modifying the solution. Next, species respecting the Quasi-Steady State (QSS) hypothesis are expressed analytically as a function of the other transported species. The procedure is completed with the use of optimisation, so that the reduction is pushed towards larger extents in comparison to the threshold levels of the traditional DRGEP and QSS approaches. Indeed, the larger error that is introduced while reducing furthermore the mechanism is corrected by the optimisation of the reactions Arrhenius constants. The methane-air premixed trajectories, recomputed with the achieved reduced mechanism are in very good agreement with the profiles of the detailed chemistry for all targets and also for the remaining set of intermediates. Thanks to these concluding results which are associated to the possible automation of the reduction process, this strategy is chosen for the next steps of the manuscript.

8.1.3 A new canonical problem for reduction

The great majority of the reduced combustion schemes are constructed and validated using perfectly premixed and homogeneous reactors simulations. Yet, a substantial proportion of the industrial applications do not operate under such theoretical conditions. For instance, a separated injection of the fuel and of the oxidiser is almost always recommended for safety reasons. In most applications, the presence of an intense turbulent mixing between these separated flows jeopardises the concept of a sequential pattern of perfectly premixed problems.

To cover at once a given range of chemical compositions, equivalence ratios and temperatures, the chemical properties of stochastic particles, submitted to micro-mixing and chemical reactions, are combined with the computation of deterministic one-dimensional composition-space trajectories, issued from an arbitrary number of inlet conditions. The discussed strategy is applied to the combustion of methane with vitiated-air and a analytical mechanism is derived for these conditions. It is demonstrated that the trajectories of the resulting reduced scheme well agree with the reference for the simulation of freely propagating one-dimensional premixed flames, at various equivalence ratios, and of strained diffusion flames in a one-dimensional counter-flowing jet configuration, up to the quenching point. This procedure is retained for the subsequent applications.

8.1.4 Applications

The developed automated reduction tool is employed to derive analytical mechanisms for two industrial applications. The first application concerns a large chemical system employed by Air Liquide for the production of syngas and the second one relates to the simulation of aeronautical pollutants emissions using a geometry provided by Safran.

- **Auto-Thermal Reforming (ATR) of methane:** The proposed stochastic mixing problem is particularly well suited to the analysis of the combustion process that is involved in the large reactors employed for syngas production. Indeed, ATR systems are relying on three separated injection of fuel, oxidiser and steam. Reactions occur primarily thanks to the very intense mixing of the three streams with the recirculating burned gases. Three detailed mechanisms from the literature are reduced for the conditions proposed by Air Liquide. The results of the obtained analytical schemes demonstrate a good reproduction of the deterministic trajectories computed with the corresponding reference mechanisms. The obtained chemistries have been assessed by Air Liquide using Fluent simulations with the Eddy Dissipation Concept (EDC) modelling. Using the analytical schemes, they reported a reduction of at least 60% of the computational time in comparison to the reference mechanisms. The results for two of the detailed mechanisms are in perfect agreement with the reference. A difference is nevertheless observed with one mechanism, probably due to the composition considered for the burned gases particles of the canonical problem which is different from the composition used for the two other schemes.
- **CO and NO_x prediction for aeronautical combustion chambers:** The strategy is then applied to the derivation of several mechanisms for the prediction of pollutants emissions. First, the set of stochastic particles is adapted to the conditions of the problem using evaporation and introducing a delay in the inclusion of the air particles. Then, the reference large chemical scheme is reduced with the full kerosene composition and for the reproduction of both CO and NO_x levels. To push further the reduction, the fuel composition is then simplified to n-decane. The achieved mechanism is validated with trajectories computed with the deterministic problem and with perfectly premixed one-dimensional flames. Finally to push the reduction towards its limits, two mechanisms with respectively 76% and 82% less species in comparison to the initial mechanism are proposed for only the reproduction of the CO emissions, flame speed and temperature equilibrium. Accurate results are achieved for both the species levels and the temperature compared to deterministic and premixed trajectories. Discrepancies increasing with the level of reduction are however observed for the flame speed with equivalence ratios above unity. A chemistry reduced to 26 transported species associated to 338 reactions is then assessed over a Large-Eddy Simulation performed on a novel multi-point injection system placed within a mono-sector. The analysis of the results shows a very good agreement with experimental data for the production of CO. Yet, a larger discrepancy is observed for the NO_x levels and must be further investigated.

The proposed automated reduction strategy allows for deriving tractable mechanisms for turbulent reactive combustion problems. The capabilities of the methodology have been assessed against a variety of complex academic and industrial applications. For instance, the skeletal and analytical mechanisms reduced using this procedure have been used for the simulation of large industrial systems employed (1) for syngas production and (2) for the manufacture of steel in blast furnaces (thesis by D. Midou [202]), (3) for the prediction of the pollutants emissions in aeronautical combustion chambers as well as for

a diversity of theoretical applications including (4) the study of flame propagation and stabilisation in micro-scale burners (thesis by K. Bioche [203]).

8.2 Perspectives

Some of the aspects studied during this thesis may be further explored in particular regarding (1) the enhancement of the stochastic modelling approach, (2) the improvement of the reduction strategy and (3) the extension to other combustion related applications. These three points are addressed in the present section.

8.2.1 Stochastic modelling

The formulation proposed for the solving of the mixing between elementary particles, of their evaporation and of their reaction offers great modularity. Nevertheless this formalism is simple regarding many subjects and may easily be improved.

8.2.1.1 Enhancing the mixing model

The mixing between the particles is performed using a stochastic selection approach and the Curl closure [159] is employed to define the new composition for the selected particles. This formulation allows for covering a large range of thermochemical compositions. However, because of its simplicity, it is obvious that there are particles facing compositions which are not representative of the simulated application. As a result, there might be a few species and reactions which are conserved within the reduced mechanism because they are important for these unrealistic compositions while they have a negligible impact on the real system. This point is currently addressed at CORIA in the thesis of A. Seltz. In addition, the analysis that is given in 7.3.2 regarding the delayed injection of air is very simple and was performed only to ensure the covering of a sufficiently wide range of equivalence ratios. In this specific context, a more realistic description may be proposed regarding the mixing of the inlet streams. For instance the pilot and multipoint region of the studied staged injection system may be seen separately so that the kerosene injected through the pilot region would mixed and react only with the air going through the same area. The same would be applied for the multipoint region. Then the two sets of particles could be assembled to simulate the mixing and burning behaviour within the combustion chamber.

8.2.1.2 Analysis of the impact of evaporation, dilution and staged combustion on the chemical reduction

Evaporation is introduced for the creation of reference trajectories in aeronautical combustion chambers but its impact on the reduced chemistry is not studied. It is of interest to perform a further analysis of the evaporation phenomena on the composition faced by the mixing particles so as to measure its influence on chemistry. Moreover, a multi-component evaporation formulation may be developed. Note that the procedure applies to any combustion system; it may also be used for burning the volatiles ejected from coal during the pyrolysis process.

The procedure would also gained from a further analysis of the impact of dilution and staged combustion on the obtained trajectories and on the reduced chemical schemes that are obtained.

8.2.2 Reduction methodology

8.2.2.1 Optimisation limits for large mechanisms

The DRGEP methodology, the lumping and the introduction of QSS hypothesis are efficient and fully automated approaches to derive reduced chemical mechanisms. The genetic algorithm procedure depicted in this thesis is also automated. Nevertheless, its use for optimising large reduced chemical mechanisms is substantially complicated by the size of the research area i.e. by the number of parameters to be optimised. For such conditions, selecting the most relevant steps for optimisation would greatly accelerate the process. As a first attempt, this selection may be based on a DRGEP analysis.

8.2.2.2 Correction function to recover flame speed for very reduced schemes

In Chapter 7, starting from a mechanism composed of 91 species and 991, an analytical mechanism based on 16 transported species and 95 reactions is derived for kerosene-air combustion. The reduction appears to be limited by the reproduction of the correct flame velocity for rich equivalence ratios. Interestingly the optimisation of the chemical constants of the mechanism have a negligible impact on the levels of CO and temperature equilibrium but strongly influences the flame speed distribution against the equivalence ratio of the mixture. It is believed that introducing a few correction functions [64] based on the local equivalence ratio could allow for recovering the proper flame speed without impacting so much the other thermochemical properties. Hence the reduction could be pushed towards larger extents.

8.2.3 Flame-turbulence interaction

The thickened flame model is employed here as a first approach for non-premixed combustion. The validity of this combustion model must be further evaluated for diffusion flames with complex chemistries.

8.2.4 Other applications

The method is currently used at CORIA by A. Bouaniche for the derivation of a kerosene-air mechanism for the prediction of the soot precursors.

Bibliography

- [1] International energy outlook 2016. Technical report, U.S. Energy Information Administration, [http://www.eia.gov/outlooks/ieo/pdf/0484\(2016\).pdf](http://www.eia.gov/outlooks/ieo/pdf/0484(2016).pdf), 2016.
- [2] Key world energy statistics 2016. Technical report, International Energy Agency (IEA), <https://www.iea.org/publications/freepublications/publication/KeyWorld2016.pdf>, 2016.
- [3] J. O. Hirschfelder, C. F. Curtiss, and R. B. Bird. *Molecular theory of gases and liquids*, volume 26.
- [4] V. Giovangigli. Multicomponent flow modeling. *Science China Mathematics*, 55(2):285–308, 2012.
- [5] C. F. Curtiss and J. O. Hirschfelder. Transport properties of multicomponent gas mixtures. *The Journal of Chemical Physics*, 17(6):550–555, 1949.
- [6] R. J. Kee, F. M. Rupley, E. Meeks, and J. A. Miller. *CHEMKIN-III: A FORTRAN chemical kinetics package for the analysis of gas-phase chemical and plasma kinetics*. 1996.
- [7] U. Maas and S. B. Pope. Simplifying chemical kinetics: intrinsic low-dimensional manifolds in composition space. *Combustion and Flame*, 88(3):239–264, 1992.
- [8] O. Gicquel, N. Darabiha, and D. Thévenin. Laminar premixed hydrogen/air counterflow flame simulations using flame prolongation of ildm with differential diffusion. *Proceedings of the Combustion Institute*, 28(2):1901–1908, 2000.
- [9] J. A. Van Oijen and L. P. H. de Goey. Modelling of premixed laminar flames using flamelet-generated manifolds. *Combustion Science and Technology*, 161(1):113–137, 2000.
- [10] D. Veynante and L. Vervisch. Turbulent combustion modeling. *Progress in Energy and Combustion Science*, 28(3):193 – 266, 2002.
- [11] T. Poinso and D. Veynante. *Theoretical and Numerical Combustion*. R. T. Edwards Incorporated, 2005.
- [12] R. J. Blint. The relationship of the laminar flame width to flame speed. *Combustion Science and Technology*, 49(1-2):79–92, 1986.
- [13] C. K. Law. *Combustion Physics*. Cambridge University Press, Cambridge, 009 2006.
- [14] R.W. Bilger. The structure of turbulent nonpremixed flames. *Symposium (International) on Combustion*, 22(1):475 – 488, 1989.

- [15] Y. Mizobuchi, J. Shinjo, S. Ogawa, and T. Takeno. A numerical study on the formation of diffusion flame islands in a turbulent hydrogen jet lifted flame. *Proceedings of the Combustion Institute*, 30(1):611 – 619, 2005.
- [16] A. N. Kolmogorov. The local structure of turbulence in incompressible viscous fluid for very large reynolds numbers. In *Dokl. Akad. Nauk SSSR*, volume 30, pages 299–303, 1941.
- [17] T. Jaravel. *Prediction of pollutants in gas turbines using large eddy simulation*. Phd thesis, INP Toulouse, 2016.
- [18] P. Moin and K. Mahesh. Direct numerical simulation: a tool in turbulence research. *Annual review of fluid mechanics*, 30(1):539–578, 1998.
- [19] J. Boussinesq. *Théorie de l'écoulement tourbillonnant*, pages 23–46. Mem. Pres. Acad. Sci., 1877.
- [20] M. Germano, U. Piomelli, P. Moin, and W. H. Cabot. A dynamic subgrid-scale eddy viscosity model. *Physics of Fluids A: Fluid Dynamics (1989-1993)*, 3(7):1760–1765, 1991.
- [21] D. K. Lilly. A proposed modification of the germano subgrid-scale closure method. *Physics of Fluids A: Fluid Dynamics (1989-1993)*, 4(3):633–635, 1992.
- [22] F. Nicoud and F. Ducros. Subgrid-scale stress modelling based on the square of the velocity gradient tensor. *Flow, turbulence and Combustion*, 62(3):183–200, 1999.
- [23] H. Pitsch. Large-eddy simulation of turbulent combustion. *Annu. Rev. Fluid Mech.*, 38:453–482, 2006.
- [24] K.N.C. Bray. The challenge of turbulent combustion. *Symposium (International) on Combustion*, 26(1):1 – 26, 1996.
- [25] E. E. O'Brien. The probability density function (pdf) approach to reacting turbulent flows. In *Turbulent reacting flows*, pages 185–218. Springer, 1980.
- [26] S. B. Pope. Pdf methods for turbulent reactive flows. *Progress in Energy and Combustion Science*, 11(2):119–192, 1985.
- [27] FA Williams. Turbulent combustion. *The mathematics of combustion*, 2:267–294, 1985.
- [28] H. Pitsch. A consistent level set formulation for large-eddy simulation of premixed turbulent combustion. *Combustion and Flame*, 143(4):587–598, 2005.
- [29] M. Boger, D. Veynante, H. Boughanem, and A. Trouvé. Direct numerical simulation analysis of flame surface density concept for large eddy simulation of turbulent premixed combustion. In *Symposium (International) on Combustion*, volume 27, pages 917–925. Elsevier, 1998.
- [30] T. D. Butler and P. J. O'Rourke. A numerical method for two dimensional unsteady reacting flows. In *Symposium (International) on Combustion*, volume 16, pages 1503–1515. Elsevier, 1977.
- [31] P. J. O'Rourke and F. V. Bracco. Two scaling transformations for the numerical computation of multidimensional unsteady laminar flames. *Journal of Computational Physics*, 33(2):185–203, 1979.

- [32] F.A. Williams. *Combustion Theory: The Fundamental Theory of Chemically Reacting Flow Systems*. Combustion science and engineering series. Perseus Books Group, 1985.
- [33] K. K. Kuo. Principles of combustion. 1986.
- [34] O. Colin, F. Ducros, D. Veynante, and T. Poinso. A thickened flame model for large eddy simulations of turbulent premixed combustion. *Physics of Fluids (1994-present)*, 12(7):1843–1863, 2000.
- [35] T. Poinso, D. Veynante, A. Trouvé, and G. Ruetsch. Turbulent flame propagation in partially premixed flames. pages 111–136. Center for turbulent reasearch, NASA Ames/Stanford University, USA, 1996.
- [36] C. Meneveau and T. Poinso. Stretching and quenching of flamelets in premixed turbulent combustion. *Combustion and Flame*, 86(4):311–332, 1991.
- [37] C. Angelberger, D. Veynante, F. Egolfopoulos, and T. Poinso. Large eddy simulations of combustion instabilities in premixed flames. In *Proc. of the summer program*, pages 61–82, 1998.
- [38] F. Charlette, C. Meneveau, and D. Veynante. A power-law flame wrinkling model for les of premixed turbulent combustion part ii: dynamic formulation. *Combustion and Flame*, 131(1–2):181 – 197, 2002.
- [39] G. Wang, M. Boileau, and D. Veynante. Implementation of a dynamic thickened flame model for large eddy simulations of turbulent premixed combustion. *Combustion and Flame*, 158(11):2199–2213, 2011.
- [40] J. P. Legier, T. Poinso, and D. Veynante. Dynamically thickened flame les model for premixed and non-premixed turbulent combustion. In *Proc. of the summer program*, pages 157–168. Citeseer, 2000.
- [41] P. Benard. *Analyse et amélioration d’une chambre de combustion centimétrique par simulation aux grandes échelles*. Phd thesis, Rouen, INSA, 2015.
- [42] B. G. Franzelli. *Impact of the chemical description on direct numerical simulations and large eddy simulations of turbulent combustion in industrial aero-engines*. PhD thesis, INPT, 2011.
- [43] S. Elgobashi. An updated classification map of particle-laden turbulent flows. In *IUTAM Symposium on Computational Approaches to Multiphase Flow*, pages 3–10. Springer, 2006.
- [44] R. L. C. Flemmer and C. L. Banks. On the drag coefficient of a sphere. *Powder Technology*, 48(3):217 – 221, 1986.
- [45] L. Schiller and Z. Naumann. A drag coefficient correlation. *Vdi Zeitung*, 77(318):51, 1935.
- [46] B. Farcy. *Analyse des mécanismes de destruction non-catalytique des Oxydes d’Azote (DeNOx) et application à la simulation aux grandes échelles (LES) d’un incinérateur*. Phd thesis, Rouen, INSA, 2015.
- [47] G. L. Hubbard, V. E. Denny, and A. F. Mills. Droplet evaporation: effects of transients and variable properties. *International Journal of Heat and Mass Transfer*, 18(9):1003–1008, 1975.

- [48] W. A. Sirignano. *Fluid dynamics and transport of droplets and sprays*. Cambridge University Press, 2010.
- [49] W. E. Ranz and W. R. Marshall. Evaporation from drops. *Chemical Engineering Progress*, 48(3):141446, 1952.
- [50] N. Enjalbert. *Modélisation avancée de la combustion turbulente diphasique en régime de forte dilution par les gaz brûlés*. Phd thesis, INSA of Rouen, 2015.
- [51] N. A. Okong’o and J. Bellan. Consistent large-eddy simulation of a temporal mixing layer laden with evaporating drops. part 1. direct numerical simulation, formulation and a priori analysis. *Journal of Fluid Mechanics*, 499:1–47, 2004.
- [52] M. Bini and W. P. Jones. Particle acceleration in turbulent flows: A class of nonlinear stochastic models for intermittency. *Physics of Fluids*, 19(3):035104, 2007.
- [53] M. Boivin, O. Simonin, and K. D. Squires. Direct numerical simulation of turbulence modulation by particles in isotropic turbulence. *Journal of Fluid Mechanics*, 375:235–263, 1998.
- [54] S. Yuu, T. Ueno, and T. Umekage. Numerical simulation of the high reynolds number slit nozzle gas–particle jet using subgrid-scale coupling large eddy simulation. *Chemical Engineering Science*, 56(14):4293–4307, 2001.
- [55] W.P. Jones, S. Lyra, and S. Navarro-Martinez. Large eddy simulation of a swirl stabilized spray flame. *Proceedings of the Combustion Institute*, 33(2):2153–2160, 2011.
- [56] M. Sanjosé, J. M. Senoner, F. Jaegle, B. Cuenot, S. Moreau, and T. Poinso. Fuel injection model for euler–euler and euler–lagrange large-eddy simulations of an evaporating spray inside an aeronautical combustor. *International Journal of Multiphase Flow*, 37(5):514–529, 2011.
- [57] DG Goodwin, N Malaya, H Moffat, and R Speth. Cantera: An object oriented software toolkit for chemical kinetics, thermodynamics, and transport processes,. 2012.
- [58] V. Moureau, P. Domingo, and L. Vervisch. From large-eddy simulation to direct numerical simulation of a lean premixed swirl flame: Filtered laminar flame-pdf modeling. *Combustion and Flame*, 158(7):1340–1357, 2011.
- [59] P. Benard, V. Moureau, G. Lartigue, and Y. D’Angelo. Large-eddy simulation of a hydrogen enriched methane/air meso-scale combustor. *International Journal of Hydrogen Energy*, 42(4):2397 – 2410, 2017.
- [60] V. Moureau, P. Domingo, and L. Vervisch. Design of a massively parallel cfd code for complex geometries. *Comptes Rendus Mécanique*, 339(2):141–148, 2011.
- [61] T. Turányi and A. S. Tomlin. *Analysis of kinetic reaction mechanisms*. Springer, 2014.
- [62] T. Turányi. Sensitivity analysis of complex kinetic systems. tools and applications. *Journal of Mathematical Chemistry*, 5(3):203–248, 1990.
- [63] M. W. Gery, G. Z. Whitten, J. P. Killus, and M. C. Dodge. A photochemical kinetics mechanism for urban and regional scale computer modeling. *Journal of Geophysical Research: Atmospheres*, 94(D10):12925–12956, 1989.

- [64] B. Franzelli, E. Riber, M. Sanjosé, and T. Poinso. A two-step chemical scheme for kerosene–air premixed flames. *Combustion and Flame*, 157(7):1364–1373, 2010.
- [65] J. Luche. *Elaboration of reduced kinetic models of combustion. Application to a kerosene mechanism*. PhD thesis, LCSR Orleans, 2003.
- [66] C. K. Westbrook and F. L. Dryer. Chemical kinetic modeling of hydrocarbon combustion. *Progress in Energy and Combustion Science*, 10(1):1–57, 1984.
- [67] W. P. Jones and R. P. Lindstedt. Global reaction schemes for hydrocarbon combustion. *Combustion and Flame*, 73(3):233–249, 1988.
- [68] E. Fernández-Tarrazo, A. L. Sánchez, A. Liñán, and F. A. Williams. A simple one-step chemistry model for partially premixed hydrocarbon combustion. *Combustion and Flame*, 147(1):32–38, 2006.
- [69] M. Cailler, N. Darabiha, D. Veynante, and B. Fiorina. Building-up virtual optimized mechanism for flame modeling. *Proceedings of the Combustion Institute*, 2016.
- [70] B. Franzelli, E. Riber, L. Y. M. Gicquel, and T. Poinso. Large eddy simulation of combustion instabilities in a lean partially premixed swirled flame. *Combustion and Flame*, 159(2):621 – 637, 2012.
- [71] W. Polifke, W. Geng, and K. Döbbeling. Optimization of rate coefficients for simplified reaction mechanisms with genetic algorithms. *Combust. Flame*, 113(1–2):119 – 134, 1998.
- [72] S. Katare, A. Bhan, J. M. Caruthers, W. N. Delgass, and V. Venkatasubramanian. A hybrid genetic algorithm for efficient parameter estimation of large kinetic models. *Computers & chemical engineering*, 28(12):2569–2581, 2004.
- [73] L. Elliott, D. B. Ingham, A. G. Kyne, N. S. Mera, M. Pourkashanian, and C. W. Wilson. Multiobjective genetic algorithm optimization for calculating the reaction rate coefficients for hydrogen combustion. *Industrial & engineering chemistry research*, 42(6):1215–1224, 2003.
- [74] L. Elliott, D. B. Ingham, A. G. Kyne, N. S. Mera, M. Pourkashanian, and S. Whittaker. Reaction mechanism reduction and optimisation for modelling aviation fuel oxidation using standard and hybrid genetic algorithms. *Comput. Chem. Eng.*, 30(5):889 – 900, 2006.
- [75] F. Perini, J. L. Brakora, R. D. Reitz, and G. Cantore. Development of reduced and optimized reaction mechanisms based on genetic algorithms and element flux analysis. *Combustion and Flame*, 159(1):103–119, 2012.
- [76] B Farcy, A. Abou-Taouk, L. Vervisch, P. Domingo, and N. Perret. Two approaches of chemistry downsizing for simulating selective non catalytic reduction DeNOx process. *Fuel*, 118:291–299, 2014.
- [77] M. Apri, M. de Gee, and J. Molenaar. Complexity reduction preserving dynamical behavior of biochemical networks. *Journal of theoretical biology*, 304:16–26, 2012.

- [78] P. Gokulakrishnan, R. Joklik, D. Viehe, A. Trettel, E. Gonzalez-Juez, and M. Klassen. Optimization of reduced kinetic models for reactive flow simulations. *Journal of Engineering for Gas Turbines and Power*, 136(1):011503, 2014.
- [79] A. Roux, L. Y. M. Gicquel, S. Reichstadt, N. Bertier, G. Staffelbach, F. Vuillot, and T. J. Poinot. Analysis of unsteady reacting flows and impact of chemistry description in large eddy simulations of side-dump ramjet combustors. *Combustion and Flame*, 157(1):176 – 191, 2010.
- [80] A. S. Tomlin, T. Turányi, and M. J. Pilling. Mathematical tools for the construction, investigation and reduction of combustion mechanisms. *Comprehensive chemical kinetics*, 35:293–437, 1997.
- [81] M. Frenklach, K. Kailasanath, and E. S. Oran. Systematic development of reduced reaction mechanisms for dynamic modeling. 1986.
- [82] E. S. Oran and J. P. Boris. Numerical approaches to combustion modeling. progress in astronautics and aeronautics. vol. 135. 1991.
- [83] D. Nilsson, T. Løvås, P. Amneus, and F. Mauss. Reduction of complex fuel chemistry for simulation of combustion in an hcci engine. *VDI BERICHTE*, 1492:511–516, 1999.
- [84] I. P. Androulakis. “store and retrieve” representations of dynamic systems motivated by studies in gas phase chemical kinetics. *Computers & chemical engineering*, 28(11):2141–2155, 2004.
- [85] M. Valorani, F. Creta, D. A. Goussis, J. C. Lee, and H. N. Najm. An automatic procedure for the simplification of chemical kinetic mechanisms based on csp. *Combustion and Flame*, 146(1):29–51, 2006.
- [86] T. Lu and C. K. Law. A directed relation graph method for mechanism reduction. *Proceedings of the Combustion Institute*, 30(1):1333–1341, 2005.
- [87] X. L. Zheng, T. F. Lu, and C. K. Law. Experimental counterflow ignition temperatures and reaction mechanisms of 1, 3-butadiene. *Proceedings of the Combustion Institute*, 31(1):367–375, 2007.
- [88] P. Pepiot and H. Pitsch. Systematic reduction of large chemical mechanisms. In *4th joint meeting of the US Sections of the Combustion Institute, Philadelphia, PA*, 2005.
- [89] W. Sun, Z. Chen, X. Gou, and Y. Ju. A path flux analysis method for the reduction of detailed chemical kinetic mechanisms. *Combustion and Flame*, 157(7):1298–1307, 2010.
- [90] X. Gou, Z. Chen, W. Sun, and Y. Ju. A dynamic adaptive chemistry scheme with error control for combustion modeling with a large detailed mechanism. *Combustion and Flame*, 160(2):225–231, 2013.
- [91] K. Edwards, T. F. Edgar, and V. I. Manousiouthakis. Kinetic model reduction using genetic algorithms. *Computers & chemical engineering*, 22(1-2):239–246, 1998.
- [92] N. Sikalo, O. Hasemann, C. Schulz, A. Kempf, and I. Wlokas. A genetic algorithm-based method for the automatic reduction of reaction mechanisms. *Int. J. Chem. Kinetics*, 46(1):41–59, 2013.
- [93] M. S. Okino and M. L. Mavrouniotis. Simplification of mathematical models of chemical reaction systems. *Chemical reviews*, 98(2):391–408, 1998.

- [94] B. Sportisse and R. Djouad. Reduction of chemical kinetics in air pollution modeling. *Journal of Computational Physics*, 164(2):354–376, 2000.
- [95] G. Li, H. Rabitz, and J. Tóth. A general analysis of exact nonlinear lumping in chemical kinetics. *Chemical Engineering Science*, 49(3):343–361, 1994.
- [96] M. R. Maurya, S. Katare, P. R. Patkar, A. E. Rundell, and V. Venkatasubramanian. A systematic framework for the design of reduced-order models for signal transduction pathways from a control theoretic perspective. *Computers & Chemical Engineering*, 30(3):437 – 452, 2006.
- [97] R. Fournet, V. Warth, P. A. Glaude, F. Battin-Leclerc, G. Scacchi, and G. M. Come. Automatic reduction of detailed mechanisms of combustion of alkanes by chemical lumping. *International Journal of Chemical Kinetics*, 32(1):36–51, 2000.
- [98] E. Ranzi, M. Dente, A. Goldaniga, G. Bozzano, and T. Faravelli. Lumping procedures in detailed kinetic modeling of gasification, pyrolysis, partial oxidation and combustion of hydrocarbon mixtures. *Progress in Energy and Combustion Science*, 27(1):99–139, 2001.
- [99] A. Stagni, A. Cuoci, A. Frassoldati, T. Faravelli, and E. Ranzi. Lumping and reduction of detailed kinetic schemes: an effective coupling. *Industrial & Engineering Chemistry Research*, 53(22):9004–9016, 2013.
- [100] J. Wei and J. C. W. Kuo. Lumping analysis in monomolecular reaction systems. analysis of the exactly lumpable system. *Industrial & Engineering chemistry fundamentals*, 8(1):114–123, 1969.
- [101] G. Li and H. Rabitz. A general analysis of exact lumping in chemical kinetics. *Chemical engineering science*, 44(6):1413–1430, 1989.
- [102] P. Pepiot-Desjardins and H. Pitsch. An automatic chemical lumping method for the reduction of large chemical kinetic mechanisms. *Combustion Theory and Modelling*, 12(6):1089–1108, 2008.
- [103] J. Y. Chen. Development of reduced mechanisms for numerical modelling of turbulent combustion. In *Workshop on Numerical Aspects of Reduction in Chemical Kinetics*, 1997.
- [104] T. Lu and C. K. Law. Toward accommodating realistic fuel chemistry in large-scale computations. *Progress in Energy and Combustion Science*, 35(2):192–215, 2009.
- [105] A. C. Zambon and H. K. Chelliah. Explicit reduced reaction models for ignition, flame propagation, and extinction of $C_2H_4/CH_4/H_2$ and air systems. *Combustion and Flame*, 150(1–2):71 – 91, 2007.
- [106] M. Frenklach, H. Wang, M. Goldenberg C. L. Yu, C. T. Bowman, R. K. Hanson, D. F. Davidson, E. J. Chang, G. P. Smith, D. M. Golden, W. C. Gardiner, and V. Lissianski. Technical report, 1995. <http://www.me.berkeley.edu/gri-mech/>.
- [107] M. Frenklach, H. Wang, M. Goldenberg, G. P. Smith, D. M. Golden, C. T. Bowman, R. K. Hanson, W. C. Gardiner, and V. Lissianski. Gri-mech—an optimized detailed chemical reaction mechanism for methane combustion. Technical Report GRI-95/0058, Gas Research Institute Topical Report, November 1995.

- [108] C. J. Montgomery, C. Yang, A. R. Parkinson, and J. Y. Chen. Selecting the optimum quasi-steady-state species for reduced chemical kinetic mechanisms using a genetic algorithm. *Combustion and Flame*, 144(1–2):37 – 52, 2006.
- [109] A. Arvidsson. *Development of an Automatic Reduction Tool for Chemical Mechanisms and an Optimized Sparse Matrix Solver for Systems of Differential and Algebraic Equations*. PhD thesis, Lund University, 2010.
- [110] T. Løvas, D. Nilsson, and F. Mauss. Automatic reduction procedure for chemical mechanisms applied to premixed methane/air flames. *Proceedings of the Combustion Institute*, 28(2):1809–1815, 2000.
- [111] T. Lu and C. K. Law. Systematic approach to obtain analytic solutions of quasi steady state species in reduced mechanisms. *The Journal of Physical Chemistry A*, 110(49):13202–13208, 2006.
- [112] N. Peters and B. Rogg. *Reduced kinetic mechanisms for applications in combustion systems*. Springer Science & Business Media, 1993.
- [113] P. Pepiot. *Automatic strategies to model transportation fuel surrogates*. PhD thesis, Stanford University, 2008.
- [114] L. D. Smoot, W. C. Hecker, and G. A. Williams. Prediction of propagating methane-air flames. *Combustion and flame*, 26:323–342, 1976.
- [115] F. A. Williams. An approach to turbulent flame theory. *Journal of Fluid Mechanics*, 40(2):401–421, 1970.
- [116] D. B. Spalding. Mixing and chemical reaction in steady confined turbulent premixed flames. *Symp. (Int.) Combust.*, 13(1):649–657, 1971.
- [117] A. Liñán. The asymptotic structure of counterflow diffusion flames for large activation energies. *Acta Astronautica*, (1):1007–1039, 1974.
- [118] W. B. Bush and F. E. Fendell. Diffusion flames in turbulent shear flows. *Combust. Sci. Tech.*, pages 35–48, 1975.
- [119] G. E. Andrews, D. Bradley, and S. B. Lwakabamba. Turbulence and turbulent flame propagation - Critical appraisal. *Combust. Flame*, 24(3):285–304, 1975.
- [120] P. A. Libby. Studies related to turbulent flows involving fast chemical reactions in analytical and numerical methods for investigation of flow fields with chemical reactions, especially related to combustion. Technical report, 1976.
- [121] J.-B. Moss and K.N.C. Bray. A unified statistical model of the premixed turbulent flame. *Acta Astronaut.*, 4:291–319, 1977.
- [122] F. Marble and J. Broadwell. The coherent flame model of non-premixed turbulent combustion. Technical report, 1977.
- [123] R. W. Bilger. The structure of diffusion flames. *Combust. Sci. and Tech.*, 13:155–170, 1976.

- [124] F. E. Marble and S. M. Candel. An analytical study of the non-steady behavior of large combustors. *Symp. (Int.) on Combust.*, 17(1):761–769, 1978.
- [125] K. N. C. Bray, P. A. Libby, and J. B. Moss. Flamelet crossing frequencies and mean reaction rates in premixed turbulent combustion. *Combust. Sci. Tech.*, 41(3-4):143–172, 1984.
- [126] C. Dopazo and E. O'Brien. Functional formulation of nonisothermal turbulent reactive flows. *Phys. Fluids*, 17:1968–1975, 1974.
- [127] G. Joulin and P. Clavin. Asymptotic analysis of a premixed laminar flame governed by a 2-step reaction. *Combust. Flame*, 25(3):389–392, 1975.
- [128] C. Bonniot and R. Borghi. Joint probability density-function in turbulent combustion. *Acta Astronautica*, 6(3-4):309–327, 1979.
- [129] E. S. Oran and J. P. Boris. Detailed modeling of combustion systems. *Prog. Energ. Combust. Sci.*, 7(1):1–72, 1981.
- [130] N. Peters. Numerical and asymptotic analysis of systematically reduced reaction schemes for hydrocarbon flames. In R. Glowinski, B. Larrouturou, and R. Teman, editors, *Numerical Simulation of Combustion Phenomena*, volume 241 of *Lecture Notes in Physics*, pages 90–109. Springer Berlin Heidelberg, 1985.
- [131] W. P. Jones and R. P. Lindstedt. Global reaction schemes for hydrocarbon combustion. *Combust. Flame*, 73:233–249, 1988.
- [132] J. Janicka, W. Kolbe, and W. Kollmann. Closure of the transport equation for the probability density function of turbulent scalar fields. *J. Non-Equilib. Thermodyn.*, 4(47), 1979.
- [133] J. Y. Chen and W. Kollmann. PDF modeling of chemical nonequilibrium effects in turbulent non-premixed hydrocarbon flames. *Symp. (Int.) on Combust.*, 22, 1988.
- [134] J.-Y. Chen and W. Kollmann. Chemical models for pdf modeling of hydrogen-air non-premixed turbulent flames. *Combust. Flame*, 79:75, 1990.
- [135] N. Peters. Laminar flamelet concepts in turbulent combustion. *Symp. (Int.) on Combust.*, 21(1):1231–1250, 1988.
- [136] J. Warnatz. The structure of laminar alkane-, alkene-, and acetylene flames. In *Symposium (International) on Combustion*, volume 18, pages 369–384. Elsevier, 1981.
- [137] T. P. Coffee. Kinetic mechanisms for premixed, laminar, steady state methane/air flames. *Combustion and flame*, 55(2):161–170, 1984.
- [138] N. Peters. *Numerical Simulation of Combustion Phenomena: Proceedings of the Symposium Held at INRIA Sophia-Antipolis, France May 21–24, 1985*, chapter Numerical and asymptotic analysis of systematically reduced reaction schemes for hydrocarbon flames, pages 90–109. Springer Berlin Heidelberg, Berlin, Heidelberg, 1985.
- [139] E. L. Petersen, D. F. Davidson, and R. K. Hanson. Kinetics modeling of shock-induced ignition in low-dilution CH_4/O_2 mixtures at high pressures and intermediate temperatures. *Combustion and Flame*, 117(1–2):272 – 290, 1999.

- [140] G. P. Smith, D. M. Golden, M. Frenklach, N. W. Moriarty, B. Eiteneer, M. Goldenberg, C. T. Bowman, R. K. Hanson, S. Song, W. C. Gardiner, V. V. Lissianski, and Z. Qin. Technical report, 1999.
- [141] R. Sankaran, E. R. Hawkes, J. H. Chen, T. Lu, and C. K. Law. Structure of a spatially developing turbulent lean methane–air bunsen flame. *Proceedings of the Combustion Institute*, 31(1):1291 – 1298, 2007.
- [142] K. J. Hughes, T. Turanyi, A. R. Clague, and M. J. Pilling. Development and testing of a comprehensive chemical mechanism for the oxidation of methane. *International Journal of Chemical Kinetics*, 33(9):513–538, 2001.
- [143] T. Lu and C. K. Law. A criterion based on computational singular perturbation for the identification of quasi steady state species: A reduced mechanism for methane oxidation with {NO} chemistry. *Combustion and Flame*, 154(4):761 – 774, 2008.
- [144] Chemical-kinetic mechanisms for combustion applications, San Diego mechanism web page, mechanical and aerospace engineering (Combustion Research), University of California at San Diego, 2017.
- [145] G. Tsatsaronis. Prediction of propagating laminar flames in methane, oxygen, nitrogen mixtures. *Combustion and Flame*, 33:217–239, 1978.
- [146] G. Dixon-Lewis and S. M. Islam. Flame modelling and burning velocity measurement. *Symposium (International) on Combustion*, 19(1):283 – 291, 1982. Nineteenth Symposium (International) on Combustion.
- [147] R. Lindow. *Brennstoff Wärme Kraft*, 20(8), 1968.
- [148] S. B. Reed, J. Mineur, and J. P. McNaughton. The effect on the burning velocity of methane of vitiation of combustion air. *J. Inst. Fuel*, 44(149), 1971.
- [149] G. E. Andrews and D. Bradley. Determination of burning velocity by double ignition in a closed vessel. *Combustion and Flame*, 20(1):77 – 89, 1973.
- [150] R. Günther and G. Janisch. Measurements of burning velocity in a flat flame front. *Combustion and Flame*, 19(1):49–53, 1972.
- [151] P. Lindstedt. Modeling of the chemical complexities of flames. *Symposium (International) on Combustion*, 27(1):269–285, 1998.
- [152] D. Goodwin. Cantera: An object-oriented software toolkit for chemical kinetics, thermodynamics, and transport processes, 2009.
- [153] C. F. Curtiss and J. O. Hirschfelder. Transport properties of multicomponent gas mixtures. *Journal of Chemical Physics*, 17:550, 1949.
- [154] V. Giovangigli. *Multicomponent Flow Modeling*. Modeling and Simulation in Science, Engineering and Technology. Birkhäuser, Springer, 1999.

- [155] J. H. Holland. *Adaptation in Natural and Artificial Systems*. MIT Press, Cambridge, MA, USA, 1992.
- [156] N. M. Razali and J. Geraghty. Genetic algorithm performance with different selection straggles in solving tsp. In *Proceedings of the World Congress on Engineering*, volume II, London, 2011. WCE.
- [157] P. Boivin, C. Jiménez, A. L. Sánchez, and F. A. Williams. An explicit reduced mechanism for H₂ air combustion. *Proc. Combust. Inst.*, 33(1):517 – 523, 2011.
- [158] J. Warnatz, U. Maas, and R. W. Dibble. *Combustion: Physics and Chemical Fundamentals, Modeling and Simulation, Experiments, Pollutant Formation, 4th Edition*. Springer, 2006.
- [159] R. L. Curl. Dispersed phase mixing: I. theory and effects in simple reactors. *AIChE journal*, 9(2):175–181, 1963.
- [160] B. Farcy, L. Vervisch, P. Domingo, and N. Perret. Reduced-order modeling for the control of selective noncatalytic reduction of nitrogen monoxide. *AIChE Journal*, 62(3):928–938, 2016.
- [161] C. Dopazo and E. E. O’Brien. Functional formulation of nonisothermal turbulent reactive flows. *The Physics of Fluids*, 17(11):1968–1975, 1974.
- [162] R. Borghi. Turbulent combustion modelling. *Prog. Energy Combust. Sci.*, 14:245–292, 1988.
- [163] R. Cabra, J. Y. Chen, R. W. Dibble, A. N. Karpetis, and R. S. Barlow. Lifted methane-air jet flame in vitiated coflow. *Combust. Flame*, 143(4):491–506, 2005.
- [164] N. Enjalbert, P. Domingo, and L. Vervisch. Mixing time-history effects in large eddy simulation of non-premixed turbulent flames: Flow-controlled chemistry tabulation. *Combust. Flame*, 159(1):336–352, 2012.
- [165] S. Candel, T. Schmitt, and N. Darabiha. Progress in transcritical combustion : Experimentation, modeling and simulation. *23rd ICDERS Conf. (2011)*, 2011.
- [166] N. Peters. Length scales in laminar and turbulent flames. In E. S. Oran and J. A. Boris, editors, *Numerical approaches to Combustion Modeling*, volume 135 of *Prog. Astronautics and Aeronautics*, pages 155–182, Washington DC, 1991. AIAA.
- [167] N. Peters. *Turbulent Combustion*. Cambridge University Press, 2000.
- [168] J. Boulanger and L. Vervisch. Diffusion edge-flame: Approximation of the flame tip damköhler number. *Combust. Flame*, 130(1):1–14, 2002.
- [169] A. R. Kerstein. Hierarchical parcel-swapping representation of turbulent mixing. part 2. application to channel flow. *J. Fluid Mech.*, 750:421–463, 2014.
- [170] D. C. Haworth. Progress in probability density function methods for turbulent reacting flows. *Prog. Energy Combust. Sci.*, 36(2):168–259, 2010.
- [171] S. Subramaniam and S. B. Pope. A mixing model for turbulent reactive flows based on euclidean minimum spanning trees. *Combust. Flame*, 115(4):487–514, 1998.

- [172] R. O. Fox. *Computational models for turbulent reacting flows*. Cambridge University Press, 2003.
- [173] J. Adanez, A. Abad, F. Garcia-Labiano, P. Gayan, and L. F. de Diego. Progress in chemical-looping combustion and reforming technologies. *Prog. Energy Combust. Sci.*, 38(2):215–282, 2012.
- [174] M. K. Drayton, A. V. Saveliev, L. A. Kennedy, A. A. Fridman, and Y.-E. Li. Syngas production using superadiabatic combustion of ultra-rich methane-air mixtures. In *Symposium (International) on Combustion*, volume 27, pages 1361–1367, 1998.
- [175] B. Stelzner, F. Hunger, S. Voss, J. Keller, C. Hasse, and D. Trimis. Experimental and numerical study of rich inverse diffusion flame structure. *Proc. Combust. Inst.*, 34(1):1045–1055, 2013.
- [176] K. Aasberg-Petersen, I. Dybkjær, C. V. Ovesen, N. C. Schjødt, J. Sehested, and S. G. Thomsen. Natural gas to synthesis gas. catalysts and catalytic processes. *Journal of Natural Gas Science and Engineering*, 3:423–459, 2011.
- [177] J. Caudal, B. Fiorina, B. Labegorre, and O. Gicquel. Modeling interactions between chemistry and turbulence for simulations of partial oxidation processes. *Fuel Processing Technology*, 134:231–242, 2015.
- [178] C. Higman and M. van der Burgt. *Gasification*. Gulf Professional Publishing, 2nd edition, 2008.
- [179] I. Dybkjær. Tubular reforming and auto-thermal reforming of natural gas: an overview of available processes. *Fuel Processing Technology*, 42:85–107, 1995.
- [180] M. Zahedi Nezhad, S. Rowshanzamir, and M. H. Eikani. Autothermal reforming of methane to synthesis gas: Modeling and simulation. *International Journal of Hydrogen Energy*, 34(3):1292–1300, 2009.
- [181] M. Vascellari, H. Xu, S. Hartl, F. Hunger, and C. Hasse. Flamelet/progress variable modeling of partial oxidation systems: From laboratory flames to pilot-scale reactors. *Chem. Eng. Sci.*, 134:694–707, 2015.
- [182] B. Farcy, L. Vervisch, and P. Domingo. Large eddy simulation of selective non-catalytic reduction (snrc): A downsizing procedure for simulating nitric-oxide reduction units. *Chem. Eng. Sci.*, 139:285–303, 2016.
- [183] A. Richter, P. Seifert, F. Compart, P. Tischer, and B. Meyer. A large-scale benchmark for the CFD modeling of non-catalytic reforming of natural gas based on the Freiberg test plan HP POX. *Fuel*, 152:110–121, 2015.
- [184] G. Lodier and B. Labegorre. *Air Liquide. Private communication*, 2016.
- [185] B. F. Magnussen. On the structure of turbulence and a generalized eddy dissipation concept for chemical reaction in turbulent flow. In *19th Aerospace Sciences Meeting*, page 42.
- [186] B. F. Magnussen. The eddy dissipation concept—a bridge between science and technology.
- [187] ICAO environmental report 2016. Technical report, International Civil Aviation Organisation, <http://www.icao.int/environmental-protection/Documents/ICAO2016>.

- [188] A. H. Lefebvre. *Gas turbine combustion*. CRC Press, 2010.
- [189] P. Gokulakrishnan, M. J. Ramotowski, G. Gaines, C. Fuller, R. Joklik, L. D. Eskin, M. S. Klassen, and R. J. Roby. A novel low nox lean, premixed, and prevaporized combustion system for liquid fuels. *Journal of engineering for gas turbines and power*, 130(5):051501, 2008.
- [190] G. G. De Soete. Overall reaction rates of no and n2 formation from fuel nitrogen. In *Symposium (international) on combustion*, volume 15, pages 1093–1102. Elsevier, 1975.
- [191] C.P. Fenimore and H.A. Fraenkel. Formation and interconversion of fixed-nitrogen species in laminar diffusion flames. *Symposium (International) on Combustion*, 18(1):143 – 149, 1981.
- [192] Y. B. Zeldovich. The oxidation of nitrogen in combustion and explosions. *Acta Physicochim. URSS*, 21(4):577–628, 1946.
- [193] J. W. Bozzelli and A. M. Dean. O+ nnh: A possible new route for nox formation in flames. *International journal of chemical kinetics*, 27(11):1097–1109, 1995.
- [194] S. Baessler, K. G. Mösl, and T. Sattelmayer. Nox emissions of a premixed partially vaporized kerosene spray flame. *Journal of Engineering for Gas Turbines and Power*, 129(3):695–702, 2007.
- [195] A. Wulff and J. Hourmouziadis. Technology review of aeroengine pollutant emissions. *Aerospace science and technology*, 1(8):557–572, 1997.
- [196] S. K. Dhanuka, J. E. Temme, J. F. Driscoll, and H. C. Mongia. Vortex-shedding and mixing layer effects on periodic flashback in a lean premixed prevaporized gas turbine combustor. *Proceedings of the Combustion Institute*, 32(2):2901–2908, 2009.
- [197] P. Dagaut. On the kinetics of hydrocarbons oxidation from natural gas to kerosene and diesel fuel. *Physical Chemistry Chemical Physics*, 4(11):2079–2094, 2002.
- [198] B. Fiorina, A. Vié, B. Franzelli, N. Darabiha, M. Massot, G. Dayma, P. Dagaut, V. Moureau, L. Vervisch, A. Berlemont, et al. Modeling challenges in computing aeronautical combustion chambers. *AerospaceLab*, (11):19–pages, 2016.
- [199] L. Guedot. *Développement de méthodes numériques pour la caractérisation des grandes structures tourbillonnaires dans les brûleurs aéronautiques: application aux systèmes d'injection multi-points*. PhD thesis, Rouen, INSA, 2015.
- [200] N. K. Rizk and A. H. Lefebvre. Internal flow characteristics of simplex swirl atomizers. *Journal of Propulsion and Power*, 1(3):193–199, 1985.
- [201] S. Freitag and C. Hassa. Spray characteristics of a kerosene jet in cross of air at elevated pressure. In *ILASS-Europe*, Italy, 2008.
- [202] D. Midou. *Optimisation d'une lance d'injection de charbon pulvérisé*. Phd thesis, Rouen, INSA, 2017.
- [203] K. Bioche. *Etude et simulation de la micro-combustion assistée par plasma et excès d'enthalpie*. Phd thesis, Rouen, INSA, 2019.